Nanotubes, Fullerenes, Nanostructured and Disordered Carbon

Nanotubes, Fullerenes, Nanostructured and Disordered Carbon

Symposium held April 17–20, 2001, San Francisco, California, U.S.A.

EDITORS:

John Robertson
Cambridge University
Cambridge, United Kingdom

Thomas A. Friedmann
Sandia National Laboratories
Albuquerque, New Mexico, U.S.A.

David B. Geohegan
Oak Ridge National Laboratory
Oak Ridge, Tennessee, U.S.A.

David E. Luzzi
University of Pennsylvania
Philadelphia, Pennsylvania, U.S.A.

Rodney S. Ruoff
Northwestern University
Evanston, Illinois, U.S.A.

MRS

Single article reprints from this publication are available through University Microfilms Inc., 300 North Zeeb Road, Ann Arbor, Michigan 48106

CODEN: MRSPDH

This book has been registered with Copyright Clearance Center, Inc. For further information, please contact the Copyright Clearance Center, Salem, Massachusetts.

Published by:

Manufactured in the United States of America

CONTENTS

FULLERENES

NANOTUBE GROWTH

NANOTUBE PROPERTIES

FIELD EMISSION

DIAMOND-LIKE CARBON

*Invited Paper

DIAMOND

PREFACE

There has been a tremendous advance in the science of carbon in the last 20 years. The discovery of the C_{60} molecule and the other fullerenes was followed by the discovery of carbon nanotubes. Earlier, it was learned how to make diamond at low pressure by chemical vapor deposition.

This symposium, "Nanotubes, Fullerenes, Nanostructured and Disordered Carbon," held April 17–20 at the 20001 MRS Spring Meeting in San Francisco, California, brought together people working in the full range of carbon phases. It covered both ordered solids and molecules and disordered solids. It ranged from the sp^2 bonded nanotubes and fullerenes to the sp^3 bonded amorphous carbons and diamond. The symposium developed from a symposium on "Amorphous and Nanostructured Carbon" held at the 1999 MRS Fall Meeting, and was also related to the "Nanotubes and Related Materials" symposium held at the 2000 MRS Fall Meeting.

The speakers covered a wide range of topics, from structure and growth of fullerenes, to the growth and application of nanotubes, to the growth and uses of diamond-like carbon. A wide range of applications were covered, and the main application described in this book is field emission.

This proceedings volume is organized into six sections. The first section deals with fullerenes. The second and third sections deal with the growth and properties of nanotubes. The fourth section deals with field emission, the fifth with diamond-like carbon, and the sixth with diamond.

<div align="right">

John Robertson
Thomas A. Friedmann
David B. Geohegan
David E. Luzzi
Rodney S. Ruoff

June 2001

</div>

ACKNOWLEDGMENTS

MATERIALS RESEARCH SOCIETY SYMPOSIUM PROCEEDINGS

MATERIALS RESEARCH SOCIETY SYMPOSIUM PROCEEDINGS

Fullerenes

Encapsulated Molecules in Carbon Nanotubes: Structure and Properties

Richard Russo, Brian W. Smith, B.C. Satishkumar, David E. Luzzi*

Laboratory for Research in the Structure of Matter
*Department of Materials Science and Engineering
University of Pennsylvania
3231 Walnut Street, Philadelphia, PA 19104-6272, USA

Harry C. Dorn

Department of Chemistry
Virginia Polytechnic Institute and State University
Blacksburg, Virginia 24061, USA

ABSTRACT

We encapsulate a number of fullerenes inside single-walled carbon nanotubes (SWNTs) including $La_2@C_{80}$ and $Er_xSc_{3-x}N@C_{80}$(x=0-3). The structural properties of these nanoscopic hybrid materials are described using high resolution transmission electron microscopy and electron diffraction. It is found that the encapsulated fullerenes self-assemble into long, one-dimensional chains. The thermal stability of these supramolecular assemblies are studied and large variations are found. The behavior is nominally consistent with the mass of the encapsulated metallofullerenes.

INTRODUCTION

Many future applications of single-walled carbon nanotubes (SWNTs) will depend upon the ability to modify their intrinsic properties by manipulating their structure. One novel means for modifying the properties of a SWNT is through the filling of its interior cavity with other molecules. For example, we have shown that "peapods," comprising SWNTs filled with 1-D chains of C_{60}, can be manufactured via a vapor phase and/or surface diffusion mechanism. This scalable process consists of annealing the sample in the presence of C_{60} at ~400°C. The presence of interior C_{60} is known to decrease the SWNT's compressibility [1] and has been shown by molecular dynamics simulation to increase its elastic modulus [2].

Our method of encapsulation has recently been extended to other related molecules, including the metallofullerenes $La_2@C_{80}$ and $Gd@C_{82}$. The case of $La_2@C_{80}@SWNT$ served as the first definitive proof that a non-intrinsic molecule could be inserted in bulk into SWNTs. In these experiments, it was directly observed by transmission electron microscopy (TEM) that the La atoms within the encapsulated C_{80} cages tumbled in a discontinuous motion [3], in direct conflict with the continuous motion detected by solution NMR experiments [4]. This was interpreted as the result of an interaction between the SWNT and the contained $La_2@C_{80}$ molecules, providing yet another

indication that interior molecules can modify the properties of a SWNT. In the case of Gd@C_{82}@SWNT, preliminary results indicate that the electrical resistance of a SWNT mat was affected by the presence of interior Gd@C_{82} [5].

The present work involves a novel endohedral metallofullerene system, $Er_xSc_{3-x}N$@C_{80} (x =0-3). This system comes with the ability to substitute several different metals in the nitrogen cluster, which will undoubtedly affect the charge transfer properties between the metal nitride cluster and the fullerene cage. These effects, when coupled with encapsulation in SWNTs, will create a series of hybrid materials with tunable electronic properties. In addition, a typical yield in the synthesis of metallofullerenes is 0.5%. It has been found that the yield of Sc_3N@C_{80} is 3-5%. Unfortunately, the physical properties of these metallofullerenes, such as sublimation temperature, equilibrium vapor pressure, as well as structural properties of this system, are not yet known. Knowledge of these quantities is helpful for the optimization of the conditions for filling carbon nanotubes.

However, the structure of the metallofullerene, Sc_3N@C_{80}, has been characterized by ^{13}C and [45]Sc NMR [6]. These results indicate that the C_{80} cage possesses I_h symmetry and the encapsulated Sc_3N cluster is not localized at specific bonding sites. In these respects, Sc_3N@C_{80} has a structure similar to that of La_2@C_{80}. However, it was found during HPLC studies that Sc_3N@C_{80} elutes with C_{84}-C_{86} cages, and La_2@C_{80} elutes with C_{88}-C_{90} cages [6]. This difference in elution time has been attributed to a decrease of approximately four Pi electrons at the fullerene cage surface relative to La_2@C_{80} and suggests significant electron withdrawal from the carbon cage surface by the central nitrogen atom. Absorption onsets at 1560 nm and 1000 nm were found by UV-Vis/NIR spectroscopy for La_2@C_{80} and Sc_3N@C_{80}, respectively. These correspond to bandgaps of 0.8 and 1.3 eV [6].

While the structural characteristics of La_2@C_{80} and Sc_3N@C_{80} are similar, their electronic properties are very different. While it is difficult to estimate the electronic properties of the other members of $Er_xSc_{3-x}N$@C_{80} (x =0-3), by comparing the filling of SWNTs with these molecules, some insight into the effect of the different charge transfer properties can be achieved. In this paper, the synthesis, structure and high temperature stability of the supramolecular assemblies ($Er_xSc_{3-x}N$@C_{80}@SWNT) are characterized and compared with La_2@C_{80}@SWNT.

EXPERIMENTAL

A detailed description of the method by which certain molecules can be inserted into SWNTs is found in our previous works. In this study, Sc_3N@C_{80} was dissolved in toluene, the remaining metallofullerenes were dissolved in carbon disulfide(CS_2). The metallofullerene solution was pipetted dropwise onto a TEM-sized sample of acid-purified SWNT paper synthesized by the arc method [3]. The solvent was allowed to evaporate, and the dry sample was inserted into a JEOL 2010F field emission TEM. The sample was annealed in-situ at 400°C for 10 h at a pressure of ~20-40 μPa. Upon cooling to room temperature, the nanotubes were examined with 97 keV electrons.

(a)

Figure 1 : (a) $Sc_3N@C_{80}@SWNT$. (b)
SAD $Sc_3N@C_{80}@SWNT$
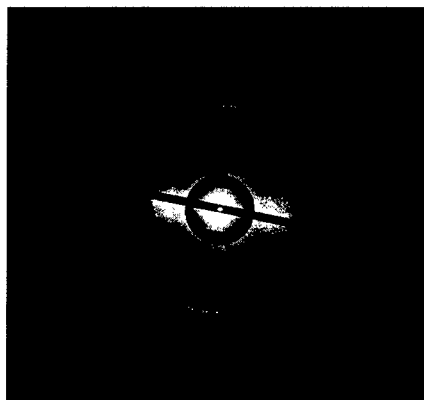
(b)

The $Er_xSc_{3-x}N@C_{80}$ (x =0-3) samples were prepared in a similar manner. However, after doping with metallofullerene/CS_2 solution, the samples were placed in a glass ampoule. The ampoule was evacuated under turbo vacuum (10^{-7} torr), the sample was annealed for one hour at 250°C to remove the solvent, and then sealed, all under vacuum. The sealed ampoule with the sample was annealed at 550°C for 44 hours. Upon cooling, the ampoule was broken and the sample was annealed, again, under dynamic vacuum (10^{-7} torr) at 800°C for one hour to remove exterior metallofullerenes. The sample was then cooled, and observed using 97 keV electrons. The $La_2@C_{80}$ sample was prepared in the same manner, however, it was annealed at 600°C for 96 hours.

After being subjected to the above procedure, high temperature experiments were performed via encapsulation under $\sim10^{-7}$ torr in a sealed quartz ampoule. Annealing temperatures were 1250°C and 950°C for $Sc_3N@C_{80}$, $La_2@C_{80}$, and $Er_3N@C_{80}$, respectively. The annealing time was 12 hours for each sample.

RESULTS AND DISCUSSION

Efficient filling of SWNTs was achieved for all of the metallofullerenes in this study. In the example in Figure 1a, it is seen that filling of SWNTs with $Sc_3N@C_{80}$ is essentially complete in certain regions of the sample. Each metallofullerene is a weak phase object, whose image is a direct projection of the three dimensional specimen potential in the direction of the electron beam. The images are darkest where the beam propagates through the greatest mass-thickness and is most strongly scattered. Thus, the dark contrast features seen around the edges of the cages are the Sc_3N clusters. There appears to be no organized motion of the endohedral atoms, such as the "ratcheting" that is seen in the case of $La_2@C_{80}$. However, the fact that the clusters are visible under ambient conditions implicates some interaction between the tube and its interior molecules.

Figure 1b shows an electron diffraction (SAD) pattern of a single nanotube rope, abundantly filled with $Sc_3N@C_{80}$, similar to those that appear in Figure 1a. Note that the central area of the pattern is printed at a different contrast scale than the outer area so that

all diffraction features can be more easily seen. This gives rise to a discontinuous contrast artifact where the two areas meet. To facilitate a detailed discussion of the pattern, we begin by defining the meridian and equator as the reciprocal space axes parallel and perpendicular to the predominant direction of the real space rope axis, respectively. The pattern consists of three features: (1) a series of low-Q arcs, centered about the equator (2) a series of high-Q arcs, centered about the meridian, and (3) a series of low-Q reflections, centered about the meridian.

The low-Q equatorial arcs arise from constructive scattering by the planes of SWNTs comprising the rope. The intensity of each arc is greatest at the equatorial axis, reflecting the predominant rope orientation, and subtends an angle corresponding to the mosaic of angular orientations contained within the rope. In other words, the reflections appear as arcs because the rope axis is not perfectly straight over the diffracting area. Due to the small number of lattice planes that comprise the rope, a finite size effect is seen in the form of radial broadening. The reflections are approximately equally spaced in the radial direction, forming a systematic row. This indicates that the rope is not appreciably twisted over the diffracting area such that only one zone axis contributes to the pattern.

The high-Q meridianal arcs arise from constructive scattering by the graphene lattice of each SWNT. The innermost arc corresponds to the graphene (10) reflection at Q ~2.94, and the second arc corresponds to the (11) at Q ~5.09. As with the low-Q equatorial arcs, the intensity profile of the high-Q arcs depend upon rope orientation over the diffracting area and coherence length. However, in this case the chiralities of the constituent tubes must also be considered. For example, consider a spot g located on the (10) arc θ degrees away from the meridian. The intensity at this spot will be the weighted sum of all independent contributions from tubes having (10) scattering that reflect into g. Two extreme cases are achiral (armchair) tubes oriented θ degrees away from the meridian and chiral tubes parallel to the meridian having (10) coherence θ degrees away from the meridian. In this way, the angular intensity profile along each high-Q arc is due to both the mosaic of chiralities and the mosaic of angular orientations of individual SWNTs contained within the rope. Note also that the mosaic of angular orientations within the rope is small, as seen in the small angular broadening of the rope lattice reflections. Thus, high-Q reflections at large azimuthal angles away from the meridian are due to chiral tubes. The corresponding graphene lattice planes have small coherence lengths, resulting in a large degree of radial broadening.

The low-Q meridianal reflections form a systematic row spaced by Q ~0.582, using the graphene lattice reflections that fall on the same axis as a standard for comparison. (This internal calibration is preferred to a more conventional camera length calibration against a known standard because it eliminates measurement errors due to elipticality in the pattern, which would arise if the diffracting rope were slightly tilted out of the object plane.) This Q corresponds to a real space periodicity of ~1.08 nm, equal to the observed periodicity of the encapsulated $Sc_3N@C_{80}$ molecules (c.f. Figure 1a). Similar Q values corresponding to a real space periodicity of ~1.08 nm, have been found for $Er_3N@C_{80}$, $ErSc_2N@C_{80}$ and $La_2@C_{80}$, which is expected given that the symmetry of the C_{80} cage is the same for each. This is consistent with electron diffraction results from $C_{60}@SWNT$, which shows a fullerene periodicity of 0.98 nm, consistent with the smaller size of the C_{60} molecule.

(a)   (b)
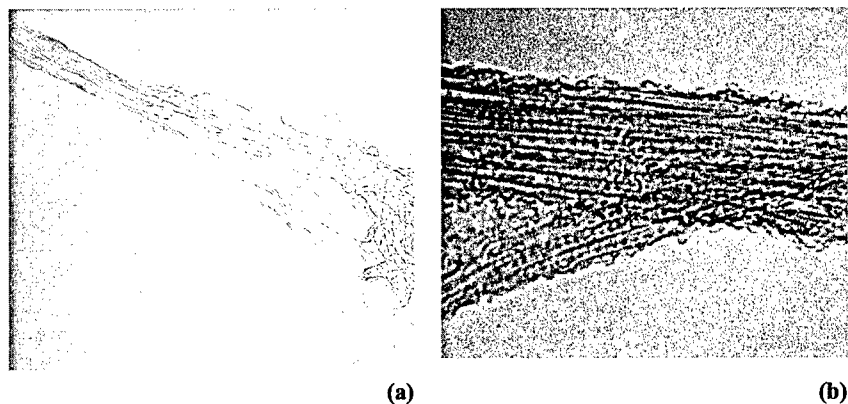
Figure 2: (a) La$_2$@C$_{80}$@SWNT at 1250 °C. (b) Sc$_3$N@C$_{80}$@SWNT at 1250 °C.

The diffraction signature corresponding to the low-Q meridianal reflections are attributed to the periodicity of the C$_{80}$ cages of the encapsulated metallofullerenes. It is possible that the diffraction could be due to the metal clusters themselves. However, the motions of the clusters are both random and independent. It is likely that the metal clusters act only as diffuse scatterers. Our hypothesis is further corroborated by previous diffraction studies of C$_{60}$@SWNT, which have shown diffraction signatures of 1-D crystals of empty fullerenes.

The materials were annealed at various temperatures between 800°C and 1250°C. Upon observation using HRTEM, prior to high temperature, the samples La$_2$@C$_{80}$@SWNT and Er$_3$N@C$_{80}$@SWNT, looked comparable to that of Sc$_3$N@C$_{80}$@SWNT (c.f. Figure 1a). However, in the Er$_3$N@C$_{80}$@SWNT sample, some breakdown of the metallofullerenes into co-axial tubes (CATs) was found along with

Figure 3: Er$_3$N@C$_{80}$@SWNT at

peapods. Thus, even relatively mild anneals of 800°C, used during specimen preparation, were sufficient to cause reaction among the $Er_3N@C_{80}$ metallofullerenes. After annealing at 1250°C, the $La_2@C_{80}@SWNT$ material was completely transformed into a variety of complex carbon cage structures and multi-wall nanotubes (Figure 2a). The $Sc_3N@C_{80}@SWNT$ remained intact (Figure 2b) even though the conditions of the treatment were identical to those of the $La_2@C_{80}@SWNT$ sample. After annealing at 950°C, $Er_3N@C_{80}@SWNT$ was found to have further CAT formation, as well as remaining peapods. An instance of a unique microstructure was observed in this sample (Figure 3). Micrographs are consistent with a CAT containing intact Er_3N clusters, or a partially transformed structure of covalently bonded metallofullerenes.

The results show a large variation in thermal stability of these C_{80}-based metallofullerenes, even between the isostructural $Er_xSc_{3-x}N@C_{80}$ materials. Variations in electronic properties and interaction with the surrounding SWNT, or cluster mass could be the origin of this behavior. Of particular interest are $La_2@C_{80}@SWNT$ and $Sc_3N@C_{80}@SWNT$ after annealing at 1250°C. At this temperature, the $Sc_3N@C_{80}$ remains stable, whereas the $La_2@C_{80}$ cages are destroyed. From the variety of reassembled large carbon cage structures in this material, it is apparent that the released La atoms are acting as catalysts for the reformation of the graphitic structures. This interpretation is consistent with the observation of large highly crystalline multi-wall nanotubes which do not exist in the pre-annealed material. The onset of this behavior lies between 1000°C and 1250°C.

The overall response of these supramolecular assemblies to temperature could be affected by the mass of the interior clusters. The heaviest cluster, Er_3N (515.8 g/mol) begins to break down at temperatures below 800°C. The next heaviest metallofullerene with La_2 (277.8 g/mol) has an onset of instability in 1-D clusters at a temperature between 1000°C and 1250°C. The lightest metallofullerene containing Sc_3N (148.9 g/mol) is stable to the highest tested temperature of 1250°C. Thus there is a nominal consistency with cluster mass. This discussion can only be speculative due to the lack of important information on these relatively new metallofullerenes, and other effects could be important in determining thermal stability. For example, it is known that six electrons are transferred to the C_{80} cage from the La atoms in $La_2@C_{80}$. [7] In $Sc_3N@C_{80}$, the electron transfer is two electrons. [6] No data is available for the other C_{80}-based metallofullerenes. These electronic effects could play a key role in determining the stability of the metallofullerenes within the SWNT and governs the strength of interaction and modification of SWNT behavior. This remains for further study.

ACKNOWLEDGEMENTS

REFERENCES

1. J.Tang, L.C.Qin, S.Bandow, M.Yudasaka, T.Sasaki, A.Matsushita, S.Iijima, presented at the 2000 MRS Fall Meeting, Boston, MA, 2000 (unpublished).
2. A.Caglar and M.Griebel (private communication).
3. B.W.Smith, D.E.Luzzi, Y.Achiba, Chem. Phys. Lett. **331,** 137 (2000).
4. T.Akasaka, S.Nagase, K.Kobayashi, M.Walchli, K.Yamamoto, H.Funasaka, M.Kako, T.Hoshino, T.Erata , Angew. Chem. Int. Engl. **36**, 1643 (1997).
5. K.Hirahara, K.Suenaga, S.Bandow, H.Kato, T.Okazaki, H.Shinohara, S.Iijima, Phys. Rev. Lett. **85**(25), 5384 (2000).
6. S.Stevenson, G.Rice, T.Glass, K.Harich, F.Cromer, M.R.Jordan, J.Craft, E.Hadju, R.Bible, M.M.Olmstead, K.Maitra, A.J.Fisher, A.L.Balch, H.C.Dorn, Nature **401**, 55 (1999).
7. K.Kobayashi, S.Nagase, T.Akasaka, Chem. Phys. Lett. **245**, 230 (1995).

External Chemical Reactivity of Fullerenes and Nanotubes

[1]Seongjun Park, [2]Deepak Srivastava, and [3]Kyeongjae Cho*
[1]Department of Chemical Engineering, Stanford University, Stanford, CA 94305-5025
[2]Computational Nanotechnology, NASA Ames Research Center, Moffett Field, CA 94035-1000
[3]Department of Mechanical Engineering, Stanford University, Stanford, CA 94305-4040
*kjcho@stanford.edu

ABSTRACT

The external chemical reactivity of graphene sheet, fullerenes and carbon nanotubes has been investigated. The total reaction energy is analyzed with several contributing terms and formulated as a function of the pyramidal angles of C atoms. We have determined the parameters for the formulae from ab initio simulation of graphene. We have applied them to predict hydrogenation energy of several nanotubes and C_{60}, and demonstrated that the predicted total reaction energies are very close to the results of total energy pseudo-potential density functional theory calculations. This analysis can be used to predict the reaction energy and local bonding configuration of a reactant with diverse fullerenes and nanotubes within 0.1 eV accuracy.

INTRODUCTION

There has been much research interest in carbon nanotubes and fullerenes since the discovery of C_{60} [1]. They have been considered as promising materials for nanotechnology applications, such as biochemical and gas sensors [2] and molecular transistor [3]. From the recent studies on possible nanodevice applications, it has been recognized that the surface functionalization of nanotubes and fullerenes would play an important role for nanodevice development. In order to functionalize nanotubes and fullerenes, the chemical reactivity of carbon atoms need to be understood with a quantitative accuracy.

Generally, the chemical reactivity on the external surface of a fullerene or a nanotube is characterized by local bonding configuration of carbon atoms, more specifically, pyramidalization (θ_p) of C atoms as illustrated in Fig. 1 [4, 5]. Since the surface of a fullerene or a nanotube is curved, it is natural to have pyramidalized C atoms as shown in Fig. 1. Pyramidalization changes the hybridization of atomic orbitals at the C atom so that the π orbital contains different portion of s and p orbitals leading to different chemical reactivity. For example, graphite has planar structure ($\theta_p = 0$) corresponding to sp^2 for σ bonds and p for π bond. However, fullerenes and nanotubes have the hybrid bonding orbitals between sp^2 to sp^3. Because of this hybridization, fullerenes and nanotubes are known to be more reactive than graphite. The degree of pyramidalization (θ_p) is defined by the angle between σ bond and π orbital and named as pyramidal angle (Fig. 1).

When a C atom interacts with an external chemical reactant, several processes occur simultaneously: orbital hybrid changing toward sp^3, π bond breaking, and reaction between free π orbital and external reactant. In order to quantify the analysis of the chemical reactivity, we divide a reaction into several contributing parts: (a) straining of surface C atom, which is changing the hybrid of atomic orbital of C atom, (b) breaking of π bond and binding with external reactant, and (c) local relaxation of neighbor C atoms. We name several energy terms

following each contributing part, such as, "strain energy" for (a), "binding energy" for (b), and "local relaxation energy" for (c). To elucidate these terms, we will use a hydrogen atom as a point probe to measure binding energy. We have analyzed and formulated these energies in terms of pyramidal angles. And we have applied them to graphene sheet, several nanotubes, and C_{60} fullerene. We have chosen graphene sheet as a representative system for large fullerenes and nanotubes. We have chosen several nanotubes with different radii such that the pyramidal angles are between those of graphene sheet and C_{60}. In the analysis, we have calculated the energy parameters for our formulae from graphene sheet data. These parameters and the energy expressions are used to predict the interaction energies of nanotubes and C_{60}. The accuracy of the prediction is tested by comparing to full ab initio simulations.
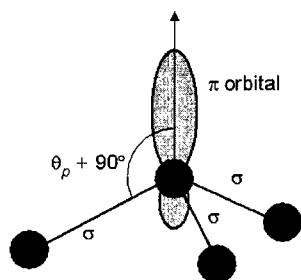
Figure 1. Pyramidal angle (θ_p) is defined by the angle between π orbital and σ bond minus 90°.

COMPUTATIONAL DETAILS

All the results in this work are calculated using total energy pseudo-potential density functional theory (DFT) method [6, 7], and a supercell approximation is used to simulate the periodic systems. In order to minimize the interactions between the repeated images, we include 5 Å vacuum separating the neighboring images. Kohn-Sham single-electron wave functions are expanded by 50,000 plane waves for C_{60}, and between 10,000 and 36,000 for nanotubes depending on their diameters, and 18,000 for graphite, corresponding to 40 Ry cut-off energy. We use single k–point for C_{60}, because it is a molecule. For a graphene sheet and nanotubes, k–point convergence was tested and it is confirmed that a single k–point sampling for graphene sheet and four k–point for nanotubes are enough for the convergence. During geometry optimizations, the atomic positions were relaxed until the forces became smaller than 0.05 eV/Å.

The initial values of the pyramidal angles θ_0 of graphene sheet, C nanotubes, and C_{60} used in this work are listed in Table I. When we compute the strain energy, we fix all the C atoms and move one C atom, on which the reaction will occur, normal to the surface in order to increase pyramidal angle artificially. We calculate the total energy of the strained structure and get the strain energy of given structure from the difference of total energies between the strained structure and the initial structure. In order to understand strain energy dependency on pyramidal angle, we have computed a set of strain energy with different pyramidal angles.

We have calculated the binding energy of H atom for each strained structure. We have introduced an H atom above the strained C atom structure generated in the previous analysis and

calculated hydrogenation energy to compare the chemical reactivity difference induced by pyramidal angle change. During the calculation of binding energies, we keep the C atoms fixed to maintain the artificially produced pyramidal angle and atomic hybrid, and relax the position of the introduced H atom. We have also simulated fully relaxed hydrogenation energy to compare with our predictions. We relax C atoms up to the third nearest neighbors for graphene sheet, up to the first nearest neighbors for nanotubes, and all the C atoms for C_{60} fullerene during the full relaxation simulations.

Table I. Initial Pyramidal Angles (θ_0) of graphene sheet, several nanotubes, and C_{60} (rad.)

	θ_0		θ_0
Graphite	0.000	(10,0) Nanotube	0.090
(15,0) Nanotube	0.059	(8,0) Nanotube	0.113
(12,0) Nanotube	0.075	C_{60}	0.202

RESULTS and DISCUSSION

When we strain one C atom, the pyramidal angle and the bond length of the pulled C atom are changed. So, we have divided strain energy into two terms, bending energy and bond stretching energy. We have analyzed those terms by force constant models and described as quadratic function of pyramidal angle (θ_p) changes from the initial equilibrium pyramidal angle (θ_0) and bond length (a) changes from the initial equilibrium bond length (a_0), respectively. When C atom is pyramidalized as shown in Fig. 1, the bottom triangle is consist of neighboring three C atoms. Because the triangle of bottom pyramid is not changed during the straining and the strained C atom is pulled up normal to the triangle, $a \cos(\theta_p)$ remains a constant and bond length (a) can be replaced by a function of pyramidal angle (θ_p) as shown in equation (1). Due to three bonds in strained C atom, there are factors of three in equation (1). Since nanotubes and fullerenes are graphite-like materials, we develop the scheme for graphene sheet and apply it for the other carbon materials with averaged bond lengths and averaged pyramidal angles due to C_3 symmetry in graphene sheet.

$$E_{strain} = \frac{3}{2} k_{bending} \left(\theta_p - \theta_0 \right)^2 + \frac{3}{2} k_{stretching} a_0^2 \left(\frac{\cos(\theta_0)}{\cos(\theta_p)} - 1 \right)^2 \tag{1}$$

DFT simulation of strain energy for graphene sheet, (10, 0) nanotube, and C_{60} is shown in Fig. 2. We fit the DFT simulation data for graphene sheet to equation (1) and determine the spring constants: 10.70 eV/rad^2 for $k_{bending}$ and 7.44 eV/Å^2 for $k_{stretching}$. In Figure 2, we plot the predicted strain energy curves for (10,0) nanotube and C_{60} and these curves show a good agreement with the DFT simulation results.
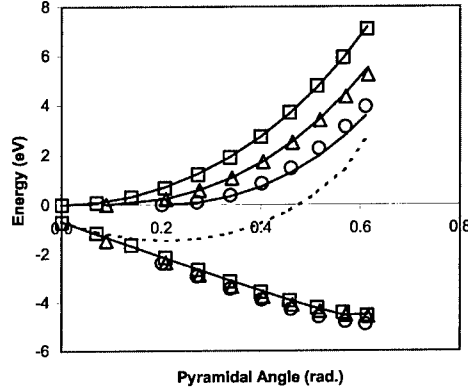
Figure 2. DFT simulation results for strain energy and binding energy. Strain energy is always positive and shown as top three set of data and binding energy is shown as bottom three set of data. We use *square* for graphene sheet, *triangle* for (10,0) nanotube, and *circle* for C_{60}. The solid line for graphene is a fitting to the equations, and the solid lines for the nanotube and C_{60} are predictions from the equations. The dotted line is the sum of strain energy and binding energy for graphene sheet.

Binding energy is composed of two different contributions, π bond breaking and reaction between external reactant and free π state. We use π bond breaking energy of graphene sheet as a reference and represent π bond breaking energy of other material based on π bond breaking energy of graphene sheet and the difference, which is shown in equation (2), where E_{shift} is the energy difference.

$$E_{\pi} = E_{graphite} + E_{shift} \tag{2}$$

For the reaction of free π state, we use POVA (π Orbital Vector Analysis) [8], which assigns one s and three p orbitals to three σ bonds and determine π state from the rest. Equation (3) shows π state in terms of the s and p orbitals derived from POVA. When an external reactant is introduced to the π state expressed in equation (3), the energy for the reaction with an external reactant (x) will be expressed by $<s|H|x>$ and $<p|H|x>$ using proper Hamiltonian H. The binding energy is the sum of π bond breaking energy in equation (2) and the energy for the reaction of free π state. And the binding energy will be expressed as equation (4), where E_{sx} and E_{px} are $<s|H|x>$ and $<p|H|x>$, respectively.

$$|\pi\rangle = \sqrt{2}\tan(\theta_p)|s\rangle + \sqrt{1 - 2\tan^2(\theta_p)}|p\rangle \tag{3}$$

$$E_{binding} = \sqrt{2}\tan(\theta_p)E_{sx} + \sqrt{1 - 2\tan^2(\theta_p)}E_{px} + E_{graphite} + E_{shift} \tag{4}$$

DFT simulation results of binding energy are also summarized in Fig. 2. We fit the graphene sheet data to equation (4) to get the parameters: -5.24 eV, -1.55 eV, and 0.87 eV for E_{sx}, E_{px} and $E_{graphite}$, respectively. The fitted binding energy curve is drawn in Fig. 2 as solid curve connecting square data points. From a comparison between this curve and other DFT data in Fig. 2, we can see that a small energy shift, around -0.2 eV ~ -0.3 eV, is needed for (10,0) nanotube and C_{60} to match the binding energy curve of graphene sheet. In equation (4), the first two terms depends only on the pyramidal angle (θ_p), and the third term is a constant. The only possible energy difference for different structured materials is coming from the last term, E_{shift}. As shown in Fig. 2, E_{shift} is not affected very much by the initial pyramidal angle, and we choose -0.2 eV as E_{shift} for other nanotube systems.

Total reaction energy is obtained as the sum of strain energy, binding energy, and local relaxation energy, as describe above. First, we try to estimate the total reaction energy using only strain energy and binding energy, which are represented by equations (1) and (4) respectively. As an example, we determine the total reaction energy of graphene sheet from the minimum of the sum of strain energy and binding energy from Fig. 1. We compare the total reaction energy from full relaxed result and get 0.16 eV of energy difference, which is the local relaxation energy.

Finally, we now predict the total reaction energy of an H atom on different nanotubes and C_{60}. We approximate that the local relaxation energy does not strongly depend on the initial structure and use the value of graphene sheet, -0.16 eV, for other nanotubes and C_{60}. Therefore, we determine the total reaction energy, especially hydrogenation energy for this case, from equation (1) for strain energy, equation (4) for binding energy, and -0.16 eV for local relaxation energy. The predicted total reaction energy results are summarized in Fig. 3 as square date points. In Figure 3, we compare the predicted data with the DFT calculations with full relaxation (circle data points). Figure 3 shows that we can predict hydrogenation energy of fullerenes and nanotubes within 0.1 eV errors compared to the full DFT simulations.

CONCLUSIONS

We have shown that the total reaction energy can be divided into three energy terms, strain energy, binding energy, and local relaxation energy. We also have shown that those energy terms can be formulated and that the total reaction energy of different carbon based materials can be predicted from four energy parameters, E_{sx}, E_{px}, $E_{graphite}$, and local relaxation energy. The parameters E_{sx} and E_{px} depend on the external reactants (x), and $E_{graphite}$ and local relaxation energy do not depend on the reactants. Therefore, once an external reactant is chosen, we can determine E_{sx} and E_{px} from DFT calculations of its reaction with the graphite. From these energy parameters, we can predict the total reaction energies and binding configurations of the reactants on diverse fullernenes and nanotubes. This analysis is based on local configurations of carbon atoms so that one can apply this method to predict local deformation effects in diverse carbon nanostructres without performing full DFT simulations.
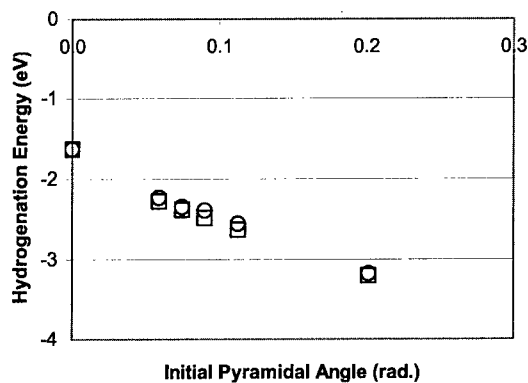
Figure 3. Hydrogenation energies of graphene sheet, various nanotubes, and C_{60}. Circles are DFT simulation data with full relaxations, and squares are the predicted values from our analysis. Data points represent from left to right, graphene sheet, and four different sizes of nanotubes listed above, and C_{60}.

ACKNOWLEDGMENTS

REFERENCES

1. H. W. Kroto, J. R. Heath, S. C. O'Brien, R. F. Curl and R. E. Smally, *Nature* **318**, 162 (1985)
2. J. Kong, N. R. Franklin, C. W. Zhou, M. G. Chapline, S. Peng, K. Cho, and H. Dai, *Science* **287**, 622 (2000)
3. S. J. Tans, A. R. M. Verschueren, and C. Dekker, *Nature* **393**, 49 (1998)
4. R. C. Haddan, *Science* **261**, 1545 (1993)
5. A. Hirsch, *Topics in Current Chemistry* **198**, 1 (1998)
6. M. C. Payne, M. P. Teter, D. C. Allan, T. A. Arias and J. D. Joannopoulos, *Rev. Mod. Phys.* **64**, 1045 (1992)
7. S. Ismail-Beigi and T. A. Arias, *Comp. Phys. Comm.* **128**, 1 (2000)
8. R. C. Haddon, *Chem. Phys. Lett.* **125**, 231 (1986)

C_{60} Clusters Self-Assembly in One-beam Optical Trap

W. Eugene Collins, Weijie Lu, Steven Morgan, and Andrey Zavalin
Physics Department, Fisk University,
Nashville, TN37208, U.S.A.

ABSTRACT

C_{60} aggregated clusters up to 20 um length were created on a glass surface within a solution inside of a gradient one-beam optical trap. It was possible to grow rod-shaped structures by motion of an optical trap parallel to the surface of the substrate. After the deposited structures became stable, the solution was dried. By AFM measurements of the stable dried structures, it was shown, that aggregations have typical sizes of 5-15 um X 1.5-2 um, and thickness near 1.5 um. The aggregations consist of thinner (30-100 nm diameter) rods, bundled together.

INTRODUCTION

During the last decade, one-beam optical trapping mostly had applications in the microbiology area [1]. Contributions of the optical trapping to the nanotechnologies could be more significant. The main advantage of the one-beam trap configuration is simplicity and a wide spectrum of possible applications. The quasi-micron size of the optical trap zone and the possibility to precisely control position and motion can satisfy the requirements of micro manufacturing in integrated optics and optical sensors, photonic crystals and bio-chip production.

In the previous experiments for behavior of many particles, trapped in the gradient one-beam optical trap [2,3], it has been shown that trapped particles create quasi-molecular dynamic structures, assembled together by photons and existing only in presence of laser field. Under the certain conditions photon bonding is converted to the chemical bonding [3]. Thus assembled C_{60} aggregated structures are stable without laser trap and can be used as elements of carbon-based devices.

EXPERIMENTAL DETAILS

The experimental setup, shown in figure 1, is basically similar to the laser tweezers configuration. Trapping laser beam (Nd-YAG, Ti:Sapphire, He-Ne or Ar-ion lasers) was used in the microscope "Nikon Optophot". Optical setup provides conditions for high-gradient laser field in trapping zone, creating 3D potential well and also photon bonding of the particles in solution. C_{60}/toluene solution in concentration of 1×10^{-3} M was placed in the 50-um-thick optical cell, made from microscope cover glasses. The images of the trapping zone and aggregation growth were monitored by a CCTV camera.

After 0.3-10 min of stable trapping under 0.5-3 mW of laser power, photon bonding is transformed to chemical bonding, providing the growth of C_{60} aggregation polymers on the substrate. By the slow motion of the optical trap along the substrate surface it was possible to grow rod-shape structures. Next, the solution was dried and AFM images of the aggregated structures on the dry glass surface were studied.
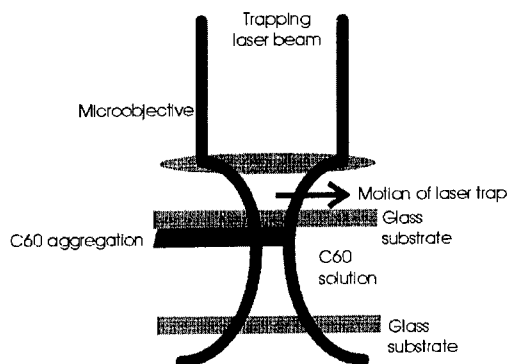
Figure 1. Simplified experimental setup for one-beam gradient optical trap.

DISCUSSION

The AFM image of the dried rod-shaped C_{60} aggregations is shown in figure 2.
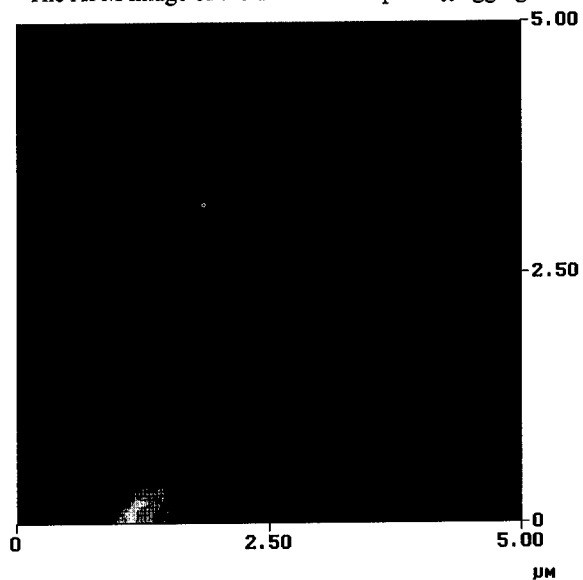
Figure 2. Dried C_{60} aggregations, grown in one-beam gradient optical trap.

Each aggregation contains thinner rods, bundled together. In figure 3, showing section analysis of an AFM image, one can see the rods having 30-100 nm diameters.

Section Analysis

L	96.680 nm
RMS	6.223 nm
Ic	DC
Ra(Ic)	3.574 nm
Rmax	14.342 nm
Rz	14.342 nm
Rz Cnt	2
Radius	93.244 nm
Sigma	0.218 nm

Spectrum

Surface distance	104.96 nm
Horiz distance(L)	96.680 nm
Vert distance	17.037 nm
Angle	9.994 °

Surface distance
Horiz distance
Vert distance
Angle

Spectral period	DC
Spectral freq	0 Hz
Spectral RMS amp	0.005 nm

azc60a.004
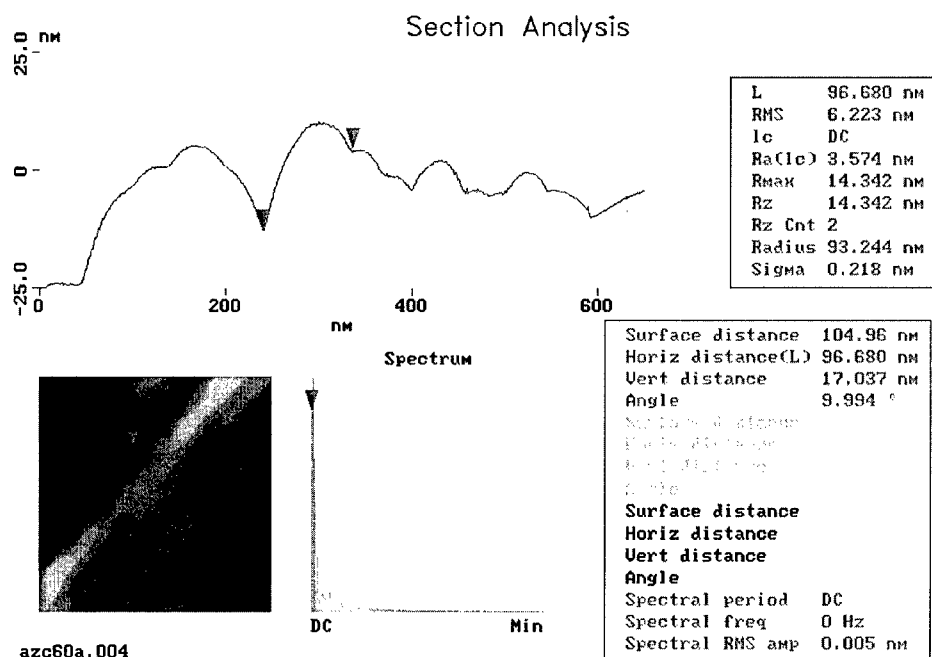
Figure 3. AFM image and section analysis of the C_{60} rods, bundled together in rod-shaped micron size structures.

In figure 4 the "joint" of the two rod-shaped structures is shown. Under the higher amplification, it is seen that the ends of the thinner rods are without holes. There is no additional information about the core of thinner rods at the present time.

It is important to know if heating of the growing aggregations by trapping laser radiation is a mechanism, which plays significant role in the creation of C_{60} aggregations. Different laser sources, mentioned above were used for trapping. Similar results were obtained for wavelengths 0.5, 0.63, 0.8, and 1.3 um, indicating the insignificance of the absorption effect. Unfortunately there was no possibility to measure absorption spectra of aggregations and this is the subject for future research.
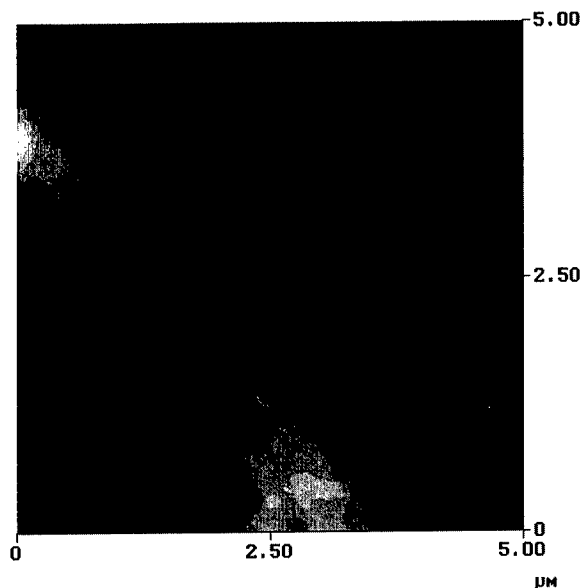
Figure 4. AFM image of the "joint" between the two rod-shaped structures.

CONCLUSIONS

The growth of C_{60} polymer clusters, aggregated inside of the one-beam gradient optical trap, has been demonstrated.

AFM measurements show aggregations having sizes 5-15 um X 1.5-2 um, and thickness near 1.5 um. The aggregations consist of thinner (30-100 nm diameter) rods, bundled together.

Shape of aggregations can be made more elongated by the motion of laser trap parallel to the substrate surface. The quasi-micron size of the optical trap zone and the possibility to precisely control position and motion can satisfy the requirements of micro manufacturing in integrated optics and optical sensors, photonic crystals and bio-chip production.

ACKNOWLEDGMENTS

REFERENCES

1. A.Ashkin, Optics & Photonics News, 41 (1999).
2. J.-M. R. Fournier, M. M. Burns, and J. A. Golovchenko in *Practical Holography IX*, SPIE Vol. 2406, pp. 101-111.
3. P. Weiss, Science News, **157**, 335 (2000).

Endo-fullerenes and Doped Bucky Onions as Seed Materials for Solid State Quantum Bits

[1]Seongjun Park, [2]Deepak Srivastava and [3]Kyeongjae Cho
[1]Department of Chemical Engineering, Stanford University, Stanford, CA 94305-5025
[2]Computational Nanotechnology, NASA Ames Research Center, Moffett Field, CA 94035-1000
[3]Department of Mechanical Engineering, Stanford University, Stanford, CA 94305-4040

ABSTRACT

Two different models for solid-state quantum bits have been investigated. Both are based on the nuclear spin of doped atoms in endo-fullerenes or bucky-onions. [1]H or ^{31}P have been tested as suitable dopant atoms because they have half nuclear spins. The thermal stability and electronic properties of the dopant atoms and the encapsulating cages have been examined with *ab-initio* pseudo potential density functional methods, and the results show that both models are suitable for single qubit applications.

INTRODUCTION

Recently a conceptual design of solid-state quantum computer, based on fabricating arrays of ^{31}P atoms in bulk Si, has been proposed. [1] When a ^{31}P donor atom is doped at a substitutional site in bulk Si, four out of five valance electrons of the ^{31}P atom form four tetrahedral covalent bonds with the Si lattice. Kane has argued that the weakly bound fifth electron of ^{31}P donor atom can be used for controlling the nuclear spin state of the donor atom, via hyper-fine interaction, for a solid-state qubit application. The main problem with this proposal, however, is the experimental difficulty involved in fabricating precise arrays of dopant atoms, ^{31}P, in bulk Si layers. Moreover, even if such arrays are fabricated, the individual donor atoms may diffuse away from their intended locations via transient induced diffusion mechanisms.

To overcome the above difficulties, we have investigated encapsulating ½ nuclear spin atoms in endo-fullerenes and bucky-onions for the above described solid-state qubit applications. If the doped endo-fullerene and bucky-onions are stable and have suitable electronic behavior for qubit applications, it may be easier to make the required arrays for solid-state quantum computer applications. The ^{1}H and ^{31}P atoms with ½ nuclear spin have been tried as suitable dopant atoms because both have ½ nuclear spin and one isotope except deuterium [2]D. Two different models have been explored for solid-state qubit applications: One model involves encapsulating ^{1}H atom in a fullerene, and the second model involves encapsulating ^{31}P atom in a few nanometer sized diamond nanocrystallite. The fabrication pathway for encapsulating a ^{31}P atom in a diamond nanocrystallite involves first encapsulating a ^{31}P atom in a fullerene at the core of a bucky-onion, and then converting the core to a diamond nanocrystallite by e-beam irradiation and annealing. [2]

All the results in this work are calculated using total energy pseudo-potential density functional theory, [3, 4] where geometry is optimized and the atomic positions are relaxed until the forces become smaller than 0.05 eV/Å.

RESULTS and DISCUSSION

The first model involves using encapsulated ^1H atom for a qubit. The ½ nuclear spin state of a bare ^1H atom can be a strong candidate to realize a quantum bit, because the atom has one valence electron in $1s$ atomic orbital and hyperfine interaction is fairly strong. For fabrication purpose, however, a bare ^1H atom is very reactive and too small to be encapsulate within any molecule or a lattice. Even if there are ways to fabricate arrays with ^1H atoms, the atoms are very reactive and form instantaneous chemical bonds with the encapsulating molecules or lattices. The main requirement for encapsulating a ^1H atom with in a fullerene is that the encapsulated atoms should stay at the center of the fullerene without forming any bond with the caging fullerene molecule. Fullerenes are the possible candidate for the caging or encapsulating molecules because it is well known that fullerenes have fairly inert internal surface due to pyramidalization. Pyramidalization increases the electron density of the exterior of the surface and decreases the electron density at the interior of the surface due to rehybridization of atomic orbitals in C atom and electron repulsion from σ bonds. [5]

The internal chemical reactivity of fullerenes is examined first. We choose C_{60} and examine the hydrogenation energy. When a ^1H atom is introduced at the center of C_{60}, the ^1H atom is stable at the center with the formation energy of –0.43 eV. The electron density of the ^1H atom at the center shows that the lone $1s$ like valence electron is localized around the ^1H atom with a strong hyperfine interaction with the nuclear spin. Though there is no significant or specific binding between the ^1H atom and the cage C atoms in C_{60}, the collective sum of small binding interactions between the ^1H atom and the cage C atoms make the total binding energy negative. The center site, however, is not found to be the global minimum energy site. The global minimum energy site is found to be due to a chemical bond formation between the ^1H atom and a cage C atom of C_{60}. The binding energy for this reaction is found to be –1.23 eV, i.e., much lower than the binding energy of ^1H atom at the center. Similar results are found for other fullerenes as well. Generally, the internal surface of a fullerene is less chemically reactive than external surface, but the reactivity is enough for a ^1H atom to bind at the cage C atom and not at the center as is desired for the qubit application.

A possible way for reducing the internal chemical reactivity is through the removal of most of the π electron density from the interior of the surface. This can be done through hydrogenation or some other reaction at the exterior of the surface. When the fullerene is fully hydrogenated, C atoms in fullerene have sp^3 atomic hybrid. Because there is no π electron density at the interior of the surface, the reactivity at the interior of the surface is decreased. However, once all the π bonds are removed, the encapsulated ^1H atom could escape by diffusion because the C atom ring sizes then increase due to the increased C-C bond lengths. Therefore, a fullerene that is fully hydrogenated on the exterior of the surface, and which has only small number of C atom rings can be a possible encapsulating material. We have investigated dodecahedrane, $C_{20}H_{20}$ for encapsulating ^1H atom for qubit application.

The diffusion barrier of ^1H atom to escape $C_{20}H_{20}$ as well as the hydrogenation of internal surface of $C_{20}H_{20}$ are examined. The ^1H atom is placed at the center of $C_{20}H_{20}$ and moved towards the wall. The changes in the binding energy are calculated at each step. There are 3 high symmetry-binding sites on the internal surface of $C_{20}H_{20}$; top of the C atoms, the center of bonds between the C atoms, and the center of C atom pentagon rings. Binding energy changes along all the three sites are computed as a function of the distance from the center and the results are shown in figure 1. Since there is no π orbital, we confirm that there are no meta-stable

configurations at the interior of the surface. The binding site at the center is the only stable configuration. The diffusion barrier to escape through pentagon ring is also calculated and found to be 1.17 eV. This shows that the system is fairly stable against diffusion at low temperatures. These results are consistent with some other recent experimental [6] and theoretical [7] studies.
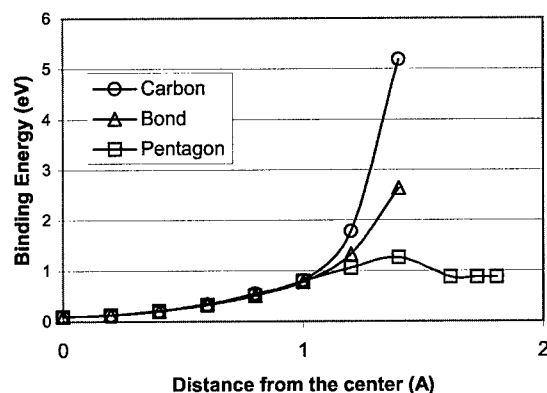
Figure 1. Binding energy of ^{1}H @ $C_{20}H_{20}$:

In order to examine ^{31}P atom in a fullerene as a qubit, the energetically favorable configurations for a ^{31}P atom in a C_{60} fullerene are examined first. For a ^{31}P atom inserted in C_{60}, we identify two energetically stable configurations; in the first case the ^{31}P atom stays at the center of C_{60} , and in the second case the ^{31}P atom is stable on top and at the center of a C-C bond that connects two pentagons on the wall of C_{60}. The binding energies of these configurations are –0.99 eV and –0.81 eV for at the center and on the bond top sites, respectively. The diffusion barrier to escape from the center is also calculated and is found to be 0.33 eV. Therefore, we expect that the ^{31}P atom in C_{60} mostly stays at the center. Recently, there have been experimental observations, which show that ^{31}P atom at C_{60} is stable at the center of the fullerene. [8] This is in agreement with our results. Either of energetically stable configurations, however, does not provide good model for qubit, because valence electrons of ^{31}P atom does not overlap with the nucleus position strongly for a strong hyperfine coupling.

However, a ^{31}P atom encapsulated in a fullerene can be used as a possible first fabrication step in encapsulating the ^{31}P atom in a diamond nanocrystallite. The subsequent steps are: (a) use the encapsulating fullerene to grown bucky onion layers around the fullerenes, and (b) irradiate and anneal the outer layers of bucky onions to convert the core into diamond nanocrystallite doped with a ^{31}P atom. Experimentally, it has been demonstrated that core fullerenes and core layers of buckly onions can be converted to diamond nanocrystallite with controlled e-beam irradiation and annealing. Since a ^{31}P atom at the substitutional site of diamond lattice is similar to ^{31}P atom doped in bulk Si [1], as was suggested by Kane, we have investigated the energetics for possible configurations of ^{31}P doped in a diamond nanocrystallite. The formation energies for possible configurations of ^{31}P atom in normal and compressed (to 20 GPa) diamond lattices, such as, at a substitutional site, a hexagonal interstitial site, and a tetrahedral interstitial site are

calculated, and summarized in table I. The results show that the formation energies for all the configurations are positive, *albeit* a small positive value for the ^{31}P atom at the substitutional site. This shows that there is a small energy cost for inserting a ^{31}P atom at the substitutional site. However, once the ^{31}P atom is trapped (by the above discussed fabrication pathway) at the substitutional site, the diffusion barriers to escape from the nanocrystallite are also very high. Once fabricated, such doped diamond nanocrystallite will be stable, and making arrays of 2-10 nm sized ^{31}P atom doped diamond nanocrystallites in any host material will be much easier than making similar arrays with bare ^{31}P atoms.

Table I. Formation Energy of ^{31}P at different sites of compressed diamond or bulk Si (eV); Formation Energy = E (Si or Diamond: [31]P) − E (Si or Diamond) − E (Atomic ^{31}P)

	Diamond			Si
Pressure	0 Pa	20 Pa	50 Pa	0 Pa
Substitution	0.88	1.99	3.85	-5.75
Hexagonal Site	15.95	18.26	21.99	-2.71
Tetrahedral Site	19.13	21.53	25.35	-1.90

CONCLUSIONS

We have discussed two different models for encapsulating nuclear spin ½ atoms for solid-state quantum bit applications. For the first model, we show a way to capture a ^{1}H atom at the center of a fully hydrogenated fullerene, $C_{20}H_{20}$. For the second model, we suggest a way to fabricate diamond nanocrystallite doped with ^{31}P atom at the substitutional site. Making arrays of such larger sized qubits in any host material will be easier than making arrays of bare ^{31}P atoms in bulk Si as was suggested originally. After this work was completed, we became aware about a European collaborative research project, Quantum Information Processing Device using Doped Fullerene, (QIPD-DF) of the similar broad nature. [9] It is very encouraging that this project also aims to apply the fullerene-encapsulated atoms and clusters for novel quantum information device applications. We note that our original research proposal was based on multi-shell fullerenes for solid state quantum computer applications, whereas the QIPD-DF project involves 8 partners with diverse quantum information device processing concepts.

ACKNOWLEDGMENTS

REFERENCES

1. B. E. Kane, *Nature* **393**, 133 (1998)
2. F. Banhart and P. M. Ajayan, *Nature* **382**, 433 (1996)
3. M. C. Payne, M. P. Teter, D. C. Allan, T. A. Arias and J. D. Joannopoulos, *Rev. Mod. Phys.* **64**, 1045 (1992)
4. S. Ismail-Beigi and T. A. Arias, *Comp. Phys. Comm.* **128**, 1 (2000)
5. A. Hirsch, *Topics in Current Chemistry* **198**, 1 (1998)
6. R. J. Cross, M. Saunders and H. Prinzbach, *Organic Lett.* **1**, 1479 (1999)
7. D. A. Dixon, D. Deerfield, G. D. Graham, *Chem. Phys. Lett.* **78**, 161 (1981)
8. C. Knapp, N. Weiden, K. Kass, K. P. Dinse, B. Pietzak, M. Waiblinger and A. Weidinger, *Molecular Physics* **95**, 999 (1998)
9. Web site of QIPD-DF project is http://planck.thphys.may.ie/QIPDDF/

In Search of the Molecular Triplet of C_{60} using Low Temperature Raman Spectroscopy.

G. Chambers, A.B. Dalton, and H.J. Byrne,
Facility for Optical Characterisation And Spectroscopy (FOCAS)/ School of Physics, Dublin Institute of Technology, Kevin Street, Dublin 8, Ireland.

ABSTRACT

The excited state properties of C_{60} thin films have been probed in the temperature range 77-273K using Raman spectroscopy. The change in the Raman, $2A_g$ mode of C_{60} (whose position is largely independent of temperature) was monitored as a function of the excitation intensity at 514.5nm. This mode normally positioned at $1469cm^{-1}$, was seen to shift reversibly to a lower Raman frequency with increasing laser intensity. Two excited state species have been identified. The first, at $1466cm^{-1}$ has been associated with the molecular triplet of C_{60}. The second species at $1463cm^{-1}$, has been speculated to be an excited state co-operative involving two or more excited states in the solid and is seen to be intrinsic to solid state C_{60} below the phase transition.

INTRODUCTION

A considerable understanding of the photophysical and photochemical properties of C_{60} both in solution and solid has evolved over the past decade [1]. However there remains a number of important questions regarding the nature of the excited states in the solid. In solution, optical excitation leads to a population of the long lived triplet state, via the singlet state. The process has been well characterised by transient absorption measurement [2] and a strong triplet-triplet absorption at 750nm is observed [3]. However this strong feature is not observed in the solid and indeed the excited state photodynamics differ considerably from those in solution [4] leading to questions as to whether the molecular triplet exists in the solid. Further to transient absorption measurements the Raman spectroscopic signature of the molecular triplet in solution has recently been associated with a positioning of the $2A_g$ mode at $1466cm^{-1}$ at room temperature [5]. Similar measurements however at room temperature in the solid are hampered by the much documented photopolymerisation of C_{60} [6] which occurs via a 2+2 cycloaddition. In this paper it is proposed that below this phase transition temperature, it should be possible to isolate the intermediate excited state species associated with the photopolymerisation and thereby identify the Raman signature of the molecular triplet of C_{60} and any differences, which exist between the excited states of isolated molecule and solid state. A temperature dependent study of the excited states will also be used to help elucidation the nature of the excited states in the solid.

EXPERIMENTAL

Gold grade C_{60} soot obtained from Hoechst was vacuum sublimed at a pressure of 10^{-6} mbar onto glass substrates using an Edwards A305 coating system. The average thickness of the resulting films was ~0.8µm. Raman measurements were taken using an Instruments S.A.

Labram 1B spectroscopic microscope (x10 objective, spot radius ~10μm) equipped with an external Argon ion laser (514.5nm) and a Linkam microscope cooling stage. The films were allowed to equilibrate for fifteen minutes at each temperature prior to illumination.

RESULTS AND DISSCUSSION

The Raman spectrum of C_{60} at 77K was monitored at laser powers of ~300Wcm^{-2}. The observed spectra were consistent with the low temperature spectra observed in previous studies where the $2A_g$ was seen to be independent of temperature and is positioned at 1469cm^{-1} [1, 6]. The frequency position of this mode was also found to be stable under prolonged low level illumination indicating that at the low temperature and low intensity no photochemistry was taking place. For the purpose of comparisons with earlier studies, this study will concentrate solely on the A_{2g} pentagonal pinch mode at 1469cm^{-1} [5,7,8].

Initially the laser was focused on to a single spot on the film. The incident power was then increased and the positioning of the $2A_g$ mode was seen to shift reversibly. In order to correlate the observed shifts with the known photodyanmics of C_{60} both in solution and solid the intensity dependent transmission of the C_{60} film was monitored. In general molecular C_{60} exhibits an inverse saturable absorption due to the strong absorption of the excited state triplet in the wavelength range 650 –790nm [2]. Figure 1(A) shows the curve obtained for the intensity dependent transmission of the C_{60} film obtained under similar conditions as the previously reported solution measurements.
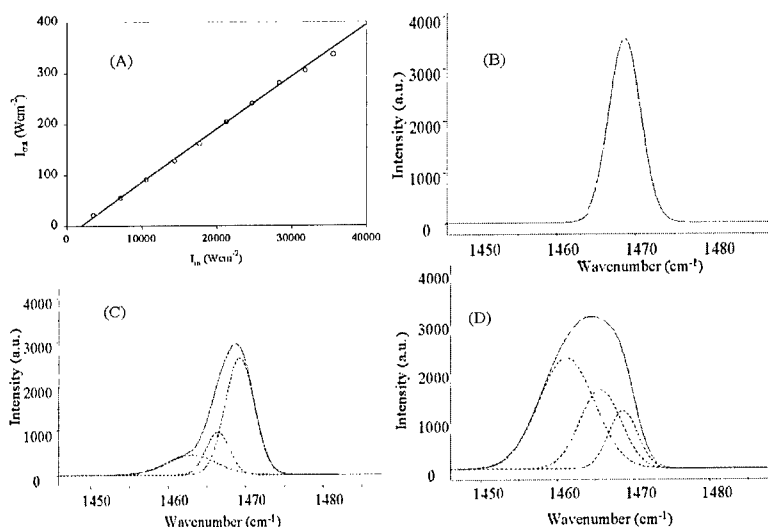
Figure 1. (A) Intensity dependent transmission curve at 77K for C_{60} film, (B), (C) and (D) are in situ Raman spectra at intensity of ~3000Wcm^{-2}, ~15000Wcm^{-2} and ~35000Wcm^{-2} respectivily.

It can be seen that the film does not exhibit an inverse saturable absorption but rather a linear curve in the range studied. The absence of a nonlinearity does not however indicate that no population redistribution is occurring in situations where the ground state absorption co-efficient (σ_{gr}) and the excited state absorption co-efficient (σ_{ex}) are approximately equal at the wavelength employed. This may indeed be the case for C_{60} films as the photoinduced absorption spectrum for C_{60} shows that 514.5nm is situated close to the 'cross-over' or null point of the spectrum [4]. The solid line of figure 1(A) is a fit of the intensity dependent transmission given by equation 1 with a value of ~ $2.5\text{x }10^{-18}\text{cm}^2$ for the ground state absorption cross-section (σ) and $2.6 \text{ x } 10^{-18} \text{ cm}^2$ for the excited state absorption cross-section (σ_{ex}) [6]. The fit yields an excited state lifetime of 7μsec for solid state C_{60} which is comparable to previously reported life times of C_{60} [6]. Although the intensity dependent transmission is linear, it has been previously shown that a considerable excited state population can be readily produced at the intensities used i.e. at an intensity of ~20000Wcm^{-2} the excited state population is ~55% of the total population N_{total}.[9]

$$T = \exp[-(N_{gr}\sigma_o+N_{ex}\sigma_3)d] \tag{1}$$

Figure 1 (B) (C) and (D) show the in situ Raman spectra taken at various points along the intensity–dependent transmission curve of figure 1(A). The dashed lines in the spectra are Lorentzian/ Gaussian fits to the various components. Figure 1(B) shows the low irradance spectrum (>10^4Wcm^{-2}) of the pentagonal pinch mode and it is seen to be positioned at 1469cm^{-1}. However at laser powers approaching ~15000Wcm^{-2} two new components appear in the spectrum figure 1(C). The first component positioned at 1466cm^{-1} has a Raman signature analogous to that reported for the molecular triplet of C_{60} in solution [5]. Indeed one would expect excited state species of C_{60} to have a lower frequency of vibration as they should be in an antibonding state and hence have a weaker intramolecular force of attraction in comparison to the ground state [8]. Van Loosdrecht et al. [8] have reported similar intensity dependent shifting of the A_{2g} pentagonal pinch mode from 1469cm^{-1} to 1459cm^{-1} in C_{60} crystals at low temperatures (~40K). They assigned the observed shifts to electronically excited C_{60} and in particular the triplet state [8]. It should be noted, however, that a population redistribution from ground to triplet state should be characterised by a decrease in the ground state mode and the emergence of a single triplet mode, rather than the quasi-continuous shifting reported by van Loosdrecht et al. Close consideration of the data in question shows an initial discontinuous emergence of a mode at 1466cm^{-1}, which, in comparison to the data presented here and previously for measurements in solution [5] should be assigned to the molecular triplet.

In addition to the feature at 1466cm^{-1} a further reversible shift to 1463cm^{-1} at higher intensities can also be identified both in our data for a thin film and van Loosdrecht's data for single crystals. This feature at 1463cm^{-1} is an excited state species that appears to be specific to the solid state, as similar measurements in solution show no Raman evolution beyond 1466cm^{-1}. This high intensity intermediate state has previously been observed in the depolymerisation of solid C_{60} [1], as well as in reversible processes in C_{60} crystals [10]. This high intensity state has been associated with that which is characterised by a nonlinear photo-luminescence and photo-conductivity [10] and has been speculated to be a co-operative interaction between excited sates in the solid, at high excitation densities [10]. That such a state is present, in the depolymerisation of C_{60} may be understood by considering the symmetry conditions of the C_{60} molecules. Initially the molecules have the same symmetry in the ground state. Upon the addition of a single photon

one molecule is promoted to an excited state creating the molecular triplet species as in the proposed 2+2 cycloaddition polymerisation mechanism [6,7]. However as the system has been maintained at 77K the photopolymerisation cannot proceed due to the orientational phase transition. Hence as the intensity is increased a high density of excited states is created in the solid. At high intensities the excited state electronic orbitals of neighbouring molecules can readily overlap and rapidly create an excited state co-operative in which the molecular excited states becomes delocalised across several molecules in the solid creating a species analogous to that observed in the photo-depolymerisation. Finally it should be noted that the pentagonal pinch mode remains ever present but experiences a loss in intensity. The evolution of the three features is evident in figure 1(D) with the feature at $1463cm^{-1}$ becoming the dominant species at high laser intensities ($35000Wcm^{-2}$). Upon return to low laser intensities the pentagonal pinch mode once again becomes the dominant spices suggesting that the photoinduced processes are fully reversible within the resolution of the instrument. The instantaneous reversibility coupled with the intensity dependence is a strong indication that the new peaks are vibrational modes of excited stated C_{60} in the solid.
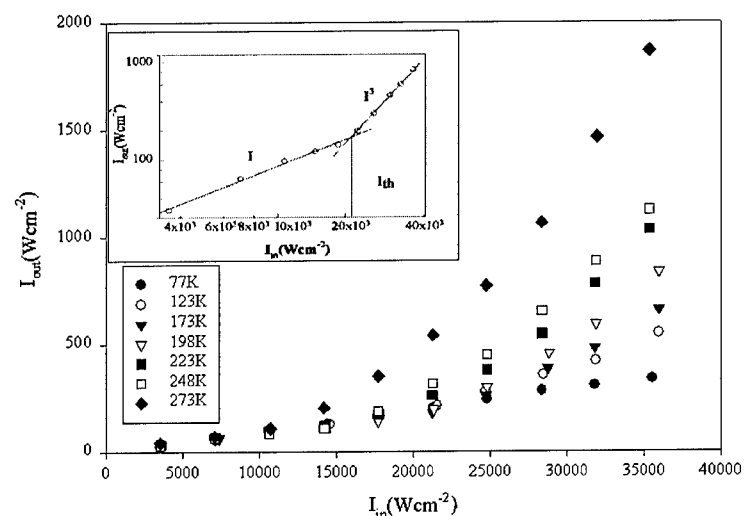
Figure 2. Intensity -Dependent Transmission curves in temperature range 77K-273K. Inset shows cubic fits at198K.

As the temperature is increased a more non-linear or cubic behaviour emerges and becomes dominant (figure 2). This behaviour is characteristic of non-linearities previously described in crystals [10]. The linear and non-linear components of the intensity dependent transmission curve at 198K are highlighted in the inset figure 2. This non-linear increase in the transmission is indicative of bleaching, in which the excited state absorption cross section is less than the ground state absorption cross section ($\sigma_{ex}<\sigma$). In general at temperatures above the phase transition (249K), the bleaching process can be attributed to the onset of irreversible

photochemical reactions [1,6]. In this case however for temperatures below ~200K, there is no evidence of any photochemical reactions occurring, as the in situ Raman spectra as well as the intensity dependent transmission curves are fully reversible, suggesting that the observed changes are purely photophysical. While the intensity dependent transmission curve for 198K is significantly different to the corresponding curve at 77K, the in situ Raman spectra and the evolution of the respective excited states at $1466cm^{-1}$ and $1463cm^{-1}$ is comparable to that shown in figure 1 for 77K. A similar temperature dependence for all temperatures below 198K has also been observed.

The change with temperature of the non-linearity can be assessed from the point at which the system deviates from a linear response to a non-linear response in the intensity dependent transmission curves, I_{th} in inset in figure 2. The in situ Raman spectrum of the onset of the non-linearity (i.e. at I_{th}) shows that the co-operative species (at $1463cm^{-1}$) is the dominant species at this point for all temperatures, suggesting that this species is non-linear in nature. Such a suggestion supports the notion that this species is analogous to the high intensity state previously reported in single crystals and characterised by a non-linear photoluminescence and photoconductivity [1,10].
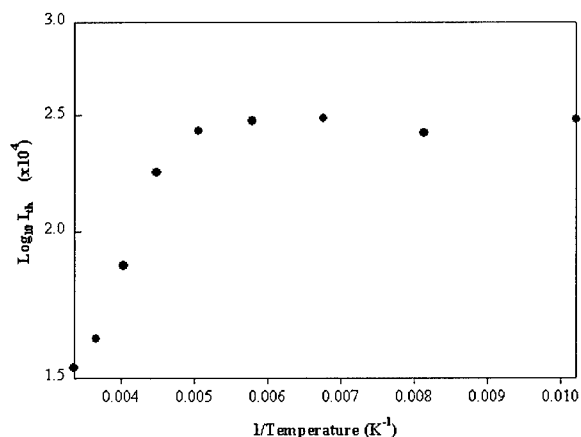
Figure 3. Temperature dependence of cubic response in transmission curves.

A plot of the intensities of the onset of the non-linearity (I_{th}) against the inverse of the temperature shown in figure 3. It can be seen that the non-linearity is independent of temperature up to ~220K. This suggests that the electronic delocalisation of the π-electron system, between the molecules in the solid state is intrinsic to the material at temperatures below 220K. It should be noted that this temperature is remarkably close to the orientational phase transition temperature of 249K particularly when one considers the effect of localised laser heating at the point of measurement. The induced Raman shifts observed with intensity are also fully reversible up until 220K however above this temperature the shifts become irreversible. In addition to the irreversibility of the Raman shifts above 220K the temperature independence of the non-linearity rapidly falls to lower intensities suggesting the non-linear delocalised species is formed at much lower intensities. A similar temperature dependence to that shown here was also

observed by Minami et al. for the luminescence spectrum [11] and was suggested to indicate that the decay route in C_{60} films should be regarded as the result of an intermolecular effect such as an intermolecular charge transfer excited state or indeed the high intensity excited state species proposed for the observed changes in our data. Absorption measurements at low temperatures also support the notion that a highly delocalised excited state similar to that proposed for the Raman mode at ~1463cm^{-1} at low temperatures and for the non-linear response observed at high intensity in the transmission curves, is possible [11].

At temperatures beyond 220K the onset of the non-linearity (i.e. I_{th}) is seen to rapidly decrease as shown in figure 3. The bleaching of the system at this temperature unlike the lower temperatures may be attributable to the initiation of irreversible photochemical processes such as the photopolymerisation. In situ Raman spectra confirms that some photochemistry is taking place as the original ground state pentagonal pinch mode is only partially regained upon reduction of the intensity. Nevertheless the data highlights the existence of a highly non-linear delocalised co-operative excited state species at low temperatures which is intrinsic to C_{60}. In addition the Raman signature of the molecular triplet has been identified for the first time in the solid state.

CONCLUSION

A full description of the photophysics of C_{60} after a decade of research has still remained elusive. The data reported here shows clearly the existence of two excited state species in solid thin films of C_{60}, the molecular triplet, positioned at 1466cm^{-1} and an excited state co-operative specific to the solid state positioned at 1463cm^{-1}. The second species has been reported to be intrinsic to C_{60} at low temperatures (<220K).

REFERENCES

1. H.J. Byrne, in "Physics and Chemistry of Fullerenes and Derivatives", H. Kuzmany, J. Fink, M. Mehring and S. Roth eds., World Scientific Singapore, pp183 (1995)
2. T.W. Ebbesen, T. Tanigaki and S. Kuroshima, Chem. Phys. Lett., **181**, 501 (1991).
3. L.W. Tutt and A. Kost, Nature, **356**, 225 (1992).
4. T.W. Ebbesen, Y. Mochizuki, K. Tanigaki and H. Hiura, Europhys. Lett., **25**, 503 (1994).
5. G. Chambers, H.J. Byrne. Chem. Phys. Lett. **302** 307-311 (1999)
6. "Science of Fullerenes and Carbon Nanotubes", M.S. Dresselhaus, G. Dresselhaus and P.C. Eklund, Academic Press, London (1996)
7. A.M. Rao, P. Zhou, K.A. Wang and P.C. Eklund, Science, <u>259</u>, 955 (1993).
8. P.H.M. van Loosdrecht, P.J.M. van Bentum and G. Meijer, Chem. Phys. Lett., <u>205</u>, 191 (1993).
9. G. Chambers, A.B. Dalton, and H.J. Byrne. Submitted to Chem. Phys. Lett. 2001
10. H.J. Byrne, A.T. Werner and S. Roth, in "Organic Electroluminescent Materials and Devices", p263, S. Miyata and H. Nalwa eds., Gordon and Breach Science,
11. N. Minami, S. Kazaoui, and R. Ross. Synthetic Metals, **70** 1397 (1995)

Spontaneous Formation and Stability of GaP Cage Structures: A Theoretical Prediction of a New Fullerene

Francesco Buda[1], Valentina Tozzini[2] and Annalisa Fasolino[2]
[1]Department of Theoretical Chemistry, Vrije Universiteit,
De Boelelaan 1083, NL-1081 HV Amsterdam, The Netherlands
[2]Istituto Nazionale per la Fisica della Materia and Scuola Normale Superiore,
Piazza dei Cavalieri, 7 I-56126 Pisa, Italy
[2]Research Institute for Materials, Institute of Theoretical Physics,
University of Nijmegen, Toernooiveld, NL-6525ED Nijmegen, The Netherlands

ABSTRACT

We report the spontaneous formation of a GaP fullerene cage in ab-initio Molecular Dynamics simulations starting from a bulk fragment. A systematic study of the geometric and electronic properties of neutral and ionized III-V (GaP, GaAs, AlAs, AlP) clusters suggests the stability of hetero-fullerenes formed by compounds with zincblend bulk structure. Our prediction is supported by several indicators: these clusters show closed electronic shells and relatively large energy gaps; the ratio between the cohesive energy per atom in the cluster and in the bulk is very close to the value found for carbon fullerenes of the same size; the clusters are thermally stable up to a temperature range of 1500-2000 K and they do not dissociate when ionized.

INTRODUCTION

The discovery of carbon fullerenes and nanotubes has opened a completely new field at the borderline between chemistry and physics leading to many new phenomena and applications. Most efforts to identify fullerenes based on other elements have focused on BN which is the most similar to carbon and exists in nature in the hexagonal(graphite-like) structure[1-8]. However, the observed (nested-)cages and wires[1,2] do not present the characteristic pentagonal rings of carbon fullerenes.

Here we explore the possibility of fullerene cages based on typical semiconductors of the III-V family, like GaAs, GaP, or AlAs, which do not possess a graphite-like bulk structure. We have recently shown[9] by means of ab-initio Car-Parrinello Molecular Dynamics[10], that a small GaP bulk fragment spontaneously organizes in a cage formed by a different number of atoms of the two elements arranged as in carbon fullerenes. Here we extend the analysis of the geometric and electronic structure of cages with the stoichiometry $III_x-V_{x\pm4}$ for various III-V clusters up to a total of 52 atoms.

COMPUTATIONAL DETAILS

Our results are obtained by means of the Car-Parrinello approach[10] using a Density Functional in the Generalized Gradient Approximation proposed by Becke and Perdew[11,12]. This approximation reproduces the experimental cohesive energy

of typical bulk semiconductors within 5 valence to conduction band excitation energies[13]. We use nonlocal norm-conserving first-principles pseudopotentials[14] and expand the single particle wavefunctions on a plane wave basis set with a cut-off of 12 Rydberg. We use a periodically repeated cubic simulation box of 24 Å side, a size found large enough to describe isolated clusters. The electronic optimization and structural relaxation have been performed using damped second order dynamics with electronic mass preconditioning scheme[15]. The symmetry of the equilibrium structure is not biased but it is reached spontaneously during the geometry optimization starting from the corresponding regular polyhedron.

RESULTS

In ref. [9] we have shown that a bulk like cluster with 41 atoms with tetrahedral bulk-like coordinations spontaneously evolves to a $Ga_{16}P_{12}$ bonded cluster with 12 pentagons and 4 hexagons during the simulated energy minimization.

The observed spontaneous formation of a $Ga_{16}P_{12}$ cage with pentagons is surprising since, in the case of BN[3-6], (deformed) squares are found to be energetically much more favorable. For $B_{12}N_{12}$[4], there is an energy difference of 9 eV between the cage with pentagons and the one with squares in favor of the latter which contains only heteropolar bonds and is favored for a material composed by atoms with very different electronegativity as B and N. Therefore, most studies have considered cages B_nN_n formed by hexagons closed by square rings[3,4,6,7].

Very recently, Fowler et al.[8] have pointed out that, among the cages with pentagons, those with one species in excess of 4 atoms (B_nN_{n+4}) minimize the number of homopolar bonds. The cage $Ga_{16}P_{12}$ which spontaneously appear in our simulation falls into this class. Therefore we focus our study on the equilibrium structure and electronic states of $III_nV_{n\pm4}$ clusters, with a total number of atoms ranging from 20 to 52 and for different III-V compounds.
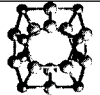
In Tables I and II we show the minimum energy structures of several GaP and GaAs fullerenes with the corresponding symmetry and HOMO-LUMO gap.

As in the case of carbon and BN fullerenes, the III-V clusters would represent metastable states with respect to the bulk equilibrium structure and only experimental observation can establish with certainty their existence. We support our prediction for the stability of the examined GaP clusters by using the following indicators: i) closed electronic shells and large energy gaps; ii) cohesive energy; iii) thermal stability; iv) stability of the ionized clusters.

The first indicator of chemical stability is the energy gap between the highest occupied and lowest unoccupied molecular orbitals (HOMO and LUMO). In carbon fullerenes a correlation between this energy and the observed fullerenes has been experimentally verified[16].

In figure 2 we show the calculated HOMO-LUMO energy gap for all the GaAs clusters studied as a function of the total number of atoms (the nuclearity). The clusters with a majority of atoms of type V show the largest HOMO-LUMO gaps. In general, the gap grows with the cluster size, with a particularly high value for the cluster with 52 atoms as found also for the analogous BN cluster[8].
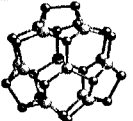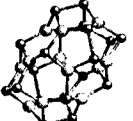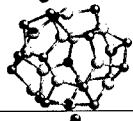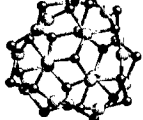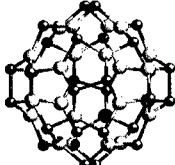
Table I. Optimised structures, symmetry, HOMO-LUMO energy gaps, cohesive energies and Ga–P binding energies for several GaP clusters. The bulk gap is given for comparison. The annealing temperature is also given for the first two structures.

		HOMO-LUMO gap (eV)	$E_{cohesive}$ (Hartree)	$E_{\mathrm{Ga-P}}$ (eV)	annealing temp. (K)
	$Ga_{12}P_8$ T_h	1.28	-2.5374	~ 2.59	~ 1500
	Ga_8P_{12} T_h	2.14	-2.8161	"	> 2000
	$Ga_{16}P_{12}$ T_d	1.09	-3.6876	"	
	$Ga_{12}P_{16}$ T_d	1.55	-3.9452	"	
	$Ga_{10}P_{10}$	1.03	-2.6632	~ 2.58	
	$Ga_{12}P_{12}$ (C_{v3})	1.24	-3.2362	"	
	$Ga_{12}P_{12}$ T_h	1.86	-3.3060	~ 2.49	
	GaP bulk	1.62			

A comparison of the binding energies per atom between the GaP cages and the zincblend bulk phase of this material is possible only for the clusters with the same number of Ga and P atoms. From the results of Table I, we find that the cohesive energies per atom for $Ga_{12}P_{12}$ with squares, $Ga_{12}P_{12}$ with pentagons, and $Ga_{10}P_{10}$ are about 10% lower than in the bulk. This result is very close to that found for BN and carbon fullerenes of the same size[3].

Table II. Optimised geometries, HOMO-LUMO gaps and bond lengths for some of the clusters of the Ga_xAs_{x+4} serie.

	gap (eV)	As–As (Å)	Ga–As (Å)
Ga_8As_{12} T_h	2.03	2.505	2.389
$Ga_{12}As_{16}$ T_d	1.57	2.535	~ 2.4
$Ga_{14}As_{18}$ D_{3h}	1.82	~ 2.5	~ 2.37
D_{3d}	1.87	2.497	~ 2.37
C_2	1.84	~ 2.503	~ 2.37
$Ga_{18}As_{22}$ C_3	1.99	~ 2.497	~ 2.37
$Ga_{24}As_{28}$ T	2.22	2.485	~ 2.0

We have also studied the thermal stability of two clusters with very different energy gaps, namely $Ga_{12}P_8$ and Ga_8P_{12} (see Table I). For both clusters, we have performed two annealing cycles of about 3 ps, up to 1500 K and up to 2000 K. The system is heated with a rate of 2×10^{15}K/s, then equilibrated for one ps at the highest temperature, and finally cooled down with the same temperature change rate. For Ga_8P_{12} no bond breaking or structural rearrangements occur in both cycles

and the structure comes back to the same minimum energy configuration when the temperature is lowered. This is also the case for $Ga_{12}P_8$ in the annealing up to 1500 K, whereas at 2000 K some structural rearrangement takes place leading to a distorted structure with higher energy when cooled down. These results indicate that the thermal stability is correlated with the width of the energy gap.
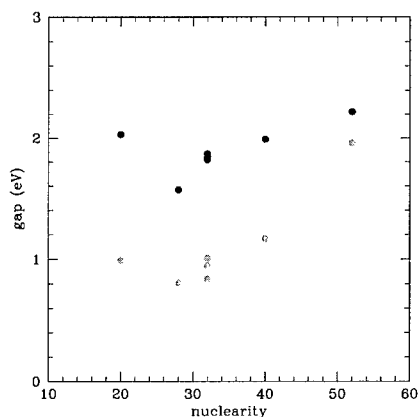
Figure 2. HOMO-LUMO gap of the GaAs clusters as a function of the number of atoms in the cluster. Dark (red) dots correspond to Ga_xAs_{x+4} clusters, light (green) dots to $Ga_{x+4}As_x$ clusters. The "magic" clusters, that is, the more stable of the serie, have been chosen.

Mass spectrometry experiments use the difference in mass-to-charge ratio of ionized atoms or clusters to select them. Therefore one basic requirement for the possible detection of such clusters is that they remain stable also when ionized. We have investigated the stability of some positively ionized clusters, $[Ga_8P_{12}]^+$, $[Ga_{12}P_{16}]^+$ and $[Ga_{16}P_{12}]^+$. The electronic structure remains almost unaffected and degeneracies are broken by negligible amounts in the order of hundredths of eV. Only minor structural distortions occur upon ionization. In particular, the six equivalent P-P (Ga-Ga) bond lengths split into three different classes. Remarkably, during a molecular dynamics run for $[Ga_8P_{12}]^+$ we observe a dynamical exchange between these three classes of bond lengths with each other. This effect produces features in the low frequency vibrational spectrum in the range $30 - 120$ cm^{-1} which might be detected by infrared multiphoton ionization spectra[17].

CONCLUSIONS

In summary, our MD results strongly suggest that small fullerenes formed with III-V semiconductor compounds could be stable, since they have high symmetry, closed electronic shells, and large HOMO-LUMO energy gaps. These clusters are thermally stable also when ionized.

The cages with the stoichiometry III_x-V_{x+4}, which minimizes the number of homopolar bonds, are particularly stable and show the largest HOMO-LUMO gaps.

We hope that this work will stimulate experimental groups to widen their search for hetero-fullerenes also to III-V semiconductor compounds.

REFERENCES

1. D. Goldberg, Y. Bando, O. Stéphan, and K. Kurashima, Appl. Phys. Lett. **73**, 2441 (1998).

2. P. A. Parilla, A. C. Dillon, K. M. Jones, G. Riker, D.L. Schulz, D.S. Ginley and M.J. Heben, Nature **397**, 114 (1999).

3. G. Seifert, P. W. Fowler, D. Mitchell, D. Porezag, and TH. Frauenheim, Chem Phys. Lett. **268**, 352 (1997).

4. F. Jensen, and H. Toftlund, Chem Phys. Lett. **201**, 89 (1993).

5. X. Blase, A. De Vita, J-.C. Charlier, and R. Car, Phys. Rev. Lett. **80**, 1666, (1998).

6. M-L. Sun, Z. Slanina and S-.L. Lee, Chem Phys. Lett. **233**, 279 (1995).

7. S. S. Alexandre, M. S. C. Mazzoni, and H. Chacham, Appl. Phys. Lett. **75**, 61 (1999).

8. P. W. Fowler, K. M. Rogers, G. Seifert, M. Terrones, and H. Terrones, Chem Phys. Lett **299**, 359 (1999).

9. V. Tozzini, F. Buda, and A. Fasolino, *Phys. Rev. Lett.* **85**, 4554 (2000).

10. R. Car and M. Parrinello, Phys. Rev. Lett. **55**, 2471 (1985).

11. A.D. Becke, Phys. Rev. A **38**, 3098 (1988).

12. J.P. Perdew, Phys. Rev. B **33**, 8822 (1986).

13. G. Ortiz, Phys. Rev. **B 45**, 11328 (1992).

14. X. Gonze, R. Stumpf, and M. Scheffler, Phys. Rev. B **44**, 8503 (1991).

15. F. Tassone, F. Mauri, and R. Car, Phys. Rev. B **50**, 10561 (1994).

16. H. Kietzmann, R. Rochow, G. Ganteför, W. Eberhardt, K. Vietze, G. Seifert, and P.W. Fowler, Phys. Rev. Lett. **81**, 5378 (1998).

17. D. Van Heijnsbergen, G. von Helden, M. A. Duncan A. J. A. van Roij and G. Meijer, Phys. Rev. Lett. **83**, 4983 (1999).

Nano-Sized [60]Fullerene-Cyclodextrin Molecules

Jeong-Seo Park, Han-Chang Kang, and Kurt E. Geckeler*
Laboratory of Applied Macromolecular Chemistry,
Department of Materials Science and Engineering,
Kwangju Institute of Science and Technology,
1 Oryong-dong, Buk-gu,
Kwangju 500-712, South Korea

ABSTRACT

As [60]fullerene is a very hydrophobic macromolecule, there have been a number of attempts to make it more hydrophilic for biomedical applications. By attaching hydrophilic moieties such as poly(oxyethylene)(POE) chains and cyclodextrin molecules to [60]fullerene, novel water-soluble and biocompatible materials have been successfully prepared [1,2].

The synthesis of novel macrocyclic fullerene conjugates which are water-soluble is reported. The telechelic fullerene derivatives have been prepared *via* addition reaction of POE-based arms with covalently bonded β-cyclodextrin (CD) to [60]fullerene. To this end, a mono-tosylated CD derivative has been prepared in pyridine and then reacted with an amino-functional POE in the presence of triethylamine. The subsequent reaction of [60]fullerene with the hydrophilic POE-conjugated CD-derivative yielded the macrofullerene after separation and purification procedures.

The macrocyclic [60]fullerene derivatives obtained were soluble in water and characterized by UV-VIS and FT-IR spectroscopy as well as light scattering measurements and thermogravimetric analysis.

INTRODUCTION

Since [60]fullerene has been made preparatively accessible [3], the promising properties of [60]fullerene stimulate an increasing interest for fullerene-containing polymers in view of biomedical applications [1,2]. There have been a number of attempts to make it more hydrophilic, as [60]fullerene possesses radical scavenging effects [4].

POE exhibits the minimal interfacial energy in an aqueous environment and an unique solubility in water. Furthermore, as POE is a very hydrophilic and biocompatible material, it is already applied in many fields such as biomedical and pharmaceutical areas [5]. And CD are water-soluble cyclic oligosaccharides built up of glucopyranose units. Thus, by using of [60]fullerene as a molecular core in linking multiple POE chains and CD molecules novel water-soluble and biocompatible materials have been successfully prepared.

EXPERIMENTAL DETAILS

The synthetic procedure consists of three steps. The first step is the preperation of mono-6-(p-tolylsulfonyl)-β-cyclodextrin (m-TsCD). m-TsCD was synthesized by following a standard procedure [6].

The second step was the preparation of mono-poly(oxyethylene)-β-cyclodextrin (POE-CD). It was synthesized by reacting equimolar quantities of m-TsCD and difunctional amino POE (aPOE) with a molecular mass 2 kg mol^{-1}.

In the final step, we synthesized the (aPOE)-poly(oxyethylene)-β-cyclodextrin (F-(POE-CD)$_n$) by reacting with POE-CD and [60]fullerene. During the reaction, the color of solution changed from purple to light-yellow, and then to pink.

UV/Vis spectra were obtained with a UV/Visible spectrometer (Perkin Elmer, Lambda 12). The particle size was measured by dynamic light scattering (Malvern Instruments Ltd. Series 4700) with argon ion laser system at 488 nm with a digital correlator.

RESULTS AND DISCUSSION

The macrocyclic [60]fullerene derivatives obtained were soluble in water and the synthesis of these conjugates was confirmed by UV-VIS Spectroscopy.

In Figure 1. it is shown that the [60]fullerene-POE conjugate absorbs in the UV-visible region showing a maximum at 250-270 nm. At higher wavelengths, the absorbance presents a smoothly decreasing shoulder without characteristic maxima. As the reaction proceeded, the peak height at around 340 nm decreased and finally disappeared. This phenomena explains the disruption of the π-bonds of [60]fullerene due to the formation of side arms which are covalently bonded to [60]fullerene.
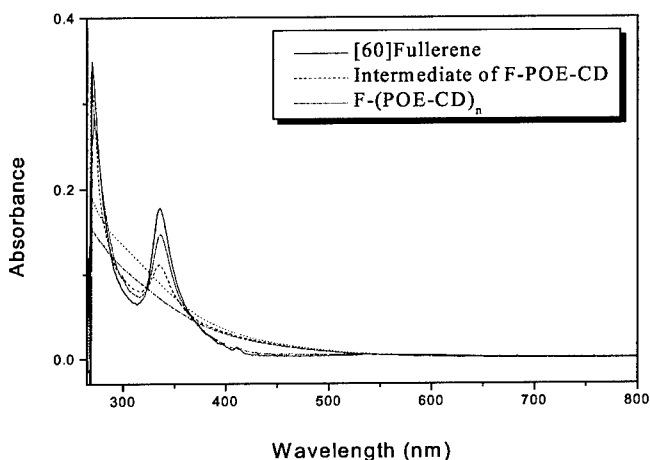
Figure 1. UV/VIS spectra showing the formation of [60]fullerene-cyclodextrin conjugates (F-(POE-CD)$_n$) by an addition reaction with reaction time

The infrared spectrum of the polymer is shown in Figure 3. It looks similar to that of the POE-CD prepolymer. A broad band around 3440 cm^{-1} corresponding to the absorption of primary and secondary amine and alcohol groups of CD is shown. It also shows a sharp peak at around 1100 cm^{-1}. Interestingly the two peaks around 520 cm^{-1} and 570 cm^{-1}, shown in both [60]fullerene and POE-CD, changed their forms to broad bands.
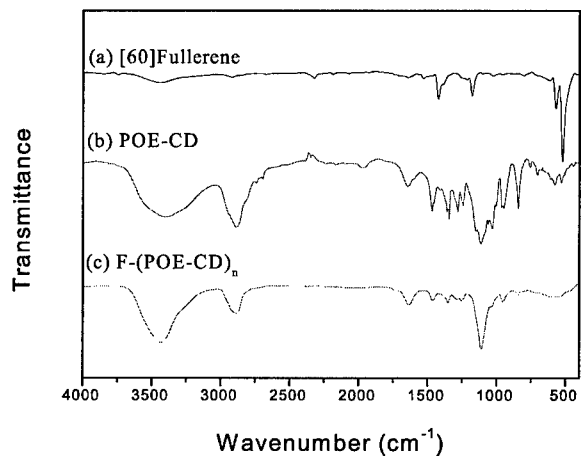
Figure 2. FT-IR spectra of (a) [60]fullerene , (b) POE-CD, and the reaction product (c) F-(POE-CD)$_n$

Figure 3 shows the particle size distribution of F-(POE-CD)$_n$ obtained by laser light scattering. The molar mass thus obtained was 13,496 g mol^{-1} and the average particle size in water was 24.6 nm with a mean value distribution of 98.7%. This value is a little smaller than the expected whole length of fully extended fullerene derivatives. Based on the thermogravimetric analysis, an average number of 2.07 side-arms could be calculated.
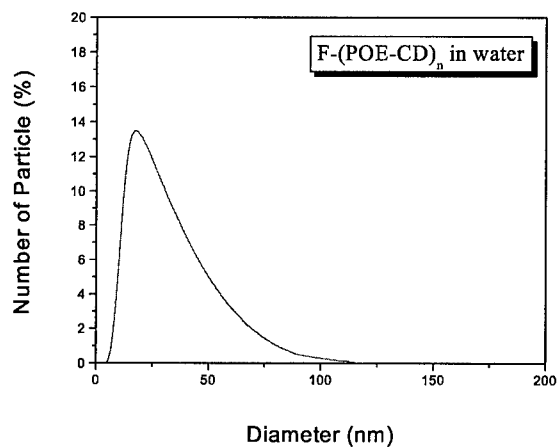
Figure 3. Particle size distribution of F-(POE-CD)$_n$ by laser light scattering

The characteristic properties such as hydrophilicity and expected biocompatibility of this novel macrocyclic molecules hold promise for a broad range of biomedical applications [7,8].

CONCLUSIONS

The synthesis of a novel water-soluble macrocyclic [60]fullerene conjugate is described. The macromolecules were prepared by the multiple addition of POE arms with covalently bonded CD to [60]fullerene. The preperation of the [60]fullerene conjugates by the addition of hydrophillic POE and CD is a useful method of imparting water-solubility of [60]fullerene derivatives.

ACKNOWLEDGEMENTS

REFERENCES

1. K. E. Geckeler, *Trends Polym. Sci.*, **2**, 355 (1994)
2. K. E. Geckeler and S. Samal, *Prog. Rubber Plast. Technol.*, **16**, 69 (2000).
3. H. W. Kroto, J.R.Heath, S. C. O'Brian, R. F. Curl and R. F. Smally, *Nature*, **318**, 162 (1985).
4. K. E. Geckeler and S. Samal, *Fullerene Sci. Technol.*, **9**, 17 (2001)
5. S. Herman, G. Hooftman and E. Schacht, *J. Bioact. Compat. Polym.*, **11**, 135 (1996).
6. T. Nazaki, Y. Maeda, K. Ito, and H. Kitano, *Macromolecules*, **28**, 522 (1995).
7. K. A. Connors, *Chem. Rev.*, **97**, 1325 (1997).
8. K. E. Geckeler and S. Samal, *Polym. Internat.*, **48**, 743 (1999).

Studies on the Interaction of Water-Soluble Fullerols with BSA and the Effects of Metallic Ions

Xu Bingshe[1], Liu Xuguang[1], Yan Xiaoqin[1], Qiao Jinli[2] and Jin Weijun[3]

[1]College of Materials Science and Engineering, Taiyuan University of Technology, Taiyuan, Shanxi, China, 030024

[2]College of Science, Taiyuan University of Technology, Taiyuan, Shanxi, China, 030024

[3]Department of Chemistry, Shanxi University, Taiyuan, Shanxi, China, 030006

ABSTRACT

The interaction of water-soluble C_{60} derived fullerols with bovine serum albumin (BSA) in physiological environment was studied in detail by the fluorescence method. Experiments showed that the interaction of fullerols with BAS is mainly in the manner of non-covalent hydrogen bond. Based on the measurements of fluorescence intensity, the apparent binding constant K and the binding site number n were obtained with K=4000 and n=1, and the energy transfer efficiency in the reaction is 0.63. Besides, the effects of metallic ions such as Cu^{2+}, Fe^{3+} and Cr(VI) on the interaction of fullerols with BSA were investigated. It was found that the effects of the metallic ions are quite different from each other. Low concentrations of Cu^{2+} can promote the interactions between fullerols and BSA, while high concentrations of Fe^{3+} or Cr(VI) favorite the interactions between fullerols and BSA.

INTRODUCTION

Fullerene C_{60} and its derivatives have attracted much interest due to their special structure, and novel chemical and physical functions[1]. However, their water-insoluble property has put much limit on their researches and applications, especially in biochemistry. The success in the synthesis of polyhydroxyl C_{60} derivative suggests the potential applications in biochemical and pharmaceutically related investigations[2-4]. In previous study, the fluorescence properties of fullerols and their interactions with various metallic ions were studied in detail[5]. Based on the study the fluorescence method was used to investigate the interaction between fullerols and BSA in physiological environment and the effects of various metallic ions, aimed at .understanding the interaction mechanism of fullerols with their biological surroundings.

EXPERIMENTAL

Apparatus and Reagents

All fluorescence measurements were carried out on a Hitachi RF-540 fluorescence photospectrometer. The wavelengthes of excitation and emission of fullerols were 340/440nm, respectively. Both of the excitation and emission slits were set as 10nm for providing the premium signals. IR spectra were recorded on a Model 1730 infrared photospectrometer, Perking-Elmer Co. and ^{1}HNMR spectra were obtained on a Hitachi R-24B Nuclear Magnetic

Resonance photospectrometer for the determination of fullerols structure.

C_{60} (99.9%) was purchased from Tri- Carbon Cluster Materials Co. Ltd., Wuhan University, China. BSA was purchased from Shanghai Lizhu Dongfeng Biotech Co. Ltd., China, with molecular weight of 65000. All chemicals used were analytical reagents. These reagents included the salts giving 3 kinds of ions, such as Cu^{2+}, Fe^{3+} and $Cr(VI)$. The salts were $CuCl_2$, $FeCl_3$, and $K_2Cr_2O_7$, respectively. The water was secondary sub-boiled distilled water.

Procedure

Fullerols were prepared according to Ref.[7]. The final product was dark-brown and easily soluble in water. The structure of the product was then identified as $C_{60}(OH)_m$ by IR and ^{1}HNMR, where m, the number of –OH group, was 23-24.

An accurate amount of fullerols was weighed and prepared as stock solution of 1×10^{-3} mol/L using phosphate buffer solution with pH 7.4. The wavelengths of excitation and emission were 340/440nm, respectively. Both of the excitation and emission slits were set as 10nm for providing the premium signals. During experiments, an accurate volume of fullerols solution was injected by microinjector into BSA solution of 1×10^{-5} mol/L containing buffer solution and predetermined amount of metallic ion, and fluorescence spectrum was measured and recorded.

RESULTS AND DISCUSSIONS

Interaction of BSA with Fullerols

When 340nm is used as the excitation wavelength, fullerols can emit strong fluorescence at the wavelength of 440nm. In the previous study, the effects of pH value on fluorescence intensity have been presented[5]. The effect of pH value on fluorescence intensity can also be observed in this study. It is clear that the strongest fluorescence can only be observed in neutral solutions, which would lead to such a conclusion that fullerols in neutral molecular form are strong fluorescent substances. Fluorescence intensity becomes much weaker in both acidic and basic solutions. Therefore, in this research pH range of 6.5~7.5 was selected as the optimum acidity to carry out the bioactivity research of fullerols in physiological environment.

The excitation and emission spectra of fluorescence are given in Figure 1 and Figure 2. It can be seen that when 340nm is used as the excitation wavelength, fullerols can emit strong fluorescence at the wavelength of 440nm.

The fluorescence spectra of fullerols-BSA systems are shown in Figure 1. It can be seen that the fluorescence intensity at ~440nm increases markedly with the increase of the concentrations of fullerols. At the same time, the maximum emissions values at ~440nm have a
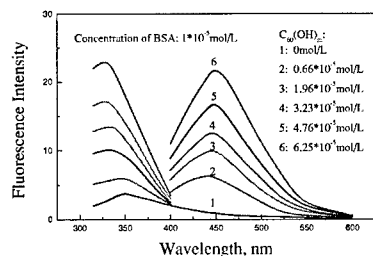
Figure 1   Fluorescence spectra of different concentrations of fullerols in the presence of BSA
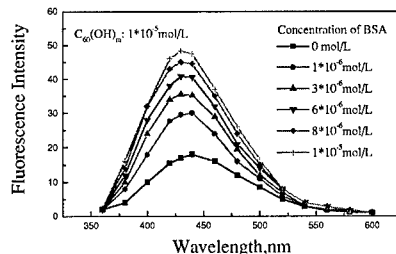
Figure 2   Fluorescence emission spectra of fullerols in the presence of different concentrations of BSA

gradual red-shift to 450nm, significant blue-shift can also be observed for excitation peaks from ~350nm to ~330nm. Based on the fact that there are only a strong absorption peak at 221nm and a weak absorption peak at 278nm, no absorption at 440nm for BSA, it can be suggested that there occurred some interaction between fullerols and BSA, which forms some kind of composite containing ground state and excited state. The absence of corresponding functional groups for chemical reaction between fullerols and BSA resulted in such a suggestion that the strong interaction between two molecules may be the hydrogen bridge bonding between the –OH in fullerols and the –NH$_2$ or –COOH in the peptide chains of BSA, which is in fact non-covalent.

The so-called bi-reciprocal method can be used to describe the interaction of fullerols with BSA[8]. From Figure 3 it can be seen that there exists very significant linear relationship in the plot of $(F-F_0)^{-1}$ against $C_{C60(OH)m}^{-1}$. The regression equation was found as follows

$$(F-F_0)^{-1} = (k'C_{BSA})^{-1} + (k'KC_{BSA})^{-1} C_{C60(OH)m}^{-1} \qquad (1)$$

where F_0 is the fluorescence intensity of BSA without fullerols added in; F is the fluorescence intensity of BSA at presence of fullerols; C_{BSA} and $C_{C60(OH)m}$ are the concentrations of BSA and fullerols, respectively; k' is apparatus constant; and K is the apparent interaction constant. This relationship means that the combination ratio of fullerols and BSA is 1:1 with the K value of 4000 obtained from the slop and intercept of the plot in Figure 3.

It was observed that the fluore- scence emission wavelength of BSA is 340nm (Figure 1), quite the same as that of the fluorescence excitation of fullerols. It is

Figure 3 Bi-reciprocal plot for fullerols-BSA system

clear that the increase in the fluorescence intensity of fullerols with the increase of BSA concentrations originates in some energy transfer between them, as showin in Figure 2. The efficiency of energy transfer(E) is defined as following equation:

$$E = 1 - F_0/F \qquad (2)$$

Where F_0 and F are the fluorescence intensities of fullerols in the absence and presence of BSA, respectively. It can be calculated that the E value is 0.63 when the concentrations of fullerols and BSA are 1:1.

The Effects of Cu^{2+}, Fe^{3+} and Cr(VI) on the Interactions of Fullerols with BSA

From previous study on the interaction of fullerols with metallic ions[5], It was found that Cu^{2+}, Fe^{3+} and Cr(VI) can quench the fluorescence of fullerols effectively. Here the three ions were introduced to investigate their effects on the interactions of fullerols with BSA.

Shown in Figure 4 are the fluorescence spectra of fullerols in the presence of Cu^{2+}, Fe^{3+} and Cr(VI) at a constant BSA concentration of 1×10^{-5} mol/L. In the case of Cu^{2+} or Fe^{3+}, with the increase of fullerols concentrations, the fluorescence intensity of BSA-M^{n+}-Fullerols increases and the emission peaks red-shifts gradually from 440nm to about 450nm, indicating the formation of more stable tri-component complex in both ground state and excited state among fullerols, BSA and Cu^{2+} or Fe^{3+} than bi-component complex between fullerols and BSA. In the case of Cr(VI), the little change in the shape and location of the peaks indicates that the formation of tri-component complex can only occur in excited state.
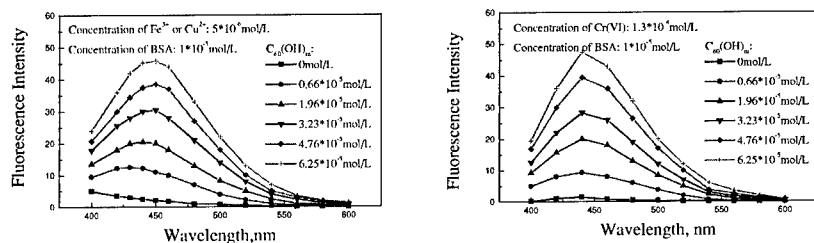
Figure 4   Fluorescence emission spectra of fullerols in the presence of BSA and in the presence of Cu^{2+}, Fe^{3+} or Cr(VI)

The K values at different concentrations of Cu^{2+}, Fe^{3+} and Cr(VI) are shown in Figure 5. An interesting phenomenon is that for all three curves a 'valley' occurs when the ratio of the concentrations of metallic ions and BSA is 1:1, indicating that competitive combination occurs between BSA and fullerols with the metallic ions. At this time, the presence of metallic ions doesn't show any promotion to the interaction of fullerols with BSA but show some role of inhibition. It can also be observed from Figure 5 that low concentrations of Cu^{2+} favorite the interaction of fullerols with BSA. When the ratio of Cu^{2+} to BSA is larger than 1:1, little apparent change can be observed,
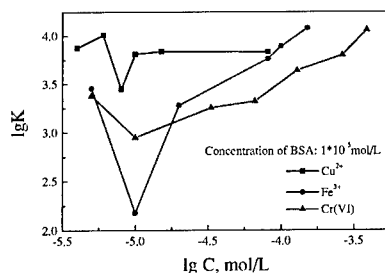
Figure 5 Binding constant K of BSA to fullerols in the presence of Cu^{2+}, Fe^{3+} or Cr(VI)

suggesting that at higher concentrations Cu^{2+} exhibit little effect on the interaction. In the case of Fe^{3+} and Cr(VI), their higher concentrations favorite the interaction of fullerols with BSA.

CONCLUSION

The interaction of water-soluble C_{60} derived fullerols with BSA in physiological environment was studied in detail. Experiments showed that the interaction of fullerols with BSA is mainly in the manner of non-covalent hydrogen bond. Based on the measurements of fluorescence intensity, the apparent binding constant K and the binding site number n were obtained with K=4000 and n=1, and the energy transfer efficiency in the reaction is 0.63. Besides, the effects of metallic ions such as Cu^{2+}, Fe^{3+} and Cr(VI) on the interaction of fullerols with BSA were investigated. It was found that the effects of the metallic ions are quite different from each other. Low concentrations of Cu^{2+} can promote the interactions between fullerols and BSA, while high concentrations of Fe^{3+} or Cr(VI) favorite the interactions between fullerols and BSA.

ACKNOWLEDGEMENT

REFERENCES

1. Y. Wang, L.T. Cheng,   J. Phys. Chem., 96(4), 1530 (1992)
2. R. Sijbesma, G. Srdannov, F. Wudl, J.A. Castoro, C. Wilkins, S.H. Friedman, D.L. DeCamp and G.L. Kenyon,   J. Am. Chem. Soc., 115(15), 6510 (1993)
3. L.Y. Chiang, F.G. Lu, J.T. Lin,   J. Chem. Soc., Chem. Commun., 12, 1283 (1995)
4. Y. M. She, Y. P. Ji, Y. F. He and S. Y. Liu,   Chem. J. Chinese Univ., 19(11), 1735 (1998)
5. X.Q. Yan, X.G. Liu, J.L. Qiao, W.J. Jin and B.S. Xu, International Journal of Materials and Product Technology, (2001) accepted
6. T.B. Li, K.X. Huang, X.H. Li, H.Y. Jiang, J. Li, X. Z. Yan, J. Cai and S.K. Zhao,   Chem. J. Chinese Univ., 19(6), 858 (1998)
7. G.Z. Chen, X.Z. Huang, and J.G. Xu, in *The Development of Fluorescence Analysis*, (Xiamen University Press, Fujian, China,1991), p174
8. X.Z. Feng, R.X. Jin, Y. Qu and H.W. He,   Chem. J. Chinese Univ., 17(6), 866 (1996)

Transformation of Active Carbon to Onion-like Fullerenes Under Electron Beam Irradiation

Bingshe Xu[1]   Husheng Jia[1]   Hefeng Zhou[1]   Hideki Ichinose[2]   Chihiro Iwamoto[2]
[1] College of Materials Science and Engineering, Taiyuan University of Technology, Taiyuan, Shanxi, China, 030024
[2] Department of Materials Science, School of Engineering, The University of Tokyo, Tokyo, Japan, 113-0033

ABSTRACT

The transformation of an active carbon film with Pt nanoparticles to onion-like fullerenes has been in-situ investigated by a high-resolution transmission electron microscope. It was found that the onion-like fullerenes/metals polycrystalline film was formed under electron irradiation. The formation process was consisted of three steps: first, the flakes of onion-like fullerenes were induced by Pt nanoparticles; second, the flakes grew into a few ellipsoidal graphite shell; and third, a gradual reorganization of the formation of quasi-spheroid graphite shells and the bond of Pt particles was took place. It was a composite film of onion-like fullerenes and metal particles. It is suggested that the transformation mechanism involves an irradiation of electron and a catalytic effect of Pt nanoparticles, while any temperature rise due to electron irradiation seems to be negligibly small.

INTRODUCTION

Since the discovery of fullerenes, their synthesis and characterization have attracted a great deal of interest in the scientific community. The fullerenes with different structure such as buckminsterfullerene[1,2], nanotubes[3], onion-like fullerenes[4], and metal-fullerenes[5] have been produced by laser vaporization, resistive heating, and arc discharge. For onion-like fullerenes (OLF), Iijima synthesized the onion structure carbon by arc discharge[4], Ugarte obtained OLF from polyhedral graphite and nanotubes by intense electron bombardment. Such OLF were usually formed from ordered structure carbons. Xu reported the transformation of an amorphous carbon film with metallic nanoparticles of Al, Au and Pt into giant onion-like fullerenes induced by electron beam irradiation in a high resolution transmission electron microscope [6-8]. They were the first experiments in which OLF were formed from an amorphous carbon film using an electron irradiation technique and metallic nanoparticle catalysts. Four kinds of onion-like fullerenes have been produced, such as signal-nuclei OLF, multiple-nuclei OLF, intercalation OLF with metal atoms inside its shells, and metallofullerene with metal atoms in its center.

Here, an experimental study is reported in which onion-like fullerenes/metals film was produced from active carbon by electron beam irradiation and Pt nanoparticle catalysts. The kinetics and mechanism of their formation were also discussed.

EXPERIMENTAL

Pt nanoparticls were prepared on amorphous carbon films by Ar^+ beam sputtering. The ion acceleration voltage was 2-4kV, with a beam current of 0.2-0.3 mA. The process was done under vacuum of 10^{-4} Pa. The size of Pt nanoparticles ranges from 1 to 6 nm in diameter. The thickness of amorphous carbon film was 20 to 25 nm. To study the transformation of active carbon to onion-like fullerenes, the Pt nanoparticles were covered with active carbon as shown in Fig.1. The thickness of film was increased to 40-50 nm.

These metal nanoparticles and active carbon film specimen were irradiated at an intensity in the range of 0.3-3.3 × $10^{20}e/cm^2$sec in a high resolution transmission electron microscope JEM-2010. The formation of onion-like fullerenes was investigated by *in-situ* observations. The vacuum was better than 10^{-5} Pa. HRTEM images were recorded with a low intensity electron beam in order to prevent electron damage and to produce good quality micrographs after the specimen were strongly irradiated.
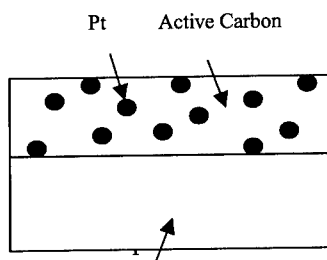
Fig.1 Schematic Diagram of HSTEM Specimen

RESULTS

Fig.2 shows an image of an active carbon film transformed into onion-like fullerenes, induced by 10% Pt nanoparticles under electron beam irradiation at an intensity of 3.3× $10^{20}e/cm^2$sec for 2800 sec. The nucleus of onion-like fullerenes was formed firstly in the area covered with active carbon. And it was achieved in the present of Pt nanoparticles. We also used an active carbon film without metal particles, and could not obtain onion-like fullerenes, even using the same experimental conditions.

The formation process of a composite film of onion-like fullerenes and metal particles was in-situ observed as Fig.3. The intensity of electron beam irradiation is 3.3×$10^{20}e/cm^2$sec. The process was divided into the following three steps. First, the nucleus and the first flake of a fullerene under the Pt nanoparticle are formed, which is indicated by the arrows in Fig.3(a). Second, the flakes grew into a few ordered structures as irregular ellipsoidal graphite shell with a large hollow interiors. It is showed in Fig.3(b). And third, a gradual reorganization of the formation of quasi-spheroid graphite shells and the bond of Pt particles was took place, as shown in Fig.3(c).
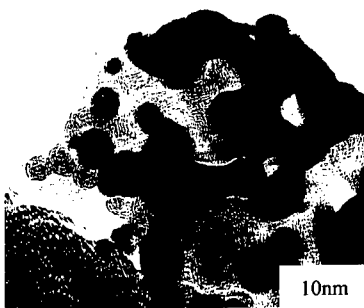
Fig.2 Onion-like fullerenes induced under 10% Pt nanoparticles by an electron irradiation at an intensity of 3.3 ×$10^{20}e/cm^2$sec for 2800 sec
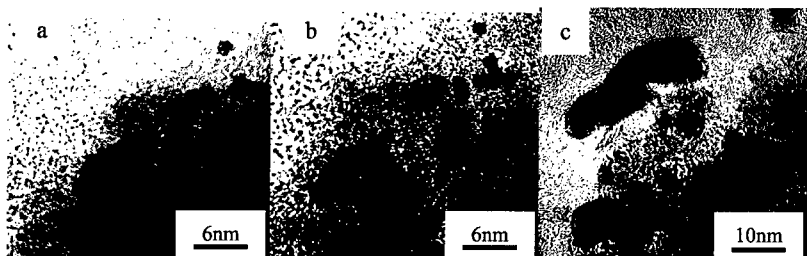
Fig.3 Onion-like fullerenes induced under 5% Pt nanoparticles by an electron irradiation at an intensity of 3.3×10^{20}e/cm^{2}sec for (a) 0 sec, (b) 1800 sec and (c) 3000 sec.

DISCUSSION

Nucleation of onion-like fullerenes

Fig.2 shows that the transformation of carbon to fullerene took place in the active carbon areas. Under the electron beam irradiation, the first elementary reaction is carbon atom catalyzed by Pt atoms on the surface of the nanoparticles to form a short range order C-C bond through rearrange from the active carbon. The catalytic effect of Pt atoms is also confirmed in Fig.3. It can be seen that all positions of the onion-like fullerenes cores correspond to the positions of Pt particles. It is clearly indicated that Pt atoms promote the formation of onion-like fullerenes. The nucleation sites are around the contact circle between Pt nanoparticles and the active carbon substrate, as confirmed by the fact that the larger fullerenes are induced around larger Pt particles.

Growth mechanism of onion-like fullerenes

As the the proceedings of the irradiation of electron beam, the C-C bond in a short range ordered structure changes into an ordered structure, such as a hexagonal or a pentagonal network, and finally forms the first flake of a fullerene by the self-diffusion of carbon atoms. The flakes grow into an ellipsoidal structure. Successive electron irradiation induces multiple ellipsoidal graphitic shells that finally change into a quasi-spheroid shape. The ellipsoidal graphitic shells expand their bonds along the surfaces of Pt nanoparticles and wrap them, thereby encapsulate them. The shells change in shape into spheres, which finally build the multiple quasi-spheroid shells, i.e. onion-like fullerenes, by an inner epitaxy[4] which eliminates the inner hollow. The driving force of onion-like fullerenes growth has been discussed in terms of a free energy minimization theory[4], which accounts for the highly stable spheroidal shape of carbon clusters and the multiple shell structure, which is more energetically favorable than a single or tubular shell. This process occurs spontaneously, and both results in the elimination of the dangling bonds, and promotes onion-like fullerenes with a maximum of 54 shells, which corresponds to about 105 carbon atoms in our experiment.

Transformation Drive Force

In the high temperature process, as in the arc discharge method, the nucleus of onion structure of carbon could be formed from a liquid drop. But, in the electron beam irradiation process, the first question is how high the temperature rise is. Recently, Xu[8] used Fisher's model to estimate the temperature rise to result in about 10 degrees at most. It is suggested that the heating effect by the electron irradiation is not a major effect for onion-like fullerenes formation. Hence, the formation and growth of onion-like fullerenes from active carbon can be considered as the electron stimulation effect and the catalysis effect of metal atoms.

CONCLUSION

Under the electron beam irradiation, the onion-like fullerenes can be transformed from active carbon film. The formation process was consisted of three steps: first, the flakes of onion-like fullerenes were induced by Pt nanoparticles; second, the flakes grew into a few ellipsoidal graphite shell; and third, a gradual reorganization of the formation of quasi-spheroid graphite shells and the bond of Pt particles was took place. It was a composite film of onion-like fullerenes and metal particles.

The transformation mechanism involves the electron stimulation effect and the catalysis effect of metal atoms, while any temperature rise due to electron irradiation seems to be negligibly small.

ACKNOWLEDGEMENT

REFERENCES

1. H. W. Kroto, J. R. Heath, S. C. O'Brien, R. F. Curl and R. E. Smalley, Nature, 318, 162(1985)
2. W. Kratschmer, L. D. Lamb, K. Fostiropous and D. R. Huffman, Nature, 347, 345(1990)
3. S. Iijima, Nature, 354, 56(1991)
4. D. Ugarte, Nature, 359, 707(1992)
5. D. Ugarte, Chem. Phys. Lett. 209, 99(1993)
6. B. S. Xu and S.-I. Tanaka, Acta Materialia, 46, 5249(1998)
7. B. S. Xu and S.-I. Tanaka, Mat. Res. Soc. Symp. Proc., 472, 179(1997)
8. B. S. Xu and S.-I. Tanaka, Proc. Int. Centennial Symp. On the Eletron, Cambridge, 355(1997)

Effect of Crystalline Structure and Impurity Content of C_{60} Thin Films on the Order/Disorder Phase Transition

Eugene A. Katz[1], David Faiman[1,2], Svetlana Shtutina[2], Aleksandra P. Isakina[3] and Konstantin A. Yagotintsev[3]
[1] The National Solar Energy Center, The Jacob Blaustein Institute for Desert Research, Ben-Gurion University of the Negev, Sede Boqer, 84990 Israel
[2] Department of Physics, Ben-Gurion University of the Negev, Beersheba, 84105 Israel
[3] Verkin Institute for Low Temperature Physics & Engineering, National Academy of Science of Ukraine, 47 Lenin Ave., Kharkov 310164, Ukraine

ABSRACT

Near the temperature of 260 K, C_{60} crystal is known to undergo a first order phase transition, associated with changes in molecular rotations. The present paper reports the effect of the crystalline structure and impurity content of C_{60} thin films on their structural behavior near this phase transition. Polycrystalline C_{60} films with different grain sizes and oxygen content were obtained by varying the conditions of their vacuum deposition and post-grown exposure. Temperature-resolved X-ray diffraction in the range 300 - 15 K was used to determine the lattice parameter and its changes near the phase transition temperature. Decrease in grain sizes and increase in oxygen content of the films are found to lead to a gradual reduction in the discontinuity in lattice parameter and the transition temperature.

INTRODUCTION

Solid C_{60} is a molecular crystal with C_{60} molecules occupying the lattice sites of a face-centered cubic (*fcc*) structure at room temperature [1]. C_{60} molecules have a rotational degree of freedom in the crystal. The C_{60} crystal is known to undergo a phase transitions associated with changes in the molecular rotations. Near the temperature $T_c = 260$ K, C_{60} crystal undergoes a first order phase transition from the *fcc* structure above T_c to a simple cubic (*sc*) structure below T_c [2-4]. C_{60} molecules have been found to rotate freely in the *fcc* phase while rotation locks into specific orientations in the *sc* phase.

However, the published data dealing with this phase transition in C_{60} thin films are very contradictory because of the fact that the films grown under different deposition conditions and/or subjected to different post-growth exposures may have substantially various crystalline structure and impurity content. On the other hand, no systematic study of the effect of the crystalline structure and impurity content of C_{60} films on their behavior near the phase transition have been performed. This paper reports the first results of such kind of study.

EXPERIMENTAL DETAILS

C_{60} thin film was deposited by a vacuum deposition technique on substrates of mica, optical glass and optical glass predeposited with an Ag sub-layer. The starting C_{60} powder ('Super Gold

Grade', > 99.9%) was commercially obtained from Hoechst AG. Detailed description of the deposition conditions was given elsewhere [5-8].

The thickness of all C_{60} films under the present study was about 100 nm.

The crystalline structure of the C_{60} films was characterized by X-ray diffraction (XRD) in Cu- and Fe-K_{α} radiation, at room temperature, and then was studied by temperature-resolved XRD in the temperature range from 300 K to 15 K, using a home-made liquid-helium cryostat. The XRD patterns also included reflections from a reference substance (high-purity Cu). Use of this modified reference XRD technique made it possible to reduce the error in our determination of the lattice parameter, which is particularly important when studying its temperature dependencies. The error in determining the lattice parameters did not exceed ± 0.02%. The sample temperature was measured with a platinum resistance thermometer.

The morphology of the front surface of the film was studied by the Atomic Force Microscopy (AFM).

RESULTS AND DISCUSSION

The film deposited at a rate of 0.2-0.4 Å/s on a glass substrate, held at 443 K (sample 1 in table I) was found to consist of two phases: amorphous and polycrystalline with grain sizes of 20 - 50 nm. The latter was characterized by the Bragg reflections (111), (220) and (311) of fcc C_{60} lattice with approximately the same intensities. The room-temperature XRD pattern of such a film is similar to one displayed in Fig. 2c in Ref. 5.

Table I. Growth conditions, structural characteristics and parameters of the fcc/sc phase transition for our C_{60} thin films together with the published data [2-4] for C_{60} single crystals.

Sample	Substrate material	Substrate temperature (K)	Depositon rate (Å/s)	Crystalline structure of the C_{60} films	Grain size in the film surface (nm)	T_c (K)	$\Delta a/a$ (%)
1	glass	443	0.2-0.4	amorphous/ polycrystalline	10 - 20	-	-
2	Ag/glass	473	18-20	<111> textured polycrystalline	100 - 200	250	0.06
3	mica	473	15	<111> textured polycrystalline	500 - 1500	252	0.22
C_{60} single crystals	-	-	-	-	-	260	0.31-0.33

Our approach for the deposition of well-ordered C_{60} films [6] requires a combination of high values of C_{60} deposition rate and substrate temperature (near to the temperature of equilibrium "adsorption (deposition) ↔ desorption" for C_{60} molecules) as well as use of a substrate with

weak surface bonding. For example, sample 2, evaporated at a rate of 18-20 Å/s onto the Ag/glass substrate at 473 K, was found to have high degree of crystallinity and strong <111>-texture. The room-temperature XRD pattern of this sample is the same as that shown in Fig. 2a in Ref. 7 and consists only of a very narrow and intensive (111) peak and its higher harmonics (222) and (333). The sizes of crystalline domains for sample 2 are relatively large. AFM measurements revealed grain sizes in the sample surface of about 200 nm.

A mica substrate also satisfies the above mentioned requirement of weak surface bonding because it is a layered material with weak van der Waals interaction between layers. We succeeded in growing C_{60} thin films on a mica substrate, with crystalline structure even better than that for the films deposited on a metal sub-layer [8]. Sample 3 deposited at a rate of 15 Å/s onto a mica substrate, held at 473 K also had strong <111>-texture. However, the intensities of the peaks in its room-temperature XRD pattern (Fig. 1 in Ref. 8) were found to be substantially higher than those we observed for sample 2. The sizes of crystalline domains are also much larger. AFM revealed grain sizes in the sample surface of 500-1500 nm.

Analysis of the XRD patterns for all polycrystalline C_{60} films studied points to the fact that the material at room temperature has *fcc* structure. Our room-temperature value of the lattice parameter $a = 14.144$ Å is in good agreement with the data published for C_{60} single crystals and powder bulk samples [3-4].

Figures 1 - 3 show the results of temperature-resolved XRD measurements of the lattice parameter for as-grown samples 1, 2 and 3. There is no indication of a first order phase transition for sample 1 (figure 1): only a strong but gradual decrease in the lattice parameter is observed during cooling of the sample in the temperature range from $T_{c2} = 250$ K to $T_{c1} = 230$ K. On the other hand, for sample 2, figure 2 demonstrates a well defined discontinuity in the lattice parameter, $\Delta a/a = 0.06$ %, near the temperature $T_c = 250$ K which corresponds to the *fcc/sc* phase transition [2]. For sample 3, one can also observed the first order phase transition with even higher values of $\Delta a/a = 0.22$ % and $T_c = 252$ K (figure 3 and table I).

Temperature dependence of the lattice parameter for sample 3 reveals two other distinct anomalies, at $T_o \approx 155$ K and $T_g \approx 95$ K, which may associate with the beginning and completion of the freezing of molecular rotation (formation of the orientational glass). These features together with their relationships with the structural characteristics of the films will be discussed elsewhere.

It should be noted that the observed values of $\Delta a/a$ and T_c for our thin films are lower than those published for C_{60} bulk samples (table I). Furthermore, we have demonstrated a gradual reduction in the $\Delta a/a$ and T_c values with decrease of grain sizes in the C_{60} films. For sample 3, with worst structural characteristics, we observed a broadening of the phase transition temperature range (phase transition of a second degree). This may be due to a relatively high density of crystalline defects (including grain boundaries), strains and impurities in C_{60} thin films (in comparison with single crystals) and/or the presence of anisotropic crystallites with oriented grain boundaries. The latter originate from the strong texture of our films. Defects of crystalline structure of solid C_{60} [9], impurities [9-11], strains [12], or an increased surface/volume ratio [13-14] have been demonstrated to result in a reduction of T_c up to 25 K. The first two factors are known to lead also to a broadening of the phase transition temperature range (phase transition of a second degree) or even to suppress the phase transition [10,14].
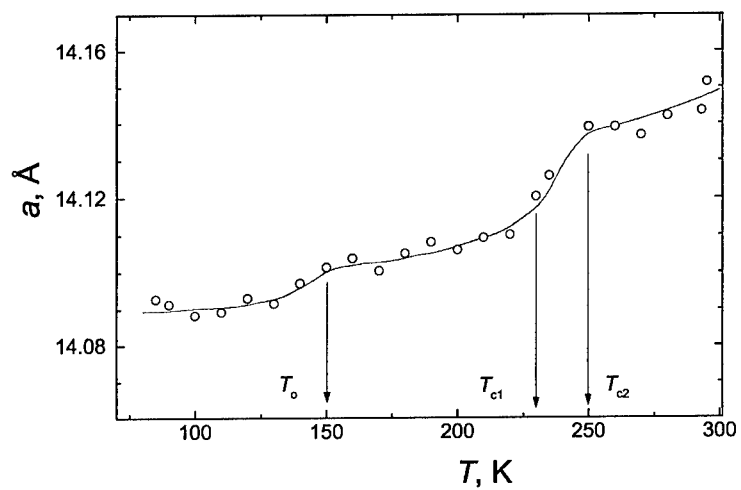
Figure 1. Results of XRD measurements of the lattice parameter for sample 1.
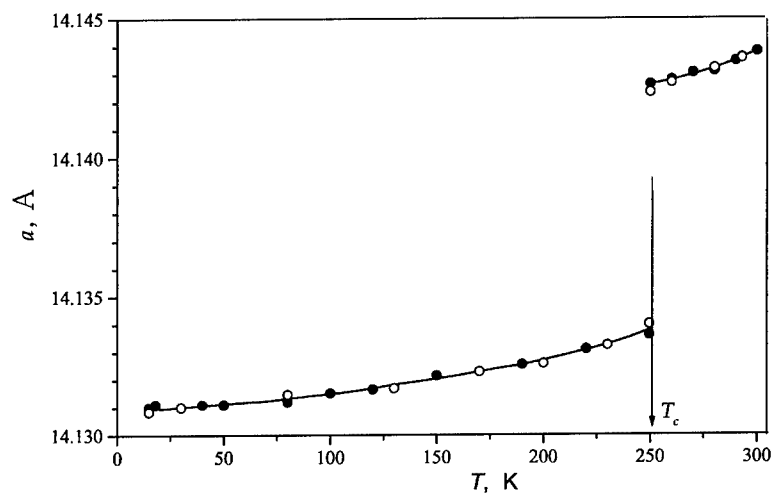
Figure 2. Results of two sets of XRD measurements of the lattice parameter for sample 2.
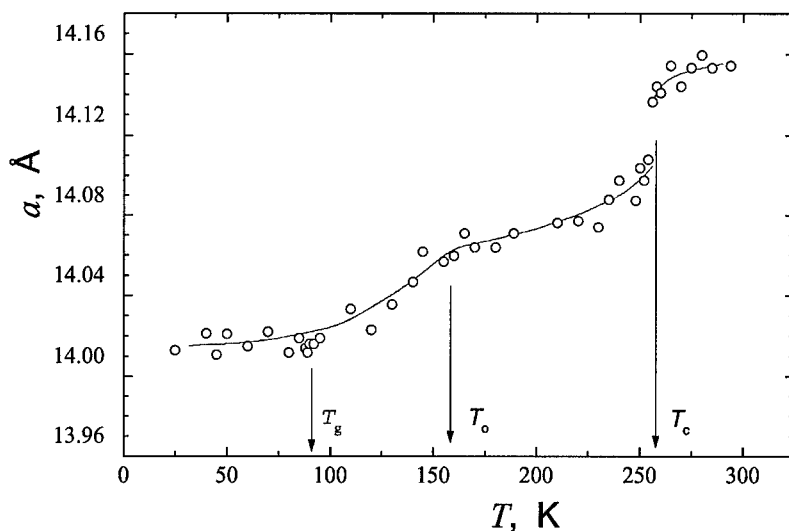
Figure 3. Results of XRD measurements of the lattice parameter for sample 3.

Given the large size of the interstitial sites in the C_{60} crystal (the corresponding voids are more than 4 Å in diameter) molecular oxygen from air is known to diffuse readily into this solid even at room temperature [15]. We revealed that post-grown exposure of our films to air leads to an increase in their oxygen content [16] and, in turn, to reduction in the $\Delta a/a$ and T_c values. Exposure of the C_{60} films to air during 10 months was found to suppress any first order and even second order phase transition in the samples [17]. However, annealing of the samples at 150°C in vacuum for 2 hours may restore the as-grown structural characteristics of the films and the phase transition parameters. We explain this effect by an effusion of oxygen during the annealing.

CONCLUSIONS

A systematic study of the effect of crystalline structure and impurity content in C_{60} films on their behavior near the *fcc/sc* disorder/order phase transition have been performed by the temperature-resolved X-ray diffraction measurements. Decrease of grain sizes in the films was found to result in a gradual reduction in the discontinuity in lattice parameter and the transition temperature. Increase in impurity (oxygen) content in the films led to the same result and even suppressed the phase transition.

REFERENCES

1. R. Tycko, G. Dabbagh, R.M. Fleming, R.C. Haddon, A.V. Makhia and S.M. Zahurak, *Phys. Rev. Lett.* **67**, 1886 (1991).
2. P.A. Heiney, J.E. Fisher, A.R. McGhhie, W.J. Romanow, A.M. Denestejn, J.P. McCauley Jr., A.B. Smith III and D.E. Cox, *Phys. Rev. Lett.* **66**, 2911 (1991).
3. H. Kasatani, H. Terauchi, Y. Hamanaka and S. Nakashima, *Phys. Rev. B* **47**, 4022 (1993).
4. S. Fomenko, V. D. Natsik, S. V. Lubenets V. G. Lirtsman, N. A. Aksenova, A. P. Isakina, A. P. Prokhvatilov, M. A. Strzhemechny and R. S. Ruoff, *Low Temp. Phys.* **21**, 364 (1995).
5. D. Faiman, S. Goren, E. Katz, M. Koltun, N. Melnik, A. Shames and S. Shtutina, *Thin Solid Films* **295**, 283 (1997).
6. E.A. Katz, US Patent No: 5,876,790 (1999).
7. E.A. Katz, D. Faiman, S. Shtutina and A. Isakina, *Thin Solid Films* **368**, 49(2000).
8. E.A. Katz, D. Faiman, S. Shtutina, A. Isakina, K. Yagotintsev and K. Iakoubovskii, in *Polycrystalline Semiconductors VI - Bulk Materials, Thin Films and Devices*, edited by O. Bonnaud, T. Mohammed-Brahim, H.P. Strunk and J.H. Werner (Solid State Phenomena, Scitech Publ., Uetticon am See, Switzerland, 2001) (in press).
9. N. A. Aksenova, A. P. Isakina, A. I. Prokhvatilov, M. A. Strzhemechny, V. N. Varyukhin, in *Recent Advances in the Chemistry and Physics of Fullerenes and Related Materials*, edited by K.M.Kadish and R.S.Ruoff (The Electrochemical Society Inc., **PV 94-24**, Pennington, 1994, p.p. 1543-1548.
10. K. Matsuishi, K. Tada, S. Onari, T. Arai, *Philosophical Magazine B* **70**, 795 (1994).
11. F. Yan, Ye-N. Wang, M. Gu, *J. Phys.: Condens. Matter* **10**, 6875 (1998).
12. Y. Yoneda, K. Sakaue, T. Terauchi, *J. Phys.: Condens. Matter* **9**, 2851 (1997).
13. A. Glebov, V. Senz, J.P. Toennies, G. Gensterblum, *J. Appl. Phys.* **82**, 2359 (1997).
14. A. Fartash, *Phys. Rev. B* **54**, 17215 (1996).
15. A. Assink, J. Schirber, D. Loy, B. Morosin and G.A. Carlson, *J. Mat. Res.* **7**, 2136 (1992).
16. E.A. Katz, A.I. Shames, D. Faiman, S.Shtutina, Y. Cohen, S. Goren, W. Kempinski and L. Piekara-Sady, *Physica B* **273&274**, 932 (1999).
17. E.A. Katz, D. Faiman, S.Shtutina, N.Froumin, M. Polak, A.P. Isakina, K.A. Yagotintsev, M.A. Strzhemechny, Y. M. Strzhemechny, V.V. Zaitsev and S.A. Schwarz. *Physica B* (2001) (in press).

Nanotube Growth

Preferential Growth of Carbon Nanotubes/Nanofibers Using Lithographically Patterned Catalysts

K. B. K. Teo, M. Chhowalla, G. A. J. Amaratunga, and W. I. Milne
Engineering Department, Cambridge University, Trumpington St, Cambridge CB2 1PZ, UK

G. Pirio, P. Legagneux, F. Wycisk, and D. Pribat
Thales Laboratoire Central de Recherches, Domaine de Corbeville, 91404 Orsay Cedex, France

ABSTRACT

In order to utilise the full potential of carbon nanotubes/nanofibers, it is necessary to be able to synthesize well aligned nanotubes/nanofibres at desired locations on a substrate. This paper examines the preferential growth of aligned carbon nanofibres by PECVD using lithographically patterned catalysts. In the PECVD deposition process, amorphous carbon is deposited together with the nanotubes due to the plasma decomposition of the carbon feed gas, in this case, acetylene. The challenge is to uniformly nucleate nanotubes and reduce the unwanted amorphous carbon on both the patterned and unpatterned areas. An etching gas (ammonia) is thus also incorporated into the PECVD process and by appropriately balancing the acetylene to ammonia ratio, conditions are obtained where no unwanted amorphous carbon is deposited. In this paper, we demonstrate *high yield, uniform, 'clean'* and *preferential* growth of vertically *aligned* nanotubes using PECVD.

INTRODUCTION

There has been considerable interest in the application of nanotubes in nanoelectronic devices [1-4], scanning probes [5-7], field emission sources [8-10] and supercapacitors [11]. The common techniques of depositing nanotubes include high pressure arcs, laser ablation and chemical vapour deposition (CVD) [12-18]. Unlike the former two deposition methods, CVD synthesis provides controlled, in-situ growth of nanotubes on substrates.

The growth mechanism of carbon nanotubes by CVD is driven by the decomposition of a hydrocarbon gas using a suitable catalyst, the dissolution of carbon in the catalyst and the precipitation of graphitic, tubular carbon from the catalyst. Arrays of 'spaghetti-like' nanotubes and aligned carbon nanotubes have been deposited using various types of CVD [19-22]. It has also been reported recently that PECVD processes induce alignment of the nanotubes due to the electric field inherent in the plasma discharge [18,19,21,23].

Patterned growth of nanotubes is achieved by lithographically defining the catalyst areas before nanotube growth. The key requirements for the patterned growth of nanotubes are yield, uniformity and the elimination of unwanted carbonaceous by-products from the deposition process. These requirements are investigated in this paper and we demonstrate uniform preferential growth of aligned nanotubes using PECVD of acetylene and ammonia gases at 700°C.

EXPERIMENTAL DETAILS

Due to the catalytic growth nature of carbon nanotubes, it is possible to define the growth areas of carbon nanotubes on a substrate by pre-patterning the catalyst prior to nanotube deposition. The nickel catalyst used in the synthesis of carbon nanotubes was deposited onto Si substrates by rf-magnetron sputtering and patterned lithographically using lift off. Nickel was either deposited directly on Si or on a diffusion barrier material to study if the thermal diffusion of Ni affects the yield of nanotubes. The substrates were then transferred to a PECVD chamber which was evacuated to 10^{-2} Torr by a rotary pump. The carbon feedstock and etching gases used for the PECVD process were acetylene and ammonia respectively. The flow rate of ammonia (NH_3) was fixed at 200sccm and the flow rate of acetylene (C_2H_2) was varied to find optimal deposition conditions.

The carbon nanotube deposition process consists of 2 main stages: (1) first, the substrates were heated to 700°C in NH_3 and nickel nanoparticles are formed [19,23], and (2) the C_2H_2 is introduced and the substrate is biased at –600V d.c. to initiate the plasma discharge for PECVD. The PECVD deposition time was fixed at 15 mins for all samples. The substrates were then observed in a Hitachi S800 Field Emission Scanning Electron Microscope. Our deposition process produces vertically aligned carbon nanotubes and further details can be found in [23]. The nanotubes produced contain structural defects and are sometimes referred to in the literature as nanofibers.
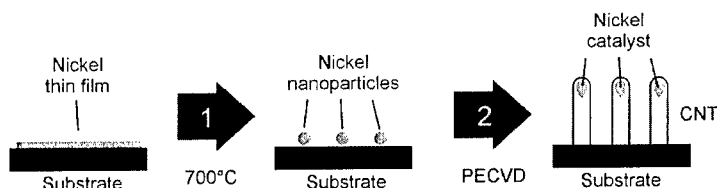
Figure 1: Two stage deposition process in which (1) Ni nanoparticles are formed by heating the substrate to 700°C and (2) PECVD to deposit the carbon nanotubes.

RESULTS AND DISCUSSION

Poor yield of nanotubes, from 1μm diameter dots of Ni, is observed when the nickel catalyst is directly deposited on the Si substrates (see Figure 1(a)). This is believed to be due to the thermal diffusion of Ni into Si to form $NiSi_x$ at temperatures above 300°C. Thus, the Ni is no longer 'active' to act as catalytic nucleation centers for the growth of nanotubes. The deposition yield of carbon nanotubes is significantly improved by depositing a diffusion barrier layer between the Ni catalyst and the Si substrate. Typical diffusion barrier materials are SiO_2 and TiN [24]. When the substrate is heated to 700°C, the Ni film breaks up and forms nanoparticles on the diffusion barrier as shown in Figure 1(b). These Ni nanoparticles remain 'active' on the diffusion barrier for the nucleation of nanotubes and a high yield of nanotubes from 1μm dots of Ni is obtained after the PECVD process as shown in Figure 1(c).
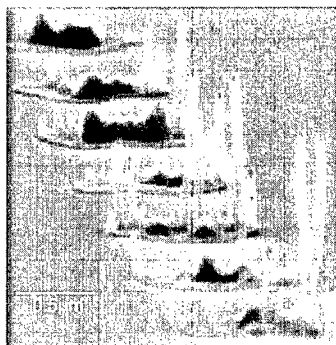
Figure 1(a). Poor yield of nanotubes is observed when Ni catalyst is deposited directly on Si. This is due to the thermal diffusion of Ni into Si which renders most of the Ni 'inactive'.
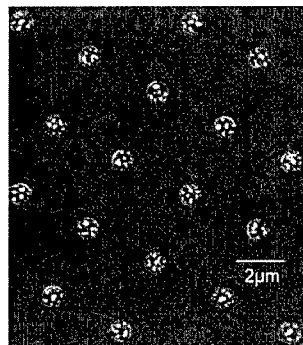
Figure 1(b). Ni nanoparticles are formed on a TiN diffusion barrier when the substrate is heated at 700°C. These nano-particles are 'active' for catalytic nanotube growth.
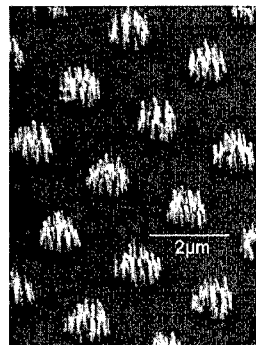
Figure 1(c). High yield of nanotubes is obtained from 1μm Ni dots on the diffusion barrier after PECVD of acetylene and ammonia at 700°C.

A by-product from the PECVD deposition of nanotubes is amorphous carbon (a-C). Unlike nanotube growth which occurs only at catalyst sites, a-C is formed by the plasma decomposition of the C_2H_2 gas and thus is deposited all over the substrate. The role of NH_3 in the plasma is to etch away the a-C as it is being deposited. Keeping the NH_3 flow rate fixed at 200sccm, the C_2H_2 flow rate was varied in a series of depositions to determine the optimal conditions at which no a-C remains on the substrate. The thickness of surface a-C was determined using a combination of cross sectional SEM and depth resolved Auger Electron Spectroscopy [25] and the results are plotted in Figure 2. Deposition gas ratios of 15% and 20% C_2H_2:NH_3 do not produce amorphous carbon on the substrate.
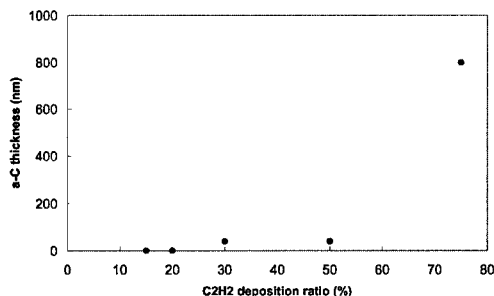
Figure 2. Plot of a-C thickness against C_2H_2:NH_3 ratio [25].

For depositions performed under a low concentration C_2H_2 (ie. high NH_3), anisotropic etching of the Si substrate in the unpatterned areas is observed as shown in Figure 3(a). For a high C_2H_2 ratio of 75%, we observe a thick a-C film covering both the nanotube and unpatterned areas as shown in Figure 3(b). The growth of the a-C proceeds in a columnar-like fashion and is 800nm in thickness as shown in Figure 3(c). Depositions performed using a 20% C_2H_2 ratio do not exhibit etching of the Si substrate nor have a surface a-C layer.

Figure 3(a). Using a C_2H_2 ratio of 15%, etching of the unpatterned Si areas is observed.
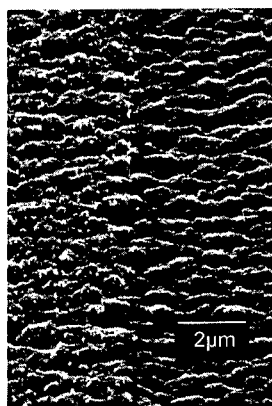
Figure 3(b). Using a C_2H_2 ratio of 75%, thick a-C covers both the nanotube (left) and unpatterned areas (right).
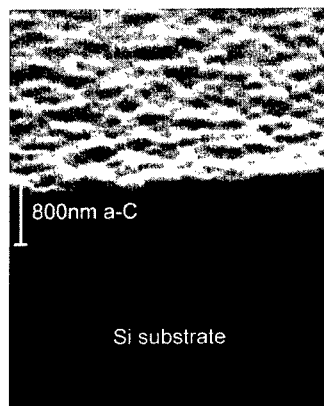
Figure 3(c). The thickness of the a-C layer is 800nm measured by cross-sectional SEM. The a-C grows in a columnar-like structure.
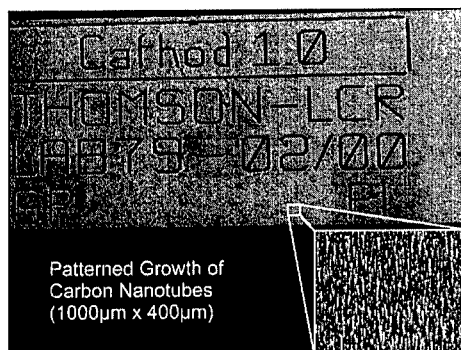
Figure 4(a). Uniform preferential growth of carbon nanotubes achieved by patterning the initial Ni catalyst by optical lithography.
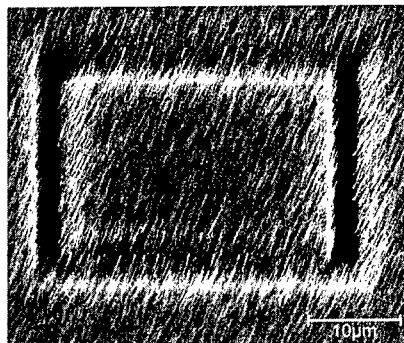
Figure 4(b). 25µm box of nanotubes produced using Ni catalyst patterned by optical lithography.

Uniform, patterned arrays of vertically aligned nanotubes have been deposited using the optimal deposition gas ratio of 20% C_2H_2:NH_3. The patterned Ni catalyst areas of Figure 4 were prepared using optical lithography. When the patterned Ni features are reduced to ~100nm using ebeam lithography, the nickel film forms only 1 nanoparticle when annealed at 700°C. Hence, it is possible to nucleate single nanotubes at precise locations as demonstrated in Figure 5.
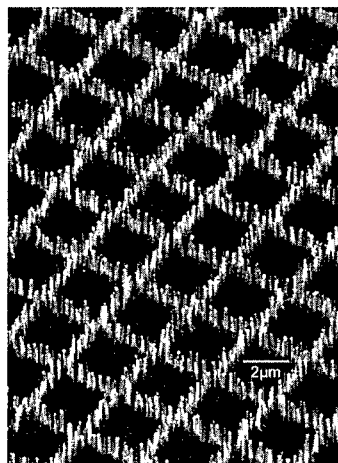
Figure 5(a). Grid lines of nanotubes produced using 100nm lines of Ni patterned using ebeam lithography.
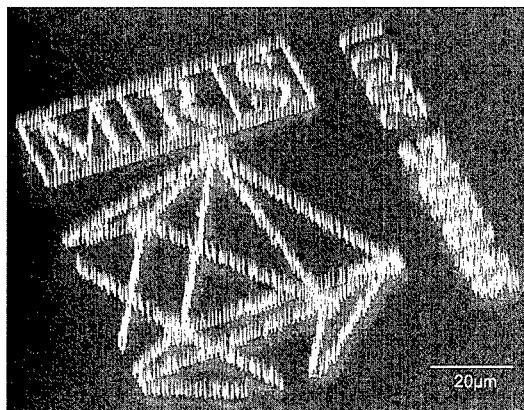
Figure 5(b). Precise placement of nanotubes is demonstrated using the MRS Spring 2001 logo. The logo was produced using 100nm nickel dots patterned using ebeam lithography.

CONCLUSIONS

Preferential deposition of vertically aligned carbon nanotubes using lithographically patterned Ni catalyst has been achieved using PECVD of C_2H_2 and NH_3 at 700°C. The two step growth process consists of Ni forming nanoparticles at 700°C and then PECVD to deposit the nanotubes. Nanotube yield is significantly improved by the use of a diffusion barrier to prevent the diffusion of Ni into Si. The PECVD gas ratio of 20% C_2H_2:NH_3 elminates unwanted a-C from the deposition process. These are the conditions necessary to produce high yield, uniform, 'clean' and selective/preferential growth of vertically aligned nanotubes.

ACKNOWLEDGEMENTS

REFERENCES

1. R. Martel, T. Schmidt, H. R. Shea, T. Hertel, and Ph. Avouris, Appl. Phys. Lett. **73**, 2447 (1998).
2. M. Kruger, M. R. Buitelaar, T. Nussbaumer, C. Schonenberger, and L. Forro, Appl. Phys. Lett. **78**, 1291 (2001).
3. K. Liu, M. Burghard, S. Roth, and P. Bernier, Appl. Phys. Lett. **75**, 2494 (1999).
4. W. Tombler, C. Zhou, and H. Dai, Appl. Phys. Lett. **76**, 2412 (2000).
5. H. Dai, N. Franklin, and J. Han, Appl. Phys. Lett. **73**, 1508 (1998).
6. H. Nishijima,, S. Kamo, S. Akita, Y. Nakayama, K. I. Hohmura, S. H. Yoshimura, and K. Takeyasu, Appl. Phys. Lett. **74**, 4061 (1999).
7. C. L. Cheung, J. H. Hafner, T. W. Odom, K. Kim, and C. M. Lieber, Appl. Phys. Lett. **76**, 3136 (2000).
8. W. A. de Heer, A. Chatelaine, and D. Ugarte, Science **270**, 1179 (1995).
9. J. M. Bonard, J. P. Salvetat, T. Stockli, L. Forro, and A. Chatelain, Appl. Phys. A **69**, 245 (1999).
10. P. G. Collins and A. Zettl, Appl. Phys. Lett. **69**, 1969 (1996).
11. E. Frackowiak, K Metenier, V. Bertagna, and F. Beguin, Appl. Phys. Lett. **77**, 2421 (2000).
12. S. Ijima, Nature **363**, 603 (1993).
13. S. Ijima and T. Ichihashi, Nature **363**, 603 (1993).
14. C. Journet, W. K. Maser, P. Bernier, A. Loiseau, M. L. delaChappelle, S. Lefrant, P. Deniard, R. Lee, and J. E. Fischer, Nature **388**, 756 (1997).
15. A. Thess, R. Lee, P. Nikolaev, H. J. Dai, P. Petit, J. Robert, C. H. Xu, Y. H. Lee, S. G. Kim, A. G. Rinzer, D. T. Colbert, G. E. Scuseria, D. Tomanek, J. E. Fischer, and R. E. Smalley, Science **273**, 483 (1996).
16. C. Journet and P. Bernier, Appl. Phys. A **67**, 1 (1998).
17. A. M. Cassell, J. A. Raymakers, J. Kong, and H. J. Dai, J. Phys. Chem. **103**, 6484 (1999).
18. Z. F. Ren, Z. P. Huang, J. W. Xu, J. H. Wang, P. Bush, M. P. Siegal, and P. N. Provencio, Science **282**, 1105 (1998).
19. V. I. Merkulov, D. H. Lowndes, Y. Y. Wei, G. Eres, and E. Voelkl, Appl. Phys. Lett. **76**, 3555 (2000).
20. H. Murakami, M. Hirakawa, C. Tanaka, and H. Yamakawa, Appl. Phys. Lett. **76**, 1776 (2000).
21. C. Bower, W. Zhu, S. Jin, and O. Zhou, Appl. Phys. Lett. **77**, 830 (2000).
22. J. I. Sohn, S. Lee, Y. H. Song, S. Y. Choi, K. I. Cho, and K. S. Nam, Appl. Phys. Lett. **78**, 901 (2001).
23. M. Chhowalla, K. B. K. Teo, C. Ducati, N. L. Rupesinghe, G. A. J. Amaratunga, A. C. Ferrari, D. Roy, J. Robertson, and W. I. Milne, J. Appl. Phys., *submitted*.
24. A. M. Rao, D. Jacques, R. C. Haddon, W. Zhu, C. Bower, and S. Jin, Appl. Phys. Lett. **76**, 3813 (2000).
25. K. B. K. Teo, M. Chhowalla, G. A. J. Amaratunga, W. I . Milne, D. G. Hasko, G. Pirio, P. Legagneux, F. Wycisk, and D. Pribat, Appl. Phys. Lett., *submitted*.

Designability of Graphitic Cones

M. M. J. Treacy and J. Kilian
NEC Research Institute, Inc. 4 Independence Way, Princeton, NJ 08540-6685, USA

ABSTRACT

We show that, with topologically flexible seeds which are allowed to explore different growth modes, graphitic cones are inherently more "designable" than flat graphitic disks. The designability of a structure is the number of seed topologies encoding that structure.

We illustrate designability with a simple model, where graphite grows onto C_n ($5 \leq n \leq 30$) ring seeds. For a wide range of ring sizes, cones are the most likely topological outcome. Results from the model agree well with data from special cone-rich carbon black samples.

The concept of designability allows entropy to be incorporated into the "pentagon road" model of the formation of curved graphitic structures.

INTRODUCTION

Recently, Krishnan et al. (1997) [1] reported a new carbon black material, made by Kvaerner Engineering a.s. Norway in a proprietary industrial process that involved the pyrolysis of methane in a plasma torch. Transmission electron microscopy (TEM) showed that the sample (designated KVR) contained high concentrations of multilayer graphitic disks, cones and tubes. Cones had been sighted before in carbon black [2], but not in the quantity and variety exhibited by KVR. Five distinct cone angles were observed, each corresponding to the inclusion of a disclination of order $1 \leq m \leq 5$. The measured cone angles, θ, were found to correspond closely to the predicted values $\theta = 2\sin^{-1}(1 - m/6)$. Although graphitic disks dominated the sample, among the cones the medium-angle 60° ($m=3$) and 38.9° ($m=4$) cones occurred most frequently.

From an energetics viewpoint, the small-angled cones (those with the sharpest cone points and largest m value) should have the highest elastic strain energy per carbon atom, particularly near the tip area where cone wall curvature is high. Furthermore, there is an additional energy penalty for forming the tip structure, which must enclose one or more disclinations. Although pentagon inclusion probably costs the least energy on forming the core of the disclination, defect structures with dangling bonds and different ring sizes are also possible. From consideration of the enthalpy of formation alone, the disk topology with no strain and no pentagons, must be the lowest energy form, and the 19.2° ($m=5$) cone and the cylinder ($m=6$) must be the highest energy forms, and therefore the rarest. An enthalpy argument would predict, in terms of θ values, the order of likelihood to be 180° > 112.9° > 83.6° > 60° > 38.9° > 19.2° > 0°. TEM shows, however, that the 180° disks, and the 60° and 38.9° cones dominate the KVR sample.

The reason must lie with the differences in Gibb's free energy, $\Delta G_{ij} = \Delta H_{ij} - T\Delta S_{ij}$. As usual, ΔH_{ij} is the enthalpy of formation when a chemical system transforms from state i to state j, and T is the temperature at which the transformation occurs. The entropy change ΔS_{ij} is a measure of the number of reaction pathways available to system i that can lead to product j. If a chemical system i is inundated with opportunities to form a higher enthalpy product j, then entropy can dominate the rate of product formation.
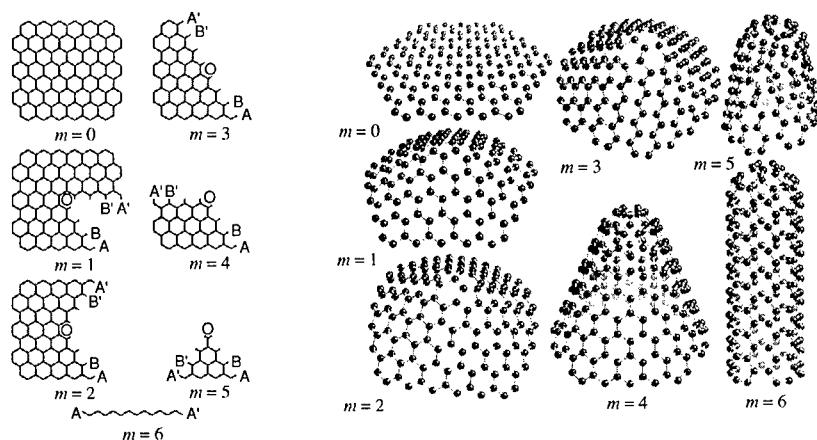
Figure 1: Illustration showing how to construct the five cones and a cylinder from a hexagonal graphite sheet. Multiples of 60° segments are systematically removed, and dangling bonds are re-connected. Each cone can be characterized by the number m of 60° segments that are removed. m is also known as the disclination number. m=1,2,3,4,5 correspond to true cones. The m=0 planar sheet, and the m=6 cylinder are considered here to be end-members of the family of cones.

In this paper we present in more detail an entropy argument, first outlined in Krishnan *et al.* (1997) [1], that explains the observed cone distribution. For simplicity, we focus the discussion on monocyclic hydrocarbon rings as model nuclei for graphitic growth. We count the number of ways in which a carbon C_n ring can be embedded into a conical structure so as to circumscribe the cone tip. This count is the "designability" of the structure [3]. We show that C_n rings ($n{\geq}5$, $n{\neq}6$) encode conical graphitic structures more prolifically than they do planar graphitic sheets. With topologically flexible seeds, cones are highly designable relative to planar graphite.

STRUCTURE OF GRAPHITE CONES

To date, there have been several theoretical papers discussing cone topologies [4, 5]. The conical shape arises naturally when 60° segments are cut out of a planar graphite sheet, and the severed edges of the segment are rejoined. A maximum of six 60° segments can be removed. Figure 1 shows how this process works. The removal of one to five 60° segments, followed by the physical connection of reference points A to A', and B to B', results in five distinct types of cone, the tips of which are girdled by a continuous curved hexagonal framework. Topologically, the removal of six 60° segments does not necessarily lead to the removal of all atoms; it is equivalent to a chain of atoms, which when connected end to end, produce a ring. The stacking of identical rings generates a cylinder. The cylinder and disk are the topological end-members of a seven-membered family of cones. The removal (or addition) of 60° segments in a planar lattice introduces defects known as *disclinations*. Cone topologies are differentiated by referring to the number of 60° segments that are removed. This is the disclination number m. For all carbon atoms to be 3-connected, cone tips must incorporate ring sizes other than 6-rings. Such rings introduce curvature into a framework, resulting in rounded cone tips. Pentagons can be sufficiently isolated so that, locally, each pentagon appears to be a part of an m=1 (112.9°) cone. Pentagons cannot be arbitrarily close to each other. The *isolated pentagon rule* (or IPR), which applies to structures formed entirely from 5- and 6-rings, stipulates that each pentagon must be
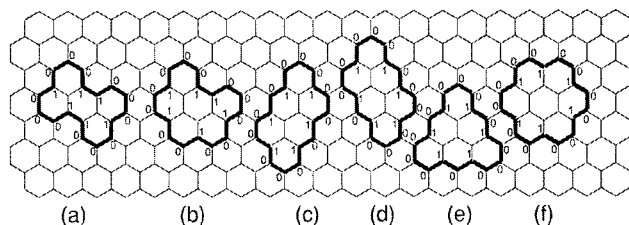
Figure 2: The six topologically distinct open-ring C_{18} circuits that occur in $m=0$ graphite. They can be represented by cyclic binary sequences, with 1 representing a bond "inwards" and 0 a bond "outwards". (c) and (d) are mirror images. There are 18 cyclic permutations of each ring type, giving a total of 108 permutations. Cross-linked modes are excluded in this example.

completely surrounded by hexagons. This rule can be justified by simple chemical arguments – the extent of sp^3 re-hybridization (in other words, the non-coplanarity of the central atom with its three bonds) must be minimized at each carbon atom.

Pentagons are generally considered to be the preferred "defect" ring size in hexagonal sp^2-hybridized networks, as evidenced by their abundance in the Fullerenes. The disclination parameter m is then equal to the number of pentagons required to form the cone tip.

CARBON *n*-RING MODES

Consider a closed C_{18} circuit in a graphite sheet. Six distinct open-ring topologies are possible (Fig. 2), presenting a total of $6 \times 18 = 108$ cyclic configurations. A convenient method of describing these circuits in planar graphite is to label the one free bond at each carbon that extends from the ring. An outward-facing bond is assigned the label "0", and an inward-facing bond the label "1". These sequences can be permuted cyclically, anti-cyclically or mirrored without changing the topology (except for the handedness – for example Figs 2c and 2d).

Upon removing these 18-carbon circuits from their graphite matrix, the "1" and "0" bonds become dangling bonds and are free to move. In fact, the ring is free to change shape. Chemically, such a ring is free to adopt one of a huge number of distinct chemical structures based on permutations of single, double or triple bonds. We ignore such distinctions, since topologically the rings are identical once they are embedded in graphite. For a cone or cylinder, the distinction between a "0" and a "1" becomes clear by executing a clockwise path along the circuit, beginning at any atom. An atom is assigned "0" when the sense of the bond rotation *in the ring* is clockwise, and "1" when the rotation is counterclockwise.

The rules for growing a closed annulus of graphite onto the perimeter of a carbon ring (or circuit) are easily derived. For planar graphite formation, the outer circuit of the graphitic annulus contains 12 additional atoms. In general, for a disclination of order m, the relationship between the size n_k of the inner, and size n_{k+1} of the outer, circuits of the graphitic annulus is $n_{k+1}-n_k=12-2m$. The number of inward-pointing bonds i_k is related to the number of outward-pointing bonds o_k by $o_k - i_k = 6 - m$, with $n_k = o_k + i_k$. There are 2^n binary representations of a C_n ring. This number is greatly reduced by the constraints on $o_k - i_k$. By examining the binary form of all integers between 0 and 2^n-1, m-values can be obtained from $m=6+i_k-o_k$. A further constraint is that atoms may not collide, disallowing modes with more than five consecutive 1's or 0's. This last constraint greatly complicates the problem of enumerating valid rings. Here, we are interested only in $0 \leq m \leq 6$ (*i.e.* cones), although other interesting m values also occur, such as saddles ($m<0$), closed shells such as buckyballs and nanotubes ($m=12$), and helicoids $m>6$.
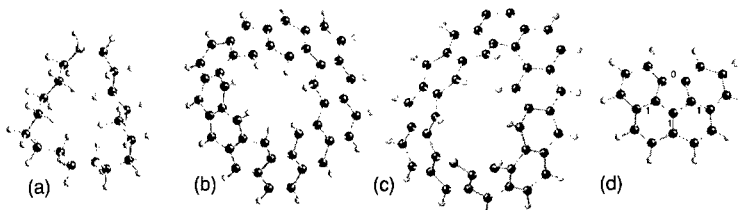
Figure 3: a) A flexible $C_{18}H_{36}$ hydrocarbon ring. b) and c) are two growth modes of graphite onto the outside of the ring, each producing an $m=2$ disclination. Pentagons have yet to appear, yet the disclination is essentially fixed. d) Cross-linking in a C_{18} ring. Internal linkages "1" can not create an odd number of pentagons. Outside linkages "0" can.

Figures 3b and 3c show two of the 16,812 possible ways that 6-rings can be added to a C_{18} ring to form a graphitic annulus corresponding to an $m=2$ cone. In each instance, the tip structure is not yet resolved, and pentagons have not yet been formed. However, the enclosed disclination is now fixed because the stiffened annulus has already lost many of its conformational degrees of freedom. The stiffened seed is now committed to a particular value of m. Tip closure, with pentagon creation, will occur early in the growth stage, but *after* nucleation of the disclination.

Table 1 lists the number of unique degrees of freedom available to an open n-ring ($5 \leq n \leq 30$) for each of the seven disclinations, $0 \leq m \leq 6$. We assume that a minimum ring size is required for each disclination. 6, 5, 12, 15, 18, 19 and 18 are the minimum circuit sizes that can circumscribe $m=0$ to 6 unconnected pentagons in a manner consistent with the isolated pentagon rule.

The Table shows that for the smallest open ring sizes, n, small m-values are favored. In this

n \ m	0	1	2	3	4	5	6
5	0	1	0	0	0	0	0
6	1	0	0	0	0	0	0
7	0	3	0	0	0	0	0
8	0	0	0	0	0	0	0
9	0	14	0	0	0	0	0
10	0	0	0	0	0	0	0
11	0	56	0	0	0	0	0
12	4	0	217	0	0	0	0
13	0	203	0	0	0	0	0
14	7	0	738	0	0	0	0
15	0	724	0	2,141	0	0	0
16	16	0	2,500	0	0	0	0
17	0	2,532	0	7,076	0	0	0
18	108	0	16,812	0	34,588	0	182
19	0	17,396	0	46,496	0	73,878	0
20	280	0	55,984	0	112,120	0	5,606
21	0	59,170	0	152,214	0	237,950	0
22	792	0	185,548	0	362,988	0	48,980
23	0	199,524	0	496,918	0	766,018	0
24	2,272	0	612,198	0	1,173,640	0	257,988
25	0	668,266	0	1,618,324	0	2,464,636	0
26	6,578	0	2,012,520	0	3,790,538	0	1,090,656
27	0	2,225,998	0	5,260,062	0	7,925,938	0
28	19,040	0	6,595,974	0	12,230,748	0	4,142,762
29	0	7,381,624	0	17,068,368	0	25,476,758	0
30	55,750	0	21,563,852	0	39,431,494	0	14,902,092

Table 1: The number of modes of an open carbon ring of n atoms that correspond to a disclination of order $0 \leq m \leq 6$. n-rings are not necessarily enclosing pentagons at this stage. Tip restructuring can occur after the disclination is committed during the growth phase.

open ring model, even-numbered rings n can only nucleate even-numbered disclinations m. Conversely, odd-numbered rings can only nucleate odd-numbered disclinations. With increasing n ($n \leq 17$), the degrees of freedom are maximum for the $m = 1, 2, 3$ disclination values. For $n \geq 18$, the distribution peaks for $m \geq 3$.

The Table also shows that large, topologically flexible, carbon rings favor the nucleation of cones rather than sheets. Cones with higher enthalpies of formation are favored because the Gibbs free energy is reduced by the increase in entropy associated with the large number of growth modes that encode cones.

More sophisticated ring-counting techniques allow us to count cross-linked modes more efficiently. There is no room here to describe our algorithm or results. The most significant result is that cross-linking of "0" bonds permits even n-rings to create odd-m disclinations, and vice-versa (e.g. Fig 3d). The inclusion of cross-linked seeds does not change significantly the relative distribution of modes given in Table 1.

Data on the KVR sample [1] reveal a bimodal distribution of cones, with a broad peak in the $m=2,3,4$ region, and a dominant peak at $m=0$, the planar graphitic disks. Cylinders ($m=6$) occur relatively infrequently. This distribution could be explained by the presence of a relatively dilute concentration of C_n rings in an abundant supply of graphitic carbon building units (i.e. C monomers, C_2 dimers etc). Self-assembly of the smaller carbon building units will inevitably favor the formation of graphite, which is the lowest energy state for sp^2 carbon. This growth mode should produce prolific quantities of graphitic sheets. A secondary growth mode involves the accretion of the smaller carbon building units onto the C_n rings. This latter growth mode clearly favors cones when $n \leq 30$. There is a third possible growth mode where rings collide with rings. This would be equivalent to the ring-stacking model of Wakabayashi and Achiba (1992) [6]. However, if monocyclic rings are dilute, this growth mode will not dominate.

The spheroidal particles commonly found in carbon black are suppressed in the KVR sample. This may be because their seeds are rapidly consumed by cone production. Ebbesen [7] has pointed out that the growth phase is probably much more rapid than the nucleation phase, since seed formation is a slow and difficult process. A high purity and yield of cones can occur if the carbon vapor/plasma is presented with ready-made flexible seeds or nuclei that possess many topological degrees of freedom. Unfortunately, the KVR synthesis conditions are unknown.

Clearly, there may be more than one nucleation mechanism present. 5-rings, as well as 6-rings and the larger n-rings, are likely to be present in the plasma/vapor. 5-rings, when present at high concentration, could accrete to form cup-like structures. The KVR sample does show some $m=2$ cones in which pentagons are separated by distances more than a micron, implying that two $m=1$ cones have merged. However, accretion alone can not so clearly explain the observed distribution of angles in cones with relatively sharp tips (i.e. pentagons closely spaced).

Figure 3 shows the distribution in m-values for Gaussian distributions of seed ring sizes,
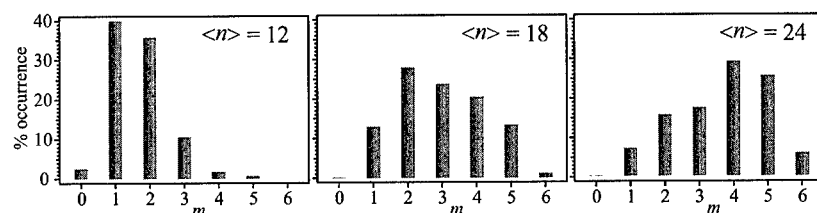
Figure 4: Distributions of m values resulting when a graphite-forming system is seeding with Gaussian distributions of monocyclic carbon rings, peaked at C_{12}, C_{18} and C_{24} rings respectively. The standard deviation is $\sigma_n = 3$ in each case.

$<n>$=12, 18 and 24, with σ_n = 3 in each case. Each distribution strongly favors cones, $1\leq m \leq5$, with the peak shifting to higher m as $<n>$ increases. A histogram for $<n>$=20, σ_n = 3 (not shown), which peaks at m=3, is qualitatively similar to that observed for the KVR sample.

There is negligible production of m=0 disks in these histograms. As explained above, disks can be formed in a separate nucleation process, with no large rings necessarily involved.

The validity of the designability argument does not rely on the assumption that monocyclic carbon rings are the seeds. Any flexible seed that is allowed to explore its topological degrees of freedom may suffice. We note that similar "designability" arguments, applied to peptide chains, have been used to explain the thermodynamic stability of certain folded protein structures [3].

The m<0 hyperboloidal structures, with negative Gaussian curvature, are not observed in the KVR sample, even though they are abundantly present as potential C_n ring modes. This appears to argue against carbon rings as seeds – they are too flexible. However, it is possible that thermal vibrations will destroy hyperboloidal structures, once seeded. In cones, thermal vibrations will resemble bell modes with the highest stresses near the open cone rim. The cone tip will not be subjected to large stresses. However, in saddle-shaped hyperboloids, the dominant vibration modes will be the "clapping", or "butterfly wing", modes. Such vibrations may subject the high curvature cores of the disclinations to large tensile stresses, ripping such hyperboloids apart. In addition, the more steeply inclined $-6\leq m\leq-4$ structures may cross-link at their open rims (literally clapped shut), leaving an unrecognizable mass. The m>0 cones are expected to be relatively stable to thermal vibrations, which may explain their survival in the KVR sample.

A consequence of our designability model is that pentagon creation becomes a structural tidying-up step that happens *after* the disclination is committed. In the "pentagon road" model [8], pentagons are formed in seed structures in order to eliminate high-energy dangling bonds, and as an annealing mechanism to reduce the overall energy of the structure. In that model, the creation of the pentagon implies the creation of the disclination. The designability argument and the pentagon road model are not in conflict. The designability mechanism implicitly refers to an earlier instant in the seed's existence, when it still possesses topological degrees of freedom. Disclinations are inherently present as conformational modes, but are not yet committed. Pentagons have yet to be formed. In a topologically flexible seed the pentagons appear "along the road", rather than at the beginning. The number of pentagons in the later seed structure is predetermined by the mode committed to by the seed at an earlier stage of growth.

The pentagon road model provides a mechanism for minimizing the enthalpy of seed structures. By incorporating the concept of designability, the pentagon road model can be extended to include entropy, which drives the emergence of preferred graphitic structures.

ACKNOWLEDGMENTS

1. A. Krishnan, E. Dujardin, M.M.J. Treacy, J. Hugdahl, S. Lynum, and T.W. Ebbesen, *Nature* **388**, 451 (1997).
2. M. Ge and K. Sattler, *Chem. Phys. Letts.* **220**, 192 (1994).
3. H. Li, R. Helling, C. Tang, and N. Wingreen, *Science* **273**, 666 (1996).
4. A.T. Balaban, D.J. Klein, and X. Liu, *Carbon* **32**, 357 (1994).
5. S. Ihara, S. Itoh, K. Akagi, R. Tamura, and M. Tsukuda, *Phys. Rev. B* **54**, 14713 (1996).
6. T. Wakabayashi and Y. Achiba, *Chem. Phys. Letts.* **190**, 465 (1992).
7. T.W. Ebbesen, Personal communication (1997).
8. R.E. Smalley, *Acc. Chem. Res.* **25**, 98 (1992).

SWNT nucleation: Energetics of zipping–edge mechanism

Slava V. Rotkin
Beckman Institute, UIUC, 405 N.Mathews, Urbana, IL 61801, USA [1]
Ioffe Institute, 194021, St.Petersburg, Polytehnicheskaya 26, Russia

Abstract. A novel mechanism of SWNT nucleation is considered in oppose to an existing model. The latter model based on the formation of a hemispherical carbon bowl nucleus has no correct description within the thermodynamics and kinetics of the nucleation process. The new mechanism can explain the prevalent formation of [10,10] armchair nanotube on the base of the continuum graphene energetics.

INTRODUCTION

It is intriguing that, despite of the years of experimental study and theoretical modeling, the formation of single wall nanotubes (SWNTs) is not fully explained. The SWNT **nucleation** is one of important questions to the theory because the subsequent growth of the nucleus can not change its helicity or radius. I consider the SWNT growth to be driven by kinetics, which means that as–formed nucleus enlarges and becomes energetically metastable (or even unstable) but its transformation to the minimum energy configuration is "frozen" at the typical synthesis conditions: temperature, growth rate, density and entangled structure of raw material etc. For the quasi–equilibrium conditions of this second stage of the synthesis (stage of enlargement of the nucleus), the change of the SWNT radius and chirality costs the energy of defect formation which is about several eV. Therefore, the prevalent nucleus radius and chirality and the degree of perfection are likely to define the properties of most abundant SWNTs. Hence, the nucleation model is the **key point** of the growth theory.

The first part of the paper deals with the nucleation starting with a hemispherical bowl. I will demonstrate that it is seldom event, basing on the growth thermodynamics and using simple kinetics arguments. The main reason is that the creation of pentagons in the graphene lattice costs a large energy. This will suppress at some extent the scrolling of the graphite–like cluster at the number of carbon atoms as low as 250. Moreover, the slightly curved lattice is unstable to the further scrolling into a complete sphere which is the dead end of the SWNT nucleus evolution.

An anisotropy of the SWNT growth is puzzling in view of the discussed formation route to the cylinder shell from the isotropic or even amorphous graphene. A novel model, proposed recently in Ref. [1], naturally explains the nucleation of 1D directed structure. The natural generatrix for the formation process is given by the edge of graphite layers. The most stable is the zigzag [1000] edge of graphite. The most probable is the formation of [0110] (armchair) nucleus making the right angle to this edge.

Thermodynamics of the edge zipping shows that the optimal diameter of a cylindrical nucleus is about 15 Å given by the ratio of the elastic energy to the van der Waals interaction. Both energies are known for the graphite. The nucleus length depends on the

---

quality of the graphene material owing to the detaching of the sleeve is likely to happen if the nucleating cylinder meets sp^3 lattice defect interconnecting two adjacent layers of graphite [2]. Of course, the catalyst free nucleation model presented here has to be viewed as an initial step to the full description of the SWNT formation mechanism. However, even this simple theory helps to understand the large yield of armchair [10,10] SWNTs observed experimentally [3].

HEMISPHERE NUCLEATION MODEL

The symmetry of the nucleus defines the symmetry of the whole tube if the growth is more or less equilibrium which is *sine qua non* condition of the synthesis of the perfect defectless SWNT. One of the earlier models [4] presumes that the growth starts from a hemispherical bowl nucleus which serves as a proper seed for the growth of capped SWNT with the radius and chirality determined by an open edge of the bowl embryo. The chirality, in turn, mainly depends on the positioning of pentagons within the bowl. How can the model explain the prevalent formation of [10,10] SWNT? The bowl has to have exactly armchair perimeter of the C_{120} hemisphere.

The bowl nucleation mechanism requires following conditions: (*i*) the probability of scrolling into (hemi)sphere must be large for the number of atoms $N \leq N_o$ (N_o is the prerequisite size of the bowl seed); (*ii*) the first pentagon has to lie in the center of the carbon flake precursor and other five pentagons must be placed from the first at the same radial distance equal to $2\pi R/5$ (= four atoms for [10,10] SWNT) and at the angles $2\pi/5$ to form the concrete armchair configuration, (*iii*) then the pentagon creation has to be completely suppressed for $N > N_o$ (that will force cylinder to grow row by row and hexagon by hexagon without eventual dome closing).

Let us consider the first assumption of the Bowl Nucleation Model (BNM). I discussed earlier [5,6] that the probability for scrolling of the planar graphite flake into the sphere fragment depends substantially on the number of atoms in the cluster. The scrolling is, in general, **favored** by the energetics of formation. That is the energy of a planar cluster decreases with decreasing perimeter (and increasing curvature) and reaches a minimum at the spherical geometry. Thus, keeping the number of atoms, the annealing of the planar fragment should result in the sphere closing. However, the scrolling probability has an exponential temperature dependence because the process has a scrolling energy barrier for the number of atoms $N < N_{th}$. Here N_{th} is the characteristic cluster size which I calculated analytically [5] as an involute ratio of the spherical cluster formation energy to the dangling carbon bond energy. The ratio reflects that this scrolling barrier is owing to the competition between (A) the energy gain due to the creation of the first pentagon (corresponding energy ~ 1.5 eV) and the elastic stress following that and (B) the energy loss due to the decrease of the open perimeter and the closing of dangling bonds (DBs). The total DB energy (single bond energy ~ 2.4 eV) is still smaller than the pentagon energy until the cluster size becomes larger than $N_{th} \simeq 250$ for some reasonable model parameters (see Ref. [7] for explanation of the parametrisation). The scrolling process phase diagram is shown in Fig.1. The gray shaded area is the region of metastable flat clusters. The metastable cluster has an energy barrier for the scrolling into the bowl (*i.e.* it has the energy hill when increasing the number of pentagons). It prevents the formation
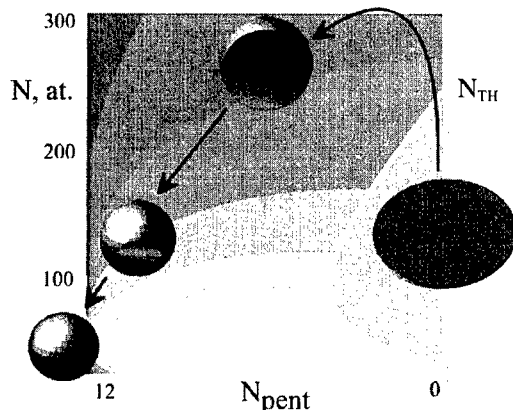
FIGURE 1. The phase diagram of the scrolling process (the contour map of the formation energy). The darker the color, the lower the cluster energy. The axes of the diagram give the total number of atoms and number of pentagons of the cluster. Some examples of these clusters are sketched. The gray shaded area divided from the rest energy map is the region of the metastable flat clusters. The cluster from this area has an energy barrier to scroll into the sphere.

of the bowl nuclei for the SWNTs of interesting radius 3-4Å$< R \leq$10Å. The size of the bowl nucleus for [10,10] SWNT is within the metastability region: $N = 120 < N_{th}$.

The BNM supposition (ii) is also controvertible. The pentagon creation is probable at the perimeter (through a fluctuation of $s - p$ carbon atom arrangement at the open edge) rather than somewhere deep inside the flake lattice. The central defect creation needs a large permutation of atoms (akin a high–temperature annealing of cluster). The initial edge position of the first pentagon is likely random. The final optimum position with the minimum energy is in the flake center [6]. Therefore, the creation is followed by the pentagon drift diffusion [8] to produce stage (ii) of the model. During this diffusion the pentagon–heptagon pair radiation happens at each step, which I name an "ice-breaking" mechanism [9]. These defects can slide [10] to the perimeter and recombine there. For the small enough cluster the creation of the next pentagon will (anti-)correlate with the position of the first one. The complicated nature of the pentagon creation shows that the formation of highly symmetrical stage (ii) is seldom. Although, this configuration has to be energetically stable.

Let us return to the condition (iii). Even if an armchair–like bowl yields, in order to grow SWNT from this nucleus the further scrolling (pentagon creation) has to stop while the same flow of carbon atoms arrives at the open edge. It is not supported by the energy consideration because there is no stable point in the energy landscape of the scrolling process at the pentagon number of six (bowl): at the fixed number of atoms the global minimum is at 12 pentagons (sphere) and the local minimum (for $N < N_{th}$) is at 0 (planar flake) and there is no local minimum at all if $N \geq N_{th}$. While the carbon cluster overcomes the barrier (if any) to curve, it will completely scroll and will form a sphere [5,6,11].

Concluding, during the BNM nucleation one needs quite special conditions which are difficult to satisfy simultaneously. Therefore, the non–catalytic formation of a perfect armchair NT from hemispherical bowl nucleus occurs seldom if ever.
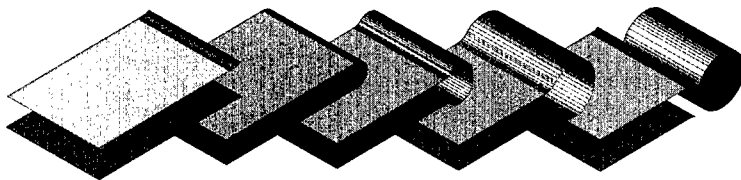
FIGURE 2. Scheme of the zipping off of SWNT from the graphite edge. From left to right: the closing of DBs (1-2) results in the bubbling of the sleeve (2-3-4) and consecutive tearing off of SWNT nucleus (4-5). The process may repeat producing bunched tubes due to van der Waals cohesion of the detached nuclei.

ZIPPING MECHANISM

The SWNT nucleation mechanism employing the creation of pentagons is contestable theoretically and has no direct experimental verification. That led us to propose the model for the formation of cylindrical nucleus from the edge of graphene [1]. The model has a benefit as it does not suffer from the well-known [12] problem of the dome-closing. Moreover, the new model explains qualitatively the chirality of the most abundant [10,10] NT and quantitatively describes its (optimum) radius $R \sim 7$Å. The carbon edge brings an natural anisotropy into the model, which unriddles why the cluster does not start to grow as a spheroidal shell[2]. The iterated zipping off of the tube nucleus from the edge and the consecutive van der Waals gluing of those could explain the rope formation.

The zipping mechanism (as shown in Fig.2) starts with the closing of two graphene sheet edges (stage 1 of Fig.2). The potential energy of the closed edge (stage 2) is high because of the large strain. In order to relax the lattice and decrease the stress one needs to increase the radius of curvature. This forms a cylindrical sleeve along the closed edge (stage 3). The sleeve radius increases until the optimum configuration is reached (stage 4). The optimal radius is analytically given by the ratio of the elastic strain energy (which is proportional to the square of the sleeve curvature) and the van der Waals energy. The latter was accumulated between graphene sheets before they formed a sleeve. The very wide sleeve is not favored because of the large loss of van der Waals cohesion energy. A narrow sleeve concedes owing to the large curvature.

The optimal structure has the radius about 7 Å. It follows from the minimization of the total energy of the structure per unit length of the edge [2].

The system can possess additional energy owing to possible dangling bonds at the open edge. It is proportional to an energy of single DB: $E_b \simeq 2.355$ eV and a DB density depending on the perimeter geometry. The model parameter responsible for the change of the DB density is a SWNT chirality. An armchair graphite edge has the maximum density while a zigzag edge has the minimum density. That is why the zigzag edge of graphene has the minimum surface energy and is the most stable configuration [13]. For an infinite sleeve I shall not consider DB energy.

---

[2] An equilibrium shape for finite size cluster is doubtless close to round (spherical) for 2D (3D) structure.

The thermodynamic reason why the most stable graphite edge is the zigzag edge explains the helicity of prevalent [n,n] tube. The zigzag edge is zipped into an **armchair** nucleus. Then supposing that the optimum diameter is 15 Å as predicted by the continuum theory (and supported by MD simulation) [2] the prevalent SWNT is [11,11] tube which is my best approximation to the experimental fact of [10,10] SWNT formation.

SUMMARY

The mechanism of SWNT nucleation from the hemispherical bowl is revised and shown to be contestable. The new model of the pentagon free nucleation from the closed edge of the graphite is considered within the continuum graphene layer energetics. The prevalent formation of the armchair SWNTs with the diameter close to 15 Å follows from the theory suppositions. Further study of the nucleation mechanism is required to uncover the catalyst role.

ACKNOWLEDGMENTS

REFERENCES

1. S.V. Rotkin, Fullerenes 2000 Volume 10: Chemistry and Physics of Fullerenes and Carbon Nanomaterials, Eds: P.V. Kamat, D. M. Guldi, K.M. Kadish. ECS Inc., Pennington, NJ, PV 2000-12, pp. 66–71 (2000).
2. S.V. Rotkin, I. Zharov, K. Hess, "Electronic Properties of Novel Materials - Molecular Nanostructures"; (XVth International Winterschool/Euroconference, Kirchberg, Tirol, Austria, 3-10 March 2001), edited by H.Kuzmany, J.Fink, M.Mehring, S.Roth. AIP Conference Proceedings (2001). In press.
3. S. Bandow, et.al., Phys.Rev.Lett. **80**, 3779, 1998; O.Jost, et.al., Appl.Phys.Lett. **75**, 2217, 1999.
4. S. Amelinckx, D. Bernaerts, X.B. Zhang, G. Van Tendeloo, J. Van Landuyt, Science **275**, 1334, 1995.
5. S.V. Rotkin, R.A. Suris, cond-mat/0007259.
6. S.V. Rotkin, Fullerenes 2001 Volume 11: Fullerenes, Nanotubes and Carbon Nanoclusters, Editors: K.M. Kadish, P.V. Kamat. ECS Inc., Pennington, NJ, PV 2001-11, in press (2001).
7. S.V. Rotkin, R.A. Suris, Phys.Lett. **A** v. **261**, 98, 1999.
8. S.V. Rotkin, unpublished.
9. S.V. Rotkin, in Ioffe Institute scientific reports (Russian). 1998.
10. M.B. Nardelli, B.I. Yakobson, J. Bernholc, Phys.Rev. **B 57** , R4277, 1998.
11. V.V. Rotkin, R.A. Suris, Proc. of IV Int. Conf. on Advanced Materials, S3-P3.4, Cancun, Mexico, 1995.
12. M.B. Nardelli, C. Brabec, A. Maiti, C. Roland, J. Bernholc, Phys.Rev.Letters **80**, 313, 1198.
13. J. Abrahamson, Carbon **11**, 337, 1973.

Synthesis of Vertically Aligned Carbon Nanofiber Films by RF Magnetron Sputtering

K. -Y. Lee, K. Fujimoto, S. Ohkura, S. Honda, M. Katayama, T. Hirao,[1] and K. Oura
Department of Electronic Engineering, Faculty of Engineering, Osaka University,
2-1 Yamadaoka, Suita, Osaka 565-0871, Japan
[1]Department of Electrical Engineering, Faculty of Engineering, Osaka University,
2-1 Yamadaoka, Suita, Osaka 565-0871, Japan

ABSTRACT

The aligned carbon nanofibers were synthesized on Si substrates using RF magnetron sputtering with a hot filament. The hot filament was made of tungsten wire and its temperature was up to 2000°C during the deposition. Nitrogen was used as the sputter gas at a relatively low pressure of 2×10^{-2} Torr. The sputtering deposition was carried out at a substrate temperature of 700°C. The nanofibers were grown vertically on the substrates. The diameters and the density of the fibers were about 30-45 nm and 10^9 cm^{-2}, respectively.

INTRODUCTION

Since the carbon nanotube was discovered [1], there have been many reports study on the aligned carbon nanotubes [2-5]. For fundamental research and applications, the alignment of carbon nanotube is important, especially in cold-cathode flat panel displays, vacuum microelectronics, chargeable batteries, and so on [6-8]. In the application of the field emission displays (FEDs), the alignment of the carbon nanotubes is of great important because of the enhancement and uniformity of the field emission [9-11].

In this study, we report a novel method of formation of aligned carbon nanofibers on Ni/Si substrates by RF magnetron sputtering with a hot filament. The carbon nanofibers grew with high density and perpendicularly to the substrates.

EXPERIMENT

The aligned carbon nanofiber films were deposited by a hot-filament-assisted RF magnetron sputtering system, as shown in figure 1. P-doped n-type Si(100) wafers were used as substrates. The substrates were patterned with Ni films by electron beam evaporation. Moreover, the patterned Ni deposited substrates were treated by dipping in a HF solution for 8 minutes, and then annealed at 700°C for one hour.
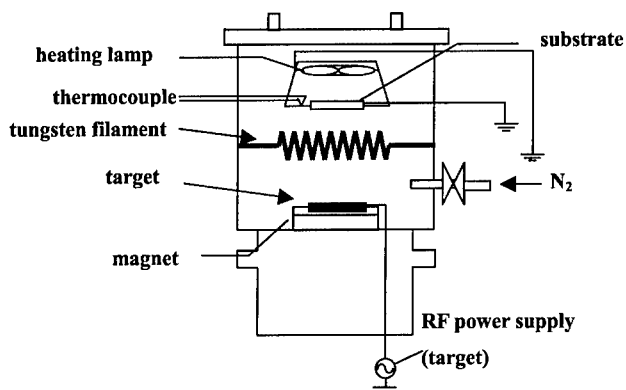
Figure 1. Schematic diagram of RF magnetron sputtering system.

The target was a high-purity graphite (99.999%) with a 50-mm diameter. The base pressure of the chamber was below 5.0×10^{-7} Torr evacuated by a turbo molecular pump. Nitrogen was flowed into the chamber to create a plasma by applying a RF power of 100W at a relatively low pressure of 2.0×10^{-2} Torr. The films were deposited at 700°C for 3 hours. The hot filament, which was made of 99.95% tungsten with 0.3 mm of the diameter, was set between the target and substrate. The distance between the substrate and target was 5 cm, and the distance between the filament and substrate was 3 cm. 6 amperes of filament current was applied and filament temperature was about 2000°C. The characterizations of the carbon nanofiber films were investigated by scanning electron microscope (SEM), and X-ray photoelectron spectroscopy (XPS). The electron field emission property of the film was measured at a pressure about of 10^{-8} Torr. The distance between the cathode (sample) and the anode was $200 \, \mu$ m. The activation time for the measurement was 60 minutes.

RESULTS

The carbon nanofibers are perpendicular to the Ni/Si substrate surface and are uniform in height. The diameters of the fibers range from 30-45 nm in diameter and about 370 nm in length, respectively. The Ni particle is on the tip of each fiber. The density of the carbon nanofibers is about 8.2×10^9 cm^{-2}.

From XPS spectrum of the film (figure 2), the peaks of binding energy of C1s is approximately 284.6 eV and N1s is approximately 400eV were observed. There are not any tungsten peaks in the XPS spectrum.
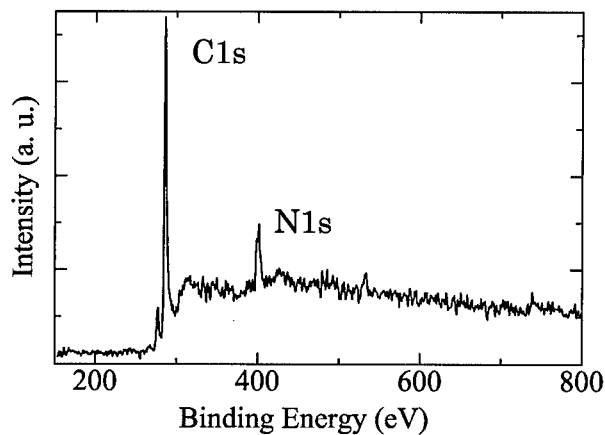
Figure 2. XPS spectrum of the film reveals the peaks of binding energy of C1s and N1s.

The current density-electric field (J-E) characteristic of this a-C film was obtained at a pressure of 5.0×10^{-8} Torr. The J-E plot shows that the electrical field emission current reach as high as 1.0×10^{-4} A/cm^2 at about 15 V/μ m.
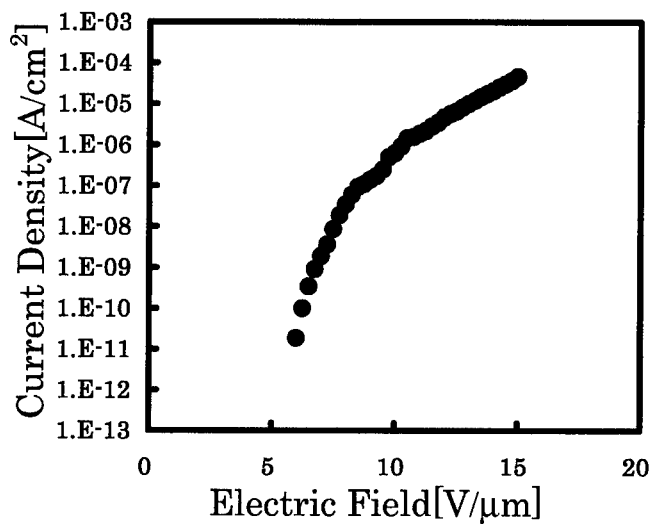
Figure 3. The current density-electric field (J-E) characteristics of this a-C film.

CONCLUSIONS

We have successfully synthesized the well-aligned carbon nanofibers on Ni/Si substrates by RF magnetron sputtering system at temperature of 700°C. The diameter and length of the fiber are about 30-45 nm and 370 nm, respectively. The density of the carbon nanofibers can reach as high as 8.2×10^9 cm^{-2}.

REFERENCES

1. S. Iijima, *Nature* **354**, 56 (1991).
2. Y. Avigal, R. Kalish, *Appl. Phys. Lett.* **78**, 2291 (2001).
3. J. I. Sohn, S. Lee, Y.-H. Song, S.-Y. Choi, K.-I. Cho, K.-S. Nam, *Appl. Phys. Lett.* **78**, 901 (2001).
4. D.-C. Li, L. Dai, S. Huang, A. W. H. Mau, Z. L. Wang, *Chem. Phys. Lett.* **316**, 349 (2000).
5. C. Bower, W. Zhu, S. Jin, O. Zhou, *Appl. Phys. Lett.* **77**, 830 (2000).
6. Z. P. Huang, J. W. Xu, Z. F. Ren, J. H. Wang, M. P. Siegal, P. N. Provencio, *Appl. Phys. Lett.* **73**, 3845 (1998).
7. H. Murakami, M. Hirakawa, C. Tanaka, H. Yamakawa, *Appl. Phys. Lett.* **76**, 1776 (2000).
8. A. N. Obraztsov, I. Pavlovsky, A. P. Volkov, E. D. Obraztsova, A. L. Chuvilin, V. L. Kuznetsov, *J. Vac. Sci. Technol.B* **18**, 1059 (2000).
9. Y. Chen, S. Patel, Y. Ye, D. T. Shaw, L. Guo, *Appl. Phys. Lett.* **73**, 2119 (1998).
10. Y. Chen, D. T. Shaw, L. Guo, *Appl. Phys. Lett.* **76**, 2119 (1998).
11. A. Cao, L. Ci, D. Li, B. Wei, C. Xu, J. Liang, D. Wu, *Chem. Phys. Lett.* **335**, 150 (2001).

Preparation of Carbon Nanotubes by Using Mesoporous Silica

Shinji Kawasaki, Shingo Komiyama, Shigekazu Ohmori, Akifumi Yao, Fujio Okino and
Hidekazu Touhara
Faculty of Textile Science & Technology, Shinshu University
Tokida, Ueda 386-8567, JAPAN

ABSTRACT

Carbon nanotubes were synthesized using several mesoporous silica templates with different
pore sizes in order to investigate the possibility of controlling the diameter of carbon nanotubes
by changing the pore size of the mesoporous silica. TEM observation confirmed that carbon
nanotubes with uniform diameter can be obtained by the present method. However, it was found
that it is difficult to prepare carbon nanotubes having diameter smaller than $\sim$20 nm by the
present method even if the template with small pore size is used.

INTRODUCTION

Owing to their new functional properties as electrode materials and hydrogen storage
materials, carbon nanotubes attract rapidly growing attention [1]. Concerning the preparation of
the carbon nanotubes, one of the most important problems is how to prepare nanotubes with
desired form. Another significant problem is how to obtain such nanotubes in a large scale.
Chemical vapor deposition (CVD) based synthesis of carbon nanotubes using an anodic
aluminum oxide (porous alumina) membrane template is an interesting way to overcome the
above mentioned problems [2, 3]. However, the tunable diameter of the nanotube prepared by the
template carbonization method using porous alumina is limited to >20 nm. Furthermore, it is not
easy to control the pore size and the thickness of the alumina membrane simultaneously. In the
last decade, several techniques for making highly ordered periodic mesoporous silica with pore
sizes of 2 - 50 nm have been developed [4, 5]. There are several types of pore alignment known as
cubic, 3d-hexagonal and 2d-hexagonal. The 2d-hexagonal silica has cylindrical pores arranged in
the honeycomb fashion. Using the ordered mesopores, nanostructured carbon materials have been
tried to be synthesized and Jun et al.[6] succeeded in making a carbon replica of mesoporous
silica. In the present study, we have tried to prepare carbon nanotubes using mesoporous silica by
template carbonization method. We have investigated the possibility of controlling the diameter
of carbon nanotubes by changing the pore size of the mesoporous silica.

EXPERIMENTAL DETAILS

Mesoporous silica with mesopores of 2 - 4 nm and 6 - 20 nm in diameter were synthesized in
the presence of cetyltrimethylammmonium bromide (CTAB, Aldrich) surfactant and triblock
poly(ethylene oxide)-poly(propylene oxide)-poly(ethylene oxide) $(P(EO)_{20}-P(PO)_{70}-P(EO)_{20})$
copolymer (Pluronic P123, BASF), respectively. Trimethylbenzene (TMB) was used as an organic
swelling agent to enlarge the mesopore. The solution mixture was aged for 24 h at 353 - 383 K.
Calcination was carried out by slowly raising the temperature from room temperature to 873 K.

CVD experiments were performed as follows. A mesoporous silica sample was evacuated in a SiO_2 tube at 383 K for 30 min. Then the reactor was filled with nitrogen gas and the temperature of the reactor was raised to 1073 K. Propylene and nitrogen gases were flowed for 1 h at flow rates of 1.25 cm^3/min and 125 cm^3/min, respectively. After the reaction, the reactor was cooled to room temperature. The mesoporous silica with carbon deposit was washed with an excess amount of HF solution at room temperature so as to dissolve silica.

The synthesized mesoporous silica and the CVD treated templates were characterized by XRD, N_2 adsorption-desorption isotherm measurements and TEM observation carried out on Rigaku RINT2200, Shimadzu GEMINI2375 and JEOL JEM2010, respectively.

RESULTS & DISCUSSION

The template designation used in the present paper is given in Table I.

The observed N_2 adsorption-desorption isotherms of the synthesized mesoporous silicas at 77 K are shown in Figure 1 (A). The pore size distributions determined from the isotherms by Barrett-Joyner-Halenda (BJH) method are shown in Figure 1 (B). The peaks in the distribution diagrams are very sharp except for the case of template P-3. Figure 2 shows the observed XRD patterns of the mesoporous silicas. All the observed peaks can be indexed with hexagonal unit cells and it indicates that the synthesized mesoporous silicas have cylindrical pores arranged in the honeycomb fashion. In the case of template P-3, no diffraction peak was observed. Assuming that template P-3 has a hexagonal unit cell of $a = 35$ nm (pore size 33 nm + wall thickness 2 nm), the d-values of 100, 110 and 200 diffraction peaks are greater than our XRD instrumentation limit (~13 nm).

Table I. Physicochemical properties, synthesis conditions of the synthesized mesoporous silica templates and the yield of carbon nanotubes

template No.[a]	TMB/surfactant weight ratio	aging temp. (K)	pore size[b] (nm)	$d_{(100)}$ (nm)	wall thickness[c] (nm)	yield of nanotubes
C-1	0.0	353	2.1	3.5	1.9	–
C-2	3.0	353	2.9	4.4	2.2	–
P-1	0.0	353	6.0	8.7	4.1	very low
P-2	0.0	383	9.6	10.4	2.4	low
P-3	0.5	353	33.0[d]			high

[a] Samples C-m and P-n were synthesized with CTAB and P123, respectively.
[b] Calculated from adsorption branch of the N_2 isotherm by BJH method.
[c] Calculated by a_0−pore size ($a_0 = 2d_{(100)}/\sqrt{3}$).
[d] Mean pore size observed by TEM is 20 - 30 nm.

Figure 3 shows TEM images of silica templates P-1 and P-3. The TEM images of template P-1 show that the mesopores are hexagonally arranged (Figure 3 (A)) and that the cylindrical pores are well aligned (Figure 3 (B)). On the other hand, although cylindrical pores are also observed in the TEM image of template P-3, the pores are not well aligned and the distribution of the pore size is relatively large. The pore sizes of template P-3 observed by TEM observation are 20 - 25 nm which is smaller than the value determined from the isotherm measurement. Physicochemical properties of the synthesized mesoporous silicas are summarized in Table I.
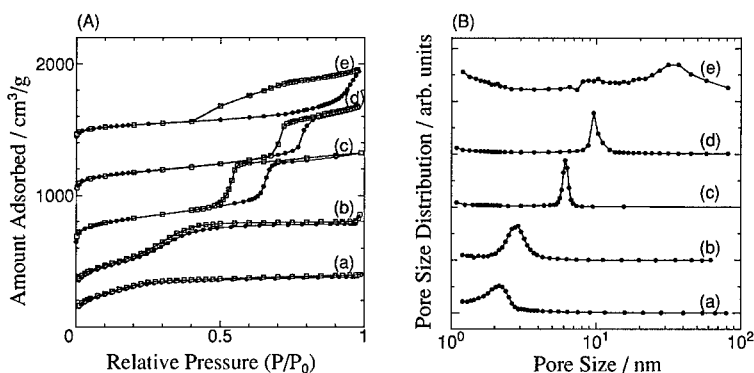
Figure 1. (A) N_2 adsorption-desorption isotherms for the prepared mesoporous silicas at 77 K. The data for (a) C-1, (b) C-2, (c) P-1, (d) P-2 and (e) P-3 are offset vertically by 0, 200, 600, 1000, and 1400 cm^3g^{-1}, respectively. (B) Pore size distributions for templates (a) C-1, (b) C-2, (c) P-1, (d) P-2 and (e) P-3.
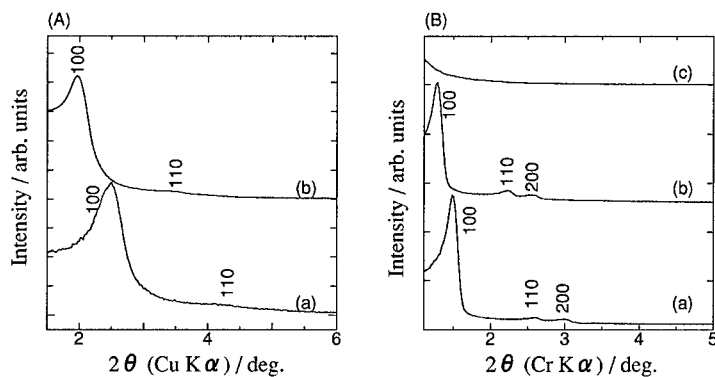
Figure 2. XRD patterns of templates (A)-(a) C-1, (A)-(b) C-2, (B)-(a) P-1, (B)-(b) P-2 and (B)-(c) P-3.

By CVD treatment, the color of the mesoporous silica changed from white to black and it indicates that the carbon deposition occurred on the surface of the silica. Figure 4 shows the XRD patterns of template P-2 before and after the CVD treatment. The ordered (hexagonal) structure of the mesoporous silica was maintained after the CVD treatment, although the diffraction peaks shifted slightly toward the higher angle side.

No carbon nanotube was found by TEM observation in the CVD treated templates C-1 and C-2 after silica templates were removed with HF solution. On the other hand, carbon nanotubes
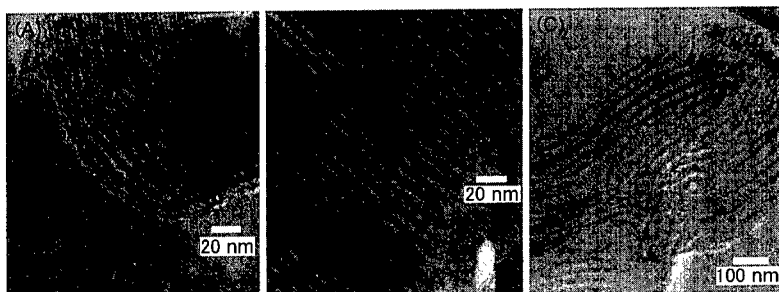
Figure 3. TEM images of silica templates (A) P-1, (B) P-1 and (C) P-3. (A) is recorded in the direction of the pore axis and (B), (C) are recorded in the direction perpendicular to the pore axis.
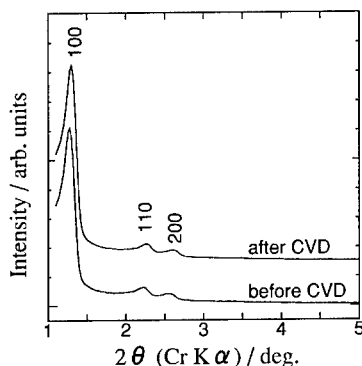
Figure 4. The observed XRD patterns of template P-2 before and after CVD treatment.

were found in the cases of templates P-1, P-2 and P-3. Although it is difficult to quantitatively determine the ratio of carbon nanotubes to the whole sample including amorphous carbon, the yields of carbon nanotubes are judged as very low, low and high for the cases of templates P-1, P-2 and P-3, respectively from TEM observation (Table I). The mean diameter of the carbon nanotubes prepared with template P-3 is ~30 nm, and agrees well with the mean pore size of the template. On the other hand, the diameters of the carbon nanotubes prepared with templates P-1 and P-2 are 10 - 20 nm and 15 - 25 nm, respectively, which are larger than the mean pore sizes of the silica templates determined from the isotherms. It is inferred that the deposition of carbon in small channels with diameter less than ~10 nm to form nanotubes is somehow mechanistically not possible, and that only those pores with larger diameters in templates P-1 and P-2 contributed to the formation of nanotubes. This also explains the low yield of nanotubes with templates P-1 and P-2. It was also found by high resolution TEM observation that the wall thickness of the nanotubes is 3 - 5 nm and that the walls of the carbon nanotubes are not well graphitized.
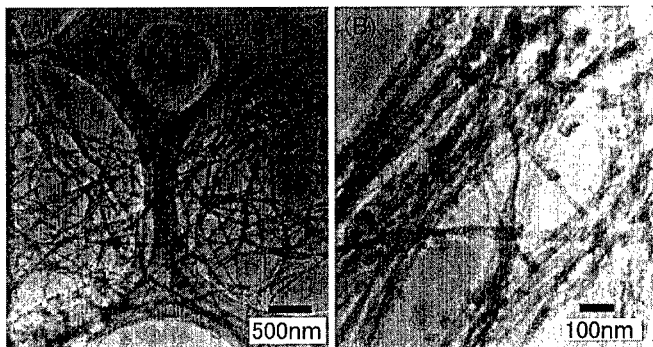
Figure 5. TEM images of the carbon nanotubes prepared using template P-3 as a template.

ACKNOWLEDGEMENT

REFERENCES

1. G. Che, B. B. Lakshmi, E. R. Fisher and C. R. Martin, *Nature* **393**, 346 (1998)
2. T. Kyotani, L. Tsai and A. Tomita, *Chem. Mater.* **7**, 1427 (1995)
3. G. Che, B. B. Lakshmi, C. R. Martin and E. R. Fisher, *Chem. Mater.* **10**, 260 (1998)
4. C. T. Kresge, M. E. Leonowicz, W. J. Roth, J. C. Vartuli, J. S. Beck, *Nature* **359**, 710 (1992)
5. D. Zhao, J. Feng, Q. Huo, N. Melosh, G. H. Fredrickson, B. F. Chmelka, G. D. Stucky, **279**, 548 (1998)
6. S. Jun, S. H. Joo, R. Ryoo, M. Kruk, M. Jaroniec, Z. Liu, T. Ohsuna and O. Terasaki, *J. Am. Chem. Soc.*, **122**, 10712 (2000)

Ab Initio Study of Si Doped Carbon Nanotubes: Electronic and Structural Properties

A. Fazzio[1,2], R. J. Baierle[3], Solange B. Fagan[2], Ronaldo Mota[2], and Antônio J. R. da Silva[1]
[1]Instituto de Física, Universidade de São Paulo, Caixa Postal 66318,
05315-970, São Paulo, Brazil
[2]Departamento de Física, Universidade Federal de Santa Maria,
97105-900, Santa Maria, RS, Brazil
[3]Departamento de Ciências Naturais e Exatas, Centro Universitário Franciscano,
97010-032, Santa Maria, RS, Brazil

ABSTRACT

We report the electronic and structural properties of silicon doped carbon nanotubes using first principles calculations based on the density-functional theory. In the doped metallic nanotube a resonant state appears about 0.7 eV above the Fermi level and for the semiconductor tube the Si introduces an empty level at approximately 0.6 eV above the top of the valence band.

INTRODUCTION

The new structural form of carbon discovered by Iijima in the early 1990 [1] has attracted the attention of several research groups due to their interesting properties from both a fundamental physics as well as the possible application viewpoint. Single-walled nanotubes, depending on their chirality and diameter, are either a one-dimensional metal or semiconductor [2]. The presence of semiconductor and metallic one-dimensional structures in the same family of materials opens up exciting possibilities of new phenomena and novel device structures. In the recent literature there are reports of several groups that have succeeded in synthesizing doped carbon tubes, using different techniques as arc discharge [3] and gas-phase pyrolisis [4]. The doped nanotubes can exibit dramatic changes with respect to the undoped material. Recently Ray *et al.* [5] have reported the synthesis of silicon doped heterofullerenes in the carbon-rich limit, where the photofragmentation spectra provide a clear evidence that such clusters have Si atoms located in the fullerene network. These results are corroborated by *ab inito* calculations [6].

In this paper we present a study about isovalent substitutional impurities in carbon nanotubes. In particular, we focus on the electronic and structural properties of silicon as the substitutional atom. This doping, due to the different sizes between carbon and silicon atoms will affect locally the lattice. As is well known, silicon, as opposed to carbon, does not have the sp^2 configuration as the most stable one [7]. As a consequence there will also be, besides the simple volume relaxation, a lattice distortion that may introduce a new state in the gap, leading to the possibility that, for instance, it can be a hole or electron trap working like an amphoteric deep center. Moreover, from a structural point of view, the lone orbital due to the Si-impurity could be a center to trap other atoms or molecules. It is important to point out that there are experimental realizations of Si doping on fullerenes [8,9], which suggests that it is quite possible to also dope carbon nanotubes with Si. In the following we present an *ab initio* calculation based on the density-functional theory addressed to understand the role played by silicon doping in both metallic and semiconducting nanotubes.

METHOD

For our study of carbon nanotubes doped with Si we have used the SIESTA code [10], which performs a fully self-consistent density-functional calculation solving the standard Kohn-Sham (KS) equation. The KS orbitals are expanded using a linear combination of pseudo-atomic orbitals proposed by Sankey and Niklewski [11]. In all calculations we have used a double-zeta basis set with polarization function (DZP) [12]. The standard norm-conserving Troullier-Martins pseudopotentials [13] are utilized. For the exchange and correlation term we use the local density approximation (LDA) [14] with the parameterization of Perdew-Zunger [15]. Our calculations were performed for two types of tubes, the (6,6) metallic and (10,0) semiconductor (diameters of 8.14 Å and 7.82 Å, respectively). We use periodic-boundary conditions and the supercell approximation, with a lateral separation of 16 Å between tube centers to make sure that they do not interact with each other. For the (6,6) tube we have performed calculations using 72 atoms in the unit cell, whereas for the (10,0) tube we have considered a unit cell with 80 atoms. These unit cells have been used both for the doped and undoped tubes. We have used 8 Monkhorst-Pack k-points for the Brillouin zone integrations. The structures of the doped and undoped tubes were obtained by minimization of total energy using the Hellmann-Feynman forces with Pulay-like correction. The structural optimizations were performed using a conjugated gradient procedure until the residual forces had values smaller than 0.05 eV/ Å. In all systems studied we allowed the cell size to change after the incorporation of the Si atom.

RESULTS AND DISCUSSION

In the figure 1 we present schematically some of the Si-C and C-C relevant distances around the Si-atom. In Figs 1(a) and 1(b) we present the results for the (6,6) and (10,0) nanotubes, respectively. For the armchair (6,6) tube, the distance between a Si atom and its image in the next cell is 7.38 Å, whereas for the zigzag (10,0) nanotube it is 8.52 Å. The lengths of the unit cells along the tube direction had negligible changes in both cases (-0.3% for the (6,6) tube and 0.09% for the (10,0) tube). Observe that, concerning the three nearest-neighbors Si-C distances, there are two equivalent bond-lengths (Si-C_1 and Si-C_2 in the figure 1), and third non-equivalent bond-length (Si-C_3 in the figure 1), which is consistent with the symmetry of the system. These bond lengths are close to the Si-C nearest distance in SiC, which we obtained as 1.88 Å using a similar method of calculation. The C-C distances within a range of approximately 5 Å from the Si atom change by at most ± 1%. Concerning the displacements along the radial directions, or the bump heights, the Si atom moves upward by 0.79 Å in the (6,6) tube and 0.78Å in the (10,0) tube. In the (6,6) tube, the C_3 carbon moves upwards by 0.29 Å, whereas the two equivalent carbon atoms C_1 and C_2 move also upwards but 0.17 Å. In the (10,0) on the other hand, the C_3 atom moves upwards by 0.19 Å, whereas the C_1 and C_2 atoms move upwards by 0.27 Å. This structural behavior for the Si in nanotubes, i.e., an outward relaxation with Si-C bond lengths between 1.7-1.8 Å, is very similar to what is obtained for Si substitutional doping in fullerenes [5][6][16], as should be expected because of the similar C-bond network in these two classes of systems.
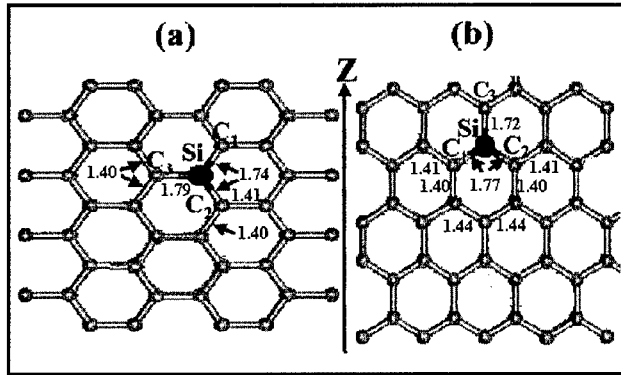
Figure 1. Some of the relevant Si-C and C-C distances (in Å) around the Si substitutional atom in the (a) (6,6) nanotube, and (b) (10,0) nanotube. The z-axis is chosen along the tube direction.

Through the total energy calculation, the formation energy (E_{Form}) is computed using

$$E_{Form} = E[tube + Si] - E[tube] - \mu_{Si} + \mu_C$$

where E[tube + Si] is the total energy of the doped tube with Si and E[tube] is the total energy for the undoped case. The μ_{Si} and μ_C are the chemical potentials for Si and C, respectively. The μ_{Si} was calculated as the total energy per atom in the Si bulk an μ_C was calculated as the total energy per atom in the undoped tubes. The formation energy was calculated for different sizes of tubes, and it nicely converges to a value of approximately 3.13 eV, which is the formation energy for the Si in the (10,0) nanotube with 80 atoms and the (6,6) tube with 72 atoms in the unit cells [17].
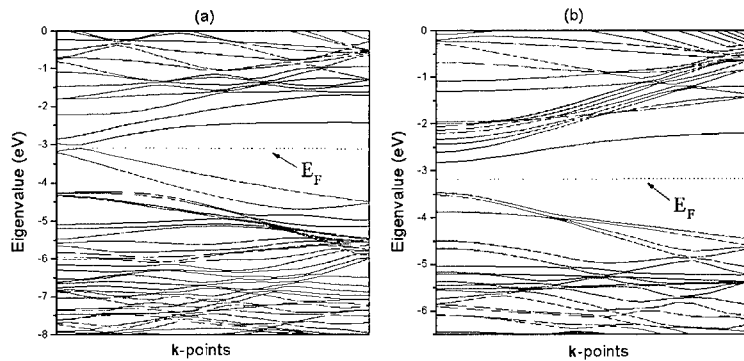
Figure 2. Band structure for carbon nanotubes with one substitutional Si (a) (6,6) tube with 72 atoms and (b) (10,0) tube with 80 atoms.
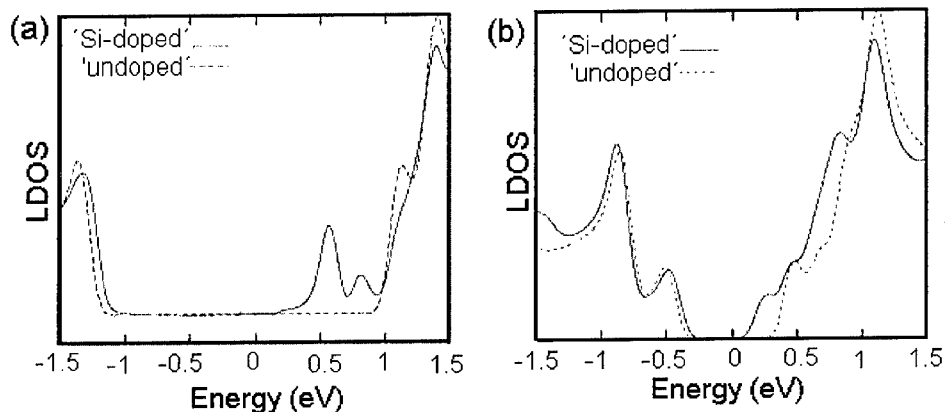
Figure 3. Electronic density-of-states (DOS) for the doped (filled line) and undoped (dashed line) nanotubes: (a) (6,6) nanotube and (b) (10,0) nanotube.

In the figure 2 we present the band structure results for the carbon nanotubes doped with silicon. For Fig 2(a) we show the (6,6) tube with 72 atoms and in Fig 2(b) the (10,0) tube with 80 atoms. The metallic tube, shows a very small gap due to symmetry break when we introduce the silicon in a finite supercell. For both system the more pronounced change due to the silicon doped is change above the Fermi-level, an empty level which is located in the foreign atom.

In the figure 3 we present the local densities of states (LDOS) around the silicon impurity for the different cases studied. For each case we report the LDOS for the doped and undoped nanotubes. The result for the (6,6) tube is shown in Fig. 3(a). As can be seen, the doping introduces two clear peaks above the Fermi level, one at 0.6 eV and another at 0.8 eV. A look at the band structure for this system shows that there is a level that starts at the Brillouin zone center, at approximately 0.8 eV above the Fermi level, which has a very small dispersion until it mixes with the pure nanotube states. There is also another band that starts at the Brillouin zone boundary with an energy of approximately 0.6 eV above the Fermi level, and also has a very small dispersion until it mixes with the pure nanotube bands. We assign these two states to a resonant Si state that gains a small dispersion due to the supercell approximation. Therefore we can conclude that Si doping (6,6) tube introduces a resonant level at approximately 0.7 eV above the Fermi level.

In the figure 4 we present the charge density for the state at the Brillouin zone boundary, located at 0.6 eV above the Fermi level. As can be seen, this state is strongly localized at the Si atom. The state at the Brillouin zone center also has a large signal at the Si atom, but shows a stronger mixing with the nanotube states, which results in a more delocalized charge density. This mixing is also observed in the charge density plot of the nanotube empty states at the Brillouin zone center close to the Fermi level.
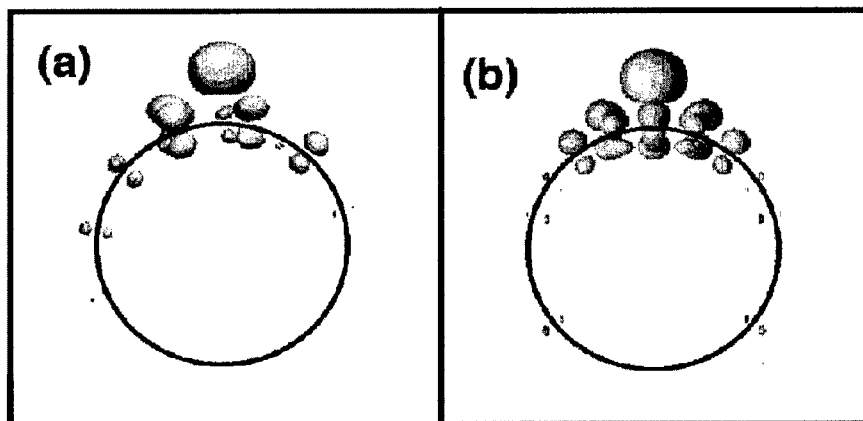
Figure 4. Electronic-charge densities for the (a) orbital at the Brillouin zone boundary located at 0.6 eV above the Fermi level, for the (6,6) doped nanotube, and (b) orbital at the Brillouin zone center located at 0.6 eV above the top of the valence band, for the (10,0) doped nanotube. The circles are guides to the eye.

The LDOS for the (10,0) tube is shown in Fig. 3(b). As can be seen, the Si introduces an empty level in the gap at approximately 0.6 eV above the top of the valence band. From the band structure calculation, we also observe this Si level in the gap, which, although the Si-Si distance is 8.52 Å, presents a small energy dispersion of order of 0.3 eV. In Fig. 4(b), the charge density for the empty level at the Γ point is shown. As can be seen, it is highly localized at the Si atom, which suggests that the silicon impurity might be an effective center to capture other atoms or molecules. A similar plot for the states at the top of the valence band shows a strong contribution from the Si atom, indicating that the Si impurity will introduce delocalized states close to the top of the valence band. It is interesting to point out that electronic structure calculations of Si doping on C_{60} [5,6][9][16] obtain that the Si introduces an occupied level very close to the highest occupied levels of pure C_{60}, as well as a level close to 0.4 eV below the lowest unoccupied levels of pure C_{60}. These findings are very similar to what we present here. However, we obtain that the levels with large Si weight, and that are close to the top of the valence bands of the pure nanotubes, are quite delocalized, as opposed to what is obtained for Si on fullerenes.

ACKNOWLEDGMENTS

REFERENCES

1. S. Iijima, *Nature* (London) **354**, 56 (1991).
2. N. Hamada, S. Sawada, and A. Oshiyama, *Phys. Rev. Lett.* **68**, 1579 (1992); R. Saito, M. Fujita, G. Dresselhaus, and M. S. Dresselhaus, *Appl. Phys. Lett.* **60**, 2204 (1992).

3. O. Stephen, P. M. Ajayan, C. Colliex, P. Redlich, J. M. Lambert, P. Bernier, and P. Lefin, *Science* **266**, 1683 (1994); K. Suenaga, C. Colliex, N. Demoncy, A. Loiseau, H. Pascard, and F. Willaime, *Science* **278**, 653 (1997).

4. M. Terrones, A. M. Benito, C. Manteca-Diego, W. K. Hsu, O. I. Osman, J. P. Hare, D. G. Reid, H. Terrones, A. K. Cheetham, K. Prassides, H. W. Kroto, and D. R. M. Walton, *Chem. Phys. Lett.* **257**, 576 (1996).

5. C. Ray, M. Pellarin, J. L. Lermé, J. L. Vialle, M. Broyer, X. Blase, P. Mélinom, P. Kéghélian, and A. Perez, *Phys. Rev. Lett.* **80**, 5365 (1998).

6. C.-C. Fu, M. Weissmann, M. Machado, and P. Ordejón, *Phys. Rev. B* **63**, 85411 (2001).

7. L. Pauling, *The Nature of the Chemical Bond and the Structure of molecules and Crystals; an Introduction to Modern Structural Chemistry*, 3rd ed., Cornell University Press, Ithaca, New York, 1960.

8. J. L. Fye and M. F. Jarrold, *J. Phys. Chem A* **101**, 1836 (1997); T. Kimura, T. Sugai, and H. Shinohara, *Chem. Phys. Lett* **256**, 269 (1996).

9. M. Pellarin, C. Ray, J. L. Lermé, J. L. Vialle, M. Broyer, X. Blase, P. Kéghélian, P. Mélinon, and A. Perez, *J. Chem. Phys.* 110, 6927 (1999).

10. P. Ordejón, E. Artacho, and J. M. Soler, *Phys. Rev. B* **53**, 10441 (1996); D. Sánchez-Portal, P. Ordejón, E. Artacho, and J. M. Soler, *Int. J. Quantum Chem.* **65**, 453 (1997)

11. O. F. Sankey and D. J. Niklewski, *Phys. Rev. B* **40**, 3979 (1989).

12. E. Artacho, D. Sánchez-Portal, P. Ordejón, A. García, and J. M. Soler, *Phys. Stat. Sol. (b)* **215**, 809 (1999) and references therein.

13. N. Troullier and J. L. Martins, *Phys. Rev. B* **43**, 1993 (1991).

14. D. M. Ceperley and B. J. Alder, *Phys. Rev. Lett.* **45**, 566 (1980).

15. J. P. Perdew and A. Zunger, *Phys. Rev. B* **23**, 5048 (1981).

16. I. M. L. Billas, C. Massobrio, M. Parrinello, W. Branz, F. Tast, N. Malinowski, M. Heinebrodt, and T. P. Martin, *J. Chem. Phys.* **111**, 6787 (1999).

17. See R. Baierle *et al*, Phys. Rev. B (to appear June (2001)) for more information about formation energy.

Nanotube Properties

Mechanics of multi walled carbon nanotubes probed by AFM

S. Decossas[1], L. Patrone[2], F. Comin[1], J. Chevrier[1,3,4]

1 *ESRF, BP 220, F38043 Grenoble Cedex FRANCE*

2 *SCM, CEA/Saclay, 91191 Gif-sur-Yvette cedex, FRANCE*

3 *LEPES-CNRS, BP 166, 38042 Grenoble Cedex 9, FRANCE*

4 *Université Joseph Fourier (UJF), Grenoble, FRANCE*

Abstract

Using the AFM tip, nanotubes are caught on a raw sample then deposited on a clean surface with an absolute precision better than 500nm. A nanostructured surface made of smooth Germanium dots on flat silicon was used as deposition sample. Nanotube mechanics is probed by AFM tip induced displacement. Nanotubes are shown to be blocked by Ge dots: it is impossible to induce a controlled displacement of the nanotube over a Ge dot when it is pushed against the dot. Elastic energy due to the bending of the nanotube is at the root of that behavior.

Introduction

Carbon nanotubes (CNT) are cylindrical carbon based molecules [1]. Due to their interesting electronic and mechanic properties, they are thought to be key element in nanotechnologies [2-3]. Atomic Force Microscope (AFM) nanomanipulation has already been used to study their mechanical properties [4-6]. Interaction of nanotubes with a nanostructured surface in term of adhesion and friction is reported elsewhere [7-8]. Understanding relevant mechanisms that control movement of nano-objects on a surface is a central issue for further development in the manipulation of biological objects, in developing micro-systems, or in molecular electronics. In this paper, we will focus on the impossibility to induce a continuous displacement of one CNT over one Ge dot by strongly pushing it against the dot.

Experimental

Thin layer of carbon nanotubes (or nanotube carpets) are grown by Hot Filament Chemical Vapor Deposition [9]. AFM and Scanning Electron Microscopy (SEM) experiments show that these carpets are made of entangled nanotubes whose length varies from hundreds of nanometers to several microns. Transmission Electron Microscopy (TEM) experiments show that the nanotubes are multi-walled with a typical diameter of 20 nm. AFM experiments have been performed in air condition at room temperature with a commercial instrument [10]. We used standard Si_3N_4 tips with apex radius of curvature and deflection spring constant respectively given to be around 30nm and 0.06 N.m^{-1}. No attempt was done to check these values. It is however not relevant for the purpose of this paper. Nanostructured surface we used to study the

AFM tip induced displacement of nanotubes are made of Ge dots grown by Molecular Beam Epitaxy (MBE) on oxidized silicon wafer [11]. Ge dots have a spherical cap shape, 50nm in height, 500nm in width, with no significant size distribution. Silicon wafer roughness is well-below nanometer scale. CNT movement is induced by lateral force applied via the AFM tip. In this paper, applied forces are compared in term of load forces. However, we have experimentally checked that, in the force range we explored, lateral forces vary linearly with load.

Results and discussion

As already pointed out, it is possible to catch nanotubes with the AFM tip by performing force curves on nanotube carpets [12]. Once caught, nanotubes can be deposited on a clean and flat Si wafer as a consequence of friction between the tip and the surface while imaging the deposition sample. Deposition process steps are the following: i) choosing a deposition area on the deposition sample (AFM images) ii) catching nanotubes on the raw sample and iii) deposit nanotubes on the deposition sample. Fig 1a is an AFM image of the deposition area before the nanotube deposition. Ge dots (numbered from 1 to 5) define a recognizable landscape. Black cross indicates the exact position where nanotubes are supposed to be deposited. To catch nanotubes with the tip on the nanotube carpet one has to move the tip more than 1 cm away from the chosen deposition area. However, using the AFM XY stage ability to reproduced defined tip displacements, deposition area can be find again after nanotube catching with an precision better than 500nm. Fig 1b is a AFM image of the deposition area after the nanotube deposition. It is clearly the same area as shown of fig 1a since we find again the recognizable landscape defined by the 5 numbered Ge dots. As we can see, the precision achieved is better than 500nm. Using this method, a limited number of nanotubes (usually between 5 an 20) are deposited. In general, deposited nanotubes form ropes. However, it is possible to isolate them into individual nanotubes by strongly press and move the tip against the rope. Thanks to the connected optical system and XY stage, we can change the tip and find again the deposited nanotubes (nano-objects) on the deposition sample (several cm^2). Fig 1b AFM image has been recorded with a new tip (tapping mode). That allows one to use all the AFM operating modes and to work with a clean tip.
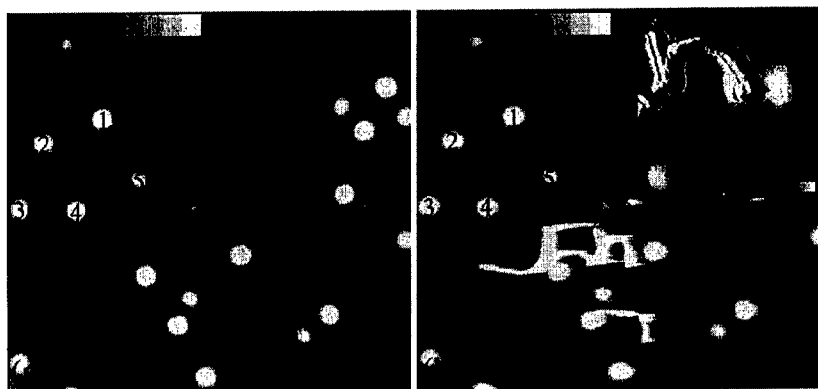
Figure 1: AFM images of the deposition area **(a)** in contact mode before CNT deposition and **(b)** in tapping mode after CNT deposition. **(b inset)** blow up of the deposited nanotubes.
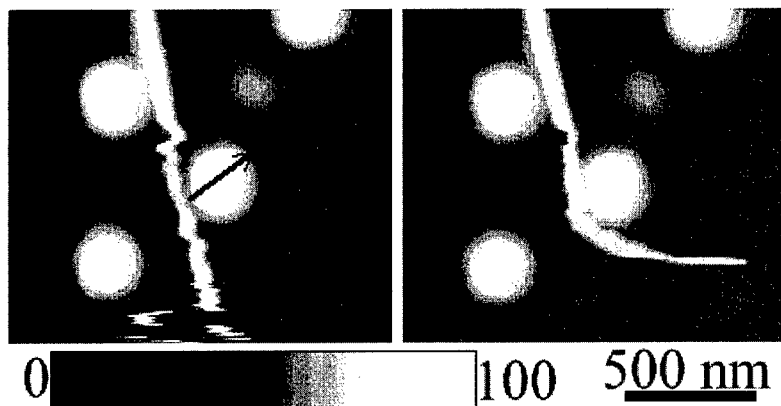
Figure 2: AFM image of **(a)** one nanotube deposited on the nanostructured surface. The arrows schematically represent the force applied via the tip and **(b)** the nanotube after displacement induced by the force (2).

Deposited nanotubes have further been manipulated with the AFM tip to be placed in contact with Ge dots (see fig 2). By pushing the nanotube against the dot with the tip (with the applied force (1) schematically represented on fig 2a), it is impossible to continuously make it climb over the dot. What happen in such a try is that the nanotube surface contact suddenly breaks and that the nanotube goes away in a totally uncontrolled process (to do that, we have to exert normal forces larger than 100nN). To understand the behavior of nanotubes when they are slowly moved under the force applied by the tip, relevant parameters are nanotube surface friction and elastic forces due to the nanotube bending and/or stretching. We have already shown that friction measured on Ge dots and Silicon wafer is equivalent [7-8]. We have never observed nanotubes with partial sticking to the surface. Then, if we want the nanotube to lie over the dot, it has to follow its profile. In a continuous approximation, we can then estimate the elastic work needed to deform the nanotube [13]:

$$U = \frac{E.I}{2} \int (\frac{1}{R} - \frac{1}{R_0})^2 \, dz \qquad \text{(equ. 1)}$$

where E is the Young modulus of the nanotube, I its moment of inertia with respect to its section, R_0 its radius of curvature at rest and R the local radius of curvature of the bent nanotube. Applying equ 2 to the CNT [14] leads to an elastic energy U equals to $3 \ 10^{-15}$ J. By equalizing U to the tip displacement work [15], the lateral force that must be applied to the CNT to follow the dot profile can be calculated to be around 60 nN. For this calculation, neither energy dissipation due to friction nor increased adhesion when the nanotube lies at the border of one dot [7-8] has been considered. Finally, the lateral force that must be applied to the nanotube for it to lie over the dot is much larger than 60 nN. By applying the force (2) on the nanotube (see fig 2a), the nanotube bent around the Ge dot, but once again, it does not climb over it.

If the nanotube ends on the dot, controlled displacement of it over the dot (see fig 3) becomes possible. AFM images (a) and (b) of fig 3 show a CNT pinned between two Ge dots before and after its manipulation. Figures 3 (c) and (d) represent height signal measured in two
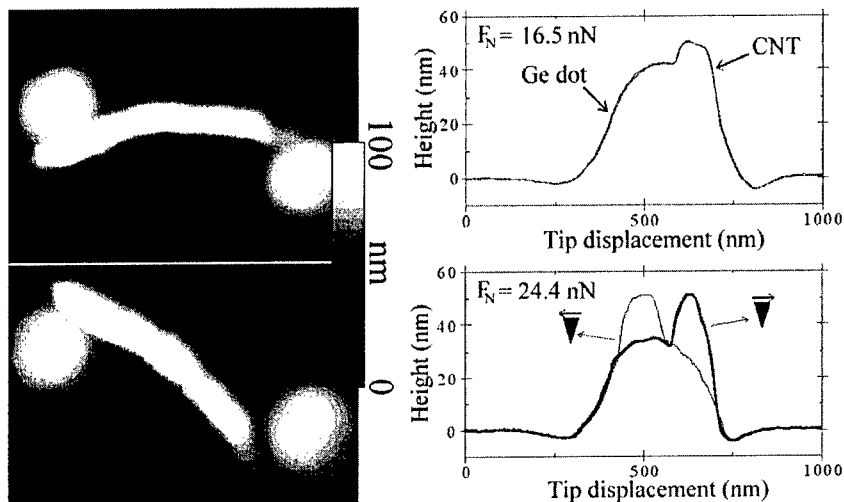
Figure 3: (a) and **(b)** AFM images of one nanotube whose ends are on one Ge dot **(c)** and **(d)** height signal recorded back and forth along the line of fig 3a for a load force respectively equals to 16.5nN and 24.4nN. Back and forth signals are perfectly superposed on (c). Back signal is represented in thin line on (d).

opposite directions while nanotube moves (recorded on a nanotube in the same position as the one on fig 3 a and b). As we can see, for a load force of about 16.5 nN, signals are perfectly superposed whatever is the scan direction (left to right or right to left). By increasing the load force up to about 24.4nN, height signals are not superposed anymore (see fig 3d). The nanotube moves under the force applied by the tip and continuously climb over the dot. In that case, the same calculation as the one done above leads to lateral force of about 12 nN (the only change in the calculation is the distance z along which the nanotube is bent and that has been estimated to be around 100 nm). Moreover, increased adhesion when nanotube lies at the border of one dot effect [7-8] is less important than in the case of fig 2 since nanotube dot contact length is shorter.

Conclusion

An experimental method used to deposit CNT with an absolute precision better than 500 nm has been reported. It allows to one to deposit a limited number of CNT at a determined place without using wet chemistry (as solvent). Manipulation using the AFM tip of the deposited CNT on a nanostructured surface reveals that CNT can be blocked by Ge dots depending on the nanotube length that has to deform. Calculation done using a very simple model shows that it is a direct consequence of the CNT elastic energy bending due to their bending. These experimental results, obtained for well characterized nanostructured surface and CNT, could be used for more precise simulation of the mechanical and tribological behavior of nanotubes.

References

[1] Iijima S., Nature (London) **354**, 56 (1991)

[2] Collins P.G., Bando H. and Zettl A., Nanotechnology **9**, 153 (1998)

[3] Dai H., Franklin N. and Han J., Appl. Phys. Lett. **73**, 1508 (1998)

[4] Yu M-F., Files B.S., Arepalli S. and Ruoff R.S., Phys. Rev. Lett. **84**, 5552 (2000)

[5] Hertel T., Martel R. and Avouris P., J. Phys. Chem. B **102**, 910 (1998)

[6] Tombler T.W., Zhou C., Alexeyev L., Kong J., Dai H., Liu L., Jayanthi C.S., Tang M. and Wu S-H., Nature **405**, 769 (2000)

[7] S. Decossas, L. Patrone, A. M. Bonnot, F. Comin, M. Derivaz, A. Barski, and J. Chevrier, submitted to *Phys. Rev. Lett.*

[8] S. Decossas, L. Patrone, C. Guillemot, F. Comin, and J. Chevrier, submitted to *Tribo. Lett.*

[9] Bonnot A.M., Séméria M.N., Boronat J.F., Fournier T. and Pontonnier L., Diamond and Related Materials **9** (2000) 852-855

[10] Digital Instrument, Inc., 6780 Cortone Drive, Santa Barbara, CA 93117

[11] Barski A., Derivaz M., Rouvière J.L. and Buttard D., Appl. Phys. Lett. **77**, 3541 (2000)

[12] Decossas S., Cappello G., Poignant G., Patrone L., Bonnot A.M., Comin F. and Chevrier J., Europhys. Lett., **53** (6), pp. 742-748 (2001)

[13] Landau L.D. and Lifschitz E.M., *Course of theoretical physics Theory of elasticity Vol. 7*, Pergamon Press Oxford (1986)

[14] $I = \pi(D_2 - D_1)^4 / 64$ where D_2 and D_1 are respectively the external and internal diameter of the CNT estimated from TEM measurement to be around 25nm and 10nm. We used $E = 1$TPa and $R_0 = \infty$. R, the local radius of curvature of the bent CNT is chosen to be constant and equal to 675 nm (that is the radius of curvature of a Ge dot). The distance z along which the nanotube is bent is calculated to be around 515 nm.

[15] $U = F_{lat} \times d$. F_{lat} is the lateral force and d is the displacement of the tip (equal to 50nm, the height of the dot).

Physical Interactions of Carbon Nanotubes and Conjugated Polymers

A.B. Dalton[1], B. McCarthy[2], JN Coleman[2], M in het Panhuis[2,] D. L. Carroll[3], R. Czerw[3,] W.J. Blau[2], H.J. Byrne[1]

[1]FOCAS/School of Physics, Dublin Institute of Technology, Dublin 08, Ireland
[2] *Physics Department, Trinity College Dublin, Dublin 2, Ireland*
[3] *Department of Physics and Astronomy, Clemson University, South Carolina, USA*

ABSTRACT

Single walled carbon nanotubes are shown to interact with a conjugated polymer in a periodic manner. Here this interaction is probed using electron microscopy, scanning tunneling microscopy optical and vibrational spectroscopy. The spectroscopic behaviour of the polymer is seen to be dramatically affected, which is attributed to conformational changes due to the effect of the nanotubes.

INTRODUCTION

Since the discovery of carbon nanotubes in 1991[1], researchers have envisaged potential applications such as nanoscale electronic circuits and the construction of complex carbon-based nano-machines. Thus, the assembly of basic building blocks of complex nano-architectures, such as conjugated polymers and nanotubes, has been a driving goal of much of the nano-science community. A first step toward realizing this goal may be the attachment to, or modification by carbon nanotubes of structures such as polymers. This leads to the possibility of assembling individual polymer molecules onto carbon nanotubes with the net effect being the modification of the polymer's electronic properties and structure in a predictable way. To accomplish this, clearly, a more detailed understanding of the interactions between conjugated polymers and carbon nanotubes must be sought. In this work, we describe the assembly of the polymer, poly(m-phenylenevinylene-co-2,5-dioctoxy-p-phenylenevinylene), (PmPV), into a coating around single walled carbon nanotubes, (SWNT). Electron microscopy, scanning tunneling microscopy and Raman spectroscopy indicate that the polymer backbone interacts with the lattice of the nanotubes. This results in pronounced alterations to the fluorescence and absorption characteristics. This is explained as a reduction in electron delocalisation due to the affected polymer conformation, and also a dilution of aggregation effects.

EXPERIMENTAL

Synthesis of the polymer has been described previously[2]. Notable about this polymer are the dioctyloxy sidegroups, which impose a linear, exposed structure onto the PmPV backbone thus allowing significant interaction with the lattice of nanotubes. SWNT were produced in a generator using the arc discharge technique[3]. Composite preparation is relatively simple; SWNT are added to a solution (typically in this case 1g/L) of PmPV in toluene. Nanotube aggregates are broken up by briefly exposing the composite solution to a high power sonic tip (3 minutes), and then sonicating for several hours in a low power sonic bath. Due to the strong tendency of SWNT to aggregate, relatively low mass fractions of SWNT to PmPV can be

achieved (typically 2-3%). In this case, to achieve as high a SWNT concentration as possible, a greater than saturation (~20% SWNT) solution was prepared. After sonication, this was allowed to stand for several days, after which the majority of the SWNT had aggregated. The unaggregated PmPV/SWNT supernatant was pipetted off, and this was used in spectroscopic measurements. Absorption measurements were performed with films spuncoat onto Spectrosil B disks. Fluourescence measurements were performed in solution. TEM (Hitachi H7000) samples were prepared by dipping copper grids into this solution.

RESULTS

Figure 1 shows a TEM micrograph of the composite. It should be noted that there is very little free polymer present, as it is mostly bound to the SWNTs. It is also evident that the SWNTs are well dispersed within the system. Figure 1b shows a magnified view of figure 1a (contrast has been enhanced for clarity). A SWNT rope can clearly be seen at the centre of the large strands present. The diameter of these strands is approximately 120 nm with the central core being approximately 4nm. This suggests a reasonably strong interaction between the SWNTs and the PmPV, given the large relative weight of PmPV that each SWNT supports. This may be beneficial for mechanical reinforcement of polymeric materials. Given the diameter of the central region, these cannot be individual coated SWNT, but are small ropes. Figure 1c shows a magnified view of nanotube with an apparent ordered cylindrical coating of the polymer. This has been previously attributed to an individual SWNT with the PmPV mapping on the tube lattice in a structured way.

Figure 1. shows a wide area view of the composite. Note the absence of free polymer, which differs from other composites of lower mass fraction. Top right micrograoh is a contrast enhanced magnified view, so the SWNT ropes within can be clearly seen. (arrows point to these SWNT cores). Lower left micrograph shows the structured periodic wrapping visible in some cases.

Raman scattering is a powerful technique to probe the structure-property relationship in both carbon nanotubes and conjugated polymers. In figure 2, the high frequency region of the PmPV spectrum is compared to that of the composite for an excitation wavelength of 676 nm.

For completeness, the spectrum of nanotube powder is also shown. In this region, the so-called G-line feature centered at 1580 cm^{-1} dominates the nanotube spectrum. This group of modes corresponds to splitting of the optical phonon, the E_{2g} mode in graphite, into longitudinal components at high energies and transverse ones at lower energies. The apparent broadening on the low frequency side has been attributed to both metallic and semiconducting nanotubes being resonant at this excitation energy[4].

In this region, the spectrum of the polymer is dominated by a multiplet of modes centered on 1600 cm^{-1}. The spectrum is fitted by searching the minimum number of frequencies that fitted the different Raman bands equally well without fixing the positions and the widths of the individual peaks. The band at 1627 cm^{-1} can be attributed mainly to the vinyl group A_g mode (stretching of C=C bond)[5, 6]. The other bands may be attributed mainly to the phenyl group A_g mode (stretching of C-C bond). There is also a number of features centred at 1300 cm^{-1}. In PPV, the main band at 1330 cm^{-1} has been assigned to a vibration associated with the vinyl bond. In the composite, the introduction of nanotubes causes a number of modifications to the spectrum. The broad band at 1627 cm^{-1} appears to evolve into two well-defined features. There also appear to be modifications to the relative intensities of the modes at 1610 cm^{-1} and 1590 cm^{-1}. This change manifests itself as the 1590 cm^{-1} band becoming dominant. These changes are more than just a superposition of modes due to the different species, indicating that the vibrational structure of the polymer is being altered. These observations agree well with the observations of polymer wrapping witnessed in the micrographs of figure 1.
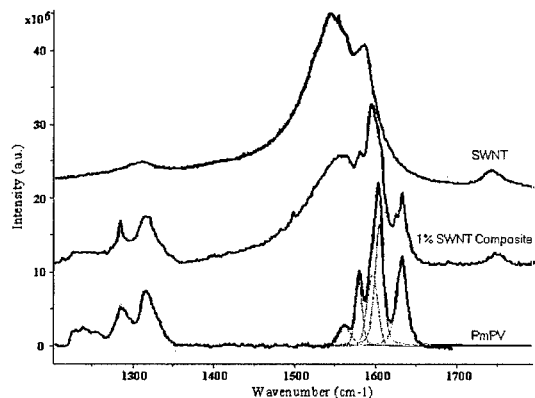
Figure 2. Raman Spectra of the high frequency region of the PmPV spectrum compared to the composite. (Excitation wavelength of 676 nm).

Scanning Tunneling Microscopy (STM) images give strong evidence for such an interaction. When the PmPV-SWNT solution is cast on highly oriented pyrolytic graphite (HOPG) an array of these wrapped structures can be observed using tunneling microscopy. The wrapped nature of two of the tubes can clearly be seen in the STM micrograph of Figure 3. Notice that again, the SWNT on the right appears to have an order to its wrapping while the SWNT on the left has no apparent structure to it. Generally, both types of coatings are found with the ordered being less common. Cross-sections of the STM image suggest that the height/width of these objects is in

agreement with that expected from a 1.2 nm − 1.4 nm SWNT coated with this coiled polymer. To confirm that a SWNT is inside the polymer coating, the tunneling spectra from the tubes is also shown and compares them with the spectra of an amorphous PmPV film on HOPG and pure HOPG itself. The tunneling spectra are collected by placing the STM tip over the object, disengaging the feedback, ramping the voltage and collecting the current. The resulting I-V spectrum reflects the electronic structure of the object. These tunneling spectra are presented as differential conductivity dI/dV (nA/V) and represent the local electronic density of states (LDOS) of the material. In the -1.0eV to 1.0 eV energy range, the clean HOPG surface yields a parabolic LDOS as expected. The amorphous film of PmPV also exhibits a relatively featureless LDOS in this energy range [7], bar a noticeable feature at 0.8eV, believed to be due to tunneling via a localized polaronic state [8]. This is because the band-gap of this polymer is approximately 3.1 eV and electrons tunnel across the polymer region into the HOPG substrate below with little scattering. The LDOS of the wrapped nanotubes, however, are quite different showing sharp, regularly spaced features. These features appear to be the van Hove singularities of the underlying SWNT as reported for clean SWNT by several groups [9,10].
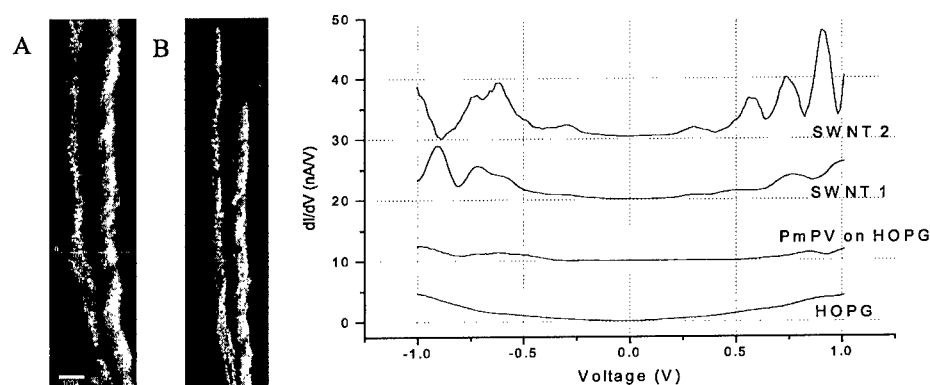
Figure 3. (Left)STM image of two polymer wrapped SWNT lying on HOPG. STM parameters were an applied voltage of 200meV, and a tunneling current of 10s of picoAmps. Line marked A denotes position at which cross-section is taken. STM used was an RHK Technologies operating in UHV (<10⁻⁹ Torr)). Films were imaged using mechanically formed Pt-Ir tips. B) The tips of the two nanotubes shown in A). (Right) Electronic Structure of the nanotubes shown in A). Curves are each offset by 10 nA/V from previous for clarity. For comparison the electronic structure of the HOPG substrate and a PmPV film lying on HOPG are shown

Figure 4 shows a comparison of the absorption spectrum for PmPV and the composite. For comparison, the spectrum of raw SWNT powder is also shown. The pristine polymer and composite spectra are normalized to the lowest energy peak near 3eV. For the polymer, this has been assigned to a transition associated with a state delocalised along the polymer backbone[11] (^1B_u exciton). The feature at 3.7 eV may be due to the effects of broken charge conjugation symmetry similar to that seen in other PPV derivatives[12]. There are three poorly resolved

features in the higher energy region (4.5 eV). These are due to localized excitations on the phenyl rings.
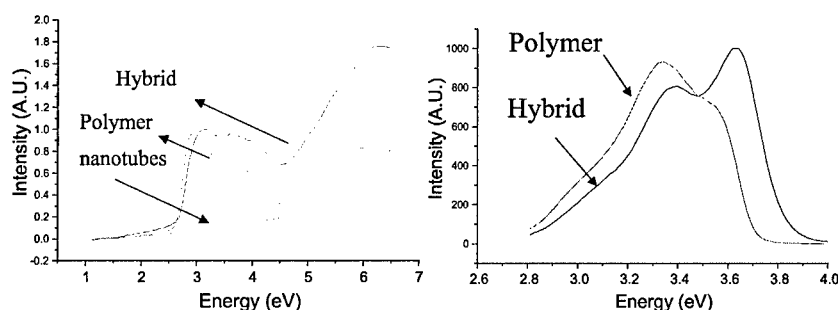
Figure 4. (Left)Absorption Spectrum of the SWNT/PmPV Composite, with PmPV and SWNT for reference. (right) Fluorescence Spectrum (Excitation wavelength of 340nm) of the SWNT/PmPV Composite and PmPV.

When comparing the absorption of the composite to the pristine polymer, it is immediately noticeable that there are many dramatic differences. The low energy peak has blue-shifted from 3 eV in the polymer to 3.15 eV in the composite. One possible explanation for this is that there is a substantial reduction in electron delocalisation along the backbone due to the conformational relaxation of the polymer around the nanotube lattice. This has previously been hypothesized by Ago *et al* [13]. Another explanation for this apparent blue-shift may be that the presence of the nanotubes are hindering the formation of inter-strand species such as aggregates which have been shown to play a large role in the photophysics of this polymer[14]. Aggregation is a result of weak inter-chain interactions. In dilute solutions, the individual strands are isolated and these interactions can therefore be neglected. In the solid, the distances between the polymer chains become appreciably smaller and these inter-chain forces become more significant. In the absorption spectrum, this manifests with the emergence of a markedly red-shifted feature in the solid state compared to the solution. Upon introduction of nanotubes, the peak at 3.7 eV broadens with the evolution of two features at 3,64 eV and 4.0 eV respectively. The relative absorbance of these features has also increased markedly becoming as intense as the peak at 3 eV, unlike PmPV where the corresponding peak is approximately 75 % of the main peak intensity. As this is due to broken charge conjugation symmetry in PmPV, it suggests that the symmetry is further broken due to the presence of SWNTs and the associated effects this has on the conformation of the polymer. There is also less noticeable structure in the high-energy region, but relatively stronger absorption. This suggests that the dominant absorption in the composite shifts to the phenyl ring of the PmPV.

Also shown in figure 4 is the fluorescence spectrum of the composite compared to the pristine polymer for an excitation energy of 3.63eV (340 nm). Similar to absorption, the presence of nanotubes dramatically effects the polymers emission spectrum. The polymer has broad emission centered in the green with a main vibronic feature at 2.58eV (480 nm) and a strong shoulder at 2.75eV (450 nm). In the composite, there is an overall red shift in the spectrum with the dominant feature centered at 2.78eV (445 nm) and a second peak at 2.61eV (475 nm). These

effects agree well with the modifications to the absorption spectra with the nanotubes acting to reduce electron delocalisation. Additionally, the aggregation effects are also diluted.

CONCLUSIONS

Our results show that it is possible to assemble polymer strands onto single walled carbon nanotubes using mechanical agitation and constitutes the first visual confirmation of such assembly. Further, we suggest that such wrapping results in the alteration of the polymer's electronic structure, as evidenced in the modified optical spectra of the bound polymer. This may well represent a previously unconsidered route to polymer-nanotube assembly for molecular scale electronics.

ACKNOWLEDGEMENTS

[1] S. Iijima, *Nature*, **56** (1991) 354.

[2] W. Holzer, A. Penzkofer, S. H. Gong, A. Bleyer and D. D. C. Bradley, Adv. Mat. 8, (1996) 974.

[3] C. Journet, W.K Maser, P. Bernier, A. Loiseau, M.L. de la Chapelle, S. Lefrant, P. Deniard, R. Lee, J.E. Fischer, Nature, 388 (1997) 756.

[4] H. Kataura, Y. Kumazawa, Y. Mainwa, I. Umezu, S. Suzuki, Y. Ohtsuka, Y. Achiba, Synth. Met., 103 (1999) 2555.

[5] A. Sakamoto, Y. Furukawa, M. Tasumi, J. Phys. Chem., 96, (1992) 1490.

[6] S. Lefrant, E. Perrin, J.P. Buisson, H. Eckhardt, C.C. Han, Synth. Met., 29, (1989) E91.

[7] McCarthy B, Czerw R, Strevens A, Davey AP, Carroll DL, Blau WJ, MRS Proceedings, Boston, Fall (1999)

[8] Lane PA, Wei X, Vardeny ZV, *Phys. Rev. Lett.* **77** (1996) 1544.

[9] Wildöer JWG, Venema LC, Rinzler AG, Smalley RE, Dekker C, *Nature* **391** (1998) 59.

[10] Odom TW, Huang J, Kim P, Lieber CM, *Nature* **391**(1998) 62.

[11] H. Mellor, A. Bleyer, D.D.C. Bradley, P.A. Lane, S. J. Martin, F. Rohlfing, A. Tajbakhsh, SPIE, 3145, 382.

[12] Y.N. Gartstein, M.J. Rice, E.M. Conwell, Phys. Rev. B, 51, (1995) 5546.

[13] H. Ago, M.S.P. Schaffer, D.S. Ginger, A.H. Windle, R.H. Friend, Phys. Rev. B, 61, (2000) 2286.

[14] A.B. Dalton, J.N. Coleman, M. in het Panhuis, B. McCarthy, A. Drury, W.J. Blau, B.Paci, J.-M. Nunzi, H.J. Byrne, J. Photochem. Photobiology A 5678 (2001) 1.

CHEMICAL BONDING OF POLYMER ON CARBON NANOTUBE

Chengyu Wei, Kyeongjae Cho, Department of Mechanical Engineering, Stanford University, California; Deepak Srivastava, NASA Ames Research Center, MST27A-1, Moffett Field, California

ABSTRACT

Recently, carbon nanotubes are considered as nanoscale fibers, which can strengthen polymer composite materials. Nanotube-polymer composite materials can be used for micron scale devices with designed mechanical properties and smart polymer coating to protect materials under extreme physical conditions such as microsatellites. To explore these possibilities it is important to develop a detailed atomic scale understanding of the mechanical coupling between polymer matrix and embedded nanotubes. In this work we study the chemical bonding between polymer molecules and carbon nanotubes (CNTs) using molecular dynamics. Study shows that the bonding between polyethylene and a CNT is energetically favorable. Chemical bonds can be formed at multiple sites, which make the mechanical load transfer from the polymer chain to the tube more favorable. We will discuss about the resulting mechanical coupling between the CNTs and polymer matrix to develop efficient nano-composite materials.

INTRODUCTION

Because of their unusual mechanical [1,2] and electronic properties [3,4], there are extensive studies on carbon nanotube (CNT) as a nano-fiber to improve the performance of a matrix or to achieve new properties [5-8]. One distinguished property of a CNT is its high strength, coming from the strong sp^2 bonds, which makes CNTs good candidates as reinforcement fibers to matrix. The other advantage of a CNT as a fiber is its large surface area, which is good for chemical bonding or adhesion, an important factor for a good composite. One essential issue in the reinforcement of a fiber composite material is that the embedded fibers must have large enough aspect ratio so that there is enough load transfer through the interfacial shear stress and consequently the full strength of the fiber can be used. For a micrometer long CNT with diameter in nano-meter scale, the aspect ratio can be 1000 or higher, which is much larger than usual common fibers. There are experiments using TEM to investigate CNTs (both multi-walled and single-walled CNTs) as reinforcement fibers in polymer matrix [6,8]. Although people found load transfers exist between CNTs and polymer matrix with cases of showing signs of quite large load transfers in some polymer-CNT composites [9], which suggest possible chemical bonding between CNTs and polymers, it is not clear what is the mechanism of the load transfer. It is thus important to understand the mechanism of load transfers at atomic level to facilitate the development of high performance CNT-polymer composites.

MOLECULAR DYNAMICS SIMULATIONS

When chemical bonding is present, the interfacial shear energy between a fiber and a matrix is typically in range of 50 to $300J/m^2$ [10]. If only Van der Waals interactions are

Table I: MD simulations of chemical bonding of hydrogen atom on several carbon systems using Tersoff-Brenner potential compared with DFT calculations [12].

Hydrogen @		C_{60}	CNT(10,0)	Graphite
Bond Energy(eV)	TB potential	-3.68	-3.00	-2.29
	DFT	-3.18	-2.39	-1.63
Bond Length(Å)	TB potential	1.085	1.087	1.092
	DFT	1.115	1.127	1.142

present, such shear energy will be in range of 50 to 350mJ/m^2 [11]. Consequently strong chemical bonding is expected to be important for high performance of fiber composites. In this work, we will study the possibility of the chemical bonding between CNTs and polymer matrix to improve the load transfers at the interfaces.

We use molecular dynamics simulation to study the CNT-polymer system. Tersoff-Brenner potential [13, 14] is used for the carbon-carbon and hydrocarbon interactions. This potential is parameterized from the structure of graphite, diamond and several hydrocarbon systems and has been used in several simulations to study the mechanical properties of carbon nanotubes [15,16]. In Brenner's original paper, the hydrogen absorption on a diamond surface was studied using this potential [14].

Before investigating the chemical bonding between CNTs and polymers, we first test the accuracy of Tersoff-Brenner potential for the bonding of hydrogen atom on several carbon systems. In Table I, the bonding energies and C-H bond lengths of hydrogen atom on C_{60}, CNT (10,0) and graphite, are listed; and compared with the results from density functional theory (DFT) calculations [12]. DFT is considered to give more accurate description of interactions. The comparison in the table shows that the bond energies and bond lengths determined by Tersoff-Brenner potential are in good agreement with the DFT results. For both cases, the chemical bond of Hydrogen on C_{60} is found to have the largest bonding energy and shortest bond length because of the high chemical reactivity induced by the higher curvature of the local carbon-bonding configuration of C_{60}.

We now proceed to study the chemical bonding between polymers and CNTs. Polyethylene (a linear chain polymer) and CNT (10,0) are chosen for our simulations. We found polyethylene can be chemically bonded to the CNT, shown in Figure 1.
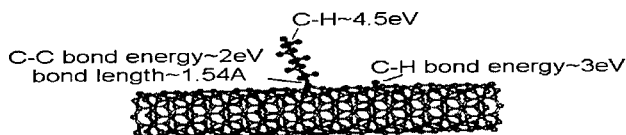
Figure 1: Chemical bonding of polyethylene on CNT (10,0)

With one hydrogen atom removed and bonded to the CNT with energy 3eV, polyethylene can form sp^3 bond with a π orbital on the CNT surface. Our MD simulation shows that the C-C bond energy between the polymer chain and the CNT is 2.0 eV, and that the bond length is 1.54 Å, which is close to the bond length of C-C in the polyethylene.

It is expected that the load transfer from polymer matrix to a CNT can be enhanced with the presence of such chemical bonding. Furthermore, the load transfer is expected to increase for more than one bond attached to the CNT. More loads can be carried over by polymer chains to larger section of the CNT surface, and the larger strain energy can then be distributed over the nanotube. In this way, the multi-site bonds can act together in response to an applied mechanical load.

We use MD simulation to study whether a multi-site bonding will increase the load transfers from polymers to CNTs. Mechanical loads to a polymer chain are applied in two cases: single site bonding (Figure 2a) and double site bonding (Figure 2b). The detailed mechanical deformations of the C-C bonds within the polymer chain and at the polymer-CNT interface in response to the external load are plotted in Figure 3a and Figure 3b for both cases.

Figure 3 shows that in both cases the C-C bond within the polymer reaches its maximum deformation (i.e. the largest C-C bond length before breaking the bond) first, followed by the C-C bond at the polymer-CNT interface. The difference in the case of single site bonding and double site bonding is that in the later case, the two C-C bonds at the interface of the polymer and the CNT induce more rigid response to the mechanical load. After the C-C bonds reach their maximum deformations, mechanical loads are
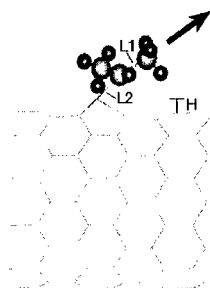
Figure 2a: single site bonding   **Figure 2b:** Double site bonding
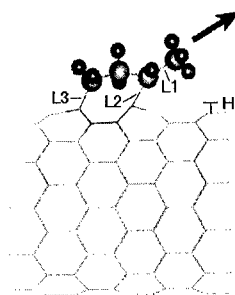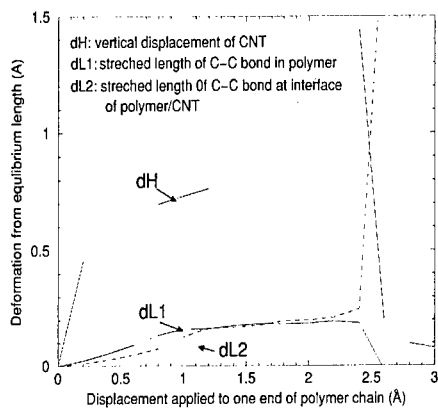
Figure 3a: single site bonding
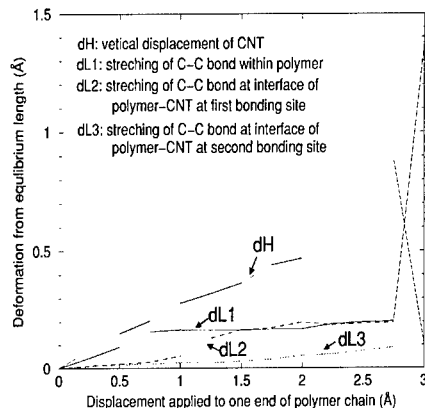
Figure 3b: double site bonding
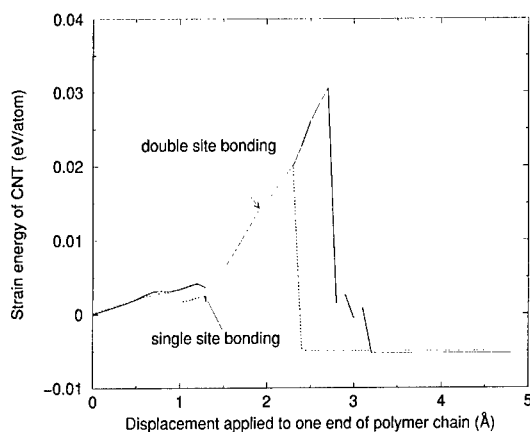
Figure 4: Strain energy transferred to CNT by mechanical loading process

continuously transferred to the CNT until bonds are broken either at the polymer-CNT interface or within the polymer chain. In Figure 4, the strain energy transferred to the CNT as a function of the mechanical loading is plotted for both cases. It is clear that more loads are transferred in the case of double site bonding, and that the CNT-polymer interface accommodates a higher shear strain.

CONCLUSIONS

In this work, we used classical molecular dynamics with Tersoff-Brenner potential to

study the chemical bonding between polymers and carbon nanotubes. We found that it is energetically favorable for polyethylene to form chemical bonding with a CNT with bond energy about 2eV. The load transfer test using MD simulations shows that a multiple-site bonding is more favorable for load transfers.

REFERENCES

[1] M. M. J. Treacy, T. W. Ebbesen and J. M. Giblson, *Nature* **381**, 678 (1996).
[2] O. Lourie, D. M. Cox and H. D. Wagner, *Phys. Rev. Lett.* **81**, 1638 (1998).
[3] R. Satio, M. Fujita, G. Dresselhaus and M. S. Dresselhaus, *Phys. Rev. B* **46**, 1804 (1992).
[4] L. Langer et. al. *Phys. Rev. Lett.* **76**, 479 (1996).
[5] L. S. Schadler, S. C. Giannaris and P. M. Ajayan, *App. Phys. Lett.* **73**, 3842 (1998).
[6] R. Andrews et. al., *App. Phys. Lett.* **75**, 1329 (1999).
[7] P. M. Ajayan, L. S. Schadler, C. Giannaris and A. Rubio, Advanced Materials **12**, 750 (2000).
[8] D. Qian, E. C. Dickey, R. Andrews and T. Rantell, *App. Phys. Lett.* **76**, 2868 (2000).
[9] H. D. Wanger, O. Louire, Y.Feldman and R. Tenne, *Appl. Phys. Lett.* **72**, 188 (1998).
[10] A. T. DiBenedetto, *Compos. Sci. Technol.* **42**, 103 (1991).
[11] M. Nardin and J. Schultz, *J. Mater. Sci. Lett.* **12**, 1245 (1993).
[12] Seongjun Park, Deepak Srivastava and Kyeongjae Cho (unpublished).
[13] J. Tersoff, *Phys. Rev. B* **37**, 6991 (1988).
[14] D. W. Brenner, *Phys. Rev. B* **42**, 9458 (1990).
[15] B. I. Yakobson, C. J. Brabec and J. Bernholc, *Phys. Rev. Lett.* **76**, 2511 (1996).
[16] M. B. Nardelli, B. I. Yakobson and J. Berholc, *Phys. Rev. Lett.* **81**, 4656 (1998).

Ab initio Study of Metal Atoms on SWNT Surface

Shu Peng and Kyeongjae Cho
Department of Mechanical Engineering, Stanford University, Stanford, CA 94305, USA

ABSTRACT

Interactions of metal atoms (Al, Ti) with semiconducting single walled carbon nanotube (SWNT) are investigated using first-principles pseudopotential calculations. Six different adsorption configurations for aluminum and titanium atoms are studied. Comparison of the energetics of these metal atoms on (8,0) SWNT surface shows significant differences in binding energy and diffusion barrier. These differences give an insight to explain why most of metal atoms (such as Al) form discrete particles on nanotube while continuous nanowires are obtained by using titanium in the experiment.

INTRODUCTION

Carbon nanotubes [1] have induced great research interests due to their unusual physical, chemical and mechanical properties [2-5]. These unique properties make them an ideal candidate for the building blocks of molecular scale machines and nanoelectronic devices [6-9]. One of the proposed applications is to use carbon nanotubes as templates to obtain a variety of nanowire materials [10]. Both experimental and theoretical studies of metal-nanotube systems are necessary to achieve metal nanowires using nanotubes [11, 12].

Recently, it has been reported that metal nanowires can be formed by coating various metals on suspended single walled carbon naotubes (SWNT) using electron beam evaporation [13,14]. Many types of metal atoms (such as Au, Al, Fe) form discrete isolated particles on nanotubes while Ti coating on the suspended tubes are continuous. Other metals can also form continuous nanowires by depositing metal atoms (Au, Al, Fe, etc) on the first coated buffer layer (or adhesion layer) of Ti nanotube nanowire. The experiments show that different metal atoms have different binding characters on the nanotube surface that correspond to different macroscopic coating phenomena. These experimental results suggest that structural and chemical characteristics of metal-tube systems are sensitive to the identity of metal atoms and motivate a detailed theoretical study to investigate the interactions between nanotubes and various metal atoms.

Although the interactions between deposited metal atoms with graphite (or graphene sheet) and C_{60} have been extensively studied [15,16], a detailed theoretical account for the interactions between various metals and nanotubes is currently lacking. The interactions of metal atoms with SWNTs offer another challenging problem since the characteristics of these interactions would be quite different from graphene sheet and C_{60}. This is because SWNTs are quasi-one dimensional, and this confined geometry makes the chemistry of SWNTs significantly different from those of two dimensional graphene sheet and finite molecule C_{60}. Nanotubes are different from graphite or graphene sheet because nanotubes have curved geometry that induces rehybridization of carbon bonding orbitals (non-planar sp^2 bonding configuration) [17,18]. These different bonding character and geometry have lead to significantly different nanotube electronic structure from that of graphite or graphene sheet. On the other hand, C_{60} is a finite

molecule, and has pentagons in its structure whereas the sidewall of a nanotube normally contains only hexagons. Consequently, C_{60}'s carbon bonding orbitals have more sp^3 like bonding character which induces much more reactive binding affinity with metal atoms than SWNTs.

Recent tight-binding study of Ni atoms on the armchair SWNTs [19] has addressed an important issue of curvature effect that the interactions of metal atoms with a nanotube is quite different from those with graphene sheet in terms of binding energy, binding character, and charge transfer. Another important issue of why some of metal atoms (Au, Al, Fe, etc) form discrete particles on nanotubes while Ti atoms form continuous nanowire coating is still calling for a detailed theoretical investigation. This paper presents results of first-principle pseudopotential calculations for two representative metal atoms (Al and Ti) interacting with (8,0) semiconducting SWNT. Six different adsorption configurations have been studied. The calculated binding energies, diffusion barriers and diffusion rates shed a light on why Ti atoms form continuous nanowires while Al atoms form isolated discrete particles.

SIMULATION METHOD

In order to obtain a detailed understanding of the metal nanotube interaction and metal coating behavior, first principles calculations are performed with the DFT++ program [20] using density functional theory (DFT) within the local density approximation (LDA) [21] for two representative systems of Al atom and Ti atom on (8,0) SWNT. Kohn-Sham single –electron wave functions are expanded by efficient plane waves in the supercell $12\times12\times4.29\text{Å}^3$ with 40 Rydberg cutoff energy. The Brillouin zone sampling is approximated by six k-points along the tube axis, which is shown to a good approximation for (8,0) and (10,0) nanotubes [22,23]. The structure of an isolated (8,0) SWNT is optimized by fully relaxing the tube structure to the minimum total energy configuration. This relaxed configuration is used for the rest of the simulations. Calculations for the Al-SWNT and Ti-SWNT systems are carried out by relaxing the position of a metal atom on the tube surface with a constraint of maintaining its relative position on a hexagon as shown in figure 1. Carbon atoms near the metal atom are also fully relaxed with the remnant forces of less than 0.1 eV/Å. For these calculations, the error bar of ± 0.05 eV was estimated for relative energy differences.

RESULTS AND DISCUSSION

To investigate and carefully study the interactions of single metal atoms (Al and Ti) with (8,0) SWNT, six distinct sites are considered for a single metal atom adsorption on the nanotube surface. Figure 1 shows schematic diagrams of six different adsorption sites for a metal atom (Al or Ti) on the (8,0) SWNT. These six sites in figure 1 are described as follows. (1) A metal atom directly above a C atom is called as Direct Top Site (DT). (2) A metal atom over a C-C bond at a distance of one quarter of C-C bond length is called Bond Quarter Site (BQ). (3) A metal atom over a C-C bond at the middle of C-C bond length is called Bond Middle Site (BM). (4) A metal atom above the long diagonal of a hexagon (Path 2 in Fig. 2) at one quarter of the diagonal length (which is twice of C-C bond length) is called Hexagon Quarter 1 Site (HQ1). (5) A metal atom above the short diagonal of a C-C hexagon (Path 3) at one quarter of the diagonal length

(which is $\sqrt{3}$ of C-C bond length) is called Hexagon Quarter 2 Site (HQ2). (6) A metal atom directly above the center of a hexagon is called Hexagon Center Site (HC).

DT   BQ   BM

HQ1   HQ2   HC
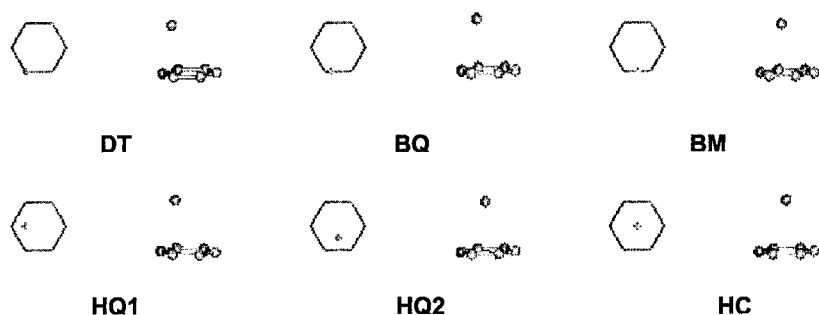
Fig. 1. Schematic diagram of six different configurations of a single metal atom on the (8,0) SWNT surface.

These six distinct sites of a metal atom on the nanotube surface described in figure 1 give three possible diffusion paths for a metal atom to follow on the surface. A schematic diagram of these three diffusion paths is shown in figure 2. Path 1 describes a metal atom diffusion along the C-C bond. Path 2 shows that a metal atom jumps from the top of a carbon atom into the center of hexagon and jumps on top of another carbon atom. Finally, path 3 shows a metal atom diffusion from the center of a C-C bond into the center of hexagon and to another BM site. Six distinct bonding sites combined with three different diffusion paths also describe the rest of the hexagon through symmetry and consequently provide a clear picture of how a single metal atom (Al or Ti) interacts with nanotube not only from the energy point of view but also from kinetics point of view.
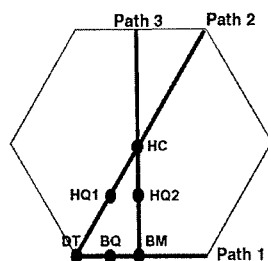
Fig. 2. Schematic diagram of three different diffusion paths representing possible paths for a metal atom to follow on the surface of a nanotube.

The calculated binding energies and binding distances for these six different binding sites are summarized in the Table 1. Table 1 shows that the metal atom over the center of a hexagon ring is the most stable binding site for both Al atom and Ti atom. The quantitative results of the binding energy and binding distance between these two metal atoms (Al and Ti) and (8,0) SWNT clearly show that the binding energy for Ti atom (2.27 ± 0.05 eV) is significantly larger than that of Al atom (1.25 ± 0.05 eV). This result is consistent with the experiment [13] where Ti atoms deposited on nanotubes exhibit the higher condensation and sticking coefficient than other metal atoms including Al atom.

Table 1. Summary of the binding energy and binding distance for Al or Ti single atom on (8,0) nanotube surface at six different locations.

Bonding Location		Binding Energy (eV) (± 0.05 eV)	Binding Distance (Å)
Al-SWNT (8,0)	Direct Top Site (DT)	-1.13	2.21
	Bond Quarter Site (BQ)	-1.17	2.17
	Bond Middle Site (BM)	-1.20	2.14
	Hexagon Quarter 1 Site (HQ1)	-1.12	2.01
	Hexagon Quarter 2 Site (HQ2)	-1.20	1.93
	Hexagon Center Site (HC)	-1.25	1.82
Ti-SWNT (8,0)	Direct Top Site (DT)	-1.63	1.97
	Bond Quarter Site (BQ)	-1.81	2.00
	Bond Middle Site (BM)	-1.87	1.98
	Hexagon Quarter 1 Site (HQ1)	-1.93	1.83
	Hexagon Quarter 2 Site (HQ2)	-1.97	2.15
	Hexagon Center Site (HC)	-2.27	1.63

Based on the quantitative result of the binding energies between metal atoms and the nanotubes, the metal atom diffusion barriers on the nanotube surface along three different paths are shown in figure 3. The result clearly indicates that path 3 in which metal atoms jump from one center of the carbon hexagon ring to a nearby hexagon center gives the lowest diffusion barrier as well as short diffusion length both for Al atom and Ti atom. It is worth to notice that Al atom shows very small energy diffusion barrier (~ 0.05 eV comparable to error bar) while Ti atom has a significant diffusion barrier (~ 0.4 eV). These different diffusion barriers allow Al atoms move around the nanotube surface much more rapidly than Ti atom since 0.05 eV is comparable to the thermal kinetic energy at room temperature. Using the transition state theory for a simple diffusion model, the kinetics of these metal diffusions on the nanotube surface can be quantitatively described. Since the diffusion frequency (Γ_{diff}) can be described by the equation $\Gamma_{diff} = \nu \exp(-\Delta E_d / k_B T)$, where ν is the attempt frequency that is 1.55×10^{12} sec^{-1} for Al and 2.84×10^{12} sec^{-1} for Ti respectively estimated from the energy curves in figure 3. ΔE_d is the diffusion energy barrier, and at T=300K, the calculated diffusion frequency for Al atom is

2.25×10^{11} sec^{-1} and that of Ti atom is only 5.57×10^{5} sec^{-1} which is 6 orders of magnitude smaller than Al atom case. These low activation barrier for diffusion and the corresponding high diffusion rate of Al atoms on (8,0) SWNT surface lead to rapid hopping of Al atoms. On the other hand, higher diffusion energy barrier and lower diffusion rate make Ti atoms stay in the middle of the hexagon ring much longer ($\sim 1\mu$ sec) before jumping to a neighboring site.
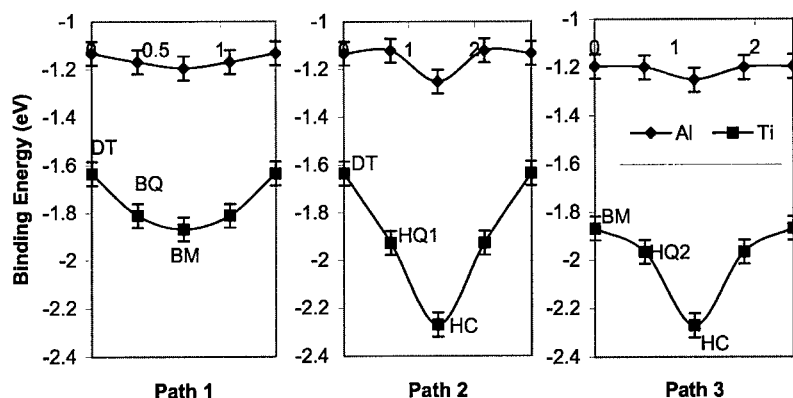
Fig. 3. Binding energy plots for Al and Ti metal atoms on the SWNT sidewall along three different diffusion paths. Error bars of $\pm$ 0.05 eV are also shown in the plots.

Combined with binding energy investigation and diffusion kinetics, the first step explanation of why Ti atoms form continuous coating while Al atoms form discrete isolated particles on the nanotube walls can be provided as follows. The weak Al-SWNT interaction due to small binding energy points to low cluster nucleation barrier. The low nucleation barrier and high diffusion rate for Al atoms cause them to easily form clusters through thermal activation processes. Since the cohesive energy of Al atom in bulk phase is 3.39 eV [24] (much higher than the Al-SWNT binding energy of 1.25 $\pm$ 0.05 eV), these Al atoms tend to form small cluster in a short time as they rapidly move on the nanotube walls and collide with each other. This mechanism qualitatively explains discrete isolated particles observed in the experiment [14]. On the contrary, Ti atoms tend form much stronger binding with nanotubes leading to high nucleation barrier and high sticking coefficient than other metals. When Ti atoms come onto the nanotube surface through electron beam evaporation, these Ti atoms will find the most favorable binding site (over the center of carbon hexagon ring). The chance of these Ti metal atoms to jump out of one site and diffuse into other location to collide with other metal atoms and to merge into a small cluster is very small (by factor of million) compared to other metal atoms. These Ti atoms stay long time at the centers of the carbon hexagon rings and uniformly cover the

nanotube surface. This qualitative argument explains why Ti coating on nanotubes is very uniform and continuous.

It is important to note the current analysis considers only single metal atom on the nanotube surface, and gives only the first step physical explanation of different coating phenomena appeared on the suspended nanotubes. The questions of what will happen when two metal atoms collide with each other and how small cluster will form for most of the metal atoms are still left for future theoretical investigations. The problem of cluster formation or continuous coating formation is under investigation now, and the results will be published later.

ACKNOWLEDGEMENTS

REFERENCES

[1] S. Iijima, Nature **354**, 56 (1991).
[2] M.R. Falvo, G.J. Clary, R.M. Taylor II, V. Chi, F.P. Brooks Jr, S. Washburn, and R. Superfine, Nature **389**, 582 (1997).
[3] M.M.J. Treacy, T.W. Ebbesen, and J.M. Gibson, Nature **389**, 678 (1996).
[4] E.W. Wong, P.E. Sheehan, and C.M. Lieber, Science **277**, 1971 (1997).
[5] J.C. Charlier and J.P. Issi, Appl. Phys. A **67**, 79 (1998).
[6] L. Chico, V.H. Crespi, L.X. Benedict, S.G. Louie, and M.L. Cohen, Phys. Rev. Lett. **76**, 971 (1996).
[7] J. Kong, N.R. Franklin, C. Zhou, M.G. Chapline, S. Peng, K. Cho, and H. Dai, Science **287**, 622 (2000).
[8] S.J. Tans, A. Verschueren, C. Dekker, Nature **393**, 49 (1998).
[9] R. Martel, T. Schmidt, H. Shea, T. Hertel, P. Avouris, Appl. Phys. Lett. **73**, 2447 (1998).
[10] S. Iijima and T. Ichihashi, Nature **363**, 603 (1993).
[11] H. Dai, E.W. Wong, Y.Z. Lu, S. Dan, C.M. Lieber, Nature **375**, 769 (1995).
[12] W.Q. Han, S.S. Fan, Q.Q. Li, Y.D. Hu, Science **277**, 1287 (1997).
[13] Y. Zhang, N.W. Franklin, R.J. Chen, H. Dai, Chem. Phys. Lett. **331**, 35 (2000).
[14] Y. Zhang and H. Dai, Appl. Phys. Lett. **77**, 3015 (2000).
[15] Q. Ma and R.A. Rosenberg, Phys. Rev. B **60**, 2827 (1999).
[16] T.R. Ohno, Y. Chen, S.E. Harvey, G.H. Kroll, P.J. Benning, J.H. Weaver, L.P.F. Chibante, and R.E. Smalley, Phys. Rev. B **47**, 2389 (1993).
[17] J.W. Mintmire, B.I. Dunlap, C.T. White, Phys. Rev. Lett. **68** (1992) 631.
[18] X. Blase, L.X. Benedict, E.L. Shirley, S.G. Louie, Phys. Rev. Lett. **72** 1878 (1994).
[19] M. Menon, A.N. Andriotis, G.E. Froudakis, Chem. Phys. Lett. **320** 425 (2000).
[20] S.I. Beigi, T.A. Arias, Computer Phys. Comm. **128**, 1 (2000) (Website, http://dft.mit.edu/dft++).
[21] M.C. Payne, M.P. Teter, D.C. Allan, T.A. Arias, and J.D. Joannopoulos, Rev. Mod. Phys. **64**, 1045 (1992).
[22] S. Peng and K. Cho, Nanotechnology, **11**, 57 (2000).
[23] D. Srivastava, M. Menon, and K. Cho, Phys. Rev. Lett. **83**, 2973 (1999).
[24] C. Kittel, Introduction to Solid State Physics, 7th ed, John Wiley & Sons, Inc., New York, Chichester, Brisbane, Toronto, Singapore, 1996.

Electrical Property of Vertically Grown Carbon Nanotube and Its Application to the Nanofunctional Devices

Jaeuk Chu*, Kwangseok Jeong*, Eunju Bae*, Inkyeong Yoo[†] and Wonbong Choi[†]
Materials and Devices Lab[†]., The National Program for Tera-Level Nanodevices* Samsung Advanced Institute of Technology, Suwon, Korea

Jujin Kim
Department of Physics, Chonbuk National University, Chonju 561-756, Korea

Corresponding Author : wbchoi@sait.samsung.co.kr, jkchu@sait.samsung.co.kr ☎ 82-31-280-9351

ABSTRACT

A highly ordered porous alumina array which hole size is decreased down to 20nm was fabricated by a two step anodization method. Carbon Nanotube was grown vertically with thermal CVD at 600~700℃. By using rapid thermal annealing method, low-ohmic contact was formed between multi wall nanotubes and metal electrode and its resistance shows tens to hundreds Ω. The alumina layer which is existed between nanotube and electrode acts as a barrier for conductance. The resistance of carbon nanotube shows the temperature(T^{-1}) dependence at 4.21K < T < 19.9K and semiconducting behavior at this temperature region.

INTRODUCTION

The 10 years of carbon nanotube (CNT) since the discovery of 1991[1] have been a marvelous period for CNT itself and scientists studying the various properties of CNT. The electrical property, especially, can be varied from semiconducting to metallic according to the CNT's diameter, chirallity and doping status.[2-4] Multi wall nanotube(MWNT) has a complicate structure rather than single wall nanotube(swnt) having a ideal one dimensional wire structure but has a merit to the easiness of synthesis and purification. The research for device using mwnt has been studied by many but the difficulties of reproducible high quality nanotube-control and selective nano-positioning to device tool remain as a barrier for advanced device. In order to overcome these barriers, CNT is grown selectively in anodic aluminum oxide(AAO) template[5] and is characterized electrical transport property. The feasibility of selectively grown CNT to the nano-functional device has been investigated

EXPERIMENTAL

Carbon nanotube arrays have been fabricated on porous anodic aluminum oxide (AAO) which is controlled by conventional anodization method.[5] High purity aluminum sheet (99.999%) was used as a substrate and highly ordered nano-pore was

a)   b)
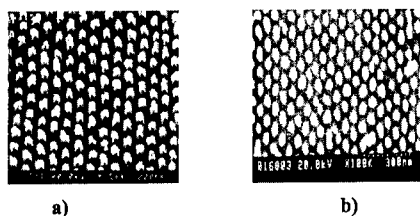
Figure 1. SEM images of carbon nanotube in porous alumina and schematic : (a) Top surface of 20nm nanotube after removing graphite layer. (b) the back side of nanotube on AAO after etching away the aluminum oxide with ion milling.

fabricated by anodization technique. Hole diameter is 20nm and fabricated by using sulfuric acid as a anodizing solution. Carbon nanotube was synthesized in the pores by thermal CVD at the temperature range of 600~700°C without catalyst. Figure 1 is scanning electron microscopy(SEM) images showing a both(top, bottom) view of the nanotube after etching the AAO template by ion milling. We carried out two probe conductance measurement of nanotube on AAO followed by metal electrode deposition in this experiment. Figure 2 shows the schematic of metal deposited test sample. The metal electrode is Au/Ti and the electrode shape is a circular type with the hole size of 70μm. The estimated number of holes in one circular electrode is around 6×10^6. The Ti was directly deposited on oxide face(bottom) of sample and Au/Ti was deposited on the top surface where graphite was removed. In this work, two types of test sample were prepared for measurement : one has aluminum oxide barrier layer at the bottom and the other has not. It is considered that the alumina layer influences conductance on each sample because the layer acts as a tunnel junction separating the nanotubes from metal electrode.

RESULTS AND DISCUSSION

I-V characterization of nanotube is shown in Figure 3 and 4. Figure 3 shows the IV measurement that was performed under the vacuum after rapid thermal annealing(RTA) at the range of 500~800°C. In case of Figure 3(a), the conductance(dI/dV) of sample having oxide layer is 1.77mS at 500°C RTA and increased 12mS at 800°C. This means that RTA plays a important role in increasing conductance by reducing contact resistance between metal electrode and nanotube. Sample (b) doesn't have an oxide layer and shows higher conductance than that of

Sample	Diameter	Surface condition
a	20nm	No Al$_2$O$_3$
b	20nm	Al$_2$O$_3$

Ti/Au

Ti

Anodic Alumina Oxide film(AAO)

Al$_2$O$_3$ layer

a)   b)
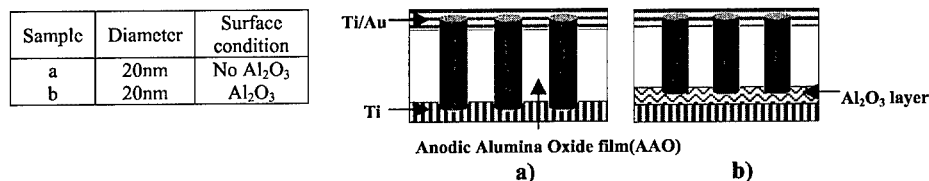
Figure 2. Table of sample types and schematic of test sample.
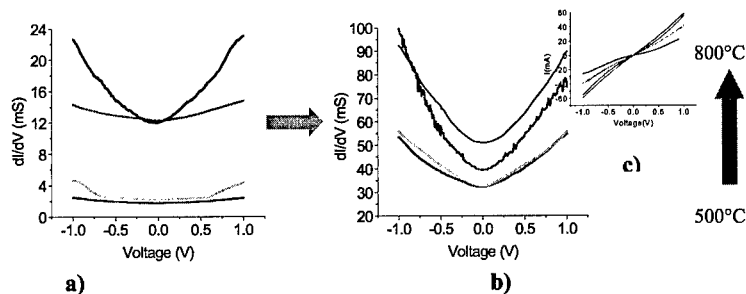
Figure 3. The conductance(dI/dV) change of nanotube due to the RTA. a) oxide layer sample b) no oxide layer sample. It shows that increased conductance value is due to the RTA and oxide barrier. c) The IV data of sample which is exposed at both side. It shows that higher current flow is increased as annealing temperature is increased

sample (a). The conductance difference is almost four times increment(50mS) when compared conductance at zero bias voltage. Zhang *et al* reported that the carbide layer begins to form at the carbon nanotube and Ti interface after above temperature(> 800°C).[6] They showed that the formation of a carbide layer is caused by the surface diffusion of metal atoms to the interface and the diffusion rate is very slow. The nanotube-carbide bulk hetero structures is made through metal atoms transfer into the nanotube by annealing for 20min and forms bulk junctions.[6] In our experiment the annealing time is relatively short (30sec) compared to the Zhang *et al*'s work and it could prevent forming bulk hetero-junctions. Therefore the short, low and rapid temperature annealing process enabled to make a better nanotube-metal(Ti) contact for electrical measurements. Figure 3(c) shows conductance comparison of sample (b) due to the RTA. The more increased annealing temperature, the conductance increased upto 60mA. Assuming the resistance of the contact and the nanotube to be R_c and R_{nt}, the total resistance(R_t) of sample (b) is given by $R_t = 2R_c + R_{nt}$ (R_c is the resistance between Ti and nanotube at both side) while the total resistance of sample (a) is $R_{ta} = R_c + R_{oxide} + R_{nt}$. To get resistance of nanotube itself, it needs to be removed oxide layer because investigating the total resistance of (a) sample is very complicated and cannot be explained clearly. Recently, Davydov et al. reported that the resistance of individual 48nm nanotube would be ~$6 \times 10^6 \Omega$ assuming a similar resistivity to carbon film ($\rho = 3{\sim}5 \times 10^{-2} \Omega$.[7] Because nanotube sample with a surface contact area of $70 \mu m$ contains approximately ~10^6 tubes, an estimated resistance of nanotube array is 6Ω. In our work, we intended to get the resistance of nanotube only through reducing contact resistance(R_c) by RTA process. As the result of that process, resistance is decreased to 20Ω. This experimentally measured value is 1 order higher than the estimated resistance. This shows significantly lower value than that of previously reported work by other group. It implies that metal electrode using Ti/Au shows better contact between nanotube and electrode and RTA process is an effective tool for reducing contact resistance. The electric characteristics at low temperature is shown in Figure 4. In case of sample (a), the shape of conductance exhibit zero-bias cusps of the form dI/dV $\approx V^\alpha$ where α is in the range 0.45~0.10 for 4.21 < T < 9.99K and zero-bias conductance shows T^{-1} dependence in the temperature range 4.21 < T < 19.99K

a)   b)
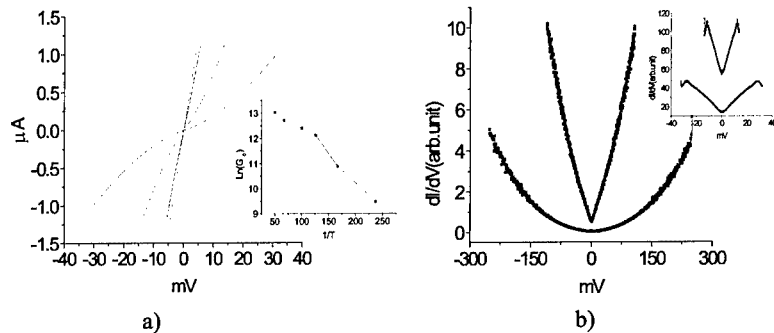
Figure 4. a) IV measurement at low temperature and inset shows temperature dependence of Ln G_o. Conductance suppressed near V=0 for T < 7.9K and ohmic behavior was shown at temperature(> 7.9K). (b) dI/dV comparison data(4.2, 6.1K) due to the oxide layer sample. Oxide layer having sample shows the coulomb blockade at 4.2K temperature

in the right inset of Figure 4(a). Through $G_o \sim exp(AT^{-1})$, activation energy(E) is 2~3meV and shows the semiconducting behavior at this temperature region. Two types of conductance pattern are exhibited in Figure 4(b). Anomaly zero-bias G_o that means oxide layer between nanotube and electrode plays a key role for current blockade. In the inset of Figure 4(a), nanotube sample which doesn't have oxide layer shows normal zero-bias conductance while conductance suppressed near V=0 at lower temperature(< 7.9K). J. Haruyama *et al* reported that nanotube sample having 5nm oxide layer shows zero-bias G_o varied near T=5K and the shape at 2K is quite different form shown as a reference 8 and also reported that it is evident that the nanomaterials connected to the single tunnel junctions strongly contribute to the G_o anomaly.[4] In our work, zero-bias G_o variation shows almost same pattern compared with J. Haruyama et al's work while oxide barrier layer between nanotube and metal electrode is almost 20nm. The shape of zero-bias G_o varied near T=6.01K and the shape at 4.21K is different from the data in right inset of Figure 4(b) although the thickness of oxide layer is bigger than that of J. Haruyama et al's sample. The contact area of metal electrode is a dot shape with 70μm diameter and it includes around 10^6 nanotubes. Each nanotube acts as a electron transfer tunnel and oxide layer acts also as a single tunnel junction. However, Such structure including many nanotubes in a dot-shape electrode can be regard as a kind of mass systematically so oxide layer between nanotube and metal can be also regard as a kind of multi-tunnel junction. Assuming all nanotubes in the electrode act as a pathway to electric current, electrons tranfer across the oxide layer easily at the temperature(> 7.9K) through carbon nanotube and coulomb blockade behavior was disappeared above same temperature region.

CONCLUSION

Highly vertically ordered anodic alumina oxide(AAO) template was fabricated by anodization method and carbon nanotube was synthesized at 600~700°C by thermal

CVD. The rapid thermal annealing process made ohmic contacts between Ti-Au electrode and carbon nanotube. The aluminum oxide layer acts as a barrier for conductance and nanotube having oxide layer shows coulomb blockade at lower temperature($< 4.21K$). Carbon nanotube shows the temperature(T^{-1}) dependent at $4.21K < T < 19.9K$ and semiconducting behavior at this temperature region.

ACKNOWLEDGEMENTS

REFERENCES

1. S. Iijima, *Nature*(London) *354*, 56 (1991).
2. J. Kong, C. Zhou, E. Yenilmez and H. Dai, *Appl. Phys. Letters* 77, 3977-3979 (2000)
3. M. Ahlskog, R. Tarkiainen, L. Roschier and P. Hakonen, *Appl. Phys. Letters* 77, 4037-4039 (2000)
4. J. haruyama, I. Takesue and Y. Sato *Appl. Phys. Letters* 77, 2891-2893 (2000)
5. J. Li, M. Moskovits, and T. L. Haslett, *Chem. Mater.* 10. 1963 (1998)
6. Zhang Y, Ichihashi T, Landree E, Nihey F and Ijima S, *Science* 285 1719 (1999)
7. D.N. Davydov, J. Li, K.B. Shelimov, T.L. Haslett, B.W. Statt and M. Moskovits
   J. Appl. Phys., 88 7205-7208 (2000)
8. D.N. Davydov, J. Haruyama, D. Routkevitch, D. Ellis, B.W. Statt, M. Moskovits,
   and J.M. Xu, *Phys. Rev. B* 57, 13550(1998)

Structural Characterization of GaN Nanowires Fabricated via Direct Reaction of Ga Vapor and Ammonia

R.N. JACOBS*, L. SALAMANCA-RIBA*, M. HE**, G.L. HARRIS**, P. ZHOU**, S. N. MOHAMMAD**, AND J.B. HALPERN**
*Dept. of Materials & Nuclear Engineering. University of Maryland, College Park, MD 20742
**Materials Science Research Center of Excellence Howard University, Washington, DC 20059

ABSTRACT

We report structural studies of large-scale wurtzite GaN nanowires fabricated by direct reaction of Ga vapor and NH_3. This recently reported growth technique [1] demonstrates processing of GaN one-dimensional structures as thin as 26 nm and up to 500 μm in length. This method is both interesting and attractive in that fabrication is carried out without the assistance of template materials as required by other methods. In this study, transmission electron microscopy (TEM) is used to characterize the nanowires, while x-ray diffraction (XRD) and energy dispersive x-ray spectroscopy (EDS) data provide supporting structural/compositional analysis. Our structural investigation reveals the presence of thin hexagonal platelets, which we believe play a critical role in the nucleation, growth, and orientation of the wires. In particular, our findings indicate that most of the wires grow along the [$2\bar{1}\bar{1}0$] direction, normal to the platelet edges.

INTRODUCTION

Since Han et al. first demonstrated the synthesis of Gallium Nitride (GaN) nanorods through a Carbon Nanotube-confined reaction [2], there has been increasing interest in finding novel fabrication techniques. Nanometer sized one-dimensional structures of various materials has potential uses in the development of nanodevices and for basic mesoscopic research [3,4]. GaN is particularly promising due to its large band-gap and high melting point, and is already being used in blue LEDs, laser diodes, and for high temperature electronic devices. Following Han's publication in 1997, Cheng et al demonstrated the synthesis of wurtzite GaN in alumina membranes [4]. In addition, Duan et al [5], grew pure [$01\bar{1}0$] oriented wires using a laser-assisted catalytic method. Here, laser ablation of a GaN-catalytic metal composite target generated reactive sites confining and directing the growth of crystalline wires. There has now been a growing number of reports on methods to fabricate nanowires of GaN and other materials [6-10]. However, these methods have all required the use of catalysts or templates. The technique used in this work (described in the next section) demonstrates a catalyst/template free nanowire fabrication route through the direct reaction of Ga and flowing Ammonia in a tube furnace.

EXPERIMENT

The schematic diagram shown in Figure 1, illustrates the basic experimental set-up used in this work. Approximately 3 g of pure Ga metal was placed in a Boron Nitride boat which was set at the bottom of a horizontal oven. The tube of the oven was lined with a
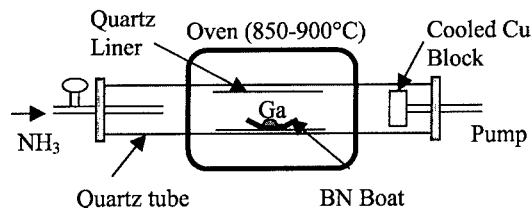
Figure 1. Experimental set-up for direct reaction of Ga vapor and Ammonia.

quartz or BN liner for protection against contamination during growth. Ammonia was injected into the tube through a mass-flow controller (MKS Instruments, Inc., model 1259B) at rates ranging from 50-100 sccm. The total upstream pressure was kept constant at 15 Torr. For GaN nanowire synthesis, the temperature in the oven was varied between 850-900 °C for 3-4 hrs. GaN is formed through the reaction [11],

$$2Ga + 2NH_3 \rightarrow 2GaN + 3H_2 \uparrow$$
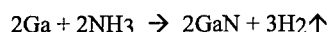
so that the overall growth kinetics are influenced by the amount of ammonia and Ga at the growth surface. The resulting reaction products were collected from the cooled Cu block (see Figure 1), BN boat, and quartz liner, and subsequently studied through SEM, XRD, EDS and TEM. TEM samples were obtained by applying small amounts of glue onto Cu mesh grids and contacting them to the reaction products. Subsequent TEM analysis was carried out on a JEOL 4000FX transmission electron microscope operated at 300 KV.

RESULTS AND DISCUSSION

Figure 2 shows an SEM image of the direct-reaction products for samples grown for 4 hrs at 900 °C and an NH_3 flow rate of 80 sccm. Polycrystalline GaN hillocks tend to form spontaneously, while thin nanowires grow on top of the hillocks. These polycrystalline hillocks are believed to play a critical role in the nucleation and growth of the wires. SEM images reveal wires as long as 500 μm. SEM images also showed what appeared to be mostly amorphous material from samples collected from the cooled copper block, compared to those collected from the BN boat and liner.

Overall structural information from these reaction products were obtained through standard θ-2θ XRD Bragg scans. Figure 3 shows typical Bragg scans obtained from samples collected from the BN boat and cooled Cu Block. For comparison, these samples were placed on Si substrates so that XRD data could be normalized under the Si (400) substrate peak. Strong peaks corresponding to a wurtzite GaN pattern were obtained from the samples collected from boat and liner, while much lower peak intensities were obtained from the samples collected from cooled Cu block. This confirms that a relatively low density of crystalline material is formed on the Cu block.

To confirm the overall purity and composition of the reaction products, a JEOL 8900 superprobe was used to carry out energy-dispersive x-ray analysis. Though the resolution of this instrument was not sufficient to isolate and analyze a single wire, an informative analysis
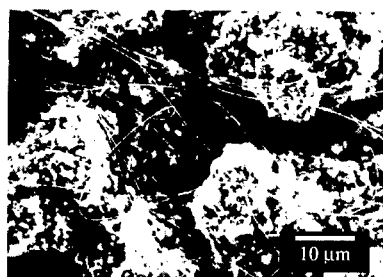
Figure 2. SEM image of reaction products showing polycrystalline hillocks and nanowires.
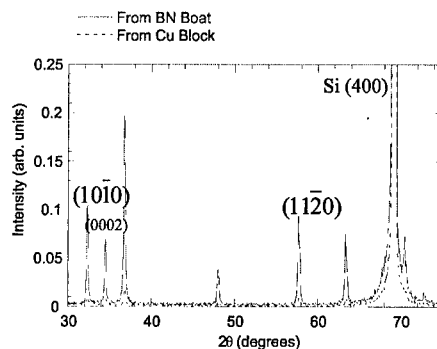
Figure 3. XRD Bragg scan of reaction products can be indexed to GaN wurtzite structure.

of selected areas was nonetheless carried out. That is, areas containing only the surrounding hillocks and areas containing both hillocks and nanowires were studied. EDS scans revealed both these areas to be very pure as evidenced by the strong Ga k_α peaks in the scan shown in Figure 4. Strong N peaks were also revealed, confirming the purity of the reaction products.
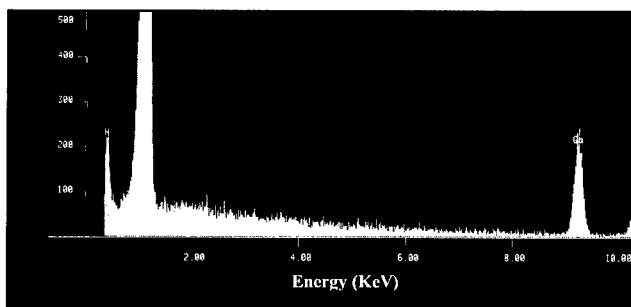
Figure 4. EDS spectrum (Counts vs. x-ray energy), of area containing at least one nanowire and surrounding area (hillocks).

TEM Analysis

Figure 5 shows TEM images of the two main types of wires observed in the reaction products. The first (Figure 5a), shows a wire with a diameter of approximately 26 nm and its (0001) selected area diffraction pattern (inset). This (0001) diffraction pattern confirms the wire has the wurtzite structure and interestingly, reveals the growth direction to be $[2\bar{1}\bar{1}0]$. While most of the wires seem to share this growth direction, a few wires exhibit features that suggest otherwise. Figure 5b shows a ~122 nm diameter wire with facets along the growth direction. Each of the two facets lie approximately 30 nm from the edge suggesting that this
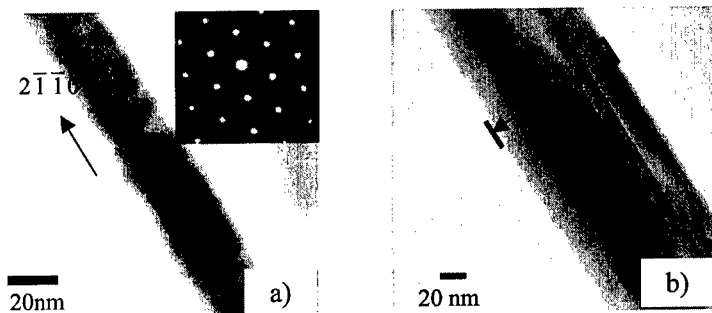
Figure 5. a) TEM image and (0001) DP (inset) showing 26 nm diameter wire.
b). TEM image showing ~122 nm wire with facets parallel to growth direction.

particular wire actually grows in the [0001] direction. However, further analysis via precise zone axis diffraction patterns (ZAP) is needed to confirm the growth direction in these particular wires. The reaction products are oriented randomly on TEM grids, making it difficult to obtain precise ZAP analysis of the nanowires.

TEM analysis was also used to gain a better understanding of the polycrystalline hillocks observed in the SEM images. These hillocks were shown to be composed of thin (and electron transparent) hexagonal platelets with the [0001] direction normal to the surfaces. Several nanowires were found to originate from the edges of the thin crystal platelets as shown in Figure 6. These images confirm that the wires do indeed grow in the
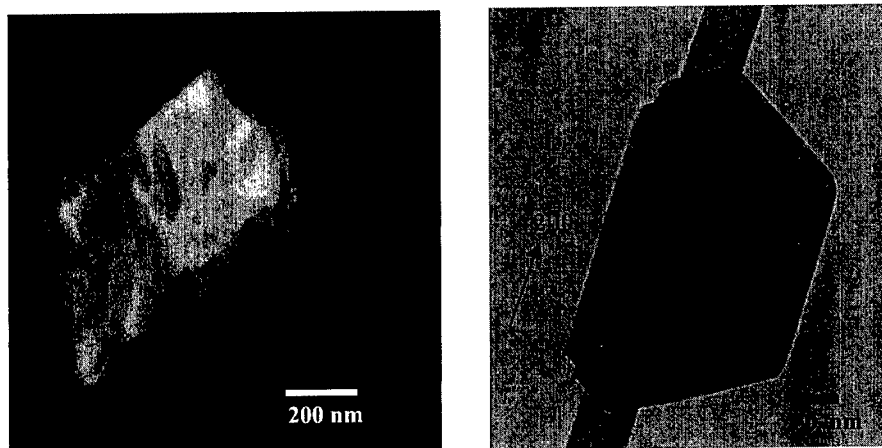
Figure 6. TEM images showing wires that were found to originate or grow from the edges of thin hexagonal platelets and along the [2$\bar{1}$10] directions.

[$2\bar{1}10$] direction, indicating that preferential nucleation and faster growth takes place along platelet edges rather than platelet faces. This is quite different from GaN nanowires reported in other studies [6-8], where growth directions are typically [$01\bar{1}0$] or [100] (in the three index system).

CONCLUSIONS

In summary, the fabrication of GaN nanowires through a direct reaction of Ga and flowing ammonia was demonstrated. SEM images showed that the reaction products consist of polycrystalline hillocks and wires with lengths exceeding 500 μm. EDS, XRD, and SAD showed that the wires are pure GaN with the wurtzite structure. TEM analysis showed that the hillocks consist of thin hexagonal platelets from which the wires tend to nucleate and grow. In particular, most wires grow along the [$2\bar{1}10$] directions, out of the hexagonal platelet edges. Thicker wires tend to show facets along the length and suggest a [0001] growth direction, or out of the platelet faces. Current work in progress includes structural analysis at the tips of the wires via high-resolution imaging to understand the overall growth mechanism. Much work is still needed to fully understand how and why nanowires grow through this relatively simple fabrication technique. Work is also underway to investigate the effect of several processing parameters including temperature and ammonia flow rate on the length and diameters of the wires [12].

REFERENCES

1. M. He, I. Minus, P. Zhou, S.N. Mohammed, J. B. Halpern, R. Jacobs, W.L. Sarney, L. Salamanca-Riba, R.D. Vispute, *Appl. Phys. Lett.* 77, 3731-3733 (2000).
2. W. Han. S. Fan, Q. Li, and Y. Hu, *Science* 277 1287-1289 (1997).
3. C.M. Lieber, A.M. Morales, P.E. Sheelan, E.W. Wong, P. Yang., *Proceedings of the Robert A. Welch 40th Conference on Chemical Research: Chemistry on the Nanometer Scale;* 165-187, (1997).
4. L.E. Brus, *J. Phys. Chem.*, 98 3575, (1994).
5. G.S. Cheng, L.D. Zhang, Y. Zhu, G.T. Fei, and L. Li, *Appl. Phys. Lett.* 75, 2455-2457 (1999).
6. X.F. Duan and C.M. Lieber, *J. Am. Chem. Soc.* 122, 188-189 (2000).
7. J.Y. Li, X.L. Chen, Z.Y. Qiao, Y.G. Cao, and Y.C. Lan, *J. Cryst. Growth* 213, 408-410 (2000).
8. W. Han, P. Redlich, F. Ernst, and M. Ruhle, *Appl. Phys. Lett.* 76, 652-654 (2000).
9. W. Han, y. Bando, K. Kurashima, and T. Sato, *Appl. Phys. Lett.* 73, 3085 (1998).
10. W. Han, Ph. Redlich, F. Ernst, and M. Ruhle, *Appl. Phys. Lett.* 75, 1875 (1999).
11. D. Elwell, R.S. Feigelson, M.M. Simkins, and W.A. Tiller, *J. Cryst. Growth* 66, 45 (1984).
12. M. He, P. Zhou, S.N. Mohammad, G.L. Harris, J.B. Halpern, R.N. Jacobs, W.L. Sarney, L. Salamanca-Riba, *J. Cryst. Growth* (in press).

Lithium Insertion in Nanoporous Carbon Materials Produced from Carbides

I.M. Kotina[1], V.M. Lebedev[1], A.G. Ilves[1], G.V. Patsekina[1], L.M. Tuhkonen[1], S.K. Gordeev[2], M.A. Yagovkina[3] , and Thommy Ekström[4]
[1]Petersburg Nuclear Physics Institute, Gatchina, Leningrad district, 188350, Russia
[2]Central Research Institute for Materials, 191014, St. Petersburg, Russia
[3]Mehanobr-Analyt Co, 199026, St. Petersburg, Russia
[4]Skeleton Technologies Group, SE-12653, Stockholm, Sweden

ABSTRACT

In this work, the results of a study of the lithium insertion process in nanoporous carbons (NPC) obtained from carbides (SiC, TiC, Mo$_2$C) by chlorination are presented. Lithium insertion was produced in the temperature range of 30-200 ^{0}C via the vacuum deposition and diffusion. The major analytical tools for study included nuclear reaction method and X-ray diffraction. Diffusion coefficients of lithium at this temperature interval were estimated. Possible mechanism of lithium diffusion is discussed. Investigation of phase composition of lithiated samples was carried out at room temperature. Phase composition is found to be dependent on the relationship between deposition and diffusion rates.

INTRODUCTION

In the past decade, significant research efforts have been focused on the search for suitable carbon materials as an alternative anode(s) for lithium rechargeable batteries. The main requirement to these materials is a high quantity of reversible lithium ion insertion. This property appears to be a function of the carbon network structure [1-2]. The structural variation of carbon materials also plays an important role in the stoichiometry and phase composition of the lithiated carbons.

In this paper, the process of lithium insertion in nanoporous carbons (NPC) obtained from carbides (SiC, TiC, Mo$_2$C) by chlorination is studied. These materials are of interest for their high-developed surface (total porosity is up to 70%) on which lithium deposition can take place and for high open nanoporosity that makes it possible to have enough value of lithium diffusion coefficient. The objectives of the study are to determine lithium diffusion mechanism and the factors that affect the stoichiometry and phase composition of lithium insertion in NPC.

EXPERIMENTAL

The samples used in this study (bulk NPC) were obtained through the temperature chlorinating process from an intermediate product prepared on the base carbide powders (SiC, TiC, Mo$_2$C). These materials have high total porosity up to 70% and nanoporosity about 50%. Their specific surface area is up to 1300 sm^2/ g. Pore sizes and value of graphitised fragments in bulk NPC under study depend on initial carbide powder [3]. So pore sizes are the largest in the npC< Mo$_2$C>B samples and are the smallest in the C< SiC>B ones. At he same time, total volume of ordered graphite fragments is the largest in the C< SiC>B samples.

Lithium insertion in the samples being studied was carried out by vacuum evaporation and subsequent diffusion at the temperatures ranging from 30 ^{o}C to 200 ^{o}C. The nuclear reaction

7Li(p,a)⁴He was applied to measure the concentration profiles of lithium. Protons with energy Ep=1,1 MeV were used and α-particles were registered with Si surface barrier detector [4]. The total quantity of the evaporated lithium was monitored with Si sample. Is is known that in this temperature interval the diffusion of lithium into silicon does not practically take place [5]. In such a situation total quantity of evaporated Li is calculated by integration of the Li concentration profile. After cooling the lithiated samples were kept in an atmosphere of dry nitrogen.

The investigation of phase composition of the lithiated samples was performed by means of X-ray diffraction measurements using a " Geigerflex" D/max-Rc Rigaku diffractometer with a Co X-ray tube.

Samples were round with their diameter larger than their height. Therefore, to estimate lithium diffusion coefficient we have used the one-dimensional solution of diffusion equation obtained under the assumption that diffusing atoms do not interact with each other and the supply of lithium is infinite:

$$N(x) = N_0 \, erfc\left(\frac{x}{2\sqrt{Dt}}\right),$$ (1)

where erfc-complementary error function, N(x)- concentration at any point x, t-diffusion time, D-diffusion coefficient, N_o –surface concentration of Li.

In some cases experimental lithium concentration profiles were given by the equation (1) with rather high accuracy (figure 1). This made it possible to determe lithium coefficient diffusion D_{Li} by the fitting of the experimental curve with one erfc function. If the fitting with one erfc was impossible, we determined D_{Li}, using the equation (1), in ten points of experimental curve and then calculated average value of diffusion constant ($<D_{Li}>$). As we will see below, the value of $<D_{Li}>$ may be used as the characteristic of the diffusion process.
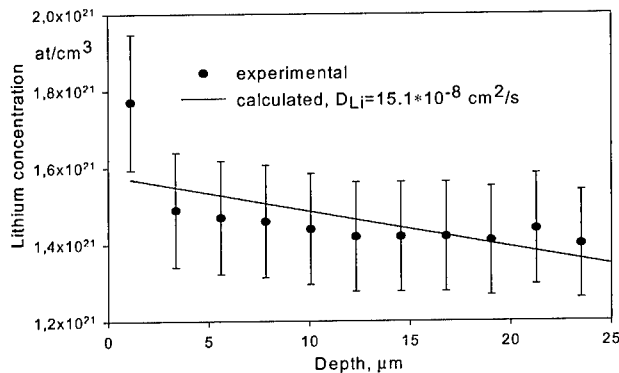
Figure 1. Lithium diffusion profile in the C<TiC>B sample .Temperature and time of diffusion are 80⁰C and 10 min respectively. Straight line is the best fit of experimental results.

First of all we have carried out an investigation of the action of preliminary vacuum annealing on Li diffusion process. Table I shows $<D_{Li}>$ values in the samples under investigation

in the temperature range of 30 °C –100 °C before and after annealing at 200 °C during 4 hours. Diffusion process was conducted for 5 min. One can see that annealing leads to increase of $<D_{Li}>$ values. Effect of preliminary annealing depends on the type of samples under study and is more marked in the NPC with larger pore sizes. Moreover, a clear correlation is observed between the values of $<D_{Li}>$ and pore sizes: D_{Li} values are maximum in the C<Mo$_2$C>B samples and are minimum in the C<SiC>B ones. It is known that disordered carbon structure does not change at annealing temperature up to 1100°C [6], so the main result of annealing is the removal of adsorbed water. Taking into account this circumstance, increase of $<D_{Li}>$ after annealing can be connected with diffusion of lithium along the pore walls.

Table I. Values of diffusion coefficients in the samples of NPC prior to and after preliminary annealing. Diffusion time 5 min.

Sample	Number	T, °C	$<D_{Li}>*10^9$ cm^2/sec prior annealing	$<D_{Li}>*10^9$ cm^2/sec after annealing
C<SiC>B	2	30	2,5	6,6
C<TiC>B	32	30	2	12,6
C<Mo$_2$C>B	6	30	3,28	76
C<SiC>B	142	80	20,4	33
C<TiC>B	32	80	13,6	57
C<Mo$_2$C>B	6	80	200	101
C<SiC>B	21	100	10,3	21
C<TiC>B	44	100	2	400
C<Mo$_2$C>B	43	100	175	164

In separate experiments we studied Li insertion in the annealed samples at different diffusion process durations. Lithium diffusion processes have been performed at temperature 80°C during 5, 10 and 20 min. It turned out that the variation in the value of lithium diffusion coefficient, taking place as a function of diffusion time, depends on NPC type (Table II). From Table II we can see that increase of diffusion time from 10 min to 20 min results in decrease of D_{Li} in the C<SiC>B sample by a factor of approximately 6. At the same time in the C<TiC>B sample lithium diffusion coefficient is constant with variation of diffusion duration in this interval. Besides, for example, if at diffusion duration 20 min the diffusion coefficient values varied from $4,1*10^{-9}$ cm^2/sec for the C<SiC>B sample to $3,5*10^{-8}$ cm^2/sec for the C<TiC>B sample, almost by a factor of 9, then at diffusion duration 5 min., the values of diffusion coefficients for these samples differ from one another by a factor of only 1,5.

Table II. Diffusion coefficients at different durations of diffusion process. Diffusion temperature 80°C.

Sample	Number	$<D_{Li}>*10^9$ cm^2/sec t_{dif}=5'	$<D_{Li}>*10^9$ cm^2/sec t_{dif}=10'	$<D_{Li}>*10^9$ cm^2/sec t_{dif}=20'
C<SiC>B	11	33,4	23	4,1
C<TiC>B	32	57	32	35
C<Mo$_2$SiC>B	6	101	–	–
	28	–	27	–
	28	101	–	–

It should be remembered that the insertion process of lithium into NPC samples is complicated. It includes lithium diffusion along pore walls and in graphitised fragments, accumulation of lithium in pores, intercalation Li in graphitised fragments and phase transition among intercalation stages. Certainly, all these processes are responsible for the value of Li diffusion coefficient. Therefore, we believe that the dependence of the diffusion coefficient on diffusion process duration can be related to intercalation or accumulation processes going simultaneously with diffusion process. It is possible that in the experiments with and without preliminary annealing Li diffusion process duration was short to manifest these processes. The results of XRD investigation of lithiated samples confirmed this assumption.

XRD phase composition examination was conducted in the samples preliminary treated at 300 °C for 70h to minimize the effects of water. Note that the formation of intercalation phase is observed mainly in the samples in which sufficient volume of the graphite-like fragments is available. This fact is in full accordance with results described in literature [7]. All the data presented below relate to the C<SiC>B samples.

To follow the structural changes during diffusion process, XRD study has been performed from both sides of the sample under investigation. It should be emphasized that Li insertion in the samples does not give a pure single-stage compound as determined by XRD patterns. Coexistence of several phases was always observed. Some of the results are shown in Figure 2. As one can see, intercalation phases LiC_6, LiC_{12} LiC_{24} and large volume of carbonate Li_2CO_3 and carbide Li_2C_2 phases are registered from the front side. At the same time from the back of the sample only small quantity of Li_2CO_3 and Li_2C_2 is seen. No evidence of Li_2CO_3 and Li_2C_2 existence was received when the sample was polished from the front side at the depth of 0,4 mm. However, the intercalation phases LiC_6, LiC_{12}, LiC_{24} are observed. Concentration profiles measured on both sides indicate that in this case high lithium gradient is available in the sample (figure 3). From this fact it transpires that the formation of Li_2CO_3 and Li_2C_2 phases strongly depends on Li concentration. We suppose that at first Li clusters arise when high concentration of lithium is available in pores and then clusters react with atmospheric CO_2 that is the cause of Li_2CO_3 formation. As for Li_2C_2, additional experiments are required to understand the mechanism of their formation.

It is evident that lithium filling pores will be dependent on the lithium deposition rate. We have examined the phase composition of the lithiated samples at different rates of Li deposition and diffusion. The total volume of carbonate and carbide phases decreased with the decrease of Li deposition rate and the increase of diffusion rate. As a result, it was stated that ratio between deposition and diffusion rates of lithium plays important role in the phase composition of lithiated samples. In order to exclude all possibility of formation Li_2C_2 and Li_2CO_3 phases we

have used the impuls deposition of lithium. The duration of impuls (5 min.) was rather less than the time interval brtween impulses (3h). Thanks to this we have produced the samples up to a thickness of about 0,6 mm uniformly impregnated by lithium and containing intercalation phases only.

(2)	351046	LI C12	35.6[15.1]%
(5)	351047	LI C24	37.8[13.2]%
(1)	221141	LI2 CO3	12.2[10.6]%
(3)	140649	LI2 C2	22.6[10.5]%
(4)	210484	LI2 C2	8.2 [15.8]%

(3)	341320	LI C6
(4)	351046	LI C12
(1)	351047	LI C24
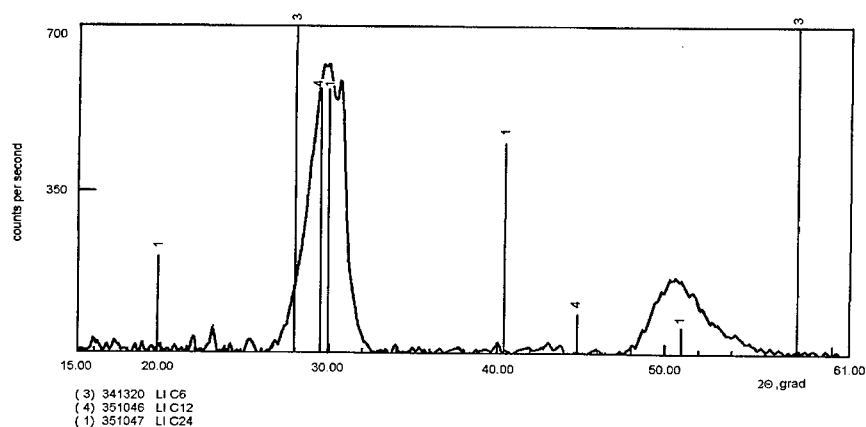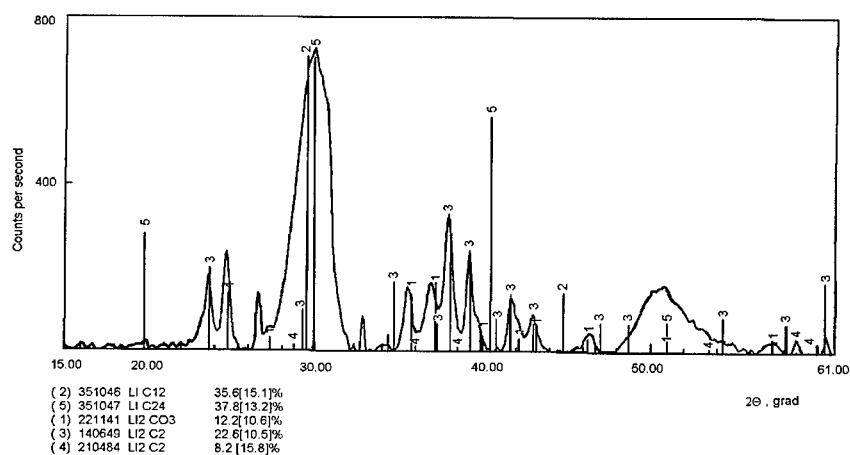
Figure 2. X-ray diffractional patterns of lithiated C<SiC>B sample for front side (a) and back side (b). Diffusion time 30 houres.
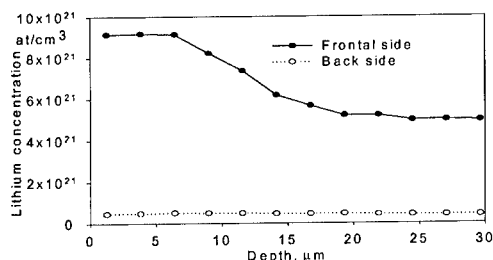
Figure 3. Concentration profiles measured on different side of sample #2 C<SiC>B

CONCLUSION

We have investigated the process of Li insertion in nanoporous carbons at the temperature range of 30-200 ^{0}C. The diffusion process was studied at different deposition and diffusion rates.

A comparison of diffusion processes in different NPC allows to conclude that the main mechanism of diffusion is lithium diffusion along pore walls. As a result of lithium diffusion process investigations in different NPC samples with and without preliminary annealing, it is stated that the value of lithium diffusion coefficient depends on the size of pores and their physical state. Values of D_{Li} in the above-mentioned temperatures vary for different samples in the range $10^{-9}-10^{-7}$ cm^2/s. The value of lithium diffusion coefficient depends on the diffusion process duration. It is elucidated that such behavior $<D_{Li}>$ reflects the different processes that occur in series during the entire insertion process: Li diffusion over pore walls, accumulation of Li in pores giving rise to Li clusters and the formation of intercalation phases.

Intercalation phases LC$_6$, LiC$_{12}$, LiC$_{24}$ and LiC$_{40}$ were observed. Besides, Li$_2$C$_2$ and Li$_2$CO$_3$ phases were registered in some cases. It was stated that the correlation between the diffusion rate and the evaporation rate is responsible for the phase composition. Based of this fact the process technology conditions for producing of lithiated samples without lithium carbide and carbonate were found. The samples up to a thickness of about 0,6 mm uniformly impregnated by lithium and containing intercalation phases only were produced.

The studies were carried out on NPC samples developed and produced in collaboration with Skeleton Technologies Group.

REFERENCES

1. A.M.Wilson and J.R.Dahn, *J.Electrochem.Soc.* **142**, (1995) 326.
2. 2.J.R.Dahn, Tao Zheng, Yinghu Liu, J.S.Xue, *Science*, **270** (1995), 590.
3. R.N.Kyutt, E.A.Smorgonskaya, A.M.Danishevskii, S.K.Gordeev, A.V.Grechinskaya, *Phys. Solid State*, **41** (1999), 808.
4. I.M.Kotina, V.M.Lebedev, G.V.Patsekina, Proceedings of International Conference on Nuclear Physics "Clustering phenomena in nuclear physics" (50 Meeting on Nuclear Spectroscopy and Nuclear Structure, June 14-17, 2000, St-Petersburg, Russia), St-Petersburg, (2000), 396.
5. *Semiconductor Detectors*, ed.by G.Bertolini and A.Coche (1968), North-Holland Publishing Company-Amsterdam, 33.
6. Edward Buiel, J.R.Dahn, *Electrochim. Acta*, **45** (1999), 121.
7. J.R.Dahn, A.K.Sleigh, H.Shi, J.N.Reimers, Q.Zhong, and B.M.Way, *Electcrochim.Acta*, **38**, (1993), 1179.

Diamond-Like Carbon

From Diamond to Carbon Nanotube Field Emitter

O. Gröning, L.-O. Nilsson, P. Gröning and L. Schlapbach
Gruppe für Festkörperphysik
Physik Departement der Universität Fribourg, Chemin du musee 3, CH-1700 Fribourg
(Switzerland)

Abstract

In this paper we review the physics and the expectations that were put into the negative electron affinity (NEA) mediated field emission of chemical vapor deposition CVD diamond films and how the emitter technology made possible by this mechanism could have challenged the classical metal micro-tip field emitter arrays. We discuss the dependency between emitter performance of micro-tip emitter arrays and feature size (size of the field enhancing tip) and due to this to the connection between emitter performance and fabrication costs.
We introduce the concept of the field enhancement distribution function $f(\beta)$ for a useful characterization of the field emission properties of thin film emitter and show how this distribution function can be measured by scanning anode field emission microscopy. Using $f(\beta)$ measured on a thin film of randomly oriented multiwalled carbon nanotubes we show that even these kinds of low cost emitters can show a field emission performance comparable to micro-tip arrays, yet that the large spread in field enhancement values between the individual emitter prevent this performance to be fully exploited. This because the field range in which such thin film emitters can be operated is limited due to emitter disruption and triggering of vacuum arcs. Simulations show how resistor-limited emission can solve these limitations.

Introduction

In recent years various kinds of carbon thin films have been recognized as interesting materials for field emission cathodes. The development of the field emission flat panel display in the same time has further boosted this interest. Therefore investigation of the field emission properties and mechanisms of carbon based materials as single crystalline and chemical vapor deposition (CVD) diamond, diamond like carbon, nanocrystalline graphite and carbon nanotubes has become a domain of very active research. Though field electron emission from a perfectly flat metal surface requires electric field on the order of 2500 $V\mu m^{-1}$, for the carbon based materials mentioned above field emission currents could be observed for applied electric fields below 10 $V\mu m^{-1}$.

Classical Fowler-Nordheim like field emission describes the tunneling of electrons close to the Fermi energy through a narrow surface potential barrier. When an electric field of the order of 2500 $V\mu m^{-1}$ is present at a typical metal surface with a work function of 5 eV the surface potential step confining the electrons to the solid, becomes a triangular shaped surface potential barrier. As the width of the barrier at the Fermi energy approaches 2 nm, the electrons have a non-negligible probability of tunneling from the solid into vacuum. Fields of the order of 2500 $V\mu m^{-1}$ can practically only be created when the field enhancing effect of conducting tip-like structures is exploited. The field amplification of a tip at its apex is in first approximation equal to the aspect ratio (height/radius) of the tip.

Although the effects of thermionic and field electron emission were discovered at about the same time, thermionic emission is almost exclusively used for technical applications where free electrons in vacuum are required. The first reasons for this is that thermionic emitters are rather simple, in the simplest case it is just a heated tungsten or tantalum wire. Further they can reliably deliver high emission currents of up to 400 Acm^{-2} for many thousand hours[1]. Field emitters on the other hand are able to deliver very high emission current densities of the order of 10^6 Acm^{-2}, but as tip like structures are needed to created the electric field required for the emission, the actual emitting area, which is the apex of the field enhancing tip, is usually very small. The higher the field enhancement the smaller the emitting area gets so that the emission

current from a single field emission tip is usually small. Therefore field emitter found applications only where the high emission current density and the small emitting area, leading to a high brightness, are advantageous and where the total emission current has not to be very high such as in high resolution electron microscopy. Though thermionic emitter have numerous advantageous features for technological applications, they are not suited for miniaturization due to the high operation temperature of 950°C-2500°C. Miniaturization of thermionic emitter means to deal with increasing temperature gradients in the device. So that devices using thermionic emitter are difficult to build smaller than a few mm. Field emitter in contrast do not have such limitations, actually the miniaturization of field emitter is a key element to their success in vacuum microelectronics. The miniaturization of field emitters to micrometer sizes allows to integrate a large number of emitting tips on a surface and therefore achieving emission current densities with respect to the device surface which are comparable to emission current densities of thermionic emitter. A simple picture of such a field emitter is an array of micrometer sized tips on a flat surface.

The metal micro-tip field emitter array

Using some basic assumptions it is possible to estimate the emission current density of such a field emitter array, where the current density is with respect to the surface of the device and not the actual emitting area of the tip apex. This definition of current density is useful for technological consideration, e.g. for the comparison of field emitter arrays with thermionic emitter.

As the basis of this estimation stands the description of the emission current of a single tip as a function of the electric field at the emission site. One has to distinguish between the applied field E_{apl} being the homogenous electric field perpendicular to the surface of the field emitter array and the local field E at the emission site (which is the tip apex). In a simple diode configuration of two parallel plates separated by a vacuum gap d the applied field would be given by $E_{apl}=V/d$, where V is the bias voltage between the plates and d being the separation of the plates. The local electric field at the apex of the ith field emitter tip is then given by $E_{apl}*\beta_i$, where β_i is the field enhancement factor of the ith emitting tip. For our estimation of the emission current density we assume that all the tips are needle shaped (cylindrical shafts with spherical caps) having the same height h and the radius of curvature at the apex r. We have shown that for a tip array of identical tips the maximum emission current at a fixed applied field is obtained, when the spacing between the individual tip in the emitter array is twice their height h. An optimal emitter array would then be a hexagonal array of tips (height h and radius at the apex r) where the next nearest neighbor distance is 2*h. For this configuration the device surface area per tip A_{tip} and the emitting surface A_E are given by:

$$A_{Tip} = 2\sqrt{3}h^2 \quad (1) \qquad A_E = \alpha\pi r^2 \quad (2)$$

where α is a proportionality factor on the order of 1. So that the emission current density J_D with respect to the surface of the emitter array is given by:

$$J_D = \frac{A_E \cdot J_{FN}(E,\phi)}{A_{Tip}} = \frac{\alpha\pi}{2\sqrt{3}}\left(\frac{r}{h}\right)^2 J_{FN}(E,\phi) = 0.9\left(\frac{1}{\beta}\right)^2 J_{FN}(E_{apl} \cdot \beta,\phi) \qquad (3)$$

where J_{FN} denotes the Fowler-Nordheim relation giving the emission current density as a function of the local field E and the emitter work function ϕ. The maximum current density J_D will depend on the maximum local current density J_{FN} which a tip can support. This value will be material dependent and will also depend on the requirements with regard to emitter life time. For a constant work function (given by the emitter material) and a given maximum local emission

current density J_{FN}, the value of $E=E_{apl}*\beta$ can be determined from the Fowler-Nordheim relation. So that the maximum device emission current density J_D can be determined as a function of the applied field at which the device should deliver the maximum current density $J_{FN,max}$. Figure 1 displays the dependence of the maximum device emission current density J_D and the applied field of operation for different maximum local emission current densities J_{FN}. As one can observe in order to achieve a J_D of the order of 10 Acm^{-2} (which is a typical current density of thermionic emitter) in an applied field range of 2-10 Vμm^{-1} requires that the single emitters can sustain local field emission current densities in the range of 10^6-10^8 Acm^{-2}.
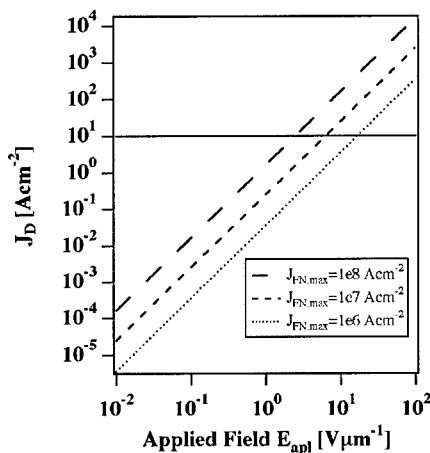
Figure 1

Emission current density with respect to the emitter array surface area J_D as a function of the applied field of operation. The dashed curves represent the maximum theoretical J_D for a hexagonal field emitter array for different max. Emission current densities per single emitter $J_{FN,max}$. E_{apl} denotes the field needed to achieve the max. single emitter current density $J_{FN,max}$.

Using high density, gated metal micro tip field emitter arrays, values of J_D of 100 Acm^{-2} can be achieved at applied fields of the order of 100 Vμm^{-1}[2]. With a J_D of the order of 100 Acm^{-2} such field emitter array can challenge thermionic emitter. However the production of metal micro tip field emitter arrays involves expensive lithographic processes, which has triggered the interest in efficient low cost field emitting materials.

One of the disadvantage of using field emitter for large area electron sources is the need to fabricate a large number ($\sim 10^6$-10^8 cm^{-2}) of micrometer or even sub micrometer sized tips. Due to the steep current-field characteristic of field emission the requirement to the geometric properties of the individual tips is very high further complicating the manufacturing process and raising production costs. For a work function of 5 eV the relative change dI/I of emission current of a single emitter is a factor of ten with a relative change of field enhancement $d\beta/\beta$ of 10%. Which means that if the aspect ratio and therefore the field enhancement of the field enhancing tip in a field emitter array is controlled within 10%, the field emission current form the individual tips will show a scatter over one order of magnitude.

The key to success of field emission tip arrays is to produce micrometer sized tips with a high density and with a high degree of control over the aspect ration of the individual tip. The fabrication techniques employed in the semiconductor industry offer the possibilities to fabricate such emitter arrays. As the Moore's law, describing the exponential decrease of feature size in semiconductor industry with time, one can expect a similar development for field emitter arrays. Here the decrease in feature size and therefore an increase in emitter density will increase the performance of the emitter array. Unfortunately there is a second Moore's law stating that the exponential decrease in feature size comes with an exponential increase of production costs and wherefore in analogy, the fabrication of micrometer sized emitter arrays is expensive.

Chemical vapor deposition diamond field emitter

CVD diamond films seemed to offer a field emitter which had not to rely on field enhancing structures and therefore not being subjected to the unfavorable relation of emitter performance and emitter cost of the field emission tip arrays. Because of the negative electron affinity (NEA) of the hydrogen terminated diamond surface it was thought that diamond could deliver electron emission at moderate local electric fields of the order of 10 $V\mu m^{-1}$ and without the need of field enhancing structures[3]. These expectations where backed by numerous experimental observations of field emission at applied fields below 20 $V\mu m^{-1}$[4].

In a semiconductor the electron affinity is defined as the energy difference between the vacuum level (lowest electron state in vacuum) and the conduction band minimum. Usually in ordinary semiconductors such as silicon or germanium this energy difference is positive. When the work function of the semiconductor is comparable to the gap energy ,as in the case of diamond, the electron affinity can become negative. This means that an electron in the conduction band can be emitted into vacuum without experiencing a surface potential barrier. This effect can be readily observed in photo- or secondary emission experiments on NEA single crystalline or CVD diamond.

A CVD diamond field emitter making use of NEA would therefore rely on three main processes:

- Injection of electrons into the conduction band of a CVD diamond thin film at the diamond-metal interface.
- Transport of the electrons in the conduction band to the diamond surface.
- Emission of the electrons into vacuum due to NEA.
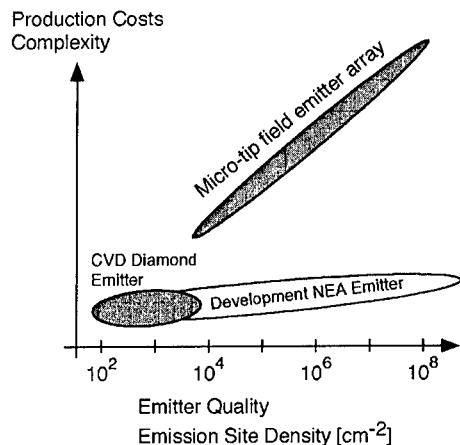
Figure 2

The diagram illustrates qualitatively the dependence between the emitter quality expressed by the emission site density and the production costs.

The way to an efficient NEA CVD diamond emitter would mean to optimize each of the three above mentioned points. The injection would require a very narrow Schottky barrier and an effective field penetration into the diamond film. The transport of the electrons to the surface requires a low defect density and a low density of grain boundaries in order to prevent trapping and recombination of electrons, which would then be lost for the emission. The emission at the diamond surface requires that the entire surface is in the NEA state, which can be controlled by the surface hydrogen termination and by the crystalline facetting of the surface.

The optimization of a NEA CVD diamond field emitter would proceed via the control of interface, bulk and surface properties of the diamond thin film. These are typical tasks in thin film deposition and can be achieved without considerably increasing the costs of the deposition process. The key point making the concept of diamond NEA emitter so attractive, is that this emitter is not submitted to the close relation between emitter performance and emitter costs as the field emission tip arrays.

Due to the second Moore's law of semiconductor industry the field emission tip arrays have to battle against the relation between feature size and production costs. Meaning that a decrease in feature size (size of the tip), giving an increased emitter density and therefore increased emitter performance, is connected with an considerable increase in the production costs. In Fig. 2 the emitter quality is expressed as the emission site (or emitter site) density on the horizontal axis. The vertical axis expresses qualitatively the production costs, where the scale would be rather logarithmic than linear.

Although the experimentally observed field emission properties of CVD diamond films, with emission site densities ranging from a few tens to 10^3 per cm^2 (dark gray ellipse), can not match the micro-tip field emitter arrays, CVD diamond thin films seemed to offer a great potential for the further development. Assuming the NEA emission mechanism, CVD diamond thin films could be developed to show emission from the hole cathode area and not from the relatively small surface area of a tip apex. The emission current density would only be limited by the injection current density at the metal-diamond interface.

The actual development in CVD diamond field emitter cathodes could not back this exciting perspective. The improvements made in the CVD diamond film emitter was just opposite to what NEA emission would require. Figure 3 shows the emission image on a phosphorus screen of a nanocrystalline CVD diamond film at different applied electric fields.

a) 3.5 $V\mu m^{-1}$ b) 5 $V\mu m^{-1}$ c) 6 $V\mu m^{-1}$
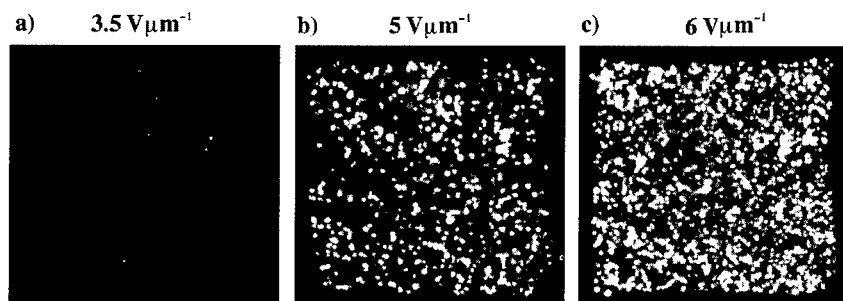
Figure 3

Field emission image on a phosphorus screen of a nanocrystalline CVD diamond film of 10x10 mm^2 at different applied fields.

Whereas the NEA emission mechanism would require high crystalline quality (as discussed above) the diamond films showing good field emission properties such as displayed in Fig. 3 are of nanocrystalline and highly defective nature. Further where NEA emission required insulative films for field penetration the nanocrystalline CVD diamond films are in general rather conductive. Also the influence of the contact-diamond interface to the field emission properties has sown not to be as essential as expected from NEA emission.

As can be seen from Fig. 3 the emission is spotty, where the spot density (emission site density) is a function of the applied field. The difficulty in the investigation of the field emission properties of these kind of thin films emitters resides to a good deal in the spotty nature of the emission. This because the field emission I-V measurements can not give conclusive information

about the emission mechanism as the work function, the electronic structure and the geometry of the emission spot are not known. Yet as the emission is originating only from a small fraction of the whole thin film these data are difficult to acquire by large area measurement techniques.

We have used field emission spectroscopy (FES) measuring the field emitted electron energy distribution in order to elucidate the field emission mechanism of CVD diamond films[5,6]. We could show that the electrons are emitted from the Fermi energy of the samples and that the shape of the energy distribution is typical for Fowler-Nordheim tunneling as opposed to NEA emission from the conduction band. FES further allowed us to determine the emitter work function of CVD diamond emitter to range between 5.5 and 6.2 eV. Further we could show that although the field emission occurred at applied electric fields on the order of 10 $V\mu m^{-1}$ the field at the emission site is enhanced by geometric field enhancement to values of the order of 3000 $V\mu m^{-1}$. It can therefore be concluded that the emission from nanocrystalline CVD diamond, as in the case of micro-tip arrays, is due to local geometric field enhancement.
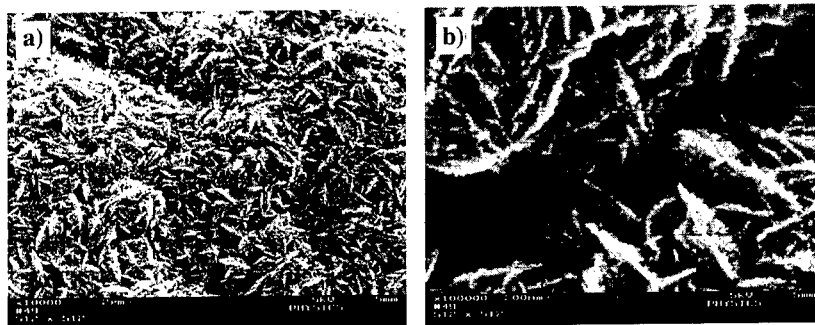
Figure 4

SEM images of a good emitting CVD diamond film grown by MW-PECVD at 950° C and 5% CH_4 in H_2 atmosphere.

Figure 4 displays SEM micrographs of a good emitting, nanocrystalline CVD diamond film, where the sharp protrusions responsible for the field enhancement are visible. As the low applied field electron emission of nanocrystalline CVD diamond is due to local field enhancement and not NEA the development of CVD diamond emitter is subjected to the same problems as the development and fabrication of metal micro-tip field emitter arrays. The envisioned low cost development route as depicted in Fig. 2 is therefore not realistic. As for metal micro-tip emitter arrays the improvement of the emission properties of CVD diamond thin film emitter goes via the control over the field enhancing structures. This submits the development of CVD diamond emitter to the same kind of cost-emitter quality relation as the metal micro-tip arrays (see Fig. 2) and therefore puts their attractivity into question.

However one should note that as a "low quality" field emitter with emission site densities on the order of 10^4 cm^{-2} and emission current density of the order of 10-100 $mAcm^{-2}$ at applied fields of about 10 $V\mu m^{-1}$ the nanocrystalline CVD diamond thin film emitter are considerably cheaper as metal micro-tip emitter arrays and might therefore still be suitable for applications where the emitter requirements are not very stringent.

Carbon nanotube thin film emitter

In the case of multiwalled (MWNT) or singlewalled (SWNT) carbon the situation is similar to the CVD diamond emitter, where field enhancing structures can be grown on surfaces

in large numbers using low cost deposition techniques. The emission of carbon nanotubes is clearly governed by their high aspect ratio and therefore by their field enhancement.
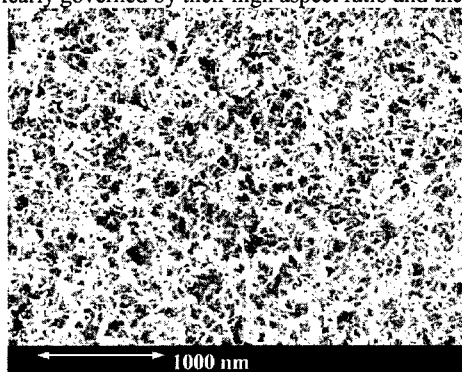
Figure 5

SEM micrograph of a randomly oriented MWNT thin film deposited on a silicon wafer.

Figure 5 displays a film of randomly oriented MWNT grown on a silicon wafer by pyrolysis of acetylene in a nitrogen atmosphere at substrate temperatures of 900° C. As catalyst for the nanotube growth 10 nm Ni was sputtered on the silicon. Such kind of randomly oriented nanotube thin films with a rather low density of tubes show already a very good field emission performance.
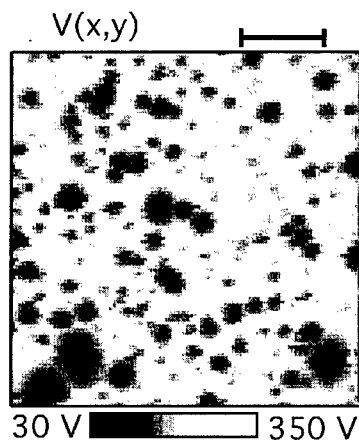
Figure 6

Scanning anode field emission measurement of a MWNT thin film (sample displayed in Fig 5). The map shows the extraction voltage as function of the x-y anode position for a constant emission current of 10 nA and an anode-sample distance of 5 μm. The scale bar is 50 μm.

Figure 6 displays a scanning anode voltage map V(x,y) of the nanotube thin film of Fig. 5 showing the voltage needed to obtain a fixed emission current of 10 nA as a function of the position of the anode. In this measurement the surface of the nanotube thin films is scanned at a constant distance of 5 μm by a tip anode of 1 μm tip radius. The resulting voltage map V(x,y) is displayed as gray scale image plot. The individual emission sites show up as dark spots in this plots indicating that a low voltage is needed at this positions to obtain the fixed emission current of 10 nA. Strong emission sites are characterized by a low value of the anode voltage at the

minimum of the emission spot and also by the size of the emission spot. As one can see there is a large scatter in the field emission performance of the individual emitters. In the scanned area of 200x200 μm^2 157 emission sites can be identified which corresponds to a density of about 400'000 cm^{-2}. It becomes clear from Fig. 6 that the characterization of the emission properties of a nanotube thin film emitter means the characterization of a large ensemble of individual emitter with different emission properties.

In order to obtain a realistic description of the electron emission from a thin film emitter ensemble, the emission properties of a single site need to be characterized. To do so we start the assumption that the FN-law correctly describes the current-field characteristics of MWNT field emitter. For our considerations we use the simplified formula of Brodie and Spindt [7]:

$$I = A \cdot \frac{1.5 \cdot 10^6}{\phi} E_{Apl}^2 \beta^2 \exp\left(\frac{10.4}{\sqrt{\phi}}\right) \exp\left(\frac{-6.44 \cdot 10^7 \phi^{1.5}}{E_{Apl} \cdot \beta}\right) \qquad (1)$$

I is the emission current of a single emitter in Ampere, ϕ the emitter work function in eV, β the field enhancement factor and E_{Apl} the applied electric field. E_{Apl} is given by the applied voltage V and the anode-cathode separation d by $E_{Apl}=V/d$. The product of β and E_{apl} gives the local electric field present at the emission site $E_{Site}=E_{Apl}*\beta$. Changes in the emission current of different emitter according to (1) arise from changes of the emitting surface A, the work function ϕ and of the field enhancement factor β. Using FES we have determined the work function of MWNT emitter to be 4.9±0.2 eV and from this value also the emitting surface could be determined to range from 10^{-8} to 10^{-10} cm^2[8]. One has to be aware that although A has the dimensions of a surface it also contains information about the electronic structure of the emitter and therefore doesn't only account for the geometric emitting surface.

If we assume that all the MWNT emitter have the same work function ϕ=4.9 eV and the same emitting area A=10^{-9} cm^2 relation (1) becomes very simple:

$$I = 3.4 \cdot 10^{-14} E_{Apl}^2 \cdot \beta^2 \exp\left(\frac{-7 \cdot 10^8}{E_{Apl} \cdot \beta}\right) \qquad (2)$$

Leaving the field enhancement β the only parameter determining the emission properties of a single emitter. To characterize the emission properties of a large ensemble of emitter such as the nanotube thin film of Fig. 5 and Fig. 6 we just need to know the field enhancement distribution function f(β)[9]. Where $\Delta N=f(\beta)\Delta\beta$ is the number of emission sites per unit area having a field enhancement factor in the interval [$\beta,\beta+\Delta\beta$]. The determination of this field enhancement distribution function f(β) characterizes the thin film field emission properties. Of course the question has to arise whether the assumption of a constant work function (justified by the fact that all emitter are of the same material) and a constant emitting surface (justified by the fact that all emitter are of the same dimensions) is not to severe. In fact one can test how a relative change of ϕ and A in relation (1) influences the value of β in order to obtain a constant emission current. For an emission current of 10 nA a relative change of the work function of 0.2 eV => $\Delta\phi/\phi$=0.2/4.9=0.04 would lead to a relative change of the field enhancement factor of only 5 % ($\Delta\beta/\beta$=0.05). Under the same conditions a relative change of the emitting surface of one order of magnitude $\Delta A/A$=10 leads to a relative change of only 11% for β ($\Delta\beta/\beta$=0.11).

From voltage maps such as displayed in Fig. 6 the f(β) can be determined. As the voltage scan is performed at a constant emission current, according to relation (2) the local value of $E_{Site}=EApl*\beta(x,y)=V(x,y)*\beta(x,y)/d$ is constant too. Here E_{Site} denotes the local electric field present at the emission site needed to obtain the fixed emission current of the voltage map. The local field enhancement $\beta(x,y)$ map can therefore be derived from the voltage map V(x,y) by $\beta(x,y)=E_{Site}*d/V(x,y)$.
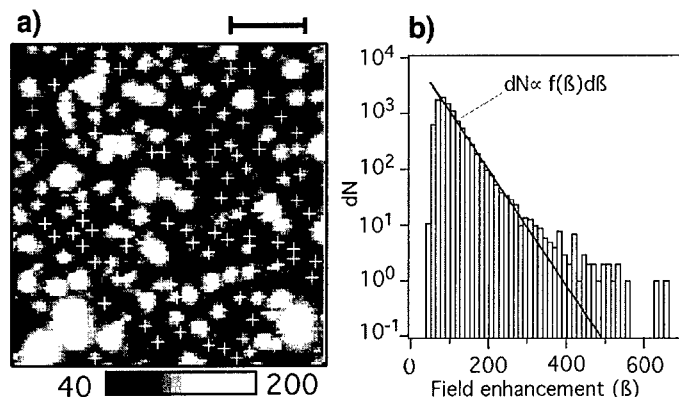
Figure 7

Diagram a) displays the field enhancement map derived from the voltage map of Fig 6. The scale bar is 50 μm and the white crosses denote the emitter positions. Diagram b) shows the histogram of the field enhancement map from which the field enhancement distribution function can be derived.

Figure 7a displays the field enhancement map $\beta(x,y)$ derived from the voltage map of Fig. 6. The emission sites now show up as local spots of high field enhancement values. The histogram of the beta map (see Fig. 7b) is now proportional to the field enhancement distribution function $f(\beta)$. Where the proportionality α factor equals:

$$f(\beta) = \alpha \cdot Hist(\beta(x,y), \Delta\beta) \qquad \alpha = \frac{N_{Emitter}}{N_{Pixels} \cdot \Delta\beta \cdot A}$$

Where $N_{emitter}$ is the number of emission sites in the β-map (157 in this case), N_{pixel} is the number of measurement points in the β-map (100*100 in this case), $\Delta\beta$ is the bin width of the histogram and A is the surface area of the β-map ($4*10^{-4}$ cm^2). As can be seen from Fig. 7b $f(\beta)$ has the shape of an exponentially decreasing function with β. The histogram over estimates $f(\beta)$ in the high β region due to the larger apparent size of high β emission sites in the β-map. From Fig. 7b one can determine the field enhancement distribution function for this sample to be: $f(\beta)=1.2e5\exp(-0.024*\beta)$ [cm^{-2}].

From the voltage map of Fig. 6 one can determine that there are about 400'000 emitter per cm^2 delivering emission currents of 10 nA for applied fields below 40 Vμm^{-1}. Compared with metal microtip arrays operating at applied fields around 100 Vμm^{-1} this figure seems very promising. The constant current measurement however is particular because a field emission cathode will be operated in most of the cases at a constant applied field. Under such condition the large spread of field enhancement values (see Fig. 7b) will lead to the situation that under constant field conditions the emission current will be carried only by a few, high β emission sites.

Figure 8 shows simulations of the emission image on a phosphorus screen (comparable to the measurements of Fig. 3 for $f(\beta)=1.2e5\exp(-0.024*\beta)$ [cm^{-2}] assuming relation (2) for the emission current of a single emitter. Figure 8a displays the emission image for an applied field of 4.4 Vμm^{-1} giving an emission current density of 0.31 mAcm^{-2}.
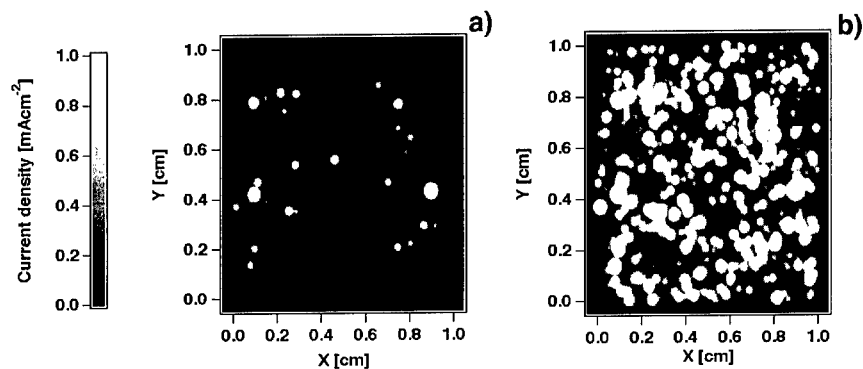
Figure 8

Diagram a) and b) display field emission simulations of an field enhancement distribution function $f(\beta)= 1.2e5exp(-0.024*\beta)$ $[cm^{-2}]$ at applied field of 4.4 $V\mu m^{-1}$ for a) and 5.6 $V\mu m^{-1}$ for b). The emission site are randomly distributed.

As one can see the current is carried only by a few emitter and that there are a large intensity differences between the emitter. When the applied field is increased to 5.6 $V\mu m^{-1}$ the emission current density has increased to 16.7 $mAcm^{-2}$. The increase in field has increased the emission site density as new emitter with lower β become visible, at the same time the high β emitter are now delivering such high emission currents that the screen is by far in saturation and that these emitter start to disrupt, burn-out or even trigger vacuum arcs. This means that for such emitting films the emission site density on the screen is not limited by the actual emitter density which as we have seen can be very high, but by the applied field level at which irreversible damage to the thin film occurs by emitter disruption or vacuum arcing.
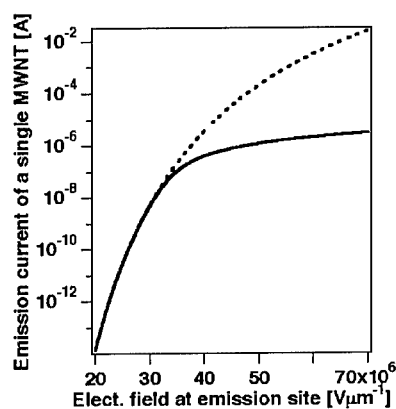
Figure 9

The diagram shows the current-field characteristics for a single MWNT emitter according to relation (2) (dashed line) and the according parallel resistor limited characteristic (solid line).

The introduction of a current limitation in the emission characteristic, e.g. by a parallel resistor for each emission site can improve this problem considerably. Figure 9 displays the current-field characteristic for a resistor limited emission (solid line) derived from relation (2) (dashed line). The resistor value has been chosen to limit the emission current of a single emission site at about 1 μA. If we now take the current limited emission characteristic for the

simulation of the emission behavior for the same f(β) as for Fig. 8 one can observe how the emission homogeneity is considerably increased at the expense of a higher field of operation.
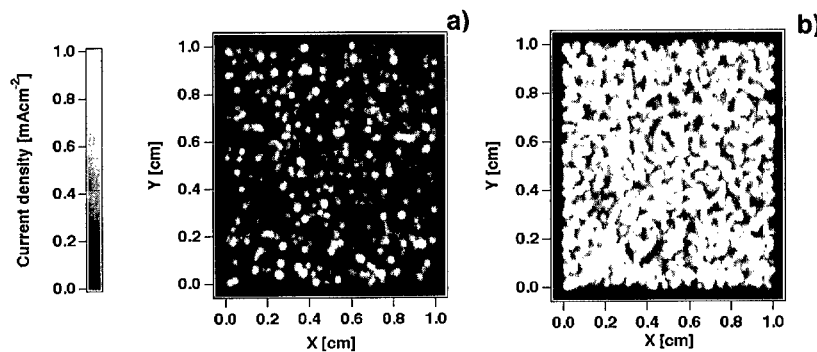
Figure 10

Simulation of the emission analog to Fig. 8 for resistor limited emission at 5.6 Vμm^{-1} a) and 6.9 Vμm^{-1} b).

Figure 10a displays the simulation of the emission image for the resistor current limited characteristic of Fig. 9 analog to the simulations of Fig. 7. One can see that for an applied field of 5.6 Vμm^{-1} the emission density is comparable to the analog simulation for the unlimited emission characteristics of Fig. 7b. But due to the current limitation the emission current density is only 0.2 mAcm^{-2} as compared to 16.7 mAcm^{-2} without current limitation. There are no emission sites reaching emission current levels critical for emitter disruption or arcing, that is why the applied field can be further increased. The emission current density is 1.2 mAcm^{-2} for an applied field of 6.9 Vμm^{-1} in Fig. 10b. One can see that for a much lower emission current density the emission homogeneity is very much increased and the problem of emitter disruption and vacuum arcing can be solved by the current limitation.

Conclusions

The attractvity of CVD diamond emitter as material for field emission cathodes had its origin in the possibility of this material to solve a major problem in the development of classical metal micro-tip field emitter arrays. The performance of a micro-tip emitter is connected to the feature size (and therefore tip density), so that better performance is linked with decreasing feature size. The problem arises from the fact the fabrication costs rapidly increase with decreasing feature size. Due to the NEA electron affinity of diamond it was thought that an emitter technology could be realized which does not depend on feature size, but on bulk, interface and surface properties of a thin film. Properties which can be controlled in the deposition process of the film and therefore development and optimization of the emitter is not necessarily connected with an increase in production costs. Today however it becomes more and more clear that the field emission of CVD diamond is also due to field enhancement at local structures and that therefore CVD diamond emitter are also subjected to the problematic relation between feature size and emitter quality. This of course, reduces the attractivety and the potential of this material for field emission applications considerably.

Carbon nanotube thin field emitter started from a similar situation as the CVD diamonds, in the sense that there is a low cost approach to fabricate thin film field emission cathodes . The difference to CVD diamond is that one agrees that the emission is due to field enhancement at small tips. We have showed that even for randomly grown MWNT thin films the emission site

density in a interesting applied field range of 50 $V\mu m^{-1}$ the emitter density can surpass 10^6 cm^{-2} and is therefore comparable to micro-tip arrays, at a fraction of the production costs. Yet the exponential field enhancement distribution of such nanotube thin film emitter exhibit is an obstacle for reaching a high emission site density as the emission current will be carried by only a few emission sites. An increase in the applied field above some critical value will further lead to irreversible damage to the emitting film due to emitter disruption and triggering of vacuum arcs. This effect leads to the situation that the emitting film can not be operated in a field range where a high emission site density can be achieved. The introduction of a current limiting mechanism, e.g. parallel resistor for each emitter, can solve this problem. As can be seen from Fig. 5 a resistive layer between the nanotube film and the substrate does not work, because the nanotube form an interconnected conducting network. The situation changes when the nanotubes are grown in small patches electrically disconnected of about $1x1$ μm^2 which is easily achieved by patterning the growth catalyst[10]. The resistive layer would therefore limit the emission current of a single patch, where it has to be expected that there will be only one dominating emitter in each patch. The emission site density is the given by the patch density, which can be easily of the order of 10^7 cm^{-2}. This would be a low cost approach for the fabrication of a thin film field emitter, which can compete against the micro-tip arrays.

In general the fabrication cost will be a key issue in the success of nanotube field emitter and therefore in the optimization of nanotube field emission cathodes one has to find the balance between improvement of the emission properties and increase in process complexity and therefore fabrication costs.

References

[1] G. Gärtner, P. Geittner, H. Lydtin, A. Ritz, Appl. Surf. Sci. 111 (1997) 11

[2] D. Temple, Materials Science and Engineering, R24 (1999) 185

[3] M.W. Geis, J.C. Twichell, T.M. Lyszczarz, J. Vac. Sci. Technol. B14 (1996) 2060

[4] C. Wang, A. Garcia, D.C. Ingram, M. Lake, M.E. Kordesch, Electron. Lett. 27 (1991) 1459

[5] O. Gröning, O.M. Küttel, P. Gröning, L. Schlapbach, J. Vac. Sci. Technol. B17 (1999) 1970

[6] O. Gröning, O.M. Küttel, P. Gröning, L. Schlapbach, J. Vac. Sci. Technol. B17 (1999) 1064

[7] I. Brodie, C. Spindt, Advances in Electronics and Electron Physics 83 (1992) 1

[8] O.Gröning, O.M. Küttel, Ch. Emmenegger, P. Gröning, L. Schlapbach, J. Vac. Sci. Technol. B18 (2000) 665

[9] L. Nilsson, O. Gröning, P. Gröning, O.M. Küttel, L. Schlapbach, J. Appl. Phys. in press (2001)

[10] L. Nilsson, O. Gröning, Ch. Emmenegger, O.M. Küttel, E. Schaller, L. Schlapbach, H. Kind, J-M. Bonard, K. Kern, Appl. Phys. Lett. 76 (1999) 2071

Three-dimensional calculation of field emission from carbon nanotubes using a transfer-matrix methodology

Alexandre Mayer, Nicholas M. Miskovsky[1] and Paul H. Cutler[1]
Laboratoire de Physique du Solide, Facultes Universitaires N.-D. de la Paix, Rue de Bruxelles 61, B-5000 Namur, Belgium
[1]Department of Physics, 104 Davey Lab, Penn State University, University Park, PA 16802, U.S.A.

ABSTRACT

We present simulations of field emission from carbon nanotubes, using a transfer-matrix methodology. By repeating periodically a basic unit of the nanotubes in the region preceding that containing the extraction field, specific band-structure effects are included in the distribution of incident states, i.e. those entering the field region. The structures considered are the metallic (5,5) and the semiconducting (10,0) single-wall carbon nanotubes. The total-energy distributions of incident states show the gap of the (10,0) and the expected flat region for the (5,5) nanotube. The field-emitted electron energy distributions contain peaks, which are sharper for the (10,0) structure. Except for peaks associated with van Hove singularities in the distribution of incident states or with the Fermi level in the case of a metallic structure, all peaks are shifted to lower energies by the electric field.

INTRODUCTION

Like other forms of nanostructured carbon, the nanotubes [1-3] show interesting field-emission properties such as low extracting field, high current density, and seemingly long operating time. In general, the current-voltage characteristics of the nanotubes are found to follow a Fowler-Nordheim type tunneling law [4] with an emitter work function varying between 4 to 5 eV depending on the type of nanotubes. Electronic states localized near or at the very end of the nanotube influence the current emission profile [5]. The localized states are relatively well documented for various kinds of tube termination [6-9]. Such localized states can be induced by the extracting electric field, as shown by recent *ab-initio* calculations [10].

To study field emission from carbon nanotubes, we used the transfer matrix technique developed in previous publications [11-13]. From a given three-dimensional potential-energy distribution (describing two biased electrodes), this methodology predicts the corresponding emitted current. For this specific application, the potential energy was calculated using for the first time the Bachelet etal pseudopotentials [14]. In addition, in order to reproduce band-structure effects in the distribution of incident states, a basic unit of the carbon nanotubes was repeated periodically, in an intermediate region between the supporting metal substrate and that containing the extraction field.
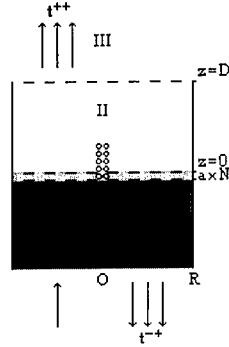
Figure 1. Geometry of the situation considered. Region I ($z \leq a.N$) is a perfect metal. The intermediate region $-a.N \leq z \leq 0$ contains N periodic repetitions of a basic unit of the nanotube. Region II ($0 \leq z \leq D$) contains the part of the nanotube subject to the electric field. Region III ($z \geq D$) is the field-free vacuum. The arrows in the Regions I and III symbolize scattering solutions, with a single incident state in Region I and the corresponding reflected and transmitted states (whose coefficients are contained in the transfer matrices t^{-+} and t^{++} respectively).

THEORY

The geometry considered in this paper is that depicted in figure 1. The emitting nanotube stands in a region (Region II, $0 \leq z \leq D$) between a supporting metal substrate (Region I, $z \leq -N.a$) and the field-free vacuum (Region III, $z \geq D$). An electric bias V is established between the two limits of Region II. The intermediate region $-a.N \leq z \leq 0$ contains N periodic repetitions of a basic unit of the nanotube.

The potential energy in Region II is calculated essentially by using techniques of Ref. [11], with a pseudopotential for the ion-core potential. For this ion-core contribution, we used the expression given in Ref. [14] for the $l=1$ states. This choice is justified by the fact that the electronic current in nanotubes is due to π electrons. The atomic orbitals, representative of the 4 valence electrons of each carbon atom, are represented here by the sum of two Gaussian distributions $\Psi = A(\exp(-\alpha_1 r^2) + \exp(-\alpha_2 r^2))$, where the two parameters $\alpha_1 = 0.35/a_0^2$ and $\alpha_2 = 1.40/a_0^2$ (a_0 =Bohr radius) are those recommended in Ref. [14]. These electronic densities are displaced from the nucleus positions by Δr quantities, which are related to the dipole p of the corresponding carbon atoms by $p = -4e\Delta r$. These dipoles are those induced by the extraction field and take account of dipole-dipole interactions. They are calculated by using the techniques of Ref. [12] for an anisotropic polarisability with radial and transversal components of 3 and 0.865 Å^3 respectively [15]. The electronic exchange term is evaluated using the Local Density Approximation $\frac{2}{3} C_X \rho^{1/3}$ (with $C_X = -\frac{3}{4} \frac{e^2}{4\pi\varepsilon_0} (\frac{3}{\pi})^{1/3}$ and ρ the local electronic density)[11].

To compute electronic scattering from the supporting metal (Region I) to the vacuum (Region III) by taking account of all three-dimensional aspects of the potential barrier in the intermediate regions, we used the transfer-matrix technique developed in previous publications

[12-13]. In this formulation, the scattering electrons remain localized inside a cylinder of radius R in the regions preceding the vacuum Region III (R is much larger than the nanotube radius). The wave function is expanded in terms of basis states

$\Psi_{m,j}^{I,\pm} = A_{m,j} J_m(k_{m,j}\rho)\exp(im\varphi)\exp(\pm i\sqrt{\frac{2m}{\hbar^2}(E-V_{met})}z)$ in the Region I and

$\Psi_{m,j}^{D,\pm} = A_{m,j} J_m(k_{m,j}\rho)\exp(im\varphi)\exp(\pm i\sqrt{\frac{2m}{\hbar^2}E}z)$ in the anode plane $z=D$. Here the $\pm$ refers to the propagation direction relative to the z-axis, which is oriented from Region I to region III. The $A_{m,j}$ are normalization coefficients and V_{met} is the potential energy in the metal. The methodology then provides the amplitudes of the reflected states $\Psi_{m,j}^{I,-}$ and transmitted states $\Psi_{m,j}^{D,+}$

corresponding to single incident basis states $\Psi_{m,j}^{I,+}$ in the metal (see figure 1 for a schematic representation). Total current densities result then from the contribution of all solutions associated with a propagative incident state in the metal.

RESULTS

The two structures considered in this paper are the armchair (5,5) and zigzag (10,0) nanotubes. To reproduce the energy distributions associated with the band structure of carbon nanotubes, $N=16$ repetitions of a basic unit of the corresponding nanotubes were inserted between the metal in Region I and the beginning of the potential barrier at $z=0$. Calculations show that 16 repetitions are sufficient to reproduce the gap of the (10,0) and the metallic plateau of the (5,5) nanotube in the distribution of incident states. The work function W of these two nanotubes have the values corresponding respectively to the middle of the gap (5.75 eV) for the (10,0) or the middle of the metallic plateau (5.25 eV) for the (5,5) structure.

An electric bias of 12 V is established between the supporting metal and the vacuum. The scattering simulations are performed by considering a confinement radius R of 4.5 nm, basis states characterized by m subscripts ranging from -10 to $+10$ and transverse wave vectors $k_{m,j}$ restricted by $k_{m,j} \leq \sqrt{\frac{2m}{\hbar^2}(E+\Delta E)}$ with $\Delta E = 4$ eV. It was found that the electron energies have to range over 16 eV below the top of the potential barrier to reproduce with reasonable accuracy the position and width of the gap and metallic plateau of the (10,0) and (5,5) nanotubes, respectively [16]. For this reason, the Fermi energy in the supporting metal was given the value $E_F=16$ eV– W.

Field emission from an open (5,5) carbon nanotube

The first simulations consider an open (5,5) carbon nanotube. This armchair nanotube is metallic. We consider in the field-free region $z\leq0$ 16 units of this molecule (corresponding to 320 atoms), which are connected to 7 units (corresponding to 140 atoms) in the region $z\geq0$ where the extraction field is present. The first and last atoms in this region are then located respectively at $z=0.061$ and 1.660 nm. The radius of the tube is 0.339 nm (the radius of a C_{60} molecule).

The extraction bias is 12 V and variations of the extraction field are obtained by changing the distance D between the two electrodes. A section of the potential-energy distribution (corresponding to an electrode separation D of 4 nm) is represented in the left part of figure 2. The nanotube acts essentially as a metallic cylinder, so its interior is nearly at a constant potential [17-18]. The carbon atoms are clearly indicated.
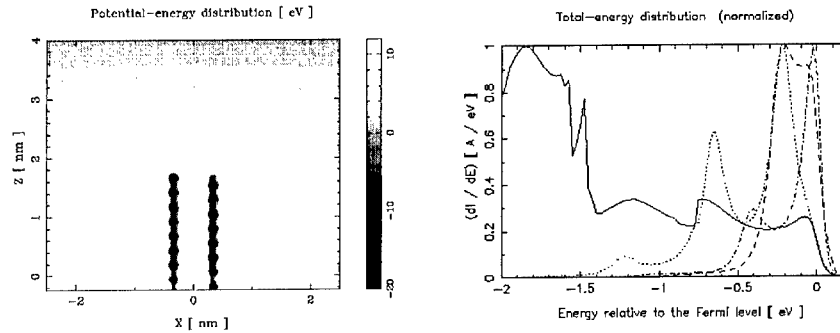
Figure 2. Left: Potential-energy distribution for an open (5,5) nanotube corresponding to an extraction bias of 12 V and a grid separation D of 4 nm. The basic unit below $z=0$ is repeated 16 times. The contour levels correspond to integer potential-energy values. A cut-off at –20 eV is applied to improve the visibility of positive values. Right: Normalized total energy distribution of the incident states at $z=0$ (solid) and of the transmitted states at $z=D$ for an applied electric field of 0.20 (dashed), 0.25 (dot-dashed) and 0.30 V/Å (dotted). The maximal values are respectively 0.23 10^{-3}, 0.11 10^{-9}, 0.87 10^{-7} and 0.81 10^{-6} A/eV.

The total-energy distribution of the field-emitted electrons is illustrated in the right part of figure 2. The four curves correspond to the incident distribution at $z=0$ and the transmitted distribution at $z=D$ for an applied electric field of 0.20, 0.25 and 0.30 V/Å. The absolute values as well as the width of the distributions are increasing with the extraction field, in agreement with elementary field-emission theories [19]. In all cases, there is a significant contribution at the Fermi level (due to a higher transmission probability and a non-zero supply function). The sharp peak at the edge of the metallic plateau is a van Hove singularity [20]. The other oscillations in the distribution of incident states are due to standing waves in the nanotube. Their period tends to decrease with the number N of repetitions of the basic unit.

There are well pronounced peaks in the distributions below the Fermi level. They move to the left with increasing extraction bias as a result of field penetration, which lowers the potential energy at the apex of the nanotube as well as its mean value in the whole nanotube. Similar displacements have been observed experimentally with carbon emitters [3,21]. The peaks tend to the positions observed in distribution of incident states at $z=0$. This can be understood if we still relate these peaks to standing states in the whole nanotube. At low electric field, the effective length of the nanotube associated with standing waves is larger (since including parts in Region II) so the separation between peaks is shorter. At high fields, the end portion of the nanotube no longer tends to contribute to these standing waves, since its mean potential energy differs significantly from that in the region $z\leq0$.

Representing $\log(I/F^2)$ as a function of $1/F$ (Fowler-Nordheim plot) gives a line, whose slope indicates [1] a field enhancement factor γ of 3.8. This small value compared to experimental data, where γ is typically found between 500 and 800 for multiwall nanotubes [1] and around 3000 and above for single-wall nanotubes [2], is obviously due to the small aspect ratio of the nanotube used in our calculation ($L/D \sim 2.5$). This also explains why the electric field used in the calculations needs to be a factor of 1000 larger than in experimental conditions [4].
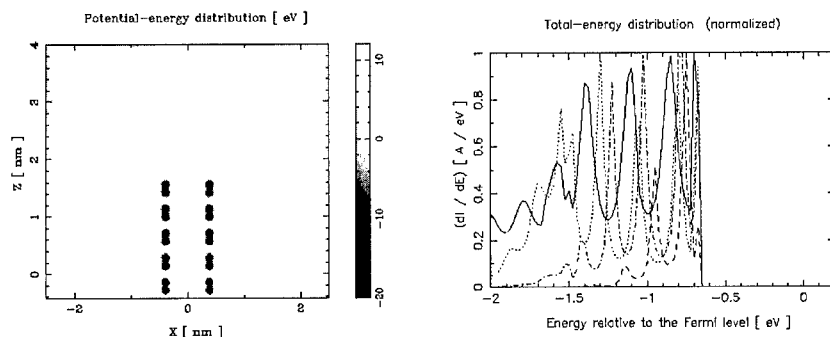
Figure 3. Left: Potential-energy distribution for a (10,0) nanotube corresponding to an extraction bias of 12 V and a grid separation D of 4 nm. The basic unit below $z=0$ is repeated 16 times. The contour levels correspond to integer values. A cut-off at -20 eV is applied to improve the visibility of positive values. Right: Normalized total energy distribution of the incident states at $z=0$ (solid) and of the transmitted states at $z=D$ for an applied electric field of 0.20 (dashed), 0.25 (dot-dashed) and 0.30 V/Å (dotted). The maximal values are respectively $0.15 \ 10^{-3}$, $0.40 \ 10^{-19}$, $0.17 \ 10^{-15}$ and $0.37 \ 10^{-13}$ A/eV.

Field emission from a (10,0) carbon nanotube

In the last simulations, an open (10,0) carbon nanotube is considered. This zigzag nanotube is semiconducting. We again consider in the field-free region $z \leq 0$ 16 units of this molecule (corresponding to 640 atoms), which are connected to 4 units (corresponding to 160 atoms) in the region $z \geq 0$ where the extraction field is present. The first and last atoms in this region are located respectively at $z=0.071$ and 1.633 nm. The radius of the tube is 0.391 nm. The geometrical dimensions are therefore close to those of the open (5,5) structure. The corresponding potential-energy and total-energy distributions are presented in figure 3. The carbon atoms are organized by pairs in the potential-energy representation, due to the figure passing exactly through C-C bonds that are parallel to the z axis.

The total-energy distributions present a gap, which is centered at the Fermi level. The peaks are sharper than for the metallic (5,5) nanotube (thus reaching the results of Adessi etal [5]). We can see that the sharp peak at the edge of the gap (which is due to a van Hove singularity) does not move significantly with the extraction field while all the others are shifted to lower energies. As in the previous case, the peaks reach the positions observed in the distribution of incident states. A field enhancement factor of 2.5 can be derived from the slope of the Fowler-Nordheim plot (essentially revealing the field-emission process to be inefficient). This small value is a consequence of the absence of emission at the Fermi level due to the gap.

CONCLUSIONS

Transfer-matrix calculations of field emission from carbon nanotubes were presented. With the use of pseudopotentials, the methodology takes account of band-structure effects (i.e. reproducing the gap of the (10,0) and the metallic plateau of the (5,5) nanotube in the distribution

of incident states) and of all three-dimensional details of the tunneling barrier. The total-energy distributions of both the semiconducting (10,0) and metallic (5,5) nanotubes contain peaks, which are sharper for the (10,0) structure. Except for peaks associated with the van Hove singularities in the distribution of incident states or with the Fermi level in the case of a metallic structure, all peaks are shifted to lower energies by the electric field.

ACKNOWLEDGMENTS

REFERENCES

[1] W.A. de Heer, A. Chatelain and D. Ugarte, Science **270**, 1179 (1995).
[2] J.M. Bonard, J.P. Salvetat, T. Stockli, L. Forro and A. Chatelain, Appl. Phys. A **69**, 245 (1999) and references therein.
[3] M.J. Fransen, Th.L. van Rooy and P. Kruit, Appl. Surf. Sci. **146**, 312 (1999) and references therein.
[4] P.G. Collins and A. Zettl, Phys. Rev. B **55** (15), 9391-9 (1997).
[5] Ch. Adessi and M. Devel, Phys. Rev. B **62** (20), 13314-7 (2000).
[6] T. Tamura and M. Tsukada, Phys. Rev. B **52** (8), 6015-26 (1995).
[7] D.L. Carroll, P. Redlich, P.M. Ajayan, J.C. Charlier, X. Blase, A. De Vita and R. Car, Phys. Rev. Lett. **78** (14), 2811-4 (1997).
[8] A. De Vita, J.Ch. Charlier, X. Blase and R. Car, Appl. Phys. A **68**, 283 (1999).
[9] Ph. Kim, T. Odom, J.L. Huang and C.M. Lieber, Phys. Rev. Lett. **82** (6), 1225-8 (1999).
[10] S. Han and J. Ihm, Phys. Rev. B **61**, 9886 (2000).
[11]. A. Mayer, P. Senet and J-P. Vigneron, J. Phys. Condens. Mat. **11** (44), 8617-31 (1999).
[12] A. Mayer and J.-P. Vigneron, Phys. Rev. B **56** (19), 12599-607 (1997).
[13] A. Mayer and J.-P. Vigneron, J. Phys. Condens. Mat. **10** (4), 869-81 (1998) ; Phys. Rev. B **60** (4), 2875-82 (1999) ; Phys. Rev. E **59** (4), 4659-66 (1999) ; Phys. Rev. E **61** (5), 5953-60 (2000).
[14] G.B. Bachelet, H.S. Greenside, G.A. Baraff and M. Schluter, Phys. Rev. B **24** (8), 4745-52 (1981).
[15] P.A. Gravil, Ph. Lambin, G. Gensterblum, L. Henrard, P. Senet, A.A. Lucas, Surf. Sci **329**, 199 (1995).
[16] R. Moussaddar, A. Charlier, E. McRae, R. Heyd and M.F. Charlier, Synthetic Metals **89**, 81-86 (1997).
[17] A. Maiti, C.J. Brabec, C. Roland and J. Bernholc, Phys. Rev. B **52** (20), 14850-8 (1995).
[18] L. Lou and P. Nordlander, Phys. Rev. B **52** (3), 1429-32 (1995).
[19] R.H. Fowler and L. Nordheim, Proc. R. Soc. London, Ser. A **119**, 173 (1928) ; R.H. Good and E. Muller, Handb. Phys. **21**, 176-231 (1956).
[20] J.M. Ziman, *Principles of the theory of solids* (The University Press, Cambridge, 1964) p. 46.
[21] K.A. Dean, O Groening, O.M. Kuttel and L. Schlapbach, App. Phys. Lett. **75** (18), 2773-5 (1999).

Effects of Sulfur Concentration on the Electron Field Emission Properties of Nanocrystalline Carbon Thin Films

S. Gupta[a], B. R. Weiner[b], B. L. Weiss[a], G. Morell[c]
[a]Department of Physics, University of Puerto Rico, San Juan, PO Box 23343, PR00931, USA
[b]Department of Chemistry, University of Puerto Rico, San Juan, PO Box 23346, PR00931, USA
[c]Department of Physical Sciences, University of Puerto Rico, San Juan, PO Box 23323, PR00931, USA

ABSTRACT

The electron field emission properties of sulfur-assisted nanocrystalline carbon (n-C: S) thin films grown on molybdenum substrates by hot-filament CVD technique using methane-hydrogen (CH_4/H_2) and hydrogen sulfide-hydrogen (H_2S/H_2) gas mixtures were investigated. The field emission properties of the S-assisted films are reported as a function of sulfur concentration. The incorporation of S caused structural and microstructural changes that were characterized with SEM, AFM and Raman spectroscopy (RS). The S-assisted films show smoother surfaces and smaller grains than those grown without. The lowest turn-on field measured was around 4.5 - 5.0 V/μm films grown with 500 ppm of hydrogen sulfide and at 900 °C. The electron field emission properties of S-assisted films were also compared to those grown without sulfur (i.e., intrinsic). An inverse correlation between the threshold field (E_c) and sulfur concentration was found. These finding are attributed to defect induced states within the electronic band structure.

INTRODUCTION

Cold cathodes as electron field emitters are potentially useful for field emission displays (FEDs) [1-3]. Recently, electron field emission (EFE) from diamond, disordered carbon and diamond-like carbon (DLC) attracted a great deal of interest for applications that require thin film cathodes and low threshold fields, in contrast to sharp metal tips (Spindt), such as flat panel displays (FPDs) [4-6]. In addition, DLC FED's are expected to be more cost-effective than the Spindt tips due to their complicated fabrication process [1]. Moreover, the excellent mechanical and chemical stability of carbon-based materials will result in highly reliable and stable emitters, even under extreme conditions.

In spite of the fact that the original work on electron field emission from diamond was motivated by the discovery of its negative electron affinity (NEA) [7], the ease of emission from many carbon materials suggests that the NEA is not a prerequisite. So far, there is lack of agreement regarding the mechanism(s) for FE, and more general emission models are desirable [8].

Although, much research has been devoted to the emission from disordered [5] and nanostructured carbon [9], a detailed investigation of the influence of impurity incorporating elements concentration is of interest for application issues as well as for fundamental understanding. The field emission properties for the undoped and doped (N, P, B) materials have been studied by several authors [9-14]. In this study, we report our findings of the EFE properties on n-C: S thin films grown by HFCVD as a function of sulfur concentration, keeping

the substrate temperature fixed at 900 °C, and the corresponding microstructural characterization. These results are also compared with those grown without sulfur (i.e., intrinsic). Recent pioneer reports on the addition of sulfur in diamond as a donor dopant, both experimental and theoretical modeling [14-17], stirred great interest in the diamond community. The n-type dopants of diamond (like N, P and now S) have the potential to enhance the electron field emission properties of disordered and nanocrystalline carbon films by providing electrons close to the conduction band. Studies of the changes in the electron field emission properties upon sulfur addition have not been conducted so far, except for the substrate temperature dependence keeping the sulfur concentration fixed [18].

EXPERIMENTAL DETAILS

The nanocrystalline carbon thin films in this study were prepared in a custom-built hot filament chemical vapor deposition (HFCVD) reactor, described elsewhere in detail [18]. The films were grown on mirror-polished molybdenum (Mo) disks of 1.4 cm diameter. All of the substrates were ultrasonically cleaned thoroughly in methanol for 15 min. They were then dried in He and placed immediately on a molybdenum substrate holder that is integrated with a graphite heater. The chamber was evacuated to 10^{-7} Torr or less before admitting the clean reactive gas mixture (s).

During the growth process for the intrinsic material a 2% CH_4:H_2 gas mixture with a total flow of 100 sccm was directed through a heated Rhenium (Re) filament. Eight cm of Re wire of 0.5 mm diameter was coiled, positioned 8 mm from the substrate, and Joule heated to 2400-2500 °C as measured by an optical pyrometer (Dual-wavelength, Mikron M90 Model). The Mo substrate was mounted on a graphite heater to intercept the excited gas downstream from the filament. It was maintained at 900-930 °C during the growth process and the total gas pressure was kept at 20 Torr. Real-time SE was used to calibrate the true temperature of the substrate surface. A polished commercial Si substrate was used for the calibration, and the E_1 transition energy from a line-shape analysis of the second derivative of the dielectric function provided the temperature of the surface, through the relationship $T[K] = \{3.486-E_1 (eV)\}/4.07x10^{-4}$ [18]. The resulting true temperature of the surface is typically ~ 30 °C higher than that if measured directly by thermocouple embedded in the heater block. Besides the above mentioned conditions, in order to incorporate sulfur (S) in the samples, hydrogen sulfide (H_2S): hydrogen (H_2) premix gas mixture was introduced in the chamber along with CH_4:H_2 mixture as feedstock gas. The S-assisted films were grown at various sulfur concentration ranging 500 ppm to 100 ppm with an interval of 100 ppm at a fixed substrate temperature of 900 °C. Some amount of sulfur becomes incorporated and hence the n-C: S notation. This presumption was corroborated and quantified by the surface analytical techniques such as energy dispersive x-ray analysis (EDX) and X-ray photoelectron spectroscopy (XPS).

Typical film thicknesses were around 0.5 μm for all of the samples, measured mechanically using Tencor surface profilometer (Alpha Step 100). The surface morphology was investigated using scanning electron microscope (JEOL Model 35 CF) and atomic force microscopy (Nanoscope IIIa, Digital Instruments Inc.). Raman spectroscopy is used to analyze the structural phases in the films. The Raman spectra were recorded using a triple monochromator (ISA Jobin-Yvon Inc. Model T64000) with around 1 cm^{-1} resolution using

514.5 nm line of Ar^+- laser. The spectra were recorded using 80x objective, and the probed area was about 1-2 μm^2.

A field emission (FE) system consists of a metal base making electrical contact to the Mo substrate and a Mo anode (area = 0.071 cm^2) attached to a micropositioner for varying the cathode-anode (d_{C-A}) spacing with an accuracy of ± 5 μm. A Keithley 6517 electrometer with a detection limit of 10-20 pA was used for measuring the emitted current and a Bertran 210-05R high voltage power supply. Measurements of the I-V characteristics were performed in a high vacuum of 10^{-7}-10^{-8} Torr. The turn-on voltage was defined as the voltage required to produce a current of 1 nA and the electric field was computed as E_c = applied macroscopic voltage/ cathode-anode spacing (V/d_{C-A} [19, 20].

Figure 1. Raman spectra for S- assisted nanocrystalline carbon thin films as a function of sulfur concentration ([S]) depicting the characteristic diamond, graphitic and disordered carbon signatures.

RESULTS AND DISCUSSION

The Raman spectra for the S-assisted nanocrytalline carbon (n-C: S) thin films grown by HFCVD as a function of sulfur concentration is shown in Figure 1. All of the samples were grown at a substrate temperature of 900 °C. The film grown with 100 ppm shows the dominant 1332 cm^{-1} (fingerprint of diamond or sp^3 bonded C). Qualitative inspection of Figure 1 also shows broad features at 1150, 1340 and 1580 cm^{-1} typical of nanocrystalline diamond (n-D) and disordered carbon dominated by microcrystalline graphitic inclusions, [20, 21] denoted by D- and G- band respectively. These latter features predominate with respect to the increase in sulfur concentration. While the film grown with 100 ppm is quite similar to intrinsic material (n-C), one

Figure 2. Typical scanning electron (A and B) and the corresponding atomic force micrographs (C and D) of nanocrystalline carbon thin films grown by S-assisted HFCVD exhibiting the change in surface morphology on sulfur addition: (A and C) 2.0% CH_4, no sulfur is incorporated in chamber, (B and D) 2.0 % CH_4, 500 ppm H_2S. All of these samples are grown at substrate temperature of 900 °C.

can note the disappearance of diamond peak right at 300 ppm of hydrogen sulfide concentration. The relative heights of the Raman peaks (D- and G-bands) differ in general. The difference among the Raman spectra can be explained by the sulfur additions. Under the specific growth condition considered in this study, sulfur tends to introduce disorder and defects considerably, similar to nitrogen incorporation, which induces graphitization of carbon films [22-24]. Changes in the surface morphological features are apparent from SEM and AFM techniques (see Figure 2). The ball-like morphology

Figure 3. Electron filed emission I-V curves for the S-assisted nanocrystalline carbon thin films as a function of sulfur concentration ([S]) deposited by hot-filament CVD. The dotted line (---) is the reference current (1 nA) to define the turn-on field (E_c).

transforms to fine-grained on S-addition and the surface becomes relatively smoother. The grain size estimated using AFM increased from 20 to 60 nm upon decreasing the sulfur concentration. In addition, the grain size distributions range from 20-60 nm to 100-150 nm. The rms surface roughness estimated from AFM becomes reduced from 64 nm (for intrinsic) to 25 nm (for S-assisted). For a particular hydrogen sulfide concentration of 500 ppm and a growth temperature of 900 °C, the amount of sulfur introduced to the films was quantified to be around 0.5 % - 1.0 % from EDX and XPS surface analytical techniques.

Figure 3 shows the typical I-V characteristics obtained experimentally for these n-C: S films as a function of sulfur concentration. The measurements were not taken above 20-25 µA in order to prevent 'breakdown'. The lowest turn-on field achieved is ~ 4.5 – 5.0 V/ µm for the sample grown with 500 ppm H_2S, while for the 100 ppm it is 10.5 -11.5 V/µm, which is around the same as for the intrinsic material (n-C). On qualitative comparison with the previous studies using nitrogen and oxygen, the films grown with higher nitrogen to oxygen ratio have shown a great promise in terms of EFE characteristics, in contrast to lower ratios and even oxygen alone [21-25]. Therefore, the

Figure 4. Shown is the variation of E_c and sulfur concentration. The dotted line is shown to guide the eye.

results obtained hereby are closer to nitrogen-like than oxygen-like [20]. The reason(s) for this behavior or characteristics is not apparent and is therefore a subject of speculation. Because of sulfur addition to the CVD process, there is a substantial amount of structural defects that become introduced distorting the lattice. These defects create additional energy bands within the bandgap of diamond and thus contribute electrons for emission at low electric fields. As initially addressed by Zhu et al. [26], the more the defective the diamond and diamond-like material, the better the emitter it is. Combining these results with the influence of sulfur concentration, two interesting noteworthy features can be seen from Figure 3: (i) the impact of sulfur concentration on the threshold field (E_c); the higher the sulfur concentration, the lower the E_c, and (ii) the exponential increase of the current amplitude at the highest sulfur concentration. This may be attributed to the tailing of the valence band maxima and conduction band minima, upon the introduction of midgap states. This scenario is more probable at higher sulfur concentration than at the lower ones. The reduction in E_c with sulfur concentration is plotted in Figure 4, which provides an inverse correlation between E_c and sulfur concentration within the range of our study. Similar observations have also been found for nitrogen-doped amorphous carbon materials [20-24] and metal-oxide-semiconductor (MOS) structures by several authors [27-29].

CONCLUSIONS

The field emission properties for the S-assisted films were investigated as a function of sulfur concentration. Low-field electron emission values were observed at 4.5-5.0 V/μm for films grown at the highest sulfur concentration (500 ppm H_2S). On comparing these results with the intrinsic material, the E_c is found to be almost half, thus indicating a strong effect of sulfur addition. The S-assisted films are relatively fine-grained and smoother. Under the specific growth condition considered in this study, sulfur tends to introduce disorder and defects considerably, similar to nitrogen incorporation. Thus sulfur incorporation in carbon films behaves similar to nitrogen doping in disorder or amorphous carbon thin films. An inverse correlation between E_c and sulfur concentration was found. The addition of sulfur enhances the field emission properties of n-C rendering it a viable cold cathode material.

REFERENCES

1. C. A. Spindt, I. Brodie, L. Humphrey and E. R. Westerberg, J. Appl. Phys. **47**, 5248 (1976).
2. J. A. Castellano, in *Handbook of Display Technology* (Academic Press, New York, 1992).
3. J. E. Jaskie, Mater. Res. Bull. **21**, 59 (1996).
4. J. Robertson, Mater. Res. Soc. Symp. Proc. **509**, 83 (1998) and references therein.
5. A. Hart, B. S. Satyanarayana, W. I. Milne and J. Robertson, Diamond and Related Materials **8**, 809 (1999).

6. A. V. Karabutov, V. I. Konov, S. M. Pimenov, E. D. Obraztsova, V. D. Frolov, V. G. Pereverzev and A. A. Smolin, J. Wide Bandgap Materials **7**, 68 (1999).

7. F. J. Himpsel, J. A. Knapp, J. A. Van Vechten and D. E. Eastman, Phys. Rev. B **20**, 624-627 (1979); J. Van der Weide and R. J. Nemanich, Appl. Phys. Lett. **62**, 1878 (1993).

8. J. Y. Shin, H. K. Baik and K. M. Song, J. Appl. Phys. **87**, 7508 (2000).

9. G. A. J. Amartunga, S. R. P. Silva, Appl. Phys. Lett.**68**, 2529 (1996); M. W. Geis, N.N. Efremow, J.D. Woodhouse, and M.D. McAleese, IEEE Trans. ED Lett. **12**, 456 (1991).

10. K. Okano, S. Koizumi, S. R. P. Silva, and G. A. J. Amartunga, Nature, **381**, 140 (1996).

11. C. Wang, A. Garcia, D. C. Ingran, M. Lake and M. E. Kordesch, Electronics Lett. **27**,1459 (1991).

12. A. A. Tallin, L. S. Pan, K. F. McCarty, T. E. Felter, H. J. Doerr, R. F. Bunshah, Appl. Phys. Lett. **69**,3842 (1996).

13. B. F. Coll, J. E. Jaskie, J. L. Markahm, E. P. Menu, A. A. Talin, P. VonAllmen, Mater. Res. Soc. Symp. Proc. **498**, xx (1998).

14. J. Shiao, C. A. Zorman and R. W. Hoffman, Mater. Res. Soc. Symp. Proc. **349**, 465 (1994).

15. R. Kalish, A. Reznik, C. Uzan-Saguy and C. Cytermann, Appl. Phys. Lett. **76**, 757 (2000) and references therein.

16. D. S. Dandy, Thin Solid Films **381**, 1 (2001).

17. M. N. Gamo, C. Xiao, Y. Zhang, E. Yasu, Y. Kikucji, I. Sakaguchi, T. Suzuki, Y. Sato and T. Ando, Thin Solid Films **382**, 113 (2001).

18. S. Gupta, B. R. Weiner and G. Morell, Diamond and Related Materials 2001 (in Press); S. Gupta, B. L. Weiss, B. R. Weiner and G. Morell, Mater. Res. Soc. Symp. Proc. xx (2001) (to be published).

19. O. Groning, O. M. Kuttel, P. Groning, and L. Schlapbach, J. Vac. Sci. Technol. B **17**, 1970 (1999) and references therein.

20. B. L. Weiss, A. Badzian, L. Pilione, T. Badzian and W. Drawl, J. Vac. Sci. Technol. B **16**, 681 (1998).

21. R. J. Nemanich, J. T. Glass, G. Luckovsky, and R. E. Sroder, J. Vac. Sci. Technol. A **6**, 1783 (1988).

22. A. C. Ferrari and J. Robertson, Phys. Rev. B **61**, 14 095 (2000).

23. S. Bhattacharyya, K. Walzer, H. Hietschold and F. Richter, J. Appl. Phys. **89**, 1619 (2001).

24. J. Shiao, C. A. Zorman and R. W. Hoffman, Mater. Res. Soc. Symp. Proc. **349**, 465 (1994).

25. R. Haubner, S. Bohr and B. Lux, Diamond and Related Materials **8**, 171 (2000).

26. I. H. Shin and T. D. Lee, J. Vac. Sci. Technol. B **18**, 1027 (2000).

27. W. Zhu, G. P. Kochanski and S. Jin, Mater. Res. Soc. Symp. Proc. **509**, 53-58 (1998); W. Zhu, G. P. Kochanski, S. Jin and L. Seibles, J. Vac. Sci. Technol. B **14**, 2011 (1996).

28. N. S. Xu, J. Chen and S. Z. Deng, Appl. Phys. Lett. **76**, 2463 (2000).

29. G. Pananakis, G. Ghibando, R. Kies and C. Papadas, J. Appl. Phys. **78**, 2635 (1995).

EFFECT OF METAL BACK CONTACTS ON TETRAHEDRAL AMORPHOUS CARBON FILMS GROWN USING THE CATHODIC ARC PROCESS.

B.S.Satyanarayana[@], H.Takahashi[*], T.Narusawa[*] and A.Hiraki.
KUT Academic & Industrial Collaboration Centre, Kochi University of Technology, Kochi, 782-8502, Japan.
[*]Electronic and Photonic Systems Engineering Dept.
[@]Also- Sistec Co Ltd, Nankoku-Shi, Kochi, 783 0014, Japan.

ABSTRACT

Reported here is a study on the effect of different metal back contacts on the electrical and structural properties of the tetrahedral amorphous carbon (ta-C). The films were grown using a pulsed cathodic arc system. Ta-C films were deposited simultaneously on silicon substrate, precoated with the following metals, namely aluminium (Al), gold (Au), chromium(Cr), molybdenum (Mo), copper (Cu), tungsten (W) and titanium(Ti). The electrical measurements and Raman response show that the back contact does influence the properties of ta-C films. These results are analysed with respect to our earlier report regarding the influence of back contacts on field emission from similar ta-C films.

INTRODUCTION

Tetrahedral amorphous carbon (ta-C) is being studied with great interest for use in diverse areas including electronics, vacuum microelectronics, sensors, MEMS and tribology.[1-4] The ta-C films have been grown using a wide variety of processes including, Filtered cathodic vacuum arc(FCVA) - direct and pulse source, Pulsed laser ablation deposition (PLAD), Mass selected ion beam(MSIB) deposition and Electron cyclotron wave resonance (ECWR) process. The interest in ta-C films, stems from the possibility of tailoring the material properties, varying from highly diamond-like (sp^3)[1-5] to highly graphite-like (sp^2)[6] materials including fullerenes[7] and nanotubes[8] by varying the growth conditions. Further in general, most of these processes are room temperature process, allowing for the use of low cost substrates like glass.

Considering the amount of ta-C work reported in literature, and the increased importance of ta-C films and carbon films in general, it is surprising to note that there are very few   reports on the effect of metal back contacts, on the properties of the ta-C films. Especially with the enhanced interest in carbon based materials for use as field assisted electron emitters[9-15] we believe there is an urgent need for study on the effect of back contacts. In the case of field emitters, the main factors that could influence emission are the barrier or interface at the back, the transport of carrier through the film and the nature of the front surface.   Among the three factors mentioned above, the aspect that has been less reported is the effect of back contacts on field emission. One of the first report on the effect of back contacts on field emission from ta-C films was by Hart et.al[16]. They had reported that the emission threshold field did not show any consistent trend or dependence on the back contacts. The threshold field was defined as the field
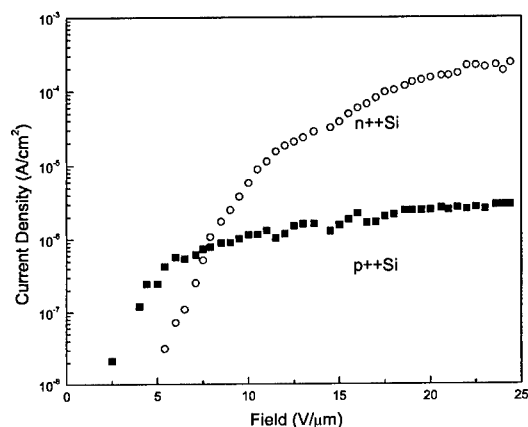
Figure 1. Field emission current density Vs applied field plot for ta-C films deposited on n++ and p++ Si substrates.

at which an emission current density of 1 $\mu A/cm^2$ was obtained [9]. However at lower current densities Satyanarayan[17] had shown that the back contact did have an influence on the emission current at a given field. Shown in figure 1 is the field emission characteristics of a highly sp^3 bonded ta-C films grown on p++ and n++ silicon substrates. It can be seen from the figure that the onset of emission is at quite low fields in the case of p++ Si substrate as compared to the n++ Si substrate. Though at the defined threshold of 1 $\mu A/cm^2$, the fields are nearly similar. Lower field emission from ta-C films deposited on P - type silicon substrates has also been reported by Cheah et.al[18]. Recently Rupesinghe et.al[19] reported observing difference in emission current at lower fields. Using *in situ* x-ray photoelectron spectroscopy and optical spectroscopy Rupesinghe et.al[19] measured the valence and conduction band offsets for ta-C films grown on *p* and *n* type Si. From the band measurements they showed the existence of a barrier and thus confirming the difference in the emission currents at the lower fields in the case of figure1. Suggesting a possible influence of the back interface on field emission from ta-C films. Also Arena et.al [20] have reported observing nanoclusters of carbon in the case of ta-C films grown on aluminium. While the ta-C films grown under identical conditions on silicon substrates were atomically smooth. Thus further indicating some dependence of the material property on the nature of the substrate or metal back contacts.

The cathodic arc process used for material growth, in all the work discussed above, is an highly energetic process. The film growth is believed to occur from the sub-surface, through a process of sub-implantation of the ions. Thus leading to a highly stressed films depending on the growth conditions[1-6]. The energetic ions during the process of sub-implantation may interact differently with the substrate, depending on the nature of substrate material or the metal back contact. Hence the study on the effect of back contacts is very essential. We report in this paper a study on the use of tungsten, titanium, aluminium, chromium, copper, gold, and molybdenum as back contact materials for the growth of ta-C films. Reported here is the

electrical and structural properties of the ta-C films grown on substrates with different metal back contacts. Raman spectroscopy was used to study the structural properties and Rutherford Back Scattering was used to estimate the possible effects at the interface.

EXPERIMENTAL CONDITIONS

First the metals for study as back contacts were deposited on to cleaned silicon substrates. The metals titanium, aluminium, chromium, copper and gold were deposited using thermal evaporation process in a vacuum of 10^{-6} torr. The metals tungsten and molybdenum were sputter coated on to the silicon substrate. Prior to deposition, the metal surfaces were cleaned in an argon plasma to remove any possible oxide layer. Then to eliminate the run to run variations in film quality all the substrates were coated simultaneously in a pulsed cathodic arc system at a substrate bias of 80V. The energy of the deposited ion is defined by the substrate bias.[1-4]The thickness of the ta-C films grown were nearly 50 nm.   Next the films were prepared for the electrical measurements. The electrical measurements were made using a sandwich configuration consisting of "back metal contact/ta-C film/top metal contact". The top contact consisted of a two layer coating of nearly 30nm of gold and 60nm aluminium, deposited by a thermal evaporation process. The measuring area of the device was defined by using a contact mask with circular holes of 250 micron diameter. The electrical measurements (I- V) were carried out using Keithley multimeter with an in-built power source. The Raman measurements were carried out using a 515nm excitation, in a Renishaw micro Raman Spectrometer .

RESULT AND DISCUSSION

Shown in figure 2 are the forward and reverse, current - voltage characteristics of some of the ta-C films deposited simultaneously on different back contact metal substrates. It can be seen from the figure that there is not much difference between the forward and reverse currents. The contacts seem to be ohmic in nature. However the measured currents are different. Shown in figure 3 is the variation of the measured forward current at 0.5 V applied voltage with the work function of the various back contact metals used as substrate.
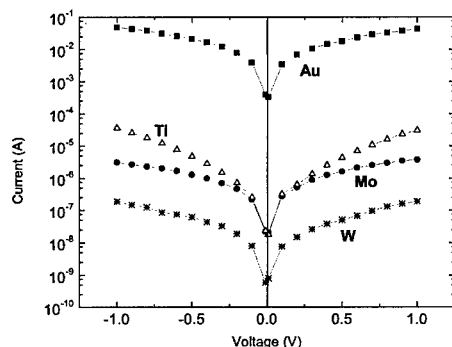
Figure 2 Current –Voltage plots of tetrahedral amorphous carbon (ta-C)
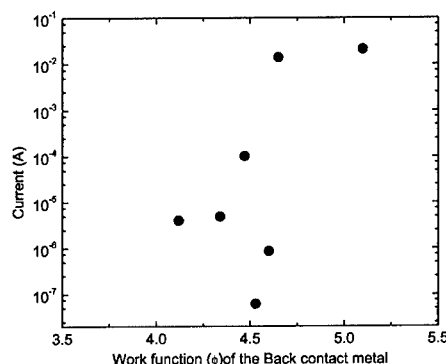
Figure 3 Variation of the measured forward current (at 0.5 V applied voltage) of ta-C
films, with the work function of the metals used as back contact on the substrate.

Figure 3 shows that even though the ta-C films were deposited simultaneously on to substrates
with different metals as back contact, the measured currents are not the same. However there
seems to be no direct co-relation between the measured forward current at a given voltage and
the work function of the back contact metal. But the figures 2 and 3 suggest that the properties
of ta-C films, even if deposited simultaneously are influenced by the back contact metal or the
substrate material. The variation in the current, could be due to numerous factors including
possible oxide layer on the contact, inter-mixing of the carbon and metal atoms at the interface,
different thermal gradients during depositions on different metal surfaces, change in stress during
growth on different substrates and change in sp^2/sp^3 bonding ratio of the ta-C films. Thus in an
effort to further understand the possible influence of the back contact metal on the material
properties of ta-C films, Raman measurements were carried out. The Raman response and the
peaks have been shown to be a good indicator of the structure and composition of the carbon
based films [21,22 and references there in].

The Raman measurements on the ta-C films deposited on various back contact metal
substrates show that the films are amorphous in nature. Shown in figure 4 is the possible relation
between the work function of the back contact metal and the Raman G_{peak} position. From the
figure it is difficult to discern a trend or relation. However the fact that the G_{peak} position has
shifted with change in the back contact metal shows that the composition of the material is
influenced. Ferrari et.al in their elegant three stage model[21] for the interpretation of the Raman
spectra in the case of carbon films, suggest that the G_{peak} position may either increase or
decrease with change in sp^3 bonding, depending on the percentage of sp^3 bonds. The G_{peak}
position is more influenced by the sp^2 phases. Further it does not depend on the stress in the case
of as grown ta-C films. J.K.Shin et.al[22] have reported that the G_{peak} position is shifted due to
the stress in ta-C films. In the present experiment, the ta-C films were deposited simultaneously
on all the back contact metal substrates. Yet, irrespective of whether the influence is due to
clustering or stress, a shift in the Raman G_{peak} was observed. Thus showing that the film
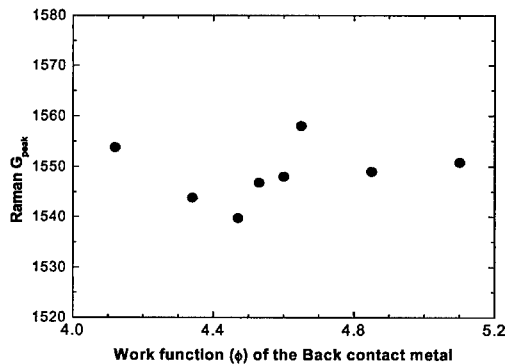property is influenced by the substrate or the back contact metal.

1580

1570

1560

Raman G_{peak} 1550

1540

1530

1520
4.0 4.4 4.8 5.2

Work function (ϕ) of the Back contact metal

Figure 4 Shift in the Raman G_{peak} of ta-C films with the
Work function (ϕ) of the back contact metal.

Further Rutherford Back Scattering experiments were carried out to study the effect at interfaces between the back contact metal and carbon film. The measurements show that in some cases the inter-mixing of the metal and carbon atoms could be up to 20nm. A detailed report on this will be presented else were. Recently Koserev et.al[23] have reported the effect of back contact on field emission from carbon films grown using very high frequency chemical vapour deposition at low temperature. They observed that there is no direct correlation between the contact metal work function and the emission current. However the back contact roughness had a substantial effect on the emission threshold field. Thus indicating that the back contacts could influence the film properties. Hence with increased use of carbon and nanostructured carbons films grown using energetic ion assisted low temperature or room temperature processes in diverse application, there is a need for more detailed study of the influence of back contacts.

CONCLUSION

We have carried out a study on the effect of different back contact metals on the electrical and structural properties of the tetrahedral amorphous carbon (ta-C). We find that even though the carbon films were deposited simultaneously on to different substrates,
(i)   There is a difference in the measured current for a given voltage or field,
(ii) All the devices show ohmic behaviour
(iii) The Raman G_{peak} seems to shift for ta-C films deposited on different substrates or back contacts metals, indicating a change in the film composition or sp^2/sp^3 bonding ratio.
(iv) However there seems to be no direct relation to the work function of the material.
(v)   RBS measurements show that the inter-mixing of the metal and carbon atoms could be upto 20nm.
Thus the study shows that even when there is no direct relation, choosing a back contact for carbon has to be done carefully. When using energetic ion assisted processes, even if the process is same, depending on the back contact metal, the properties of the films may vary. The back contact may be chosen based on the film growth process, film thickness requirement and application.

REFERENCES

1. D.R.Mckenzie, Rep.Prog.Phys, **59**, 1611, (1996).
2. W.I.Milne , J.Non.Cryst.Solids, **198-200**, 605, (1996).
3. J.Robertson, Amorphous carbon : State of art, Ed. S R P Silva J.Robertson, W.I.Milne & G.A.J.Amaratunga, , World Scientific p-32, (1998).
4. Y.Lifshitz, Diamond Relat. Mater. **8**, 1659, (1999).
5. P. J. Fallon, V. S. Veerasamy, C. A. Davis, J. Robertson, G. A. J. Amaratunga, W. I. Milne, and J. Koskinen, Phys. Rev. B **48**, 4777 (1993).
6. B S Satyanarayana, J Robertson, W I Milne, J. App. Phys. **87**, 3126, (2000)
7. F.Diederich, R.Ettl, Y.Rubin, R.L.Whetten, R.Beck, M.Arvarez, S.Anz, D.Sensharuma, F.Wudl, K.C.Khemani, & A.Koch. Science **252**, 548 (1991).
8. S.Iijima, Nature **354**, 56 (1991).
9. B S Satyanarayana, A Hart, W I Milne & J Robertson, App Phys Lett **71**, 1430 (1997)
10. A.R. Krauss, O. Aiciello, T. D. Corrigan, and R. P. H. Chang, J. Vac. Sci. Technol. B **17**, 705 (1999)
11. W. S. Xu, T. Zheng, and R. V. Latham, J. Phys. D **26**, 1776 (1993).
12. A.A. Talin, T. E. Felter, T. A. Friedmann, J. P. Sullivan, and M. P. Siegal, J. Vac. Sci. Technol. A **14**, 1719 (1996)
13. G.A.J.Amaratunga, M.Baxendale, N.Rupasinghe, I. Alexandrou, M.Chhowalla, T.Butlere, A.Munindradasa, C.J.Kiley, L.Zhang, T.Sakai, New Dia. & Frontier Carbon tech. **9**, 31, (1999).
14. O.N.Obraztsov, I.Yu.Pavlovsky and A.P.Volkov, J. Vac. Sci. Technol. **B 17** , 674, (1999).
15. A.C.Ferrari, B.S.Satyanarayana, P.Milani, E.Barborini, P.Piseri, J.Robertson and W.I.Milne. Europhys. Lett, **46**, 245 (1999).
16. A.Hart, B.S.Satyanarayana, J.Robertson & W.I .Milne , Appl. Phys. Lett. **74**, 594,(1999).
17. B.S.Satyanarayana, Ph.D thesis, Univeristy of Cambridge, UK, (1999).
18. L.K.Cheah, X.Shi, B.K.Tay, S.R.P.Silva & Z.Sun, Diamond Relat. Mater. **7**, 640, (1998).
19. N. L. Rupesinghe, M. Chhowalla, G. A. J. Amaratunga, P. Weightman, D. Martin, P. Unsworth, and J. Murray, App Phys Lett,**77**, 1908, (2000).
20. C. Arena, B. Kleinsorge, J. Robertson, W. I. Milne, and M. E. Welland, J. Appl. Phys. **85**, (1999) 1609.
21. A.C. Ferrari and J. Robertson Phys.Rev.B. **61**, 14095, (2000)
22. Jin-Koog Shin,Churl Seung Lee,Kwang-Ryeol Lee, and Kwang Yong Eun, Appl Phys Lett **78**, 631, (2001).
23. A.I. Kosarev, A. N. Andronov, A. J. Vinogradov, T. E. Felter, A. N. Titkov, I. V. Makarenko, M. Z. Vaqar, S. V. Robozerov, M. V. Shutov, J. Vac. Sci. Technol. **B 19** , 39, (2001).

FIELD EMISSION SITE DENSITIES OF NANOSTRUCTURED CARBON

J B Cui, J Robertson, W I Milne,
Department of Engineering, Cambridge University, Cambridge CB2 1PZ, UK

ABSTRACT

The field emission properties of nanostructured carbon films deposited by cathodic vacuum arc in a He atmosphere have been studied by measuring the emission currents and the emission site density. The films have an onset field of ~3 V/μm. The emission site density is viewed on a phosphor anode and it increases rapidly with applied field. It is assumed that the emission occurs from surface regions with a range of field enhancement factors but with a constant work function. The field enhancement factor is found to have an exponential distribution.

INTRODUCTION

Electron field emission from various carbon films, such as chemical vapour deposited (CVD) diamond, CVD graphite, carbon nanotubes, amorphous carbon and nanostructured carbon is of great interest because it occurs from flat films without the need to form microtips [1-19]. Emission from these materials can occur for applied fields of 10 volts per micrometer or less. The emission is however discontinuous, and occurs as the series of spots [20]. The emission site density is therefore an important parameter, particularly for displays. This paper describes field emission properties of nanostructured carbon films deposited at room temperature by cathodic arc. The emission I-V curve and the emission site density were both measured. The discontinuous nature of the emission indicates that emission occurs preferentially from different parts of the surface. We have found that the work function for these carbon films is quite large and varies from 4.5 to 5.0 eV. We propose that the preferential emission therefore arises from a variation in the local field enhancement factor. The emission can be described by a distribution of field enhancement factors.

EXPERIMENT

The nanostructured carbon films were deposited at room temperature using a cathodic vacuum arc system. The base pressure of the deposition chamber was about 5×10^{-7} mbar and the deposition pressure could be varied from 1×10^{-6} to 1 mbar by introducing helium gas into the chamber. The He thermalises the carbon ions and atoms and allows them to form fullerene-like clusters [21], which are incorporated in the growing film. The thickness of the carbon film is between 10 and 100 nm. The films are deposited onto conductive Si substrates on which there is a 1.5 μm thick resistive ballast layer of photoresist. The function of the ballast layer is to limit the emission current from individual emission spots, and to allow the range of the emission sites to be seen, without saturating the phosphor screen [22]. Ballast resistors are frequently used in Spindt tip field emission devices to even out the current distribution and to prevent excessive currents [23].

The emission is measured in a parallel plate configuration. The anode-to-sample spacing was 50 or 100 μm by using PTFE spacers. An ITO (indium-tin-oxide) or phosphor coated glass is used as an anode to collect the emitted current. The emission spots are displayed on the anode and recorded by a CCD camera while the
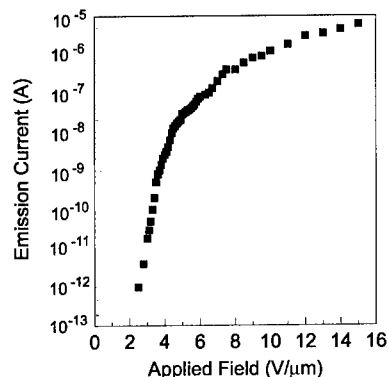
Fig. 1. Field emission I-V curve of carbon film on Si wafer with a ballast layer. Inset is the corresponding Fowler-Nordheim plot.

emission I-V curve is measured. The pressure in the measurement chamber is maintained at 10^{-7} mbar during measurements by a turbo-molecular pump. It should be emphasised that no conditioning process was used for the field emission measurement, unlike is often needed for DLC films [15], because the emission of the nanostructured carbon samples is stable and repeatable.

Fig. 2. Field emission images at different applied fields: (a) 4, (b), 6, (c) 8, (d) 11, (e)15, and (f) 20 V/μm.

RESULTS AND DISCUSSION

Fig 1 shows the measured emission current as a function of applied field. The detection limit of our system is ~1 pA. The current rises rapidly above 3 V/μm. The current then rises more slowly above 1 μA due to the effect of the ballast layer. The current limiting causes a downward curvature in a Fowler-Nordheim plot.

Fig. 2 shows the emission image recorded on a CCD camera at increasing applied fields. The emission site density (ESD) was counted at each field after digitisation, and this is plotted against applied field in Fig. 3.

The emission current density J (A/m²) is expected to obey the Fowler and Nordheim law

$$J = A \cdot \frac{(\beta F)^2}{\phi} \cdot \exp\left(-\frac{B\phi^{3/2}}{\beta F}\right) \qquad (1)$$

F is the applied electric field in V/m, β is the field enhancement factor and φ is the potential barrier for the emission surface in eV. A and B are constants equal to 1.56×10^{-2} and 6.83×10^9, respectively. To a first approximation, β=h/r, where h is the height of the emission tip and r the radius of curvature of the tip.

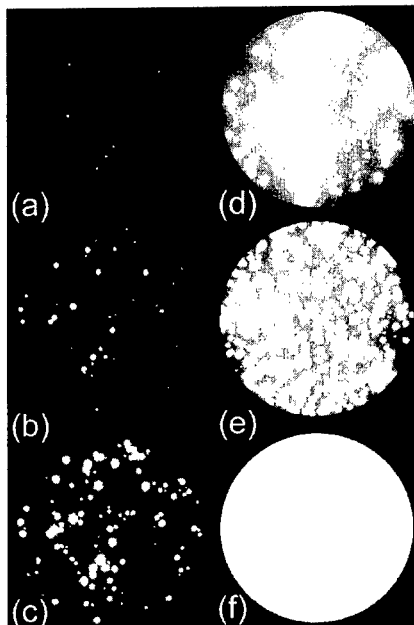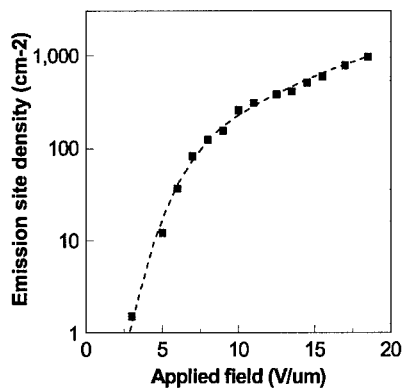Fig. 3 Field emission site density as
a function of applied field. The solid
line is a fit for eq (2).
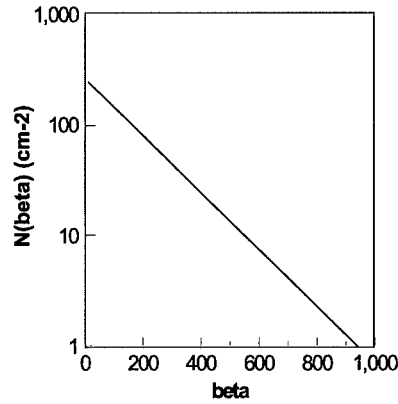
Fig. 4. Emission site density versus
field enhancement factor β. The solid
line is the fit by eq.(4).

The variation of emission site density with applied field F in Fig. 3 can be fitted
by the probability distribution

$$N(F) = N_0 \exp(-\frac{b}{F}) \qquad (2)$$

b is a constant. This function is the curve plotted in Fig. 3.

In principle, the ESD could depend on many factors. However, the functional
form of eq (2) suggests a simple model. The emission depends on two parameters in
(1), the barrier height ϕ and the field enhancement factor β. There has been
considerable effort to identify the value of the emission barrier in carbon systems, in
part to answer the fundamental question of why emission occurs at relatively low
fields [23]. In the case of diamond, the fully hydrogenated surface has a negative
electron affinity and the work function can be lower than 3.5 eV [25,26]. Diamond-
like carbons are found to have work functions of 4.3 to 5 eV, and they are less
sensitive to the surface termination than is diamond [14]. Nanotubes also have a work
function of order 5 eV [8]. The work function of the films in this study was measured
by Kelvin probe and it lies in the range 4.7±0.1 eV [27].

We therefore approximate that the *local* barrier ϕ is constant, and attribute the
discontinuous emission to a variation in the local field enhancement factors at the
sites. Following Groning et al [8], if an emission site becomes visible at a certain
value of current, then (1) implies

$$F_{loc} = \beta F = const \qquad (3)$$

Thus, the distribution (2) can be expressed as an exponential distribution of β values

$$N(\beta) = N_0 \cdot \exp(-\frac{\beta}{\beta_0}) \qquad (4)$$

where β_0 is a constant. This distribution is plotted in Fig. 4.

Groning et al [8] used a similar analysis to describe the ESD in carbon nanotube films. In carbon nanotubes, if we assume that the tubes have a similar radius and length, then the β distribution arises from the effect of inter-tube screening. The presence of nearby nanotubes screens the electric field intensification at a tube tip [9], unless the tube separation d is about over twice the tube height h, d>2h. This is not true in typical nanotube mats, and this accounts for the observed β distribution. It is likely that a similar effect occurs in nanostructured carbon. The entire surface has a similar work function. There may be many regions with a large β. The screening effect of one on the other and fractal effects in the surface curvature are likely to lead to a Poisson distribution of β values as seen here.

The total emission current, I, can be estimated by adding the current from all sites. If we assume that once on, a site emits a current given by eq (1), then

$$I = \int J(\beta).S.N(\beta).d\beta = \int_0^{\beta_{max}} J \cdot S \cdot \exp(-\frac{\beta}{\beta_0})d\beta \tag{5}$$

where the β_{max} is the maximum β that is observed experimentally, S is the emission area of one site. An effect of the distribution of β's is that while each emission site will obey the Fowler-Nordheim (FN) equation, the total emission current from (5) does not. The FN plots for each emission site is a straight line with a slope of $6.83 \times 10^9 \phi^{1.5}/\beta$. The effect of the β distribution is to produce a slight upward curvature of the FN plots. This contrasts with the downward curvature at high currents caused by current limiting by the ballast layer.

A more detailed analysis of FN plots with a β distribution was given by Levine [28]. He described the case of emission from Spindt tips, and assumed a gaussian distribution of a 'tip bluntness' parameter B in the reduced FN equation

$$J = A.\exp(-\frac{B}{V}) \tag{6}$$

with

$$N(B) = N_0 \exp(-\frac{(B-B_0)^2}{2\sigma^2}) \tag{7}$$

The advantage of a gaussian distribution is that the integral (5) is now analytic. Qualitatively, β is proportional to 1/B, so our exponential distribution corresponds to the lower wing of the gaussian distribution of B.

REFERENCES

1. N.S. Xu, R.V. Latham, Y.Tzeng, Electron. Lett.**29**, 1596 (1993).
2. A. A. Talin, L. S. Pan, K. F. McCarty, T. E. Felter, Appl. Phys. Lett. **69**, 3842(1996).

3. F Lacher, C Wild, D Behr, P Koidl, Diamond Related Mats **6** 1111 (1997)
4. D.Zhou, A.R. Krauss, D.M. Gruen, J.Appl.Phys. **83**, 4546(1997).
5. W. Zhu, G.P. Kochanski, S. Jin, Science **282**, 1471 (1998).
6. K. A. Dean and B. R. Chalamala, Appl. Phys. Lett. **76**, 375(1999).
7. W Zhu, C Bower, O Zhou, G Kochanski, S Jin, App Phys Lett **75** 873 (1999)
8. O Groning, O M Kuttel, C Emmenegger, P Groning, L Schlapbach, J Vac Sci Technol B **18** 665 (2000).
9. L Nilsson, O Groning, C Emmenegger, O Kuttel, E Schaller, L Schlapbach, H Kind, J M Bonard, K Kern, App Phys Lett **76** 2071 (2000)
10. V I Merkulov, D H Lowdnes, L R Baylor, J App Phys **89** 1933 (2001)
11. J M Bonard, N Weiss, H Kind, T Stockli, L Forro, K Kern, A Chatelain, Advanced Mats 13 184 (2000)
12. J M Bonard, H Kind, T Stockli, L O Nillson, Solid State Electronics (2001)
13. B. F. Coll, J.E. Jaskie, J.L. Markham, E.P.Menu, A.A. Talin, and P. von Allmen, Mater. Res. Soc. Symp. Proc. **498**, 185 (1998).
14. V I Merkulov, D H Lowndes, L R Baylor, App Phys Lett **75** 1228 (1999)
15. B S Satyanarayana, J Robertson, W I Milne, J App Phys **87** 3126 (2000)
16. A Ilie, A Hart, A J Flewitt, J. Robertson, W I Milne, J App Phys **88** 6002 (2000)
17. A N Obratztsov, I Y Pavlovsky, A P Volkov, J Vac Sci Technol B **17** 674 (1999)
18. B.S. Satyanaryana, A. Hart, W.I. Milne, and J. Robertson, Appl. Phys. Lett. **71**, 1430 (1997).
19. A Hart, B.S. Satyanarayana, W. I. Milne, and J. Robertson, Appl. Phys. Lett. **74**, 1594 (1999).
20. A A Talin, in 'Amorphous Carbon, State of Art', ed S R P Silva et al, (World Scientific, Singapore, 1998)
21. P Milani, S Iannotta, 'Cluster beam synthesis of nano-structured materials', (Springer, Berlin, 1999)
22. J.B. Cui, J. Robertson, and W.I. Milne, J App Phys **89** 3490 (2001).
23. A Ghis, R Meyer, P Raumbaud, F Levy, T Leroux, IEEE Trans ED **38** 2520 (1991)
24. J Robertson, J Vac Sci Technol B 17 659 (1999), Mat Res Soc Symp Proc **621** xxx (2000)
25. J. B. Cui, J. Ristein, M. Stammler, K. Janischwosky, G. Kleber, and L. Ley, Diamond Rel. Mater. 9, 1143 (2000)
26. R.Schlesser, M.T. McClure, W.B. Choi, J.J.Hren, and Z. Sitar, Appl. Phys. Lett. **70**, 1596(1997).
27. A Ilie, A. C Ferrari, T Yagi, J. Robertson, J App Phys (Aug 1, 2001)
28. J. D. Levine, J. Vac. Sci. Technol. **B 13** 553 (1994).

Diamond

Synthesis of Ultrathin ta-C Films by Twist-Filtered Cathodic Arc Carbon Plasmas

André Anders[1] and Ashok V. Kulkarni[2]
[1]Lawrence Berkeley National Laboratory, University of California, Berkeley, California 94720
[2]Read-Rite Corporation, 44100 Osgood Road, Fremont, California 94539

ABSTRACT

The application of cathodic-arc-deposited films has been very slow due to the infamous macroparticle problem. We report about the application of the open Twist Filter as the key component to an advanced filtered cathodic arc system. Ultrathin tetrahedral amorphous carbon (ta-C) films have been deposited on 6 inch wafers. Film properties have been investigated with respect to application in the magnetic data storage industry. Films can be deposited in a reproducible manner where film thickness control relies on arc pulse counting once deposition rates have been calibrated. Films of 3 nm thickness have been deposited that passed acid and Battelle corrosion tests. Monte Carlo Simulation of energetic carbon deposition shows the formation of an intermixed transition layer of about 1 nm. The simulation indicates that because the displacement energy of carbon is not smaller than of magnetic materials, films thinner than 2 nm are either not high in sp^3 content or represent a carbidic phase, i.e. contain substrate material. The last finding is general and not limited to cathodic arc deposited ta-C films.

INTRODUCTION

Diamondlike films are characterized by an outstanding combination of advantageous properties: they can be very hard, tough, super-smooth, chemically inert, well adherent to the substrate, and compatible with lubricants. They can be deposited fast, efficiently, at low cost, and on room temperature substrates. The various deposition methods result in a variety of diamondlike films. Widely used is hydrogenated diamondlike carbon (DLC or a-C:H), nitrogen-doped amorphous carbon (a-C:N) or amorphous carbon nitride (CN_x) [1-3], hydrogenated carbon nitride (CH_xN_y), non-hydrogenated amorphous carbon (a-C), silicon-doped amorphous carbon (a-C:Si) or silicon carbide (SiC) [4], and metal-doped amorphous carbon (a-C:Me) [5]. Amorphous carbon films (a-C) often have a very high percentage of tetrahedral (sp^3) bonding and therefore they are referred to as tetrahedral amorphous carbon (ta-C).

Ultrathin (< 5 nm) hard carbon films are being used as protective overcoats on hard disks and read-write heads. The tribological properties of the head-disk interface are not only mechanical but also chemical in nature: the overcoat is required to protect the magnetic layer against wear and corrosion [6, 7]. As the areal density (of information stored) increases at a breathtaking rate of about 100% per year [8], the "magnetic spacing" between the magnetic layer of the disk and read/write sensor of the head must decrease. The magnetic spacing includes magnetically dead layers, carbon overcoats, lubrication, pole tip recession, and the fly height. Thinner overcoats allow the head to be closer to the disk, and hence, the size of individual bits to be smaller. Areal densities of 70 Gbit/in^2 have recently been demonstrated in the laboratory, and the industry is working toward 100 Gbits/in^2. The magnetic spacing approaches the sub-10-nm regime and overcoat thickness must shrink to 1-2 nm. Overcoats currently used are sputtered or ion-beam deposited diamondlike carbon films, typically doped with hydrogen or nitrogen. They cease to provide acceptable levels of corrosion protection and wear resistance for films thinner than 4 nm.

The challenge of ultrathin film synthesis is to make the films as thin as possible and still continuous, as opposed to an assembly of islands. There are large variations even within each class of materials, depending on the method and parameters of deposition.

Tribological properties and fracture toughness of ultrathin amorphous carbon coatings (hydrogenated and non-hydrogenated) deposited by different deposition techniques have been compared. Films synthesized by filtered cathodic arc deposition were shown to exhibit good properties even at very small film thickness [9, 10].

Non-hydrogenated tetrahedral amorphous carbon films, ta-C, can be synthesized by argon sputter deposition using a graphite target, by pulsed laser ablation of graphite, by mass-selected ion beam deposition of C^+, or by cathodic arc plasma deposition. The latter can be performed in continuous or pulsed mode. Pulsed filtered cathodic arc plasma deposition has been identified as a promising technique [11]. The greatest challenge is the complete removal of "macroparticles" that are generated at the cathode spot. In this paper, we focus on pulsed filtered cathodic plasma deposition of ta-C films and report about the progress made towards the synthesis of high-quality, ultrathin films suitable for application in the magnetic storage industry.

CATHODIC ARC CARBON PLASMA

Generally, cathodic arc plasmas are fully ionized, often with multiply charged ions present [12]. Cathodic arc carbon plasma is in some respect an exception because the ion charge state is only 1+. However there are a few percent of 2+ at the beginning of each arc pulse [13]. The plasma ions move with supersonic velocity of about Mach number 5, corresponding to kinetic carbon ion energy of about 54 eV [14]. This recent result indicates that the carbon ion energy can be significantly higher than the about 20 eV that is usually quoted [15]. It is known that the ion energy is critical for the properties of ta-C films such as sp^3 content, hardness, Young's modulus, density, and stress (see, for instance, [16]). Very recent (still unpublished) results indicate that the ion energy can further be manipulated for instance with magnetic fields, and carbon ion energies exceeding 100 eV can be achieved without biasing the substrate.

The formation of carbon plasma is unusual for those who are not familiar with cathodic arc plasmas. The arc current, typically 100 A or more, is concentrated at the cathode surface in micron-size cathode spots, i.e. cathode spots are locations of extreme current density. Because most of the voltage drop (~ 20 Volts) is in the cathode fall, the power is concentrated at cathode spots. Power densities can reach 10^{13} W/m^2, leading to explosive transition of solid cathode material to the dense plasma state. This process of often called "arc evaporation" but one should keep in mind that plasma, not neutral vapor, is the result of the powerful phase transition. The dense carbon plasma has a very high pressure, exceeding atmospheric pressure by orders of magnitude, and it expands in the vacuum ambient.

Not only plasma is produced at cathode spots but also debris particles, usually referred to as "macroparticles." For carbon, large chunks of graphite (fractions of millimeters) are sometime ejected from the cathode – it is believed that shock-heated gas inclusions of the graphite cathode contribute to these massive cathode losses. However, smaller macroparticles are much more frequent, and their distribution extends well down into the nanoparticle range [17]. The presence of macroparticles is not acceptable for ta-C films in magnetic storage applications. Macroparticles could lead to crashes of the head as well as to pinholes and defects that will cause ta-C films to fail in corrosion tests.

MACROPARTICLE FILTERS

A common approach to macroparticle removal is based on the vast mass-to-charge difference of macroparticles and plasma particles; see reviews [18-21]. The plasma can be guided out of the line-of-sight from the cathode using curved magnetic fields, employing combined magnetic and electric mechanisms for electrons and ions, respectively. The motion of macroparticles is almost independent of the presence of fields; thus they move along straight trajectories, thereby being separated from the plasma. This concept was originally introduced by Aksenov and coworkers in the late 1970s [22].

In the literature, two basic constructions and filter philosophies have been described. They can be labeled as closed and open filters. The "classic" 90° filter duct [22] employs a duct, i.e. a closed tube, surrounded by a set of magnetic field coils. The interior wall of the duct is equipped with baffles designed to catch or reflect macroparticles. Graphite particles may suffer multiple reflections, and may fracture into several "sub-macroparticles" [21]. Consequently, there is a significant likelihood that carbon macroparticles, or fractions of them, arrive at the substrate via multiple reflections. Additionally, small nanoparticles may be transported through momentum exchanged with ions ("ion wind"). There are a numerous *closed* filters derived from the classic 90° filter, including 45° filters [23], S-filters [24], segmented filters [25], filters of rectangular cross section [26, 27], and out-of-plane double-bent filters [28, 29].

In contrast to conventional closed filters, *open* filters address the issue of particle reflection by removing the particle from the filter and plasma volume via openings [30-32]. Figure 1 shows an S-shaped open filter that consists of a bent solenoid. It is obvious that most macroparticles can leave the plasma volume, and some are removed even if they hit a turn of the magnetic field coil.
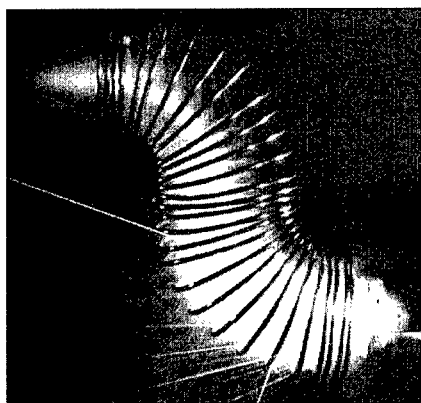
Figure 1 S-shaped open filter guiding carbon plasma from a cathodic arc plasma source (right) to the substrate region (left). Carbon macroparticles are hot and can therefore easily be identified by their bright traces. Open-shutter photograph, arc current 1000 A, pulse length 1 ms.
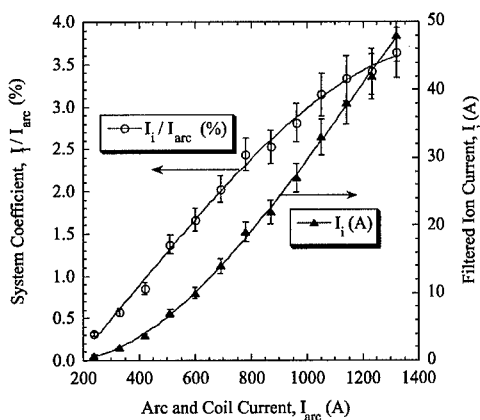

Fig. 2. Output of the Twist Filter prototype as described by the filtered ion current and the system coefficient. Arc and filter-coil are electrically in series.

THE TWIST FILTER SYSTEM

A new open filter design was presented [33] that is essentially a "twisted" S-shaped open solenoid, or "Twist Filter." Twisting refers to a rotation of one bend of the S-filter with respect the other bend.

The design of the system is not a marginal improvement but based on paradigms derived from physical and empirical laws:

1. Plasma losses in filters scale exponentially with the filter path length [30]. Therefore, the filter must be short.
2. Because the filter path is short, its inner radius must be small to prevent a line-of-sight between filter entrance and exit.
3. The plasma source (specifically its cathode) must be small to match the size of the filter entrance, otherwise the plasma produced will not enter the filter.
4. If the cathode is small, it needs to be replenished e.g. via a cathode feed mechanism.
5. If the source and filter are small, heating constraints can be alleviated by operating in a pulsed mode. Pulsed mode could also be beneficial in addressing the "plasma wind" issue.
6. In pulsed mode, the high arc current can be used to generate a strong magnetic filter field that is in perfect synchronization with the plasma production.
7. Repetitively pulsed operation requires simple and very reliable arc initiation such as the "triggerless" mechanism [34]. This mechanism relies on the formation of plasma at a location where the cathode touches a conducting layer that is connected to the anode.
8. The macroparticles that have left the plasma volume must be prevented from reaching the substrate. Therefore, the system needs to have a macroparticle "firewall", i.e. a wall separating source and filter area from the clean substrate area.
9. The system needs to have a designated region in which macroparticles are collected for removal on a regular maintenance schedule. This area is located under the plasma source and filter.
10. The plasma exiting the filtered is highly focused but a uniform deposition over a relatively large area (e.g. wafer of 95 mm diameter) is required. Therefore, a plasma expansion zone and a plasma homogenizer are needed.
11. All parts of the system (source, filter, homogenizer, power supply, firewall, etc) need to be considered as a unit with well-matched parameters.

The Twist Filter system is a consequent realization of the design paradigms. The Twist Filter system consists of several matching components: the cathodic arc plasma source, the Twist Filter, the macroparticle "firewall," a plasma expansion zone, a plasma homogenizer, and a substrate positioning mechanism.

Arc plasma source, filter, and homogenizer are electrically in series and powered by a compact, rack-mounted pulse forming network (PFN) [35]. The cathode of the plasma source is a graphite rod of 6.25 mm diameter. The rod can be slowly and precisely advanced via a micrometer drive to compensate for the erosion at its front face. High arc current and small cathode area lead to uniform erosion of the cathode without spot steering or any other specific means of spot control. The anode is grounded while all other components are free of ground, thus their potentials are in reference to the anode. The anode itself is an open baffle structure made from copper; it serves as a pre-filter: A large fraction of macroparticles are already removed from the plasma when it enters the filter. The repetitively pulsed arcs are initiated by simply switching the high (open-circuit) supply voltage of 1 kV to anode and cathode; a conducting layer on the ceramic between anode and cathode lead to hot-spot and plasma

formation at the cathode. This "triggerless" mechanisms shows exceptional reliability [34]. The arc current is typically 1.5 kA with pulse duration of about 1 ms and a pulse repetition rate of 3 p.p.s. The duration of arc pulses is given by the PFN while all other parameters can easily be adjusted. The base pressure of the vacuum system is about 1 x 10^{-7} Torr but pressure increases during deposition to the 10^{-5} Torr region, presumably due to outgassing caused by heating of the filter and other components.

Due to the design of the Twist Filter [33], the likelihood of macroparticle transport is greatly reduced while the plasma transport is impressive compared to other filter designs. The filtered ion current may reach close to 4% of the arc current (Fig. 2). The ratio of filtered ion current to arc current can be named "system coefficient". For comparison, most filtered arc systems have a system coefficient of about 1%. It is important to realize that one not only needs to reduce macroparticles to a minimum but also maximize the plasma output because only the ratio of filtered plasma to residual macroparticles is what really matters.

The coil turns of the Twist-Filter have a flat cross-section promoting macroparticle reflection towards the outside of the filter volume, i.e., the coil represents a baffle structure (Fig. 3). The Twist Filter has a strong magnetic field (0.25 mT/A) providing excellent plasma confinement. At high currents (> 1 kA), not only electrons but also carbon ions are magnetized. The fringe field at the filter entrance is well suited for source-filter coupling.

The plasma at the exit of the Twist Filter is highly focussed. The streaming plasma expands on its way to the substrate. With special means, a deposited film will have a Gaussian thickness distribution with the thickest area in the center. A magnetic multipole, also known as a magnetic bucket, can be used to flatten the plasma density distribution. Magnetic multipoles can be made from strong permanent magnets or by using a wire structure as shown in Fig. 4. The homogenizer is located in the center between the filter exit and the substrate location.

PERFORMANCE OF THE TWIST FILTER SYSTEM

The Twist Filter System operates with typically 1500 A arc current in 1 ms pulses, giving about 30 A of filtered carbon ion current during the pulse. As usual for pulsed systems, one has to distinguish between instantaneous and average values. The duty cycle is defined by $\delta = t_{on}/(t_{on} + t_{off})$. For instance, when using 3 pulses per second, the duty cycle is 3×10^{-3} or 0.3%, thus the averaged ion current is 90 mA. This is comparable to the output of conventional filtered cathodic arcs that operate in continuous mode. This ion flux corresponds to about 150 pulses that are needed to deposit a 3 nm film on a 6 inch wafer. With 3 pulses per second, one would need a deposition time of about 50 s. Faster deposition is possible and has been demonstrated, but cooling of the filter becomes an issue that must be solved in a next generation system.

Film thickness and graphite cathode rod usage are very reproducible and can be predicted simply by counting arc pulses, provided that cathode advancement is periodically performed and controlled (e.g. every 1000 pulses). The pulse number – thickness relationship is about linear although we found that the output per pulse increases slightly and reproducibly during a deposition run. We attribute this to the increasing cathode temperature. The film thickness was measured by ellipsometry and calibrated by AFM step height measurements.

Film uniformity was a major issue since deviation from the targeted thickness are requested not to exceed 3% (however, one has to realize, that 3% of a nominal thickness of 3 nm is 0.09 nm, that is about half the average bond length between individual carbon atoms of ta-C!). For thicker films (> 10 nm) deposited with the Twist filter system, a uniformity of ±2% could be

achieved while ultrathin films showed somewhat larger non-uniformity. Since the plasma distribution should not depend on the pulse number, it is believed that the ellipsometric determination of film thickness for films under 5 nm is difficult, to say the least. To be complete we need to mention that the substrates were mounted on a rotating holder (20 rpm) and a typical pulse repetition rate was 3 p.p.s.
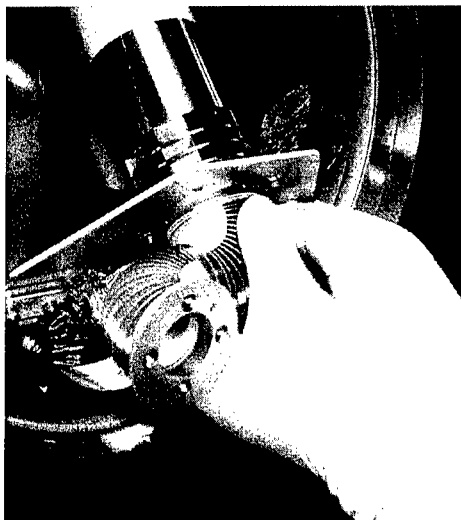

Figure 3. Mounting of the alpha-version Twist Filter to the plasma source. Note the compact size compared to the often 1-m long filters of dc filtered cathodic arcs.
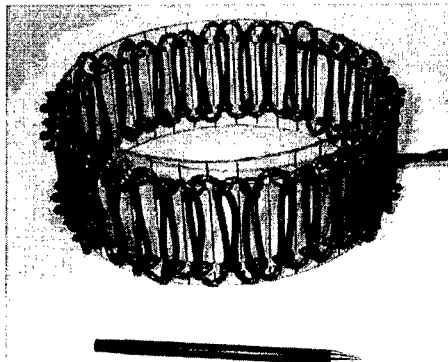

Figure 4. A simple electromagnetic multipole or "bucket" used to flatten the plasma density distribution in the alpha-version of the Twist Filter System. As with the Twist Filter, the arc current itself (usually 1.5 kA, pulsed) were used to generate the magnetic field. The pen is for size comparison.

PROPERTIES OF ta-C OBTAINED BY THE TWIST FILTER SYSTEM
Corrosion resistance

Corrosion resistance is the key property of ta-C films for 100 Gbit/in^2. When a film thickness is approached that is better described by the number of atoms than nanometers, some properties such as hardness become very difficult to measure or even ill-defined. However, the requirement of corrosion protection of the magnetic layers remains.

Preliminary measurements of ultrathin films obtained by using a prototype S-filter and Twist Filter have been reported elsewhere [36, 37]. Two major steps were done recently: one was the development of an alpha-version Twist Filter system, and the other was its installation in a class 100 cleanroom at Read-Rite corporation.

First corrosion tests indicate that corrosion protection can be achieved with 3 nm films (Fig.5), and one may speculate that even somewhat thinner film might serve for this purpose. In one experiment, 3 nm and 4 nm ta-C coatings were deposited on sets of read/write heads. Corrosion was tested using the standard Battelle test. The Battelle test consists of 48 hours exposure at 30°C, 65% relative humidity, in the presence of 8 ppb hydrogen sulfide, 8 ppb chlorine gas, and 80 ppb nitrous oxide). The heads coated with the Twist Filter System survived the corrosion test, indicating that the 3 nm overcoats are continuous.

corrosion

before   after   before   after

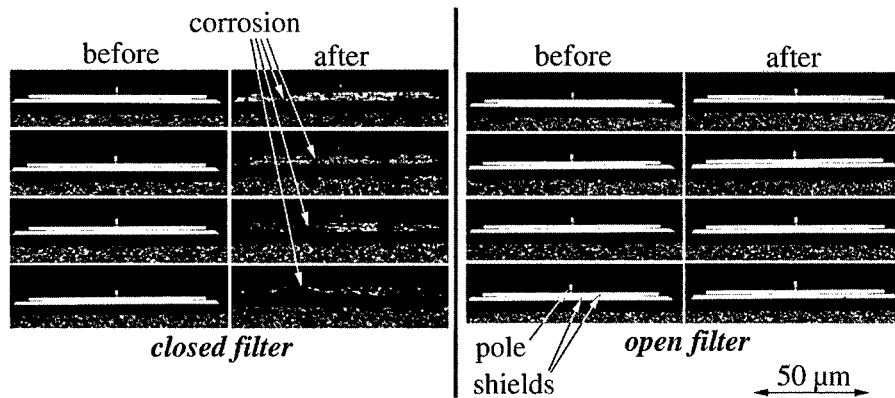*closed filter*   pole *open filter*
shields   50 µm

Figure 5. Battelle corrosion test of 3-nm ta-C coated read/write heads. Optical micrographs of NiFe shields before (left columns) and after (right columns) the test. The two left columns show heads that were coated using a DC carbon vacuum arc with a closed filter; and the two right columns rows show heads coated with the open Twist Filter system.

Surface analysis by atomic force microscopy (AFM)

Films of ta-C were deposited on <100> Si wafers using a closed filter and the Twist Filter system. Ultrathin films usually have too few particles to be quantified by AFM, therefore, relatively thick films of 40 nm were used for this study. Figure 6 shows clearly that macroparticle reflection is practically eliminated in the Twist Filter system.
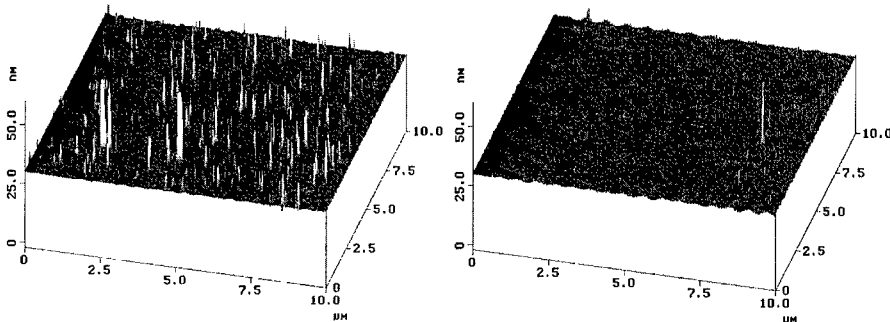

Figure 6. AFM pictures of the surfaces coated with ta-C (10 µm x 10 µm, height scale 25 nm). Left: Film of 41 nm deposited with DC-arc and closed filter. Right: Film of 40 nm deposited with a prototype Twist Filter system in a laboratory (non-cleanroom) environment.

Hardness and elastic modulus

Hardness and elastic modulus of filtered arc ta-C films have often been measured (see, for instance, [38]). The values reported are among the highest for the various kinds of diamondlike carbon. Peak hardness is typically 60 GPa and Elastic modulus up to 400 GPa if the average carbon ion energy is of order 100 eV, obtained by biasing the substrate. For thick (> 100

nm) ta-C films, it is known that hardness and modulus of these films have a maximum about 10-20 nm below the surface.

Nanoindentation of ultrathin films is difficult because the effect of the substrate increases with decreasing film thickness, and the indenter tip radius is much larger than the indentation depth. Other methods such as dispersion measurements of ultrasonic waves are being perfected for ultrathin films [39]. Young's modulus measurements performed this way often give greater values than nanoindentation.

To check the general quality of twist-filtered ta-C, relatively thick films of 100 nm have been deposited and measured by nanoindentation. The result is shown in Figure 7. Note that the high hardness was obtained without biasing the substrate: yet another indication that the ion energies are greater than the usually quoted 20 eV.

Raman Spectroscopy

Raman Spectroscopy is frequently used to "fingerprint" ta-C films by looking at the G and D peak intensities. We found that Raman spectroscopy can be used for control of deposition reproducibility, provided the deposition conditions were kept constant. Figure 8 shows Raman spectra where the targeted thickness was 3 nm and 4 nm for 3 samples each. After deposition calibration with AFM and ellipsometry, the thickness was targeted simply by counting the number of arc discharge pulses. This figure indicates that (i) ta-C films can be produced reproducibly, and (ii) Raman intensities represent a suitable signal for film control. These statements do not necessarily imply that long-term shifts do not occur and that the Raman intensity is simply proportional to thickness.
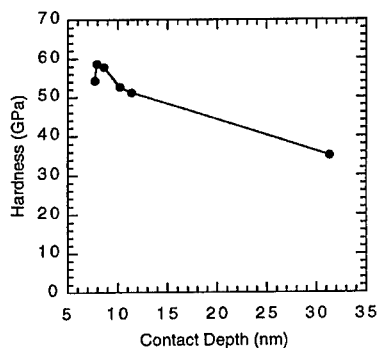
Figure 7. Hardness measurement by nanoindentation; total ta-C film thickness 100 nm.
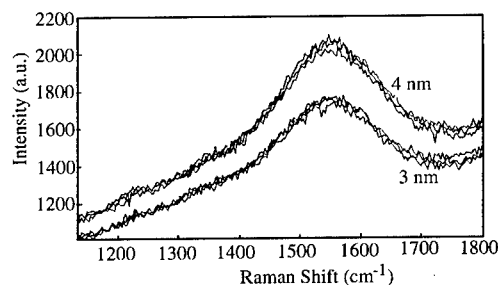
Figure 8. Raman spectra of three samples each, with targeted thickness of 3 nm and 4 nm.

Magnetically dead layer

The slider pole (shield) material consists of NiFe (Fe 18-22%) and the magnetoresistive element (MRE) is sandwiched between two shields. The MRE is composed of numerous materials stacked in a multilayer with copper for contacts. The iron percentage in the writer pole is much higher than in the shields (typically 50%). The primary function of the overcoat is to protect the slider poles and the MRE against corrosion. When the overcoat is applied, the surface of the magnetic multilayer is disturbed and loses its magnetic properties. Therefore, a thin

"magnetically dead" layer appears (also referred to as "magnetic dead layer"). These layers (one on the disk and one on the head) add to the magnetic spacing and hence need to be accounted for when budgeting the spacing between disk and head. The dead layer is believed to be the result of the subplantation nature of the deposition process, interface roughening, and formation of silicides at the interface if a silicon interlayer is used. Note that the deposition process with the Twist Filter system does not use a silicon interlayer.

To investigate the dead layer thickness, a layer of 20 nm NiFe (18% Fe) was coated on Si substrate. The saturated magnetic flux density B_s was measured before and after ta-C deposition using a B-H looper. From the loss of B_s one can calculate the approximate thickness of the dead layer. This technique was applied to ta-C films synthesized with the Twist Filter System, and the magnetically dead layer was found to be about 0.5 nm which is close to the resolution limit of the method.

Hydrogen content

The hydrogen content in the film was determined by Nuclear Resonance Analysis (NRA). The method is based on the nuclear reaction $^{15}N + {}^{1}H \Rightarrow {}^{12}C + {}^{4}He + \gamma$ where the ^{15}N ions have an energy greater than the resonant energy of 6.385 MeV. After the ^{15}N ions penetrate the sample surface, they lose energy, and when they reach the resonant energy at some depth, γ-rays are produced whose intensity is proportional to the hydrogen content at that depth. By measuring the γ-ray yield as a function of beam energy, the H concentration as a function of depth can be determined.

A silicon specimen deposited with a Twist Filter ta-C film of about 10 nm thickness yielded an H-concentration of 9-11%. Although this value is much lower than hydrogenated diamondlike carbon (a-C:H), the value is surprisingly high for a process that uses graphite only. Although one may question the accuracy of the measurement, there is evidence that a pulsed vacuum arc process with a strong magnetic field in a high-vacuum environment does indeed produce significant amounts of hydrogen. Schneider et al. [40, 41] have shown that residual water vapor can be efficiently ionized when a magnetic field is present. The hydrogen content in alumina films deposited by filtered cathodic arcs was found to be about 8% [42]. Interestingly, cathodic arc ta-C films made several years ago at Berkeley Lab with a 90° filter at much lower magnetic field strength showed 1-3% hydrogen content. These (unpublished) measurements were made with Elastic Recoil Spectroscopy (ERS). The difference in the results could be associated with not only possibly different vacuum base pressures but also by the degree of ionization of the water vapor due to the higher magnetic field of the Twist Filter.

MONTE CARLO SIMULATIONS

Monte Carlo codes such as the well-known TRIM (transport of ions in matter [43]) are suitable for the determination of the mean projected range (penetration depth) and many other parameters of stopping of energetic particles in matter. TRIM was originally developed to calculate element profiles obtained by ion implantation. For the calculation of film growth one needs to use a *dynamic* version of TRIM, i.e. a version that updates the composition of the substrate by the incorporation of the arriving ions. In this work we use the dynamic TRIM version T-DYN 4.0 by Biersack [44]. One has to be careful when approaching the range of very low energy (very low energy in this context is less than 100 eV) because the interaction potential functions used in the simulation are optimized for much higher energies (usually keV to MeV). The actual interaction at very low energy is not very accurately described by the two-body

interaction functions used in the simulation. Molecular dynamics simulations (see e.g., [45]) may be a better approach but they are computationally intensive and still limited to a relatively small number of atoms. It is believed that T-DYN simulations give a correct qualitative and approximate quantitative description of films growth when using cathodic arc plasmas with ion energies greater than the displacement energy.
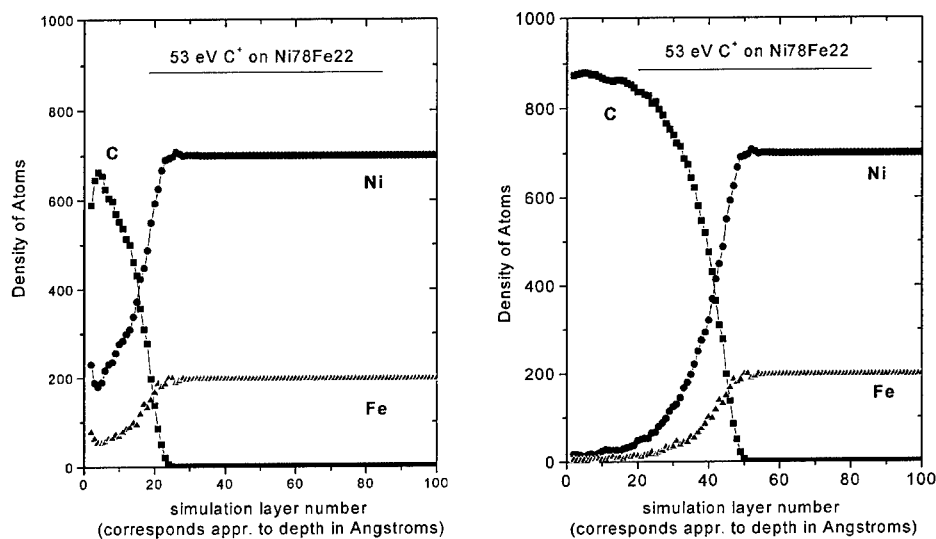

Figure 9. Dynamic TRIM simulation of carbon film growth on Ni78Fe22 alloy, assuming a carbon ion energy of 53 eV; the left figure shows the situation when a nominally 1 nm thick ta-C film is deposited (nominal 1 nm of ta-C with 2.9 g/cm^3); the right figure represents a continuation of the deposition to nominal 3 nm of ta-C film. The density in these figures refers to the atom number per volume of a simulation cell. Such a cell has a volume of about 10^{-20} cm^3.

Figure 9 illustrates the growth of cathodic arc ta-C film on NiFe alloy. A carbon ion energy of 53 eV was chosen based on measurements by Yushkov at al. using a similar cathodic arc system [14]. At the beginning of the deposition process, carbon ions penetrate the magnetic alloy with an average range of 0.5 nm (1 nm = 10 Å). With increasing carbon dose (i.e. deposition time or arc pulse number), the Ni and Fe concentrations decrease while the carbon concentration increases. At about 2 nm (nominal) film thickness one can actually speak of a film because the carbon concentration approaches 100%. An intermixed layer between the carbon and the metal alloy remains and it will not be changed when film growth continues because the mean projected range is less than the film depth. The intermixed layer is believed to have a beneficial effect for the adhesion of the growing ta-C film. On the other hand, this intermixed layer contributes to the magnetic spacing since one can assume that it is magnetically dead, and thus it must not be too thick. The mean projected range of 0.5 nm can be associated with a magnetically dead adhesion layer, in good agreement with experimental data for the thickness of the magnetically dead layer (see above). Note that in all of the here described experiments, no

silicon interlayer was used. Such an interlayer is conventionally applied to enhance adhesion of the carbon overcoat. The fact that a thin magnetically dead layer of ~ 0.5 nm exists in our experiments is acceptable since the need for a silicon interlayer is eliminated.

DISCUSSION AND OUTLOOK

An interesting question is what will happen when the film thickness is further reduced in order to reach and go beyond the 100 Gbit/in^2. Dynamic Monte Carlo simulations indicate that thinner films (e.g. a nominal 1 nm) deposited with ions having an energy of about 50 eV are not films made exclusively from the arriving ion species but they consist of the ion species intermixed with the substrate material (Fig. 8, left). It is likely that the carbon atoms in this layer will form C-C bonds as well as C-metal bonds (carbidic bonds). One cannot exclude that a carbidic layer may serve as the protective layer, as opposed to the ta-C film, perhaps at least for certain environments. The formation and thickness of a carbidic layer depends critically on the ratio of the incident carbon ion energy to the displacement energy of the substrate material. Displacement and intermixing will occur when the carbon ion energy exceeds the displacement energy. The minimum displacement energies for Cr, Fe, Co, Ni are 28 eV, 17 eV, 22 eV, 23 eV, respectively [46], that is, about the same value as usually assumed for the kinetic energy of cathodic arc carbon ions [15]. We have used higher energies based on recent measurements for pulsed arcs [14]. Future energy measurements should be done at systems actually used for carbon deposition on magnetic layers. That is particularly important since cathodic-arc ion energies are not only material-specific but can be manipulated by the arc discharge conditions.

If the kinetic energy of carbon ions is less than the displacement energy, one can assume that a very thin carbon overcoat can be obtained that has not an intermixed layer. However, such a carbon film is likely to be graphitic because the (subplantation) growth conditions for an sp^3-rich phase are not fulfilled (the minimum displacement energy for graphite and diamond is 25 and 35 eV, respectively). It is likely that such film is neither continuous, nor tough, nor adherent.

Summarizing, it has been shown that 3 nm films can be deposited by advanced filtered cathodic arc deposition. It can be argued that ta-C overcoats have a principal physical limit at about 2 nm: thinner films will either not exhibit the ta-C characteristic sp^3-rich phase or consist of both carbon and the base metal. In the latter case, one may speculate about protection of the magnetic layer by a carbidic phase. These conclusions are based on energy arguments and therefore not limited to cathodic arc deposited films.

REFERENCES

[1] B. Wei, B. Zhang, and K. E. Johnson, *J. Appl. Phys.* **83**, 2491-2499, 1998.

[2] A. Stanishevsky, *Chaos, Solitons & Fractals* **10**, 2045-2066, 1999.

[3] M. Bai, K. Kato, N. Umehara, Y. Miyake, J. Xu, and H. Tokisue, *Surf. & Coat. Technol.* **126**, 181-194, 2000.

[4] J. R. Shi, X. Shi, Z. Sun, E. Liu, B. K. Tay, and X. Z. Jin, *Int. J. Mod. Phys. B* **14**, 315-320, 2000.

[5] O. R. Monteiro, M.-P. Delplancke-Ogletree, and I. G. Brown, *Thin Solid Films* **342**, 100-107, 1999.

[6] H. Tsai and D. B. Bogy, *J. Vac. Sci. Technol. A* **5**, 3287-3312, 1987.

[7] C. S. Bhatia, W. Fong, C. Y. Chen, J. Wei, D. Bogy, S. Anders, T. Stammler, and J. Stöhr, *IEEE Trans. Magnetics* **35**, 910-915, 1999.

[8] P. R. Goglia, J. Berkowitz, J. Hoehn, A. Xidis, and L. Stover, *Diamond Rel. Mat.* **10**, 271-277, 2001.

[9] X. D. Li and B. Bhushan, *J. Mat. Res.* **14**, 2328-2337, 1999.

[10] X. Li and B. Bhushan, *Thin Solid Films* **355-356**, 330-336, 1999.

[11] S. Anders, C. S. Bhatia, W. Fong, R. Y. Lo, and D. B. Bogy, *Mat. Res. Soc. Symp. Proc.* **517**, 371-382, 1998.

[12] I. G. Brown, *Rev. Sci. Instrum.* **65**, 3061-3081, 1994.

[13] A. Anders, *IEEE Trans. of Plasma Sci.* **29**, in print, 2001.

[14] G. Y. Yushkov, A. Anders, E. M. Oks, and I. G. Brown, *J. Appl. Phys.* **88**, 5618-5622, 2000.

[15] J. Kutzner and H. C. Miller, *J. Phys. D: Appl. Phys.* **25**, 686-693, 1992.

[16] P. J. Fallon, V. S. Veerasamy, C. A. Davis, J. Robertson, G. A. J. Amaratunga, W. I. Milne, and J. Koskinen, *Phys. Rev. B* **48**, 4777-4782, 1993.

[17] O. Monteiro and A. Anders, *IEEE Trans. Plasma Sci.* **27**, 1030-1033, 1999.

[18] D. M. Sanders, D. B. Boercker, and S. Falabella, *IEEE Trans. Plasma Sci.* **18**, 883-894, 1990.

[19] R. L. Boxman, V. Zhitomirsky, B. Alterkop, E. Gidalevitch, I. Beilis, M. Keidar, and S. Goldsmith, *Surf. & Coat. Technol* **86-87**, 243-253, 1996.

[20] R. L. Boxman and S. Goldsmith, *Surf. & Coat. Technol.* **52**, 39-50, 1992.

[21] A. Anders, *Surf. & Coat. Technol.* **120-121**, 319-330, 1999.

[22] I. I. Aksenov, V. A. Belous, and V. G. Padalka, *Instrum. Exp. Tech.* **21**, 1416-1418, 1978.

[23] D. A. Baldwin and S. Fallabella, "Deposition processes utilizing a new filtered cathodic arc source," Proc. of the 38th Annual Techn. Conf., Society of Vacuum Coaters, Chicago, 1995, pp. 309-316.

[24] S. Anders, A. Anders, M. R. Dickinson, R. A. MacGill, and I. G. Brown, *IEEE Trans. Plasma Sci.* **25**, 670-674, 1997.

[25] T. Witke, T. Schuelke, B. Schultrich, P. Siemroth, and J. Vetter, *Surf. & Coat. Technol.* **126**, 81-88, 2000.

[26] R. P. Welty, Rectangular vacuum-arc plasma source, US 5,480,527, 1996.

[27] V. Gorokhovsky, Apparatus for Application of Coatings in Vacuum, Rectangular Filter, US 5435900, 1995.

[28] X. Shi, B. K. Tay, H. S. Tan, E. Liu, J. Shi, L. K. Cheah, and X.Jin, *Thin Solid Films* **345**, 1-6, 1999.

[29] X. Shi, B. G. Tay, and S. P. Lau, *Int. J. Mod. Phys. B* **14**, 136-153, 2000.

[30] J. Storer, J. E. Galvin, and I. G. Brown, *J. Appl. Phys.* **66**, 5245-5250, 1989.

[31] J. Koskinen, A. Anttila, and J.-P. Hirvonen, *Surf. Coat. Technol.* **47**, 180-187, 1991.

[32] A. Anttila, J. Salo, and R. Lappalainen, *Mat. Letters* **24**, 153-156, 1995.

[33] A. Anders and R. A. MacGill, *Surf. & Coat. Technol.* **133-134**, 96-100, 2000.

[34] A. Anders, I. G. Brown, R. A. MacGill, and M. R. Dickinson, *J. Phys. D: Appl. Phys.* **31**, 584-587, 1998.

[35] A. Anders, R. A. MacGill, and T. A. McVeigh, *Rev. Sci. Instrum.* **70**, 4532-4534, 1999.

[36] W. Fong, "Fabrication and evaluation of 5 nm cathodic-arc carbon films for disk drive applications," in *Department of Mechanical Engineering, Computer Mechanics Laboratory*. Berkeley, CA: University of California at Berkeley, 1999.

[37] A. Anders, F. R. Ryan, W. Fong, and C. S. Bhatia, "Ultrathin diamondlike carbon films deposited by filtered carbon vacuum arcs," IXX Int. Symp. on Discharges and Electrical Insulation in Vacuum, Xi'an, P.R. China, 2000, pp. 541-547, accepted for publication in IEEE Trans. Plasma Sci. (2001).

[38] G. M. Pharr, D. L. Callahan, D. McAdams, T. Y. Tsui, S. Anders, A. Anders, J. W. Ager, I. G. Brown, C. S. Bhatia, S. R. P. Silva, and J. Robertson, *Appl. Phys. Lett.* **68**, 779-781, 1996.

[39] D. Schneider, T. Witke, T. Schwarz, B. Schöneich, and B. Schultrich, *Surf. & Coat. Technol.* **126**, 136-141, 2000.

[40] J. M. Schneider, A. Anders, B. Hjörvarsson, and L. Hultman, *Appl. Phys. Lett.* **76**, 1531-1533, 2000.

[41] J. M. Schneider, A. Anders, and G. Y. Yushkov, *Appl. Phys. Lett.* **78**, 150-152, 2001.

[42] J. M. Schneider, A. Anders, B. Hjörvarsson, I. Petrov, K. Macak, U. Helmerson, and J.-E. Sundgren, *Appl. Phys. Lett.* **74**, 200-202, 1999.

[43] J. F. Ziegler, J. P. Biersack, and U. Littmark, *The Stopping and Range of Ions in Solids*. New York: Pergamon Press, 1985.

[44] J. P. Biersack, *Nucl. Instrum. Meth. Phys. Res. B* **59/60**, 21-27, 1991.

[45] S. Uhlmann, T. Fraunheim, and Y. Lifshitz, *Phys. Rev. Lett.* **81**, 641-644, 1998.

[46] M. Nastasi, J. W. Mayer, and J. K. Hirvonen, *Ion-Solid Interactions*. Cambridge, UK: Cambridge University Press, 1996.

A MODEL TO INTERPRET THE RAMAN SPECTRA OF DISORDERED, AMORPHOUS AND NANOSTRUCTURED CARBONS

Andrea Carlo Ferrari
Department of Engineering, University of Cambridge, Cambridge, CB2 1PZ, UK

ABSTRACT

Raman spectroscopy is a very popular, non-destructive tool for the structural characterisation of carbons. Raman scattering from carbons is always a resonant process, in which those configurations whose band gaps match the excitation energy are preferentially excited. The Raman spectra of carbons do not follow the vibration density of states, but consist of three basic features, the G and D peaks around 1600 and 1350 cm^{-1} and an extra T peak, for UV excitation, at ~980-1060 cm^{-1}. The Raman spectra at any wavelength depend on 1) clustering of the sp^2 phase, 2) bond length and bond angle disorder, 3) presence of sp^2 rings or chains, and 4) the sp^2/sp^3 ratio. It will be shown how the basic features of the Raman spectra vary by rationalising them within a three-stage model of order of carbons. It is shown how the three-stage model can account for the vast range of experimental data available for Raman experiments at any excitation wavelength. This model can also account for apparently contradictory trends reported in literature, since the clustering of the sp^2 phase and the sp^3 to sp^2 conversion are separately treated.

INTRODUCTION

Carbon is unique in the way that simple changes in its local bonding can give rise materials as diverse as diamond, graphite, fullerenes, carbon nanotubes, and disordered, nano-structured and amorphous carbons. These materials have a remarkable range of mechanical, electronic and electrochemical properties and many possible applications [1,2]. It is thus very useful to develop fast, reliable, non-destructive techniques to probe the key parameters which control their physical behaviour.

We are particularly interested in amorphous carbons. We define diamond-like carbon (DLC) as an amorphous carbon (a-C) or an hydrogenated amorphous carbon (a-C:H) with a significant fraction of sp^3 bonds. A-C:H often has a rather small C-C sp^3 content. DLC's with highest sp^3 content (80-90%) are called tetrahedral amorphous carbon (ta-C) and its hydrogenated analogue ta-C:H. The key parameters of interest in such materials are: 1) the sp^3 content; 2) the clustering of the sp^2 phase; 3) the orientation or anisotropy of the sp^2 phase; 4) any cross sectional structure; 5) the H content. The sp^3 content alone mainly controls the elastic constants, but films with the same sp^3 and H content but different sp^2 clustering, sp^2 orientation or cross-sectional nano-structure can have different optical, electronic and mechanical properties.

Raman spectroscopy is a popular, non-destructive tool for structural characterisation of carbons [3-12]. It is traditionally carried out at the commonly available wavelengths in the blue-green spectral region (488-514.5 nm), but multi-wavelength Raman (MW Raman) studies are becoming increasingly used. Indeed, Raman scattering from carbons is always a resonant process, in which configurations whose band gaps match the excitation energy are preferentially excited. Any mixture of sp^3, sp^2 and sp^1 carbon atoms always has a gap between 0 and 5.5 eV, and this energy range matches that of IR-vis-UV Raman systems. This implies that understanding the resonant Raman process in carbon systems will give a powerful, fast means for their structural and electronic characterisation. For example, MW Raman has recently been used to distinguish the metallic and semiconducting forms of single

wall carbon nanotubes [10,11]. It has also been used to investigate the origin of the peaks at ~1150 cm^{-1} and ~1450 cm^{-1} in nano-crystalline diamond [13].

The Raman spectra of all carbons show several common features in the 800-2000 cm^{-1} region, the so-called G and D peaks, which lie at around 1560, 1360 cm^{-1} for visible excitation, and the T peak, seen for UV excitation at around 1060 cm^{-1}. The G and D peaks are due to sp^2 sites only. The G peak is due to the bond stretching of all pairs of sp^2 atoms in both rings and chains [7]. The D peak is due to the breathing modes of sp^2 atoms in rings. The T peak is due to the C-C sp^3 vibrations and appears only in UV excitation.

Although Raman spectroscopy of carbons has continued for 30 years, there have been significant advances in our understanding recently. Firstly, C-C sp^3 vibrations were directly detected using UV Raman spectroscopy at 244nm [14-16]. The second major advance is the understanding of the origin of the D peak. Pocsik et al. [17] and others [18,19] proposed empirically that the D peak arises as a resonant Raman coupling to the phonon of wave vector q when it equals the wave vector k of the electronic transition excited by the incident phonon. We called this a k=q "quasi selection rule", since it qualitatively explains the observed trends, but the physical mechanism behind the resonance was not fully understood [7]. Recently, Thomsen and Reich [20] showed how the D peak arises from a double resonant Raman process. For a particular excitation energy E, an electron-hole pair is created at the k point matching the energy gap between the conduction and valence band. The electron is then scattered across the zone by a phonon ω(q), this being the phonon for which the double resonance occurs. The electron is then scattered back elastically by lattice defects or disorder and recombines with the hole, conserving k in the process. It can be seen that this double resonance occurs when [20, 12]:

$$k \approx \frac{1}{2}q \qquad (1)$$

rather than the k≈q originally heuristically proposed [17,18,7]. This, in contrast to what stated in ref.[20], does not affect our conclusions on the nature of the D peak and on which optical branch contributes to the peak [7]. It generalises the concept of L_a in case of graphite to being an inter-defect distance.

For disordered carbons, one can map the energy levels and vibration modes of carbon clusters onto those of graphite [7]:

$$1/L_a \Leftrightarrow k \text{ and } 1/L_a \Leftrightarrow q \qquad (2)$$

where L_a is the cluster size or in plane correlation length. (2) is the basis to explain the origin and dispersion of the D peak in disordered and amorphous carbons and to derive the real space motions (breathing modes) of the phonons giving rise to this band [7,21,22]. We could thus propose a three-stage model to relate the visible Raman spectra of disordered and amorphous carbons to their local bonding [7].

Mapelli et al.[21,22] showed that the breathing motions of clusters of increasing size could be mapped on the upper optical branch of the graphite dispersion relations from K to (K-M)/2, with q=(K-M)/2=π/(3a)~1.05/a corresponding to coronene. In graphitic clusters, the π states have minimum band energies of roughly [1,7]:

$$E_g \approx \frac{2\gamma}{M^{0.5}} \approx 2\gamma \frac{a}{L_a} \qquad (3)$$

where M is the number of aromatic rings in the cluster and L_a is the cluster diameter. For example, coronene is composed of 7 rings, and from (3) we can estimate its optical gap as $6/\sqrt{7}$ eV. This corresponds to the gap of graphite at $k=2/\sqrt{21}$ a~0.44/a [12]. Thus eq. (1) links breathing modes of clusters, and thus L_a, with k and q. This implies that, for all modes satisfying the double resonance condition, the breathing modes on the upper optical branch are enhanced due to their high polarizability. This allows a unified interpretation of the origin

of the D peak in amorphous carbons and polycyclic aromatic hydrocarbons, due to the mapping of the electronic and vibrational states of carbon clusters onto those of graphite.

We show that the peak dispersions in a-C, ta-C, ta-C:H, diamond-like a-C:H and polymeric a-C:H can be considered as canonical cases in the ternary phase diagram of the disordered C:H system [7,1]. We propose a general explanation of the trends in peak positions and intensities, and extend the previous 3-stage model [7] to spectra excited at many wavelengths [12]. A main conclusion is that the spectra and their dispersion are characteristic of each type of carbon, while their single wavelength Raman spectrum may be indistinguishable. We then show how a simpler 2-wavelength (visible-UV) study can provide most of the information on the fraction and order of sp^2 sites in amorphous carbons.
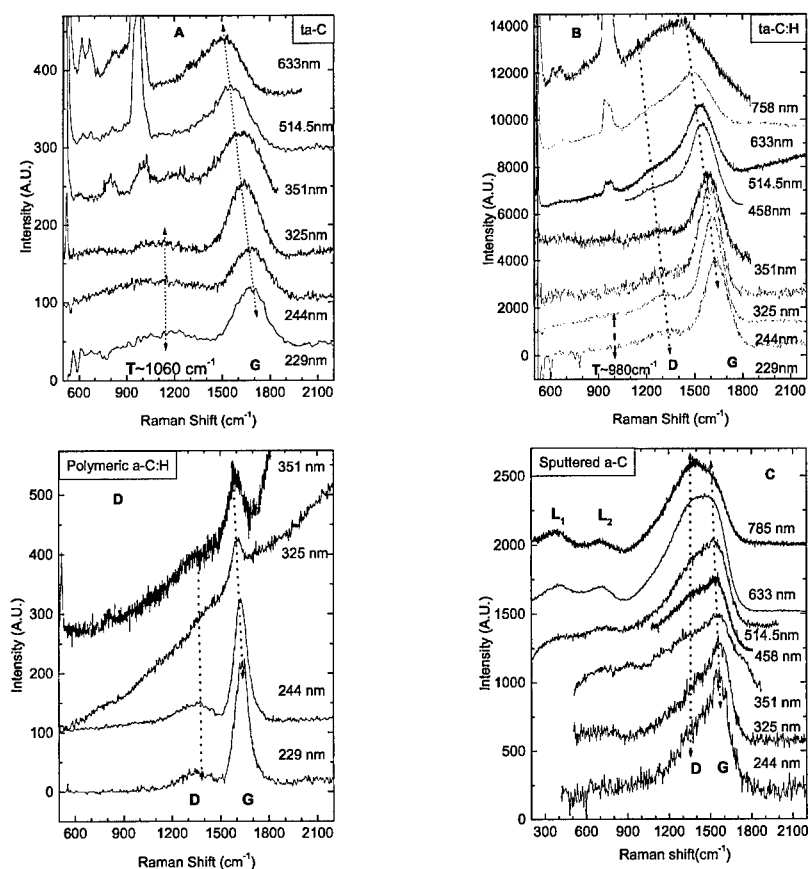
Fig 1: Multi-wavelength Raman spectra of (A) ta-C, (B) ta-C:H, (C) sputtered a-C and (D) polymeric a-C:H. The peaks' trends and labels are indicated. Two extra peaks at ~400 and 800 cm^{-1} are seen in the sputtered a-C; these are typical of low sp^3 a-C and are not discussed here.

EXPERIMENTAL

Unpolarised Raman spectra were acquired at λ=229, 244, 325, 351, 458, 514.5, 532, 633, 785 nm (5.41-1.58 eV) using a variety of spectrometers. The power on the sample was
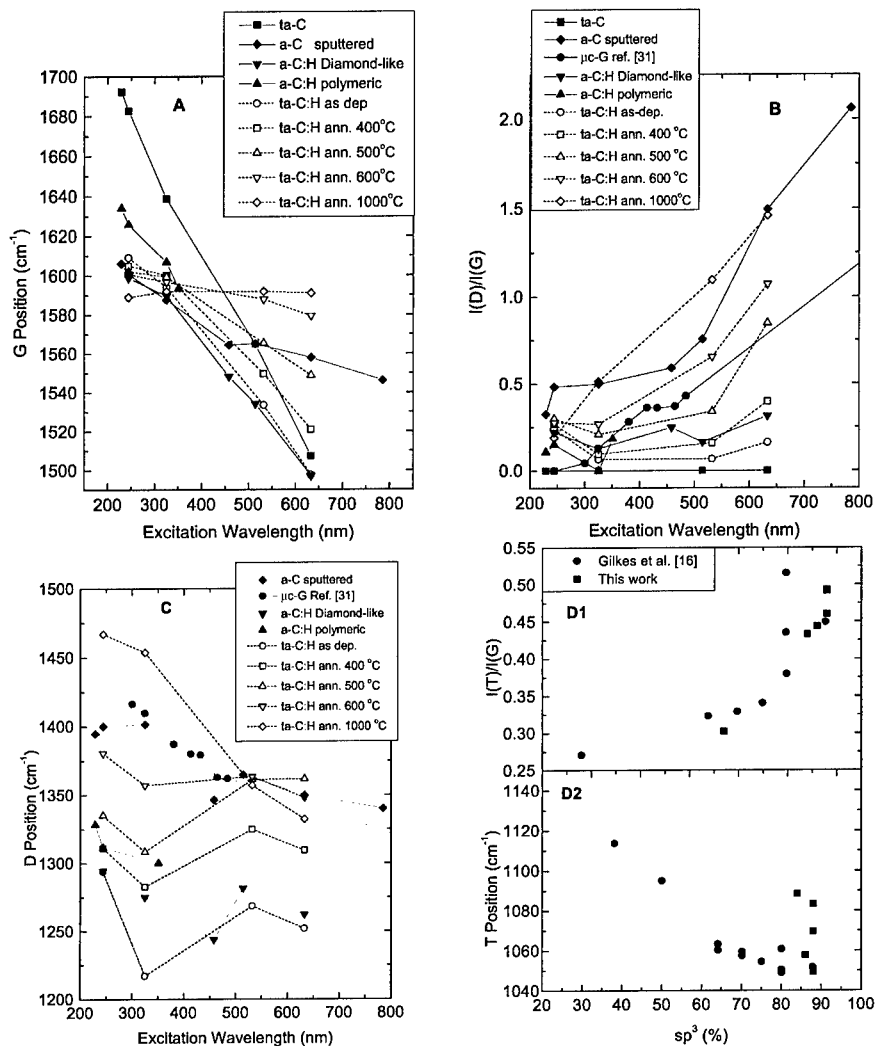
Fig.2: A,B,C) Dispersion of G peak, I(D)/I(G) and D peak vs. excitation wavelength for a series of template samples; (D1,D2) I(T)/I(G) and T peak position vs. sp^3 fraction for non hydrogenated carbon films. Note that data on a series of annealed ta-C:H, on diamond-like a-C:H and on micro crystalline graphite are also shown. 600 ^{0}C is the onset of major H effusion and sp^3 to sp^2 conversion in ta-C:H [23,24]

kept well below 1mW. Sample damage is always an issue in Raman measurements, but it is particularly serious for UV excitation. For H containing samples, in order to be sure that the signal we measured is a genuine feature of a-C:H samples, we performed measurements with samples rotating at a very high speed (>3000 rpm) with a random XY movement superimposed. We have analysed a variety of carbon samples. As we focus on general trends, we discuss only selected cases. Fig 1 shows the multi-wavelength Raman spectra of ta-C, ta-C:H, a-C and polymeric a-C:H samples [12].

The spectra in general show three features, around 1560, 1360 (for visible excitation) and 1060 cm^{-1} (detected only in UV excitation), which are labelled as the G, D and T peaks, respectively. The G and D peaks are due to sp^2 sites only. The G peak is due to the bond stretching of all pairs of sp^2 atoms in both rings and chains [7]. The D peak is due to the breathing modes of rings. The T peak is due to C-C sp^3 vibrations and appears only for UV excitation. The trends in the D, G and T peaks are indicated in Fig 2.

For visible excitation, the sp^2 sites have such a high cross-section that they dominate the spectra, the sp^3 sites are invisible and the spectrum responds only to the configuration or order of the sp^2 sites. As the excitation energy rises, two effects occur, resonance causes the excitation of those sp^2 configurations with a wider gap, and then in the deep UV the modes of σ states of C-C bonds are seen.

TRENDS IN RAMAN PARAMETERS

Three stage model

The trends in the Raman parameters for different laser excitation can be rationalised by extending the three-stage model that we proposed to explain the trends in visible Raman spectra [7]. This model considers an amorphisation trajectory, consisting of three stages from graphite to ta-C (or diamond):

1) graphite→nanocrystalline graphite (nc-G)
2) nanocrystalline graphite→ sp^2 a-C
3) a-C→ta-C (→ 100 sp^3 ta-C, defected diamond),

Broadly, stage 1 corresponds to the reduction of the in-plane correlation length L$_a$ within an ordered graphite layer. Stage 2 is the introduction of topological disorder into the graphite layer. Stage 3 is the conversion of sp^2 sites to sp^3 sites and the consequent change of sp^2 configuration from rings to chains.

The Raman spectra depend on

1) clustering of the sp^2 phase
2) bond length and bond angle disorder
3) presence of sp^2 rings or chains
4) the sp^2/sp^3 ratio

We note that any features above ~1360 cm^{-1} cannot be due to C-C sp^3 vibrations, being this the band limit for C-C sp^3 vibrations [7]. Thus, it is clear that the presence of G peaks in Fig 1 means that sp^2 vibrations still dominate even in the UV Raman excitation. In the following sections we will discuss the G, D and T peaks, extending the 3-stage model to multi-wavelength excitation.

The G peak

Fig 2(A) shows the variation of the position of the G peak with excitation wavelength and energy. The G peak does not disperse in graphite itself, nanocrystalline (nc)-graphite or glassy carbon [25, 29-31]. The G peak only disperses in more disordered carbon, where the dispersion is proportional to the degree of disorder. This is an important finding, by which the physical behaviour of the G peak in disordered graphite is radically different from amorphous carbons, even though the G peak positions might accidentally be the same at

some excitation energy. The G peak in graphite cannot disperse because it is the Raman-active phonon mode of the crystal. In nc-graphite, the G peak shifts slightly upwards at fixed excitation energy due to phonon confinement, but it cannot disperse with varying excitation energy, still being a density of states feature. The G peak dispersion occurs only in more disordered carbon, because now there are a range of configurations with different local band gaps and different phonon modes. The dispersion arises from a resonant selection of sp^2 configurations or clusters with wider π band gaps, and correspondingly higher vibration frequencies. The G peak dispersion separates the materials into two types. In materials with only sp^2 rings, the G peak dispersion saturates at a maximum of ~ 1600 cm^{-1}, the G position in nc-graphite. In contrast, in those materials also containing sp^2 chains, particularly ta-C and ta-C:H, the G peak continues to rise past 1600 cm^{-1} and can reach 1690 cm^{-1} at 229 nm
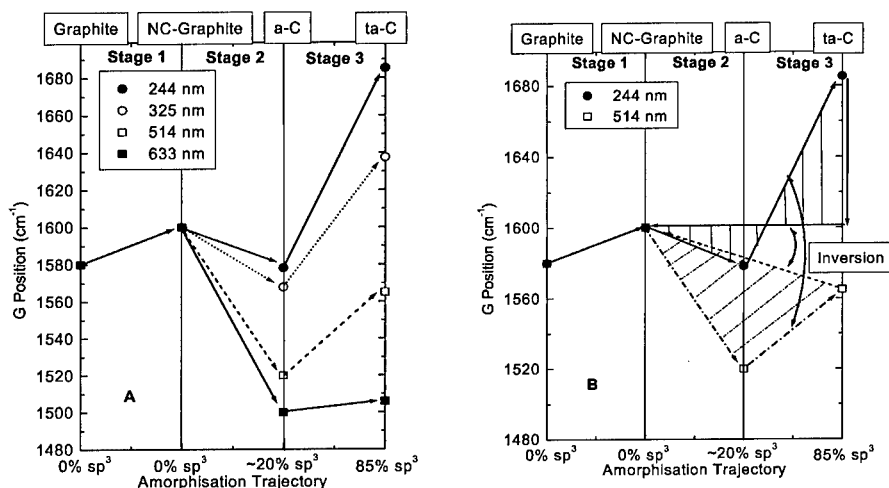
Fig 3: (A) Amorphisation trajectory, showing the schematic variation of G peak position for four typical wavelengths; (B) Amorphisation trajectory, showing the possibility of hysteresis in stages 2 and 3 for two typical wavelengths (514.5 and 244 nm). The regions span by hysteresis at 514.5 nm and 244 nm are evidenced by lines. Note the different shape of the hysteresis region for UV excitation: an inversion of the trends happens, with the highest shift Vis->UV for samples having the least ordered sp^2 phase.

excitation in ta-C. This high G peak position can only be due to short, strained C=C bonded chains, if one notes that the C=C stretching vibration in ethylene is at ~ 1630 cm^{-1}.

This range of behaviours of the G peak can be understood within the three-stage model of Raman spectra [7]. This plots the G mode against an *amophorisation* trajectory. The model is extended to show the variation of G position with excitation wavelength, as shown in Fig. 3 (A) for four typical wavelengths. In ref [7] we pointed out that following the reverse, *ordering* trajectory, from ta-C to graphite (by high temperature deposition, annealing after deposition, or low-dose ion implantation) there is hysteresis [7]. This means that there can be sp^2 clustering or π electron delocalisation without a corresponding $sp^2 \rightarrow sp^3$ conversion. For visible excitation, sp^2 clustering and ordering will always *raise* the G peak in stages 2 and 3. In contrast, in UV excitation, increasing clustering *lowers* the G position, as noted above. This is shown schematically in Fig 3(B). Comparing visible to UV excitation, there is an *inversion* of the trends. This is another remarkable result, since it allows for a

distinction of samples which, although having different structures, may accidentally show very similar Raman spectra at a certain wavelength.

The D peak and I(D)/I(G)

The D peak arises from the breathing motion of sp^2 rings. I(D)/I(G) is highest for IR excitation, and it decreases strongly at higher excitation energy. Although there is no D peak in the UV Raman for nc-graphite, Fig 1 suggest that there is some residual intensity in the D region in UV Raman in the more disordered carbons, those with stage 2 disorder.

Fig 2(B,C) plot the I(D)/I(G) intensity ratio and the D peak position as a function of excitation wavelength. In contrast to the G peak dispersion, the I(D)/I(G) ratio and the D peak have maximum dispersion for micro and nano-crystalline graphite, and the dispersion decreases for increasing disorder, i.e. the dispersion is proportional to order.
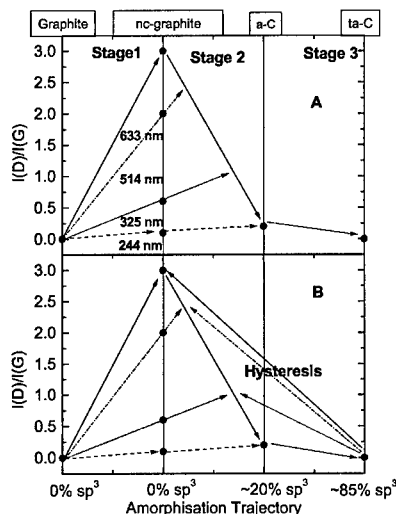
Fig 4: (A) Amorphisation trajectory, showing the schematic variation of I(D)/I(G) for four typical wavelengths. Note that for increasing excitation energy the maximum of I(D)/I(G) corresponding to the transition between stage 1 and 2 shifts to higher disorder, i.e. lower L_a. Note also that I(D)/I(G)>0 even at UV excitation. (B) amorphisation trajectory for I(D)/I(G), showing the possibility of hysteresis.

The origin and dispersion of the D peak in disordered graphite arises from the double resonance mechanism corresponding to the k=0.5q condition of eq (1) [17-20,7]. In particular, symmetric breathing modes have the highest modulation of the polarizability and thus the highest Raman cross-section for k=0.5q [7]. Furthermore, there is a simultaneous mapping of the vibrational modes and electron energy levels of aromatic clusters onto those of graphite, according to the same k=0.5q condition. Aromatic clusters act as part of a graphite superlattice, both electronically and vibrationally [7]. Longer excitation wavelengths excite larger clusters with lower band gaps and lower frequency breathing modes. This is confirmed by calculations of Raman intensities of polycyclic aromatic hydrocarbons of increasing size, which exhibit two main bands corresponding to the G and D peaks in graphite [21,22]. As disorder increases, the I(D)/I(G) ratio disperses less. This means that the

D peak disappears for UV excitation in disordered and nanocrystalline graphite, but it is still present for amorphous carbons. In effect, for large disorder, as in sputtered a-C of Fig. 1(C), the D peak behaves like a non-dispersive vibrational density of states feature for the breathing modes of all ring-like sp^2 configurations. The presence of a residual D peak in UV Raman spectra of a-C's is a new finding, which can affect our deriving sp^3 content from the T peak, as discussed later.

Ideally, for an excitation energy E_{ex}, from (3) we expect clusters of size $L \propto 1/E_{ex}$ to give the largest contribution. Thus, for the highest E_{ex}, a-C with the smallest aromatic clusters will have the highest I(D)/I(G) with respect to nc-graphite. On the other hand the I(D)/I(G) ratio is bigger for bigger clusters, as shown by ab-initio calculations of Raman intensity [22], thus explaining the over-all decrease in I(D)/I(G) intensity for increasing excitation energy. Furthermore, very disordered amorphous carbons have a specific size distribution of clusters, and cannot span all the breathing mode frequencies of clusters of rings of arbitrary size, unlike in defected graphite, where all the upper optical branch is spanned by the double resonance condition for varying excitation energies. We therefore expect an almost constant I(D)/I(G) and D position for a-C. This is indeed seen experimentally, in Figs 2(B,C). In ta-C, there is no D peak at any wavelength, due to a complete absence of rings. These trends in I(D)/I(G) can be summarised by extending the three-stage model to many wavelengths, as in Fig 4(A). Note that the maximum of I(D)/I(G) versus L_a shifts to smaller L_a for increasing E_{ex}, as seen in Fig 4(A). Fig 4(B) shows the effect of hysteresis.

The T peak and sp^3 content

The first UV Raman studies [14,15] found a new peak at ~1060 cm^{-1} labelled T. This peak, seen only in UV excitation, is due to a resonant enhancement of the σ states, and it directly probes the sp^3 bonding. This peak corresponds to the peak in the CC sp^3 vibration density of states (VDOS) of ta-C in simulations [32,33] and EELS data [34]. Gilkes et al. [16] gave some empirical relations between the I(T)/I(G) ratio, the T peak position and the sp^3 content, Fig 2(D). Fig 5 compares the 244 nm UV Raman spectra of ta-C, ta-C:H, diamond-like a-C:H and polymeric a-C:H, with the peak fits adopted in this paper, to show the differences in their spectra in the T and D region.

The 244nm UV Raman spectra is a favoured means to derive the sp^3 content of amorphous carbons. This requires an understanding of how the spectrum develops with sp^3 content. For example, the variation of I(T)/I(G) with the sp^3 content is quite non-linear for 60 to 90% sp^3 contents, Fig 2(D1). The spectrum possesses the large G peak. If this is subtracted, this leaves the T peak, which arises from a peak in the sp^3 VDOS. As the sp^3 content falls, the sp^3 VDOS peak at 1060 cm^{-1} shifts upwards to that of a sp^2 network at 1400 cm^{-1} [34]. A shifting T feature is also seen in the UV Raman spectra of ta-C:N with increasing nitrogen content [35]. Alternatively, the changes could be represented as a reduction of the T peak at 1060 cm^{-1} and the rise of a peak around 1400 cm^{-1}, a D-like peak. This is consistent with the discussion in the previous section. There we noted that a small D peak can survive in UV in sp^2 a-C, where it becomes like a VDOS feature of sp^2 rings. Thus, as the sp^2 content of ta-C rises, the T peak intensity (corresponding to the CC sp^3 VDOS) is reduced, with a corresponding increase of a D peak. We use this model here.

A complication is that the D peak intensity depends not only on the sp^2 fraction, but also on its order. If the sp^2 sites have graphitic order, the D peak is absent in UV, if the sp^2 sites are in chains the D peak is absent, only if the sp^2 sites are in disordered rings does a residual D peak survive in UV.
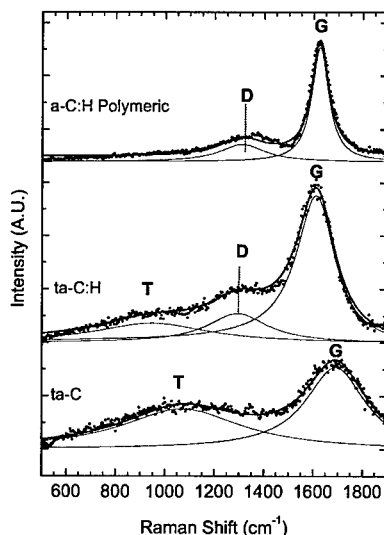
Fig 5: UV Raman spectra of polymeric a-C:H, ta-C:H and ta-C with the peak fits. The fitted peaks are correspondingly labelled. Note that for polymeric a-C:H a clear dip at ~1500 cm^{-1} exists between the D peak at the G peak. For ta-C:H (or diamond-like a-C:H) the residual D peak fills the dip around 1500 cm^{-1}.

This can then explain the range of I(T)/I(G) values seen for high sp^3 content ta-C. This could be attributed to the sensitivity of the T peak to small changes of sp^3 content at high sp^3 content. More likely, a slightly different amount of sp^2 clustering can fill in the dip around 1400 cm^{-1} so smearing the T peak intensity (clearly seen in the ta-C spectrum of Fig. 5). This could be overcome in principle by introducing an extra D peak in the fitting, even in samples with low sp^2 content, but a physically meaningful fit is difficult in these cases as this implies using two peaks to fit a broad feature with no clear modulations. Thus, the empirical relations of Gilkes et al. [16], obtained with a simple 2 peak fit (1 T peak and 1 G peak) that allows an up-shift of the T peak, are useful benchmarks.

The increase of sp^2 content and clustering both tend to reduce T peak intensity relative to the G peak. However, the T peak disappears only for large sp^2 contents. Thus, the effect of clustering is to reduce the direct correlation between T intensity and sp^3 content. Nevertheless, we can still distinguish high sp^3 contents from low sp^3, unlike in visible Raman spectra. Indeed, a T peak around 1060 cm^{-1} and an I(T)/I(G) ratio of about ~0.4-0.42 in H-free samples is a sufficient condition to estimate an sp^3 content of ~80%. An I(T)/I(G) ratio of 0.3-0.4 still indicates a sp^3 content of 60-80%, but sp^2 clustering makes it difficult to give a precise figure. Finally, I(T)/I(G)<0.2 indicates a sp^3 content lower than 20-30%. Thus the presence of a T peak is a powerful qualitative means to cut through the hysteresis. Indeed, a sample with high sp^3 fraction and large hysteresis will show a T peak (even if smaller than a similar sp^3 content sample, but with limited clustering of the sp^2 phase). On the other hand, a sample with low sp^3 fraction but with the same I(D)/I(G) in visible excitation will not show any T peak in the UV.

The analysis of T peaks extends to hydrogenated samples. Figs 1(B) shows that the T peak in ta-C:H or a-C:H is around ~980 cm^{-1}, lower than in ta-C. This is consistent with the

simulations of the C-C sp^3 VDOS in ta-C:H [36]. The presence of the residual D peak must be taken into account when fitting. As a first approximation, we use three Lorentzians to fit the spectra (Fig. 5). For hydrogenated samples, EELS gives the total amount of sp^3 bonded C atoms, in both C-C and C-H sp^3 bonds, but the T peak is sensitive only to C-C sp^3 bonds. Indeed, comparing the UV Raman spectra of ta-C:H and polymeric a-C:H (Figs 1(B) and 1(D)), it is clear that most C sp^3 atoms are bonded to H in polymeric a-C:H, due to the absence of a clear T peak, whilst in ta-C:H there is a sizeable amount of C-C sp^3 bonds. Empirically, I(T)/I(G)~0.1-0.2 in (t)a-C:H indicates an overall sp^3 content of ~70%. Further work is needed for more detailed conclusions. Clearly, as sp^2 clustering also contributes of a D peak, this can make things more difficult.

A final question for the I(T)/I(G) ratio in UV Raman is the cross-sectional uniformity of the sample. The samples here discussed are extremely uniform in the z direction [37]. However, it is possible to have quite layered ta-C films, with surface layers thicker than the penetration depth of UV light (~10-15 nm) [37]. In that case, UV Raman provides information on the outer part of the sample. On the other hand, this surface sensitivity can be exploited to investigate the changes induced by surface treatments.

CONCLUSIONS

We have presented the dispersion of Raman peaks with varying excitation energy for a comprehensive series of amorphous carbons. We showed how most trends can be classified and explained by extending the three-stage model developed to explain the visible Raman spectra of disordered and amorphous carbons.

We showed how amorphous carbons can have a D peak even in UV excitation, in contrast to disordered graphite. We discussed the origin of the trends of the T peak with sp^3 content for hydrogenated and hydrogen free samples. We showed how its blue-shift is due to the appearance of a residual D peak, due to the vibrations of all ring-like structures, and not to a change in the sp^3 VDOS, as sometimes suggested.

We also stress how the clustering of the sp^2 phase is the major parameter controlling the Raman spectra at any wavelength. Probing the same sample with visible and UV excitation allows us to derive the amount and clustering of sp^2 sites, at least qualitatively. This is due to the inversion of the trend of the G peak, resulting in a shift from visible to UV, which is larger for less sp^2 clustering. The appearance of the T peak gives a direct indication of the presence of sp^3 bonds. This means that a two wavelength study (eg at 514 nm and 244 nm) can provide a fast and powerful characterisation tool for amorphous and disordered carbons since the peaks' dispersion is a fingerprint which is specific to each different carbon system.

ACKNOWLEDGEMENTS

REFERENCES

1. J. Robertson, Prog. Solid State Chem **21**, 199 (1991); Pure Appl. Chem. **66**, 1789 (1994); J. Robertson, Adv. Phys., **35**, 317 (1986)
2. M. S. Dresselhaus, G. Dresselhaus, P. C. Eklund, *Science of Fullerenes and Carbon Nanotubes*, Academic Press, New York, 1996.
3. F. Tuinstra and J. L. Koening, J. Chem. Phys. **53**, 1126 (1970)
4. R. J. Nemanich, S. A. Solin, Phys. Rev. B, **20**, 329 (1979)
5. P. Lespade, A. Marchard, M. Couzi, F. Cruege, Carbon **22**, 375 (1984)
6. M. A. Tamor, W. C. Vassel, J. Appl. Phys. **76**, 3823 (1994)
7. A. C. Ferrari, J. Robertson, Phys. Rev. B, **61**, 14095 (2000)
8. A.M. Rao, E. Richter, S. Bandow, B. Chase, P. C. Eklund, K. A. Williams, S. Fang, K. R. Subbaswamy, M. Menon, A. Thess, R. E. Smalley, G. Dresselhaus, M. S. Dresselhaus, Science, **75**, 187 (1997)
9. D. S. Bethune, G. Meijer, W. C. Tang, H. J. Rosen, W. G. Golden, H. Seki, C. A. Brown, M. S. De Vries, Chem. Phys. Lett. **179**, 181 (1991)
10. S.D.M. Brown, P. Corio, A. Marucci, M. A. Pimenta, M. S. Dresselhaus, G. Dresselhaus, Phys. Rev. B, **61**, 7734 (2000)
11. S. D. M. Brown, P. Corio, A. Marucci, M. S. Dresselhaus, M. A. Pimenta, K. Kneipp, Phys. Rev. B, **61**, R5137 (2000)
12. A.C. Ferrari, J. Robertson, Phys. Rev. B, submitted (2000)
13. A.C. Ferrari, J. Robertson, Phys. Rev. B **63**, 121405(R) (2001).
14. K. W. K. Gilkes, H. S. Sands, D. N. Batchelder, J. Robertson, W. I. Milne, Appl. Phys. Lett. **70**, 1980 (1997)
15. V. I. Merkulov, J. S. Lannin, C. H. Munro, S. A. Asher, V. S. Veerasamy, W. I. Milne, Phys. Rev. Lett. **78**, 4869 (1997)
16. K. W. R. Gilkes, S. Prawer, K. W. Nugent, J. Robertson, H. S. Sands, Y. Lifshitz, X. Shi, J. Appl. Phys. **87**, 7283 (2000)

17. I. Pocsik, M. Hundhausen, M. Koos, L. Ley, J. Non-Cryst. Solids **227-230,** 1083 (1998)
18. M. J. Matthews, M. A. Pimenta, G. Dresselhaus, M. S. Dresselhaus, and M. Endo, Phys. Rev. B, **59**, 6585 (1999)
19. A.V. Baranov, A.N. Bekhterev, Y. S. Bobovich, V. I. Petrov, Opt. Spectrosc. **62**, 612 (1987)
20. C. Thomsen, S. Reich, Phys. Rev. Lett. **85**, 5214 (2000).
21. C. Mapelli, C. Castiglioni, G. Zerbi, K Mullen, Phys. Rev. B, **60**, 12710 (2000)
22. C. Castiglioni, C. Mapelli, F. Negri, and G. Zerbi, J. Chem. Phys. **114**, 963 (2001); M. Rigolo, C. Castiglioni, G. Zerbi and F. Negri, J. Mol. Structure, to be published (2001).
23. N.M.J. Conway, A.C. Ferrari, A. J. Flewitt, J. Robertson, W.I. Milne, A. Tagliaferro, W. Beyer, Diam. Relat. Mater. **9**, 765 (2000)
24. A. Ilie, A. C. Ferrari, T. Yagi, J. Robertson, Appl. Phys. Lett. **76**, 2627 (2000)
25. R. P. Vidano, D. B. Fishbach, L. J. Willis, T. M. Loehr, Solid. State Comm. **39**, 341 (1981)
26. P. Tan, Y. Deng, Q. Zhao, Phys. Rev. B, **58**, 5435 (1998)
27. Z. Wang, X. Huang, R. Xue, L. Chen, J. Appl. Phys. **84**, 227 (1998)
28. Y. Kawashima and G. Katagiri, Phys. Rev. B, **52**, 10053 (1995)
29. K. Sinha and J. Menendez, Phys. Rev. B **41**, 10845 (1990)
30. Y. Wang, D. C. Alsmeyer, R. L. McCreery, Chem. Mater. **2**, 557 (1990)
31. I. Pocsik, M. Koos, M. Hundhausen, L. Ley, in *Amorphous Carbon: State of the Art*, ed. by S. R. P. Silva et al. (Word Scientific, Singapore, 1998), p.224

32. T. Kohler, T. Frauenheim, G. Jungnickel, Phys. Rev. B **52**, 11837 (1995)
33. D. A. Drabold, P. A. Fedders and P. Strumm, Phys. Rev. B **49**, 16415 (1994)
34. G P Lopinski, V I Merkulov, J S Lannin, App Phys Lett 69 3348 (1996)
35. J. R. Shi, X. Shi, Z. Sun, E. Liu, B. K. Tay, S. P. Lau, Thin Solid Films **366**, 169 (2000)
36. F. Mauri, A. Del Corso, Appl. Phys. Lett. **75**, 644 (1999)
37. A.C. Ferrari, A. Libassi, B.K. Tanner, V. Stolojan, J. Yuan, L. M. Brown, S. E. Rodil, B. Kleinsorge, J. Robertson, Phys. Rev. B **62**, 11089 (2000)

X-RAY REFLECTIVITY OF ULTRA-THIN DIAMOND-LIKE CARBON FILMS

B. K. Tanner[1], A. LiBassi[1]*, A. C. Ferrari[2], and J. Robertson[2]

[1]Physics Department, University of Durham, Durham, DH1 3LE, UK
[2]Engineering Department, University of Cambridge, Cambridge, CB2 1PZ, UK
*Now at: Dipartmento di Ingegneria Nucleare, Politecnico di Milano, 20133 Milano, Italy

ABSTRACT

Grazing incidence x-ray reflectivity has been employed to investigate ultra-thin films of tetrahedral amorphous carbon (ta-C) grown with an S-bend filtered cathodic vacuum arc. The results indicate that x-ray reflectivity can be used as a metrological tool for thickness measurements on films as thin as 0.5 nm, which is lower than the range required for carbon overcoats for magnetic hard disks and sliders if they are to reach storage densities of 100 Gbits/in^2. The density of the films was derived from the best-fit to simulated reflectivity profiles from models for the structural parameters. In such thin films, the x-rays are reflected mainly at the film substrate interface, rather than the outer surface, so that the film density is derived from analysis of the oscillations of the post-critical angle reflectivity.

INTRODUCTION

Hard amorphous diamond-like carbon (DLC) coatings exhibit mechanical, thermal and optical properties close to those of diamond. They can be deposited over a wide range of thickness by different deposition processes, on a variety of substrates at or near room temperature. This versatility, combined with high hardness, good wear and corrosion resistance properties has resulted in their extensive use as ultra-thin overcoats for magnetic media.

In the past, electron energy loss spectroscopy (EELS) has been used to obtain the sp^3 content (from the size of the π^* peak in the carbon K edge absorption spectrum), and the mass density (deduced from the valence plasmon energy in the low energy loss spectrum). However, this analysis is dependent on choice of an electron effective mass and there has been extensive argument in the literature as to the correct value [1-3]. Grazing incidence x-ray reflectivity measurements permit the near surface mass density to be determined independently of the plasmon energy [4]. We have recently shown that the combination of electron energy loss spectroscopy and grazing incidence reflectivity resulted in the identification of a unique effective mass for all amorphous carbons and diamond to be used to convert the plasmon energy in mass density [5]. The correct general relation between density and coordination for carbons could then be determined [5].

In Ref. [5] we also showed, from the grazing incidence x-ray reflectivity data, that layering was not intrinsic to DLC films, but a function of deposition conditions. Most of the data were from films typically 20-100nm thick. As the thickness of films for application in magnetic recording media is typically only a few nanometers, we have examined the limits to the sensitivity of the x-ray technique for thickness and density measurement. In this paper we show that the technique is capable of being used as a metrological tool for nanometer thick DLC films. In such thin films, the x-rays are reflected mainly at the film substrate interface, rather than the

outer surface, so that the film density is derived from analysis of the oscillations of the post-critical angle reflectivity.

SAMPLE PREPARATION

The ta-C films were deposited using a Filtered Cathodic Vacuum Arc (FCVA) with an integrated off plane double bend (S-Bend) magnetic filter. The deposition chamber was evacuated to 1×10^{-8} Torr using a turbo molecular pump. Ta-C films with particle area coverage of less than 0.01% and uniform cross section are consistently deposited using this system [5,6]. A series of films was grown for increasing deposition times of 6,10 and 20 seconds defocusing the beam in order to achieve a small deposition rate and so to produce ultra-thin samples in a more controlled way. Another sample was grown for 15 seconds, but in this case the plasma was not stable and thus the effective deposition time was lower.

EXPERIMENTAL TECHNIQUE

Specular x-ray reflectivity measurements were made with a Bede GXR1 reflectometer using CuK$_\beta$ radiation (λ=1.3926 Å). In all cases, the forward diffuse scatter was measured by recording a coupled θ-2θ (specimen-detector) scan with the specimen offset by -0.1° from the specular condition. The intensity in this scan was subtracted form the measured specular scatter to obtain the true specular scatter. These data were automatically fitted, with little constraint on the available parameters, to the scatter simulated from model structures using the Bede REFS-MERCURY code [7]. The program uses a genetic algorithm to avoid trapping in local minima in searching for the least absolute logarithm of the difference between experiment and the simulation. The simulation is based on the fractal model developed by Sinha et al. [8] and extended by Wormington et al. [9].

RESULTS

Even for the shortest deposition time, a distinct difference could be detected between the reflectivity profiles from the bare silicon substrate and those wafers on which carbon films had been deposited. Fig. 1 shows the reflectivity curves multiplied by the fourth power of the incidence angle. This method of data presentation enhances the visibility of low contrast fringes. For a perfectly smooth surface and in the absence of noise, beyond about twice the critical angle, such a plot is parallel to the x axis. As the deposition time increases, there is a displacement of the broad fringe towards smaller angle, consistent with increasing thickness of the ta-C film. For the longest deposition time, a second fringe becomes visible as the period decreases. There is no doubt that a film is present following only 6 seconds deposition.

The critical angle is defined by the spike in the plot (at about 700 arc seconds) and from its position the near surface density can be determined. Within the accuracy of this measurement, there is no significant variation in the critical angle between the samples.

Fits between the simulation from a model structure consisting of a single carbon layer and the observed specular reflectivity are shown for samples deposited in 6, 10 and 20 seconds in Figs 2(A,B,C). Fig 2(D) shows the silicon substrate. Best-fit parameters are listed in Table 1. Figure 3 shows the carbon thickness as a function of deposition time. We note that the intercept at t=0 is 1.7nm, suggesting that this corresponds to the thickness of native oxide film. The

thickness of the film deposited for 15 seconds is low due to instability of the plasma during a significant part of the deposition time.
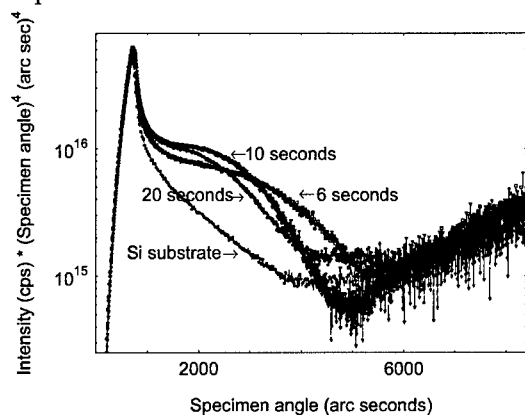
Fig 1: Specular intensity multiplied by the fourth power of the incidence angle for films with various deposition times
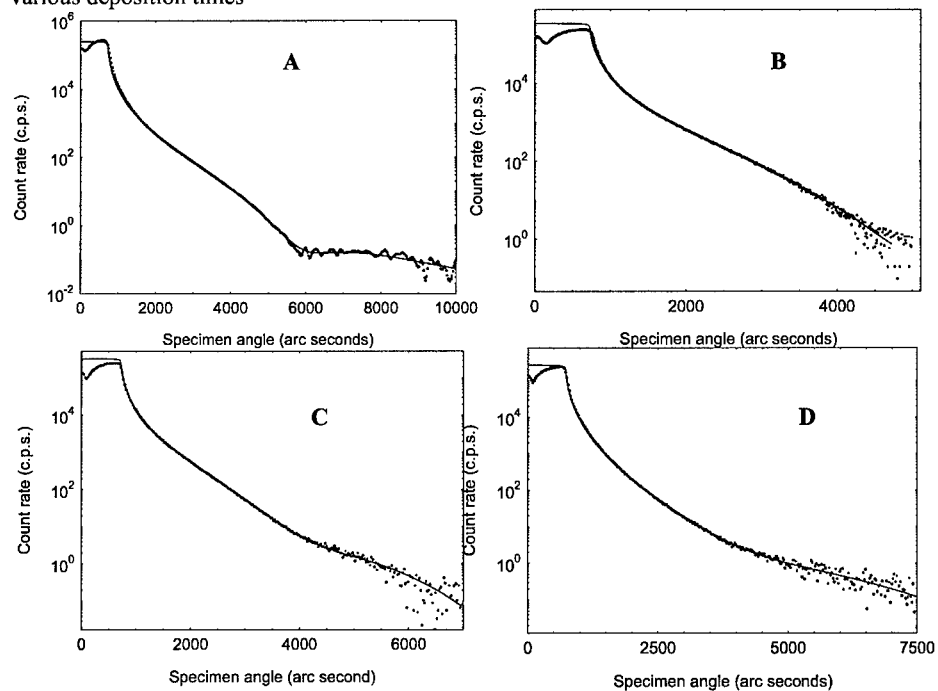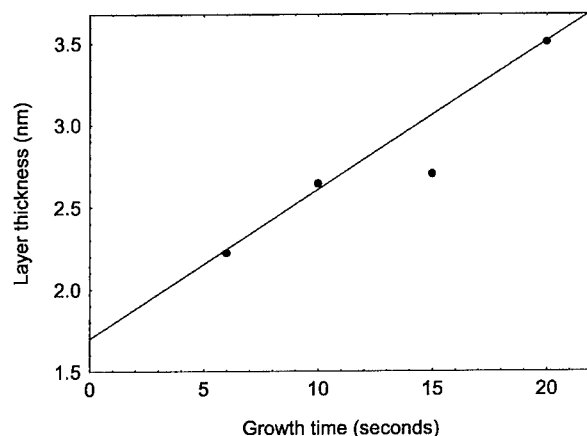

Fig 2: Experimental (points) and best-fit simulations (lines) to ta-C films deposited for (A) 6 seconds, (B) 10 seconds, (C) 20 seconds and (D) Si substrate.

In order to fit the specular reflectivity of the bare substrate, it proved essential to include the presence of a native oxide film within the simulation model. Figure 2(D) shows the best fit between experiment and simulation and here the silicon oxide thickness was determined to be 1.75nm, with 0.48nm effective roughness. The effective roughness arises principally from the density gradient through the oxide layer; specular reflectivity measurements cannot distinguish between compositional grading and true roughness, as there is no component of the scattering vector in the plane of the sample. However, an equally good statistical fit could be found for a number of oxide thickness and densities. Within the dynamic range of the laboratory experiments, it is impossible to define the oxide properties more tightly.

Table 1

Layer parameters (thickness, t, interface width, σ, and density, ρ) derived from best-fit simulations. (Silicon substrate density 2.33 g/cm^3)

Dep. time (s)	σ(Si) nm	t(ta-C) nm	σ(ta-C) nm	ρ(ta-C) g/cm^3
6	0.05	2.22	0.8	3.2
10	0.05	2.64	0.94	3.12
15	0.05	2.70	0.72	2.74
20	0.05	3.51	0.66	2.72

Fig. 3: Film thickness versus carbon deposition time.

The fit shown in Fig 2(D) corresponds to a film of thickness consistent, within the measurement precision, with the extrapolated value from Fig 3. The success of fitting a single layer to the data for the ta-C films suggests that the density of the silicon oxide is increased during the initial deposition stages of the ta-C film, probably by intermixing of C ions. Indeed, given the initial HF cleaning of the substrate, even if the deposition were not performed

immediately afterwards, we do not expect a pure SiO_2 interface, but a mixture of Si, C and oxygen, as shown by cross sectional EELS measurements of the interface [10].

DISCUSSION

As is evident from Fig. 3, measurement of a film of 2 nm thickness is quite within the capability of the technique. Measurement of the thickness of films, typically 2-4nm, used for magnetic recording coatings is thus feasible. While the statistical precision on the best-fit parameter is sub-Ångstrom, it is difficult to be confident in the thickness measurement to better than 0.1nm. At this level, errors in alignment, resulting in slipping off the specular ridge, and incomplete subtraction of the forward diffuse scatter can result in different best-fits being returned.

Unlike the case of thicker films [5], for the ultra-thin carbon films the critical angle is not strongly influenced by the film density. This is because the evanescent wave reaches the silicon substrate below the critical angle and the substrate density determines the critical angle. Forward simulations of thin films of differing density confirm the insensitivity. Only for ta-C films on silicon over about 20nm thickness can the critical angle be used reliably to measure the near-surface density. Although the density influences the fringe contrast, the film interface width also influences the contrast. On the other hand, the film density does affect the position of the fringe maximum. Despite the ability to measure quantitatively the precision of the fit as the two parameters vary, a degree of uncertainty remains in the determination of the film density for these ultra-thin layers. X-ray reflectivity is not composition-specific and we have already noted that success of fitting a single layer to the data for the ta-C films suggests that the density of the silicon oxide is increased during the initial deposition stages of the ta-C film, probably by intermixing of C ions. In any case our data show that a density of $\sim$3 g/cm^3 can be attained even for such ultra-thin ta-C films, which suggests that the high corrosion resistance can be maintained down to the nm scale, together with a sufficiently high Young's Modulus of at least 300 GPa [12]. Note as well that the structure of the ultra-thin S-bend FCVA films resembles that of the thicker S-bend films, with a scaling of the bulk layer thickness, but not of the surface ond interface layers (which are in the sub-nanometer range both in thick and thin films).

CONCLUSION

Grazing incidence reflectivity does provide a non-destructive metrological tool for the measurement of the thickness of nanometer thick diamond-like carbon films The X-ray reflectivity technique for film thickness measurement is directly traceable to international standards of length [11]. Measurement of the density, on the other hand is more difficult and less reliable for these ultra-thin carbon films. It can only be deduced by careful fitting of a number of interacting parameters in model structures of the films and the density values derived should be interpreted cautiously.

ACKNOWLEDGEMENTS

REFERENCES

1. D.R. McKenzie, D. Muller, B.A. Pailthorpe, Phys. Rev. Lett **67**, 773 (1991)
2. P.J. Fallon, V.S. Veerasamy, C.A. Davis, J. Robertson, G.A.J. Amaratunga, W.I. Milne, J. Koskinen, Phys. Rev. B **48**, 4777 (1993)
3. J. Schwan, S. Ulrich, T. Theel, H. Roth, H. Ehrhardt, P. Beker, S.R.P. Silva, J. Appl. Phys. **82**, 6024 (1997)
4. A. Libassi, A. C. Ferrari, V. Stolojan, B. K. Tanner, J. Robertson and L. M. Brown, Diamond Relat. Mater. **9**, 771 (2000)
5. A C Ferrari, A Li Bassi, B K Tanner, V Stolojan, J Yuan, L M Brown, S E Rodil, B Kleinsorge and J Robertson, Phys Rev B **61** 11089 (2000).
6. K. B. K. Teo, S. E. Rodil, J. T. H. Tsai, A. C. Ferrari, J. Robertson, and W. I. Milne, J. Appl. Phys. **89**, 3706 (2001)
7. M Wormington, C Panaccione, K M Matney and D K Bowen, Phil. Trans. Roy. Soc. **357** 2827 (1999)
8. S K Sinha, E B Sirota, S Garoff and H B Stanley Phys Rev. B **38** 2973 (1988)
9. M Wormington, I Pape, T P A Hase, B K Tanner and D K Bowen, Phil . Mag. Letts **74** 211 (1996)
10. C. A. Davis, G. A. J. Amaratunga, Phys. Rev. Lett. **80**, 3280 (1998)
11. D K Bowen and R D Deslattes, in: Characterization and Metrology for ULSI Technology 2000, eds. DG Seiler, AC Diebold, TJ Shaffner, R McDonald, WM Bullis, PJ Smith and EM Secula, Am. Inst. Phys. Conf. Proc. **550**, (2001) 570
12. M.G. Beghi, C. E. Bottani, A. LiBassi, A.C. Ferrari, K.B.K. Teo, J. Roberstson, these proceedings.

Elastic Constants of Nanometer Thick Diamond-like Carbon Films

Marco G. Beghi, Carlo E. Bottani, Andrea LiBassi, Rosanna Pastorelli, Brian K. Tanner[1],
Andrea C. Ferrari[2] and John Robertson[2]
INFM and Nuclear Engineering Department, Politecnico di Milano, I-20133 Milan, Italy,
[1] Physics Department, University of Durham, Durham, DH1 3LE, UK
[2] Engineering Department, Cambridge University, Cambridge CB2 1PZ, UK

ABSTRACT

Carbon films of thickness down to 2 nanometers are necessary to achieve a storage
density of 100 Gbit/in^2 in magnetic hard disks. Reliable methods to measure the properties of
these ultrathin films still have to be developed. We show for the first time that combining
Surface Brillouin Scattering (SBS) and X-ray reflectivity measurements the elastic constants of
such films can be obtained. Tetrahedral amorphous carbon films were deposited on silicon, by an
S bend filtered cathodic vacuum arc, which provides a continuous coverage on large areas free of
macroparticles. Films of thickness down to 2 nm and density of ~3 g/cm^3 were produced and
characterized. The dispersion relations of surface acoustic waves are measured by SBS for films
of different thickness and for the bare substrate. Waves can be described by a continuum elastic
model. Fitting of the dispersion relations, computed for given film properties, to the measured
dispersion relations allows the derivation of the elastic constants. For a 8 nm thick film we find a
Young's modulus E around 400 GPa, with a shear modulus G lying in the 130 – 210 GPa
interval. For a 4.5 nm thick film, E is around 240 GPa, with G lying in the 70 – 130 GPa interval.
Results for even thinner films become highly sensitive to the precision of the substrate
properties, and indicate that the above values are lower bounds. We thus show that we can grow
and characterize nanometer size tetrahedral amorphous carbon films, which maintain their
density and mechanical properties down to the nm range.

INTRODUCTION

The storage density of magnetic hard disks is steadily increasing [1,2]. Technological
developments are required to maintain the increasing trend. Namely, the distance between the
recording head and the magnetic material has to be decreased, and this requires a reduction of the
thickness of the protective coatings of the disk and the head. Carbon coatings are presently the
standard choice: they provide protection against corrosion, grafting sites for the lubricant
molecules and mechanical protection [1,2]. The continuity of the film is a crucial requisite. The
achievement of a storage density of 100 Gbit/in^2 requires a reduction of coating thickness down
to 2-5 nanometers. The characterization of such thin films is still an open question. The elastic
constants provide useful information: beside the direct characterization of the mechanical
behavior, they give indirect indications on the quality and the continuity of the film. Although a
film of few nanometers on a softer substrate cannot provide a strong mechanical protection [2],
measurement of its elastic moduli provides however significant indications on film quality,
including the fraction of sp^3 bonding.

The stiffness of an amorphous, and therefore mechanically isotropic, film is fully
characterized by two independent parameters, which are typically taken among Young's
modulus E, shear modulus G, bulk modulus B, Poisson's ratio ν or among the elements C_{ij} of the

elastic tensor. Any two of them determine all the others. Their measurement for ultra-thin films is arduous. Indentation directly supplies the hardness, and is commonly adopted to measure also the elastic constants [3-5]. However for film thicknesses below ~1 μm the requisite of indentation depth significantly smaller than film thickness is met with difficulties, and, especially for hard films on softer substrates, the behaviour of the substrate can affect the results. For thicknesses of a few nanometers indentation is no longer viable. The elastic properties must be probed by other methods, namely exploiting acoustic waves.

Brillouin scattering, i.e. the scattering of an electromagnetic wave (a photon) by an acoustic wave (a long wavelength acoustic phonon) provides a convenient, contact less way to measure the spectrum of acoustic waves. Both bulk acoustic waves and surface acoustic waves (SAWs) can be measured. Brillouin scattering relies on thermally activated phonons, meaning that the acoustic amplitudes are small and that measurements are time consuming. However the exchanged wavevector is fully determined by the scattering geometry: surface phonons can be probed at wavelengths down to a quarter of a micron. Such acoustic wavelengths are significantly shorter than those probed by any other measurement technique. Since the acoustic velocities can be accurately computed as functions of the elastic moduli and the mass density, their measurement provides an access to the elastic properties. Brillouin scattering has proved able to measure the elastic properties of materials, exploiting either bulk acoustic waves [6] or Surface Brillouin Scattering (SBS), i.e. scattering by SAWs [7-12]. In particular in the case of layered structures, namely of a single isotropic layer on an anisotropic substrate, the elastic constants of films have been measured, for film thicknesses ranging from hundreds to tens of nanometers [10-12]. The measurement of film properties of thickness below 10 nm remained a challenge, which has been faced in this work.

EXPERIMENT

The tetrahedral amorphous carbon (ta-C) films were deposited using an S-Bend Filtered Cathodic Vacuum Arc (FCVA) with an integrated off plane double bend (S-Bend) magnetic filter. The deposition chamber was evacuated to 10^{-8} torr using a turbomolecular pump. ta-C films with particle area coverage of less than 0.01% and uniform cross section are consistently deposited with this system [13,14]. A series of films was grown for increasing deposition times defocusing the beam in order to achieve a small deposition rate and so to produce ultra-thin samples in a more controlled way. Thickness density and layering of these ultra-thin samples were derived by X-Ray reflectivity [15], Table I. Note that the structure of the ultra-thin S-bend FCVA films resembles that of thicker S-bend films [14], with a scaling of the bulk layer thickness, but not of the surface and interface layers (which are in the sub-nanometer range both in thick and thin films). Four samples are considered here: a bare silicon substrate, with a thin layer of native oxide due to exposition to air, and three carbon films.

SAW velocities of all the samples were measured by SBS: the specimen is illuminated by laser light and the spectrum of the scattered light is analyzed. Beside the strong peak of the elastically reflected light at frequency Ω, the spectrum contains the doublet at frequencies $\Omega \pm \omega$, shifted by the SAW frequency ω. The SAW wavevector $q_{\parallel}$ is selected by the scattering geometry (in backscattering, at incidence angle θ, $q_{\parallel} = 2 (2\pi/\lambda) \sin \theta$, where λ is the laser wavelength) and the SAW velocity $v = \omega/ q_{\parallel}$ is directly obtained. Measurements were performed with SAW propagation along the [100] direction on the (001) face of the Si substrate, at room temperature, in backscattering, with incidence angle θ from 30° to 70° (see Fig.1). The incident light is p-

Table I: Samples' properties

Specimen	Film nature	Film density (g/cm^3)	Film thickness (nm)
A	SiO_x.	--	~2
B	ta-C	2.8	8
C	ta-C	2.8	4.5
D	ta-C	3.2	2.2

polarised; the scattered light is collected without polarisation analysis, and analysed by a tandem 3+3 pass high contrast interferometer of the Sandercock type. The light source was an Argon ion laser operating at $\lambda = 514.5$ nm. The incident power on the specimen was around 100 mW, focused into a spot of the order of 10^3 μm^2; irradiation did not induce film modifications

RESULTS

Due to the low film thickness a single SAW is present, the Rayleigh wave modified by the presence of the film (Modified Rayleigh Wave, MRW). Its velocity can be computed [16] as function of the elastic constants and mass density of both the film and the substrate, of film thickness and on the wavevector $q_{\parallel}$. It is thus possible to solve the inverse problem, i.e. the derivation of the elastic constants from measured SAW velocities [17]. The elastic constants and mass density of the anisotropic Si substrate are known (C_{11}=166 GPa, C_{12}=63.9 GPa, C_{44}=79.6 GPa, ρ=2.33 g/cm^3 [20]), as well as the SAW wavevector and the film thickness and density. Thus the acoustic velocities remain functions of the unknown elastic constants of the film. It is
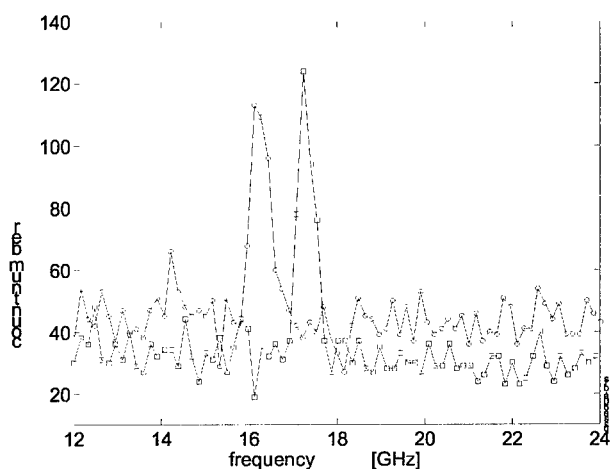
Figure 1. Portions of Brillouin spectra at 60° incidence showing the peak due to modified Rayleigh wave, measured under identical conditions on specimens A (circles) and B (squares).

known [11] that in this kind of films the properties can have a gradient in proximity of the outer surface and the inner interface but, to avoid exceeding complexities, the films are modeled as a single homogeneous equivalent film, with a sharp interface with the substrate.

It has been shown [18] that among the various elastic moduli that can represent the stiffness of an isotropic material the (E,G) pair is the most appropriate for the solution of the inverse problem. The velocities $v_c(E,G)$ are computed for each value of $q_\parallel$ (i.e. for each incidence angle) at the nodes of a rectangular mesh. The couple $(E,G)_{film}$ is obtained by a least squares fit of the computed velocities v_c to the measured ones v_m :

$$R = \sum \left(\frac{v_c^i(E,G) - v_m^i}{\sigma_e^i} \right)^2 = \min,$$

where σ_e^i are the variances of the corresponding v_m^i due to the various uncertainties connected to the measurement (geometrical imperfections [19], statistical errors). The (E,G) couple which minimizes R is the most probable solution of the inverse problem, and the regions corresponding to any fixed confidence level are also obtained.

It must be remembered that not all the (E,G) plane is physically meaningful. In this plane the v=const lines are straight lines through the origin, and the v=0.5 and v=0 line delimit the triangle which is fully meaningful. The v=0.5 line is the limit for thermodynamic stability. When approaching or crossing this limit, the computed SAW velocities remain finite and continuous, but the bulk modulus B diverges. This means that if the confidence region falls close to the stability limit even a small region in the (E,G) plane, i.e. a good determination of both E and G, still corresponds to a wide interval of B, which remains poorly determined. At the same time a physical plausibility limit can be imposed, considering only the part of the confidence region which corresponds to values of B below a pre-determined value. In this work the diamond value B = 445 GPa is taken a physically plausible upper limit. On the other side the v=0 line does not mark a thermodynamic instability but, since negative values of Poisson's ratio can at most be found in extremely rare and peculiar cases, the v=0 line is taken as a physically plausible limit. Figure 2 shows the confidence regions found for specimen B. The confidence regions cross the physically acceptable region, meaning that v and B remain essentially undetermined, while reasonably well defined intervals are found for E and G: E = 350 ÷ 420 GPa and G = 130 ÷ 210 GPa. For specimen C the intervals are E = 220 ÷ 260 GPa and G = 70 ÷ 130 GPa, v and B remaining also undetermined. This is in agreement with the outcome of a sensitivity analysis study [18] which showed that E and G can be determined much better than v and B. The confidence regions must be seen as the real outcome of the measurements. Further resolution within the confidence regions has not a real significance. The obtained values of the elastic constants allow to fit the measured dispersion relations, as shown in Fig. 3. Figure 3 also explains the difficulty in obtaining the film elastic constants for specimens A and D, whose measured velocities are lower than those of a bare silicon substrate of nominal properties [20]. The fit for specimen A is in fact bad, and a better fit would require negligible film elastic constants and an unreasonably high mass density of silicon oxide. Also specimen D (carbon) seems to be acoustically slower, i.e. more compliant, than silicon. These findings suggest that in reality the actual properties of the silicon substrate are slightly different from the accepted values for pure silicon [20]. The stiffness of the substrate is slightly overestimated, implying that the film stiffness is underestimated. Due to the very small film thickness a very small overestimation of substrate stiffness is sufficient to lead to a significant underestimation of film stiffness.
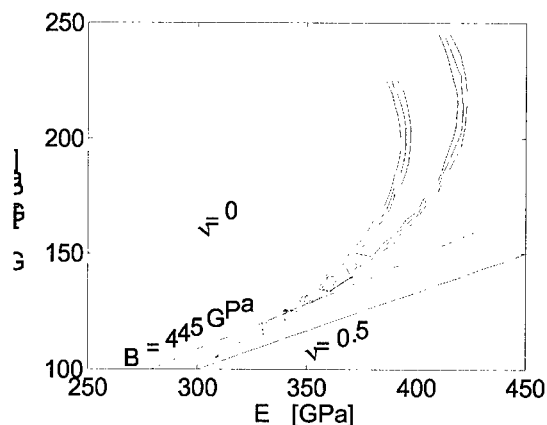
Figure 2. 90%, 95% and 99% confidence regions in the (E,G) plane for specimen B

DISCUSSION AND CONCLUSIONS

It has been shown that films only a very few nanometers thick exhibit dispersion relations of the modified Rayleigh wave that are measurably different. The analysis of these dispersion relations allows to measure the elastic constants of ta-C films, which have a significant stiffness also in films of 8 and 4 nanometres thick. For thinner films the analysis shows that a very precise characterization of the substrate is needed. The results for the thinnest films indicate that the values of the elastic constants found for the other films must be viewed as lower bounds.
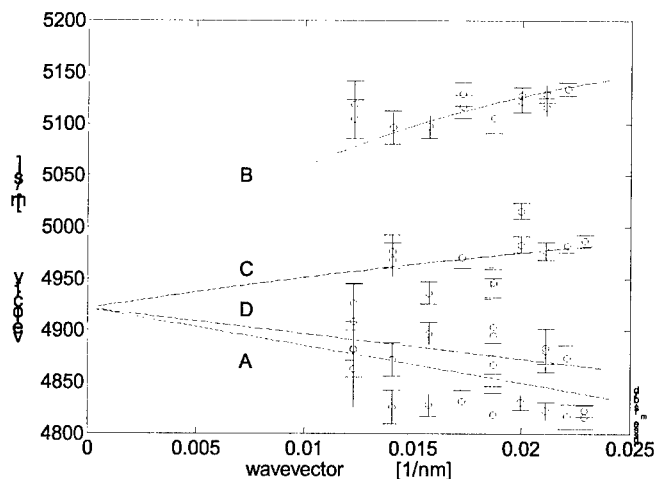
Figure 3. Measured velocities for the four specimens; dispersion relations computed with the film elastic moduli obtained from the best fit procedure, and accepted values of silicon properties [20]. The limit at null wavevector is the Rayleigh velocity of a bare silicon substrate.

ACKNOWLEDGEMENTS

REFERENCES

1. P. R. Goglia, J. Berkowitz, J. Hoehn, A. Xidis and L. Stover, *Diamond Relat. Mater.* **10**, 271-277 (2001)
2. J. Robertson, *Thin Solid Films* **383**, 81-88 (2001)
3. G.M. Pharr, D.L. Callahan, S.D. McAdams, T.Y. Tsui, S. Anders, J.W. Ager, I.G. Brown, C.S. Bhatia, S.R.P. Silva and J.Robertson, *Appl. Phys. Lett.*, **68**, 779 (1996)
4. J.A. Knapp, D.M. Follstaedt, S. M. Myers, J.C. Barbour and T. A. Friedmann, *J. Appl. Phys.* **85**, 1460 (1999)
5. T. A. Friedmann, J. P. Sullivan, J.A. Knapp, D. R. Tallant, D.M. Follstaedt, D. L. Medlin and P. B. Mirkarimi, *Appl. Phys. Lett.,* **71**, 3820 (1997)
6. M. Grimsditch, in *Handbook of elastic properties of solids, liquids and gases, Vol. 1,* M. ed. by Levy et al. Academic Press / Harcourt Publishers Ltd., Sidcup, UK, 2000.
7. J. D. Comins, in *Handbook of elastic properties of solids, liquids and gases, Vol. 1,* ed. by M. Levy et al. Academic Press / Harcourt Publishers Ltd., Sidcup, UK, 2000.
8. P. Zinin P., M. H. Manghnani., S. Tlechev, V. Askarpour, O. Lefeuvre and A. Every, *Phys. Rev. B,* **60** 2844 (1999).
9. M.G. Beghi, C.E. Bottani, P.M. Ossi, T. Lafford and B.K. Tanner, *J. Appl. Phys.*, **81**, 672 (1997), and references therein
10. A.C. Ferrari, J. Robertson, M.G. Beghi, C.E. Bottani, R. Ferulano and R. Pastorelli, Appl. Phys. Lett. **75**, 1893 (1999)
11. A.C. Ferrari, J. Robertson, R. Pastorelli, M.G. Beghi and C.E. Bottani, Mat. Res. Soc., Symp. Proc. **594**, 289 (2000)
12. M.G. Beghi, C.E. Bottani, and R. Pastorelli, in *Mechanical Properties of Structural Films, ASTM STP 1413,* ed. by C. Muhlstein and S. B. Brown, American Society for Testing and Materials, West Conshohocken, PA, 2001.
13. K.B.K. Teo, S.E. Rodil, J. T. H. Tsai, A. C. Ferrari, J. Robertson and W.I. Milne, *J. Appl. Phys.* **89**, 3706 (2001)
14. A.C. Ferrari, A. LiBassi, B. K. Tanner, V. Stolojan, J. Yuan, L. M. Brown, S. E. Rodil, B. Kleinsorge, and J. Robertson, *Phys. Rev. B* **62**, 11089 (2000).
15. B.K. Tanner, A. LiBassi, A.C. Ferrari and J. Robertson, *these Proceedings.*
16. G.W. Farnell and E.L. Adler, in *Physical Acoustics*, Vol. 9, ed. by W. P. Mason and R. N. Thurston, Academic, New York, 1972, p.35
17. R. Pastorelli, S. Tarantola, M.G. Beghi, C.E. Bottani, and A. Saltelli, in *Mechanical Properties of Structural Films, ASTM STP 1413*, ed. by C. Muhlstein and S. B. Brown, American Society for Testing and Materials, West Conshohocken, PA, 2001.
18. R. Pastorelli, S. Tarantola S., M.G. Beghi, C.E. Bottani and A. Saltelli, *Surf. Sci.* **468**, 37 (2000).
19. R.P. Stoddart, Crowhurst J. C., Every A. G. and Comins J. D, *J. Opt. Soc. of America B,* **15**, 2481 (1998)
20. H.J. McSkimin and P. Andreatch, *J. Appl. Phys.* **35**, 3312 (1964)

Acoustic Microscopy and Surface Brillouin Scattering
of Amorphous Carbon Pressure-Synthesized from C_{60}

Pavel V. Zinin[1], Murli. H. Manghnani[1], Sergey Tkachev[1], Xinya Zhang[1]
Alexander G. Lyapin[2], Vadim V. Brazhkin[2], Ivan A. Trojan[2]
[1] School of Ocean and Earth Science and Technology, University of Hawaii
Honolulu, HI 96822, USA
[2] Institute for High Pressure Physics, Russian Academy of Sciences
Troitsk, Moscow District 142092, Russia

ABSTRACT

Here, we report successful measurements by surface Brillouin scattering (SBS) and scanning acoustic microscopy (SAM) of the elastic properties of small specimens of amorphous carbon obtained from C_{60} under high pressure and temperature. The superhard phases of amorphous carbon were synthesized from C_{60} at pressure 13 - 13.5 GPa and temperature 800-900 °C. Two types of acoustic waves have been detected by SBS in superhard samples: surface Rayleigh wave and bulk longitudinal wave. The longitudinal velocity (v_L) in the hardest sample is slightly lower than longitudinal wave velocity in diamond in [110] direction. Simultaneous measurements of the Rayleigh and longitudinal wave velocities make it possible to determine shear and bulk elastic moduli of the specimens. Obtained elastic properties for amorphous carbon synthesized under pressure 13.5 GPa and temperature 900°C are close to those for diamond, indicating that bonds among amorphous carbon network are diamond bonding dominated.

INTRODUCTION

Recent interest in new superhard materials triggered by the discovery of the fullerene molecule C_{60} has led to a series of extensive experimental studies of amorphous and nanocrystalline carbon phases and their properties in both bulk [1] and deposited as a thin film [2-4] states. Heating at relatively low pressures ($P<8$ GPa) has revealed one-dimensional (1-D)- and two-dimensional (2-D)-polymerization [5] of C_{60} and subsequent collapse of the fullerene structure into graphite-like disordered carbon [6]. Heating the fullerite up to 1000-1300 K under the pressure 3 to 8 GPa leads to a formation of disordered phases with carbon atoms predominantly in sp^2 states. Heating C_{60} at $P>8$ GPa results in formation of three-dimensional (3-D) polymerized amorphous phases of C_{60}, with large number of sp^3 atomic sites [7] and nanocrystalline composites (nanoceramics) of diamond and graphite [8], fueling the most recent debates on the existence of ultrahard fullerene-based phases with hardness higher than diamond [9]. The structure of all these phases contain large amount of 4-fold sp^3 atomic states. The existence of ultrahard fullerene phase with hardness higher than diamond was recently discussed [7, 9]. Such phases can be obtained only in extremely small size.

Here, we report successful measurements by surface Brillouin scattering and scanning acoustic microscopy of the elastic properties of two small bulk specimens of amorphous carbon synthesized from C_{60} under high pressure and temperature. The results of these measurements are of importance in understanding the problem of phase transition of C_{60} under high pressure and temperature and particularly the issue of existing ultra and superhard phases.

It has been shown that under high pressure and temperature C_{60} crystals transform through a series of intermediate polymeric, amorphous and nanocrystalline carbon phases. Heating at relatively low pressures (P < 8 GPa) results in 1-D and 2-D polymerization of C_{60} [5, 10] and subsequent collapse of the fullerene structure into graphite-like disordered carbon [6, 10]. The 3-D polymerized phases of C_{60} [7], amorphous phases with a large amount of sp^3 atomic sites [11], and nanocrystalline diamond and graphite [7] are formed upon heating at these pressures. The formation of covalent bonds makes the new phases very stable. Hirai *et al.* [12] reported amorphous diamond prepared from C_{60} by shock compression. Based on the indirect scratching observations [13] and measurements made by time-resolved acoustic microscopy [14], Blank *et al.* [9] postulated that superhard and ultrahard phases could be synthesized from C_{60}. However, their experimental results have not been independently confirmed. Further, there might exist some discrepancy in their measured values of elastic constants [7] as fullerite materials obtained under high pressure are not homogeneous and consist of several phases with different elastic properties. The dimensions of the different phases vary from tens to hundreds of microns. Thus, Brillouin spectroscopy and acoustic microscopy, which provide high lateral (1 - 30 μ) and axial (1 - 100 μ) resolution in elastic properties measurements, are valuable tools for characterizing such specimens.

The first experimental SBS study of the fullerene product resulting from laser irradiation of a C_{60} single crystal [15] revealed that high laser intensities must be used to detect Brillouin scattering. Sound velocities measured in that experiment (280-700 m/s) are substantially lower than the value reported in literature for solid C_{60}. The shift of the Brillouin doublets observed by Manfredini *et al.* [15] was in the energy range typical for slow polymer or carbon gels. Polymerized phases obtained under high T-P are much stiffer. One would therefore expect normal laser intensity to produce SBS spectra from hard fullerene materials. To our knowledge Brillouin scattering studies of bulk hard phases synthesized from C_{60} have not been conducted yet.

EXPERIMENTAL DETAILS

Specimens

Two bulk amorphous carbon (a-C) samples, employed in this study, were synthesized from C_{60} fullerite powder at 13 to 13.5 GPa, 800±100°C (sample A) and 900±100°C (sample B) at the Institute for High Pressure Physics, Moscow. Fullerite powder was produced at the Russian Scientific Center "Kurchatov Institute".

Brillouin light scattering

Brillouin light scattering is generally referred to as inelastic scattering of an incident optical wave field by thermally excited elastic waves in a sample [16]. The phonons moving in thermal equilibrium with very small amplitudes can be viewed as a moving diffraction grating by an incident light wave. Mechanism of the light scattering by moving diffraction gating can be explained by the two concepts of Bragg's reflection and Doppler shift. Brillouin light scattering can be viewed as a Bragg's reflection of the incident wave by the diffraction grating created by thermal phonons [17].

For the backscattering geometry, the surface acoustic modes which cause the diffraction of the incident light have wave vector q given by

$$q = \frac{4\pi \sin \theta}{\lambda},$$

λ is the wavelength of the incident laser light, and q is the projection on the surface of the scattering wave vector. The moving corrugating surface scatters the incident light with a Doppler shift, giving scattered photons with shifted frequencies. The frequency shift δf in the light scattering is related to the surface wave velocity v_{SAW} by equation

$$v_{saw} = \frac{\lambda}{2\sin\theta} \delta f$$

At room temperature and above, the Brillouin scattering efficiency or intensity for scattering from the surface of an opaque materials by dynamic rippling of the surface can be represented as [17]

$$I(\omega) = A \frac{T}{\omega} \operatorname{Im} g_{33}(q,\omega)$$

where ω is the angular frequency shift of the light; T is the absolute temperature; factor A depends on the medium (density and permittivity), scattering geometry, polarization and incident photon frequency; $g_{33}(q,\omega)$, Fourier coefficient of the elastodynamic Green's function. A comprehensive description of how $g_{33}(q,\omega)$ is calculated for a multilayered anisotropic medium is given in [17].

Elasto-optic interaction or scattering of light by bulk sound waves result from fluctuations in the dielectric constant caused by the phonons moving in thermal equilibrium. The interaction arises from changes in the refractive index produced by the strain generated by sound waves; the change in refractive index is related to the strain through the elastooptic constants p^{mn}, which determine the degree of interaction between the light and the material [16]. In backscattering, sound velocity (V) can be expressed as a function of the frequency shift and refraction index n by the following formula

$$V = \frac{\lambda \delta f}{2n}$$

Brillouin light scattering technique is ideally suited for studying the elasticity of bulk materials and, especially, thin films [18, 19]. It has proven to be a very effective technique for investigating the near-surface elastic properties of opaque bulk materials.

Acoustic Microscopy

Acoustic microscopy is a relatively new technique that has been developed for non-destructive characterization of the mechanical microstructure of solid materials with a resolution

of 1 μm [20]. A schematic diagram of an acoustic microscope working in the reflection mode is presented in Fig. 1. In conventional acoustic microscopy, a monochromatic sound wave is focused onto a specimen by means of an acoustic lens. The same lens is used to record the signal reflected back from the sample. A liquid couplant, usually water, is placed between the lens and the sample. The spherical lens, i.e. the lens with a spherical cavity, focuses sound onto a spot of size comparable to the sound wavelength in the fluid. The fringes, appearing in the acoustic images around cracks and other discontinuities, are Rayleigh wave fringes; they are seen on defocused images as a result of the interference between waves reflected normal to the specimen surface and waves associated with surface Rayleigh waves [20].
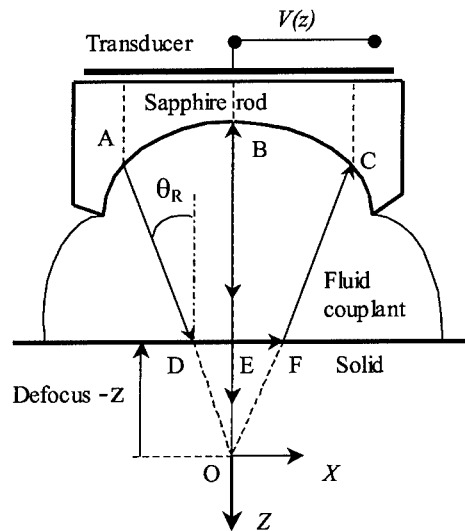
Figure 1. Schematic geometry of the defocused acoustic lens. BE is the trajectory of specular wave, and ADFC is the trajectory of leaky Rayleigh surface acoustic wave (SAW). In the ray model the leaky Rayleigh wave is excited by ray AD, striking the surface at the angle $\theta_R = V_W/V_R$. Here V_W is the velocity of the longitudinal wave in coupling liquid and V_R is the velocity of Rayleigh wave.

RESULTS AND DISCUSSION

Surface scattering from the Rayleigh waves (incident angle = 60°) gives the velocity of 6.5 km/s for the top face of the sample A and 10.1 km/s for the top face of sample B. The top face is a surface where pressure has been applied. The velocity of surface wave along sample surface B is 8% lower than that for [100] diamond. Bulk scattering from the bulk longitudinal wave (LW) can be observed for sample B. Refractive index for the sample is not known. Assuming it to be

close to that for C_{60} (n=2.52) [15], the longitudinal velocity in sample B is then equal to 17.5 km/s. The longitudinal velocity (v_L) in the sample B (17.5 km/s) is higher than that in cBN (15.8 km/s) or in ta-C films (15.5 km/s) and is slightly lower than longitudinal wave velocity (18.6 km/s) in diamond in [110] direction.

An acoustic image of sample A made by acoustic microscope (Leitz ELSAM) is shown in Fig. 2. The image was taken from the side surface of sample A. The fringe width in the cross section of the fibers can be used to determine the Raleigh velocity. The fringe distance is simply half a wavelength of the Rayleigh wave. This gives the Rayleigh wave velocity of 8.0 ± 2.1 km/s. We note that, though the error in the measured Rayleigh wave velocity by SAM is higher than that determined by SBS, the SAM measurements have revealed strong anisotropy in the elastic properties of sample A.

(a)   (b)
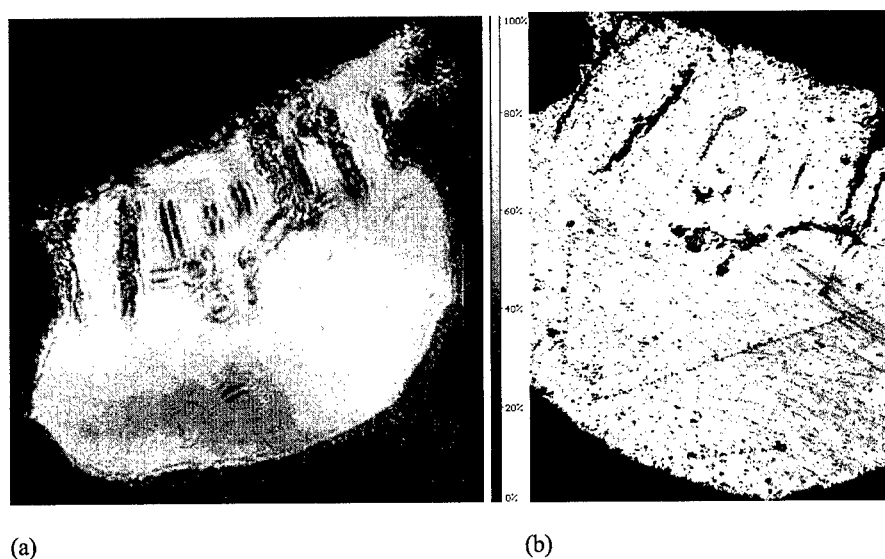
Figure 2. (a) Acoustic image of sample A at 400 MHz, and at a defocus z = -20 μm, field of view 700 μm x 700 μm. (b) Optical image of the same sample field of view 700 μm x 700 μm.

CONCLUSIONS

1. Elastic properties of the superhard phases of amorphous carbon synthesized from C_{60} at pressure 13 - 13.5 GPa and temperature 900±100°C have been obtained by surface Brillouin spectroscopy.
2. The longitudinal velocity in the sample B is higher than that in cBN or in ta-C films and is slightly lower than longitudinal wave velocity in diamond in [110] direction.
3. Measured elastic properties for amorphous carbon obtained under pressure 13 - 13.5 GPa and temperature 900±100°C are close to those for diamond.

4. The SBS and SAM techniques have potential value in characterizing extremely small size specimens such as hard amorphous carbon phases.

ACKNOWLEDGEMENTS

REFERENCES

1.   B. Sundqvist, *Advances in Physics* **48,** 1 (1999).
2.   R. Pastorelli, A.C. Ferrari, M.G. Beghi, *et al.*, *Diamond Relat. Mater.* **9,** 825 (2000).
3.   A.C. Ferrari, J. Robertson, M.G. Beghi, *et al.*, *Appl. Phys. Lett.* **75,** 1893 (1999).
4.   C.E. Bottani, A.C. Ferrari, A.L. Bassi, *et al.*, *Europhys. Lett,* **42,** 431 (1998).
5.   M. Nunez-Regueiro, L. Marques, J.-L. Hodeau, *et al.*, *Phys. Rev. Lett.* **74,** 278 (1995).
6.   J.L. Hodeau, J.M. Tonnerre, B. Bouchetfabre, *et al.*, *Phys. Rev. B* **50,** 10311 (1994).
7.   V.V. Brazhkin, A.G. Lyapin, S.V. Popova, *et al.*, *J. Appl. Phys.* **84,** 219 (1998).
8.   V.V. Brazhkin, A.G. Lyapin, R.N. Voloshin, *et al.*, *JETP Letters* **69,** 869 (1999).
9.   V.D. Blank, S.G. Buga, G.A. Dubitsky, *et al.*, *Carbon* **36,** 319 (1998).
10. L. Marques, J.L. Hodeau, M. Nunez-Regueiro, *et al.*, *Phys. Rev. B* **54,** 12633 (1996).
11. H. Hirai and K. Kondo, *Phys. Rev. B* **51,** 15555 (1995).
12. H. Hirai, Y. Tabira, K. Kondo, *et al.*, *Phys. Rev. B* **52,** 6162 (1995).
13. V.D. Blank, S.G. Buga, N.R. Serebryanaya, *et al.*, *Phys. Lett. A* **205,** 208 (1995).
14. V.D. Blank, V.M. Levin, and N.R. Serebryanaya, *JETP* **87,** 741 (1998).
15. M. Manfredini, C.E. Bottani, and P. Milani, *Chem. Phys. Lett.* **226,** 600 (1994).
16. W. Hayes and R. Loudon, *Scattering of Light by Crystals.* 1978, New York: Wiley. x.
17. J.D. Comins, Surface Brillouin Scattering, in *Handbook of Elastic Properties of Solids, Liquids, and Gases. Volume I: Dynamic Methods for Measuring the Elastic Properties of Solids,* edited by M. Levy, *et al.,* (Academic Press, New York, 2001) pp. 349.
18. R. Pastorelli, P.M. Ossi, C.E. Bottani, *et al.*, *Appl. Phys. Lett.* **77,** 2168 (2000).
19. M. Chirita, R. Sooryakumar, H. Xia, *et al.*, *Phys. Rev. B* **60,** 5153 (1999).
20. P.V. Zinin, Quantitative Acoustic Microscopy of Solids, in *Handbook of Elastic Properties of Solids, Liquids, and Gases. Volume I: Dynamic Methods for Measuring the Elastic Properties of Solids,* edited by M. Levy, *et al.,* (Academic Press, New York, 2001) pp. 187.

MEDIUM-RANGE ORDER STRUCTURES OF AMORPHOUS DIAMOND-LIKE CARBON FILMS

Xidong Chen [*], J. Murray Gibson [*], John Sullivan [**], and Tom Friedmann [**]

[*] Materials Science Division, Argonne National Laboratory, Argonne, IL 60439
[**] Nanostructure and Semiconductor Physics Department, Sandia National Laboratories, Albuquerque, NM 87185-1421

Abstract

In this paper, we have studied medium-range order structures in amorphous diamond-like carbon films with fluctuation microscopy. Medium-range order structures are quantified by a specific form of a general four-body correlation. We name this function as a pair-pair alignment correlation function. By analyzing speckle dark-field images taken over different areas as a function of momentum transfer in reciprocal space, we measured the pair-pair alignment correlation function for both thermally annealed samples and unannealed samples. We have found that thermal annealing introduces medium-range order in amorphous diamond-like carbon films, causing more pairs of atoms to be aligned. These results agree with density-functional simulations. Larger-scale simulations will be needed to fully understand our experimental results.

Introduction

Hydrogen-free amorphous diamond-like carbon films have stimulated great interest because of their useful properties, such as high hardness, chemical inertness, thermal stability, wide optical gap, and negative electron affinity[1]. Consequently, they may have various potential applications in mechanical and optical coatings, MEMS systems, chemical sensors and electronic devices. Amorphous diamond-like carbon films often contains significant amounts of four-fold or sp^3 bonded carbon, in contrast to amorphous carbon films prepared by evaporation or sputtering which consist mostly of three-fold or sp^2 bonded carbon. The ratio and the structure configurations of these three-fold and four-fold carbon atoms certainly decide the properties of these amorphous diamond-carbon films. Although the ratio of three-fold and four-fold carbon has been studied with Raman spectroscopy and electron-loss-energy spectroscopy, very little has been understood regarding key questions such as how the three-fold and the four-fold carbon atoms are integrated in the film, and what structures those three-fold carbon atoms take [2]. These questions cannot be simply answered by normal diffraction technique because they involve structures beyond short-range order.

Theory

Through the history of studying amorphous materials, the radial distribution function (RDF) has played an important role. While it is equivalent to an atomic pair correlation function, its importance relies on the fact that this function can be directly measured from diffraction experiments. The RDF gives good quantitative descriptions of short-range order (2 – 5 Å). However, it is almost impossible to interpret the third and the fourth peaks in the RDF. This is because the number of atoms filling a shell of r increases significantly as r increases. At a very large r, the RDF is approaching to the average number density of atoms. Therefore, the RDF is an ensemble average of the short-range order structures (2 – 5 Å) of the whole sample. It can not provide information on local

structure changes at length scales larger than 5 Å, i.e., the medium-range order structures [3].

For studies of medium-range order structures in the region from 1 nm to 5 nm, either imaging with a resolution of the same order of magnitude or micro-diffraction with a beam size of nanometers is needed. Only transmission electron microscopy (TEM) and scanning transmission electron microscopy (STEM) can provide this kind of resolution. In TEM or STEM experiments, it is straightforward to measure the fluctuation of intensities in an image, in addition to diffraction patterns. While a diffraction pattern yields two-body correlation functions, this variance function of k yields information about correlations beyond the two-body correlation.

In TEM imaging mode, what is projected on the detector is actually the wave front of the electron wave that just leaves the sample. Therefore, under coherent illumination, the intensity of each pixel in a dark-field TEM image is contributed only by a small column of atoms from the sample [4]. Fluctuation microscopy utilizes a phenomenon called the speckle. Although speckle has been found in all types of coherent imaging for many years [5], this microscopy technique is relatively new [6]. Speckle patterns are generated by interference under coherent scattering conditions. Since the intensity in a pixel in a speckle image is actually contributed by a small column of atoms, fluctuations in local structures are reflected in fluctuations in the speckle intensity, as shown in figure1.

Counting:
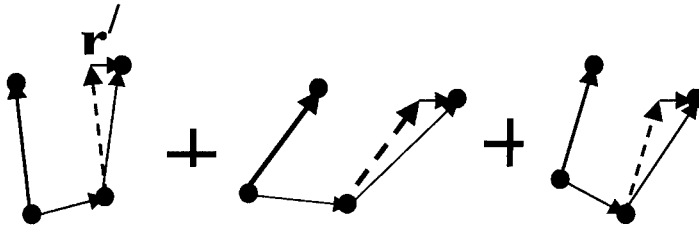
Figure 1 An illustration of the pair-pair alignment function. It counts all atom pairs with the same end vector. These pairs can have varied distances.

The length scale of the sampling column is directly determined by the resolution within the resolution limit of a particular electron microscope. By tuning the resolution, the volume of the sampling column under investigation can be tuned also. Therefore, fluctuation microscopy with varied resolutions will be of great interest in future. With varied resolution, we can study structure changes at different length scales. Hence the scaling behavior of that particular sample can also be studied.

We have for the first time developed a theory to quantify the medium-range order structure [7]. A summary of this theory is the following. A pair-pair alignment function is defined as:

$$G_{2,2}(r^{/}) = \int G_4(r_1, r_2, r^{/}) dr_1 dr_2 \qquad (1)$$

where $G_4(r_1, r_2, r')$ is a four-body correlation function with $r' = r_3 - r_1, r_1, r_2,$ and r_3 give the position of the second , the third and the fourth atom respectively. Therefore, this new function $G_{2,2}(r')$ is the number density of an end vector generated by all possible three-body or four-body configurations. This end vector is a summation of two vectors from a three-body configuration or a four-body configuration. The number distribution of this end vector directly yields information regarding three-body configurations and four-body configurations, which contain correlations beyond the two-body correlations revealed by standard diffraction patterns. The meaning of the above function is shown in figure 1.

It is then easy to prove that $G_4(r_1, r_2, r')$ is actually directly related to the Fourier transform of the intensity fluctuation in speckle images:

$$g_{2,2}(r) \propto r \int_{k_{min}}^{k_{max}} k \sin(kr) DW(k)(<I^2> - <I>^2)dk \quad (2)$$

where $g_{2,2}(r') = r' G_{2,2}(r')$. This is the function measured in practice. It is a measure of how many pairs of atoms are aligned in a certain volume.

Experimental details

We use DigitalMicrograph^{TM} to control a JEOL-4000EX microscope in our experiments. A DigitalMicrograph script was written to control the whole experiment. Once an area on the sample is chosen, the script prompts inputs of necessary parameters in the beginning of a session. Then it scans the electron beam through reciprocal space in an interval decided by the operator and takes a dark-field image with each momentum transfer value. Then each dark-field image is saved in a designated folder on the computer attached to the microscope. The same process is typically repeated for several different areas to gain good statistics. Typically a few hundred images are taken in a single experiment.

Another script has been composed to analyze these images. This script opens images in a designated folder on the computer. With each image, it removes distortion caused by modulation transfer in the CCD camera, whose modulation transfer function is pre-measured. Then the script does a Wiener filtering and a frequency filtering. Finally it yields a measured value of the fluctuation of intensity. With the momentum transfer value associated with each image, the intensity fluctuation as a function of the momentum transfer value is eventually obtained. Finally, a Fourier transform is performed on this function to yield the pair-pair alignment function in real space.

Results

We have studied effects of thermal annealing on the medium-range order in amorphous diamond-like carbon films. Amorphous diamond-like carbon films were

fabricated on a silicon wafer by pulsed-laser deposition using a KrF laser and a graphite target. They are hydrogen free and contain about 70% four-fold (sp^3) carbon with the rest being three-fold (sp^2) carbon. These films were divided into two groups. One group was processed by thermal annealing while the other stayed in the as-grown state. TEM samples were made from the films by core-drilling and chemical etching. The film thickness under TEM observations is about 30 nm.

Interestingly, thermal annealing caused great property changes in those films. For example, before annealing, the film was under great stress, up to 7 GPa. But after annealing, the stress was released to below 1 MPa. Stress relaxation measurements [8] also showed that the percentage of three fold carbon atoms was increased from 30% to about 37%. Therefore, thermal annealing causes structure changes. Our goal is to understand those changes.

The radial distribution is measured from diffraction patterns. The results are given in figure 2. Figure 2 shows that the annealed and unannealed films have the same short range order structures, although their properties are dramatically different. This verifies our point that short-range order is not enough to give a complete description of amorphous structures.
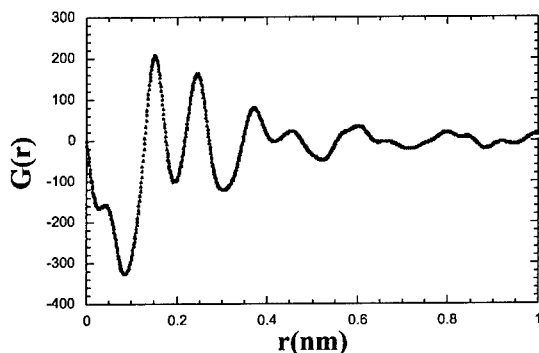
Figure 2. Measured reduced distribution functions show that thermal annealing does not change short-range order while causing great properties changes.

Our results on the intensity fluctuation are plotted as a function of k in figure 3. This variance function of k is directly related to a pair-pair correlation function that defines medium-range order at nanometer scale. From the intensity fluctuation function, we can measure the pair-pair alignment function with Fourier transform. Our results are given in figure 4.

There are pronounced differences for annealed and unannealed films, which indicates that there are medium-range order structure changes in these carbon films due to thermal annealing.
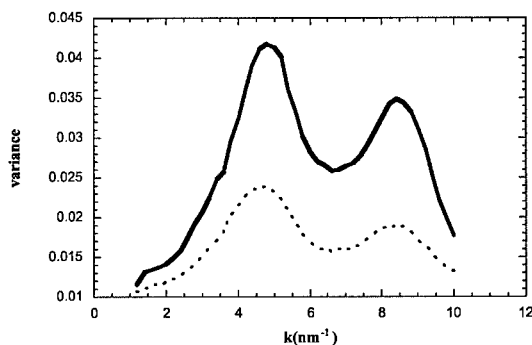
Figure 3. Plots of the variance as a function of k for amorphous diamond-like carbon films with or without annealing. The solid curve corresponds to the annealed sample and the dotted line is for the unannealed sample. The medium range order, indicated by the peaks, is increased after thermal annealing.
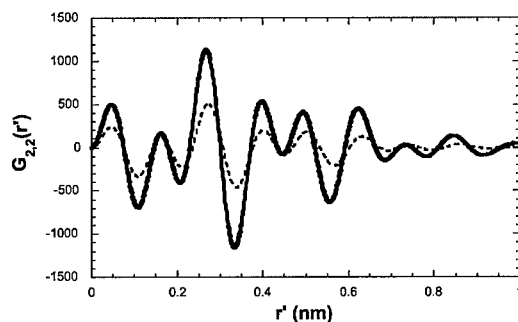
Figure 4. The measured pair-pair alignment function. The solid curve corresponds to the annealed sample and the dotted line is for the unannealed sample. More pairs of atoms are aligned after thermal annealing

For example, the first peak is positioned at around 0.46 Å. From the radial distribution function, we already know that the average bond length is about 1.51Å. Noticing that r' is the magnitude of an end vector generated by two pairs of atoms, we can infer that this peak comes from two identical pairs of atoms that are closely parallel from simple geometrical considerations. The length of each pair is the bond length, as

illustrated in figure 1. The magnitude of this end vector, i.e. the position of this peak, directly measures how these two identical pairs of atoms are aligned statistically. The nearer the position is to the origin point, the more parallel these pairs are. On the other hand, the height of each peak is proportional to the number density of the corresponding configuration. The annealed sample has a higher peak than the unannealed one at the same position, which means thermal annealing aligns more pairs. This agrees with electronic property measurements and density functional simulations.

Discussions

It is interesting to notice that thermal annealing increases the medium-range order in amorphous diamond-like carbon films. The increased medium-range order is correlated to the released stress [8]. This process can be explained well by thermodynamics. Growing films is a non-equilibrium process. During the growth, the system usually does not have time to relax into a minimized free energy state if the growth rate is too high or the substrate temperature is too low. Therefore, the resulted film is highly stressed. Thermal annealing provides the system a channel to relax into a smaller free energy state. Therefore, after thermal annealing, more pairs of atoms are aligned and the stress is released correspondingly.

Conclusions

We applied fluctuation microscopy technique to study medium-range order in amorphous tetrahedral semiconductor materials. It is shown that this technique is very sensitive to local structure changes in the medium range order and promises solutions to open questions that cannot be answered by current techniques. With this technique, we found that thermal annealing introduces medium-range order in amorphous diamond-like carbon films. A thermodynamic model is suggested to explain those results. Future studies will be focused on modeling and systematic exploration of annealing effects.

References

1. J. Robertson, "Hard Amorphous (Diamond-like) Carbons", Progress in Solid State Chemistry, Vol. 21, pp. 199, 1991
2. J. P. Sullivan, T. A. Friedmann, and A. G. Baca, J. Electron. Mater. 26, 1021 (1997).
3. S. R. Elliot, "Physics of Amorphous Materials", Longman Scientific & Technical, 1 990.
4. P. B Hirsh, A. Howie, R. B. Nicholson, and D. W. Pawshley, "Electron Microscopy of Thin Crystals", Butterworths, Washington, 1965.
5. J.W. Goodman "Statistical Properties of Laser Speckle Patterns", in "Laser Speckle and Related Phenomena" Editor: J.C. Dainty, Springer-Verlag, 1984.
6. J. M. Gibson and M.M. J. Treacy, "Diminished Medium-Range Order Observed in Annealed Amorphous Germanium", Physical Review Letters, Vol. 78, pp. 1074, February 1997.
7. Xidong Chen and J. Murray Gibson, "A pair-pair alignment correlation function that quantifies medium-range order in amorphous materials", submitted to Physical Review B, November 2000.
8. T. A. Friedmann, J. P. Sullivan, J. A. Knapp, D. R. Tallant, D. M. Follstaedt, D. L.Medlin, and P. B. Mirkarimi, Appl. Phys. Lett. 71, 3820 (1997).

NANO-STRUCTURED AMORPHOUS CARBON FILMS SYNTHESISED USING DECR PLASMA

André Golanski[1], Dieter Grambole[3], Jean Hommet[2], Folker Herrmann[3], Philippe Kern[1], Liam McDonnell[4], Fabrice Piazza[1] and Jean-Paul Stoquert[1]

[1] Centre National de la Recherche Scientifique (CNRS), Laboratoire PHASE,
    B.P.20, F-67037 Strasbourg, France.
[2] Centre National de la Recherche Scientifique (CNRS), Laboratoire IPCMS
    B.P. 20, F-67037 Strasbourg, France
[3] Forschungszentrum Rossendorf e.V., Institut für Ionenstrahlphysik und
    Materialforschung
    Postfach 51 01 19, 01314 Dresden, Germany
[4] Centre for Surface and Interface Analysis, Dept. of Applied Physics and Instrumentation,
    Cork Institute of Technology
    Rossa Av., Cork, Ireland

ABSTRACT

A Distributed Electron Cyclotron Resonance plasma reactor powered by a microwave generator operating at 2.45 GHz was used to deposit ta-C:H (Diamond-Like Carbon, DLC) thin films at RT. A graphite sputtering target immersed in an argon plasma was used as carbon source. The Ar plasma density was about 5×10^{10} cm^{-3}. Single crystal <100> Si substrates were RF biased to a negative voltage of -80 V. Atomic force microscopy (AFM), X-ray photoelectron spectroscopy (XPS), nuclear reaction analysis (NRA) using the resonance at 6.385 MeV of the reaction: $^{15}N + ^{1}H \rightarrow ^{12}C + ^{4}He + \gamma$, elastic recoil detection analysis (ERDA) and Rutherford backscattering (RBS) were used to investigate the early phase of the growth. The morphology of the films grown at low pressure (0.3 mTorr) is shown to be dominated by stress-mediated nucleation leading to formation of basket-like clusters of circular hillocks 20 nm high surrounded by a planar, mostly sp^2 bonded film ~8 nm thick. With increasing plasma pressure the spatial frequency of the hillocks becomes random and the growth is dominated by the Stranski-Krastanov mode. The XPS data taken at decreasing emergence angles show that the structure of the hillocks is dominated by sp^3 bonded carbon. The XPS argon signal disappears at 10° emergence angle indicating that integration of argon occurs mainly within the sp^2 bonded regions. The NRA and ERDA analysis show that the amount of integrated hydrogen decreases with increasing substrate current density. RBS data indicate that increasing bias enhances argon integration.

INTRODUCTION

In the plasma deposition process where a negatively biased substrate is immersed in a carbon-rich plasma, the nucleation and growth are controlled by the flux and energy of the incoming species (charged and neutral). The results of the competition between integration of the incoming species and sputtering erosion depends on the precursor gas, ion energy and dose rate. Addition of argon to a carbon rich precursor such as acetylene is known to reduce the growth rate but momentum transfer being a forward-peaking process, argon bombardment may lead to a densification of the film and stress generation. Stress may in turn lead to transformation of sp^2 sites to sp^3 sites. Despite considerable experimental study over the last decade [1-6 and ref. therein] the effects of energy deposition on the morphology and physical properties of the DLC films are incompletely understood. The goal of the present work is to shed some more light on the impact of the energy deposition processes on the microstructure of the DLC thin films. The assumption here is that the binary collision theory may provide

some guidance as it enables assessment of the average energy density E_d deposited in binary collision cascades. Most of the experiments were performed using a constant substrate bias of -80 V corresponding to a maximum E_d value of ~14 eV/atom. The preliminary results reported below highlight the impact of the dose-rate effects on the materials structure.

EXPERIMENTAL DETAILS

Diamond-like amorphous carbon (DLC) thin films were deposited on single crystal <100> Si substrates using a plasma source operating in a Distributed Electron Cyclotron Resonance (DECR) configuration. The microwave power operating at a frequency of 2.45 GHz was applied to several antennae located in the vicinity of the cylindrical reactor walls that are equipped with magnetic racetracks designed to provide an appropriate confinement of fast electrons. At sufficiently low pressure (10^{-4} mTorr) the plasma diffuses under the influence of the density gradients and a uniformly distributed, cold, high density (~5×10^{10}/cm^3) diffusion plasma is obtained across the reactor volume. The plasma chamber was equipped with a water cooled graphite sputtering target located in the top part of the reactor and biased by a pulsed DC power supply producing negative voltage of tuneable amplitude. The graphite target and substrate to be coated were located at the opposite extremities of the reactor facing each other and immersed in the argon plasma. The substrate holder was water-cooled enabling the deposition temperature to be kept below 70°C for deposition time of a few minutes. The substrate bias of - 80 V was kept constant using a RF power supply operating at 13.5 MHz. The DLC films were analysed by atomic force microscopy (AFM), X-ray photoelectron spectroscopy (XPS), nuclear reaction analysis (NRA) using the resonance at 6.385 MeV of the reaction: $^{15}N + {}^{1}H \rightarrow {}^{12}C + {}^{4}He + \gamma$ rays, elastic recoil detection analysis (ERDA) and Rutherford backscattering (RBS). The XPS analysis was performed using AlK$_\alpha$ (1486.6eV) X-ray radiation from a VG Microtech XR2E2 dual anode (aluminium/magnesium) X-ray source that was operated at 300 W power. XPS analysis was carried out using a VG Microtech VG100AX electron energy analyser. Angle resolved XPS spectra were obtained by rotating the sample holder with respect to the X-ray source and the input lens of the VG100AX analyser. Spectra were obtained for angles of emergence of photoelectrons from the surface of 90°, 70°, 50°, 30° and 10°. Data was acquired using VG Microtech VGX800 software and quantified using VG Microtech Presents software. XPS survey spectra were acquired using pass energy of 100 eV while high resolution spectra were acquired using a pass energy of 20 eV. No charge compensation has been used during acquisition.

RESULTS AND DISCUSSION

TABLE I and FIG.1 summarise the results of SRIM-2000 simulations performed for 80 eV Ar$^+$ ions in carbon, assuming the displacement energy for carbon atom to be of 15 eV. The average energy density E_d was estimated assuming a cylindrical geometry for an individual collision cascade. The radius of the cylinder was assumed to be of (R+σ_R) where R and σ_R are radial projected range and straggling, respectively. The length of the cylinder was assumed to be of 2.5 σ_L where σ_L is the longitudinal straggling of the Ar distribution. For the sake of simplicity the total ion energy was taken into account in the assessment of E_d. Yet, the maximum calculated E_d values are lower than the displacement threshold. The maximum E_d values are seen to correspond to the Ar$^+$ ion energy of 80 eV. We note that for the 80 eV C$^+$ ion the E_d value is almost an order of magnitude lower than for Ar$^+$ ion of the same energy. Most of the experiments reported in this work were performed using the substrate bias of $U_S=$ -80V. The corresponding sputtering yield values shown in TABLE I indicate that
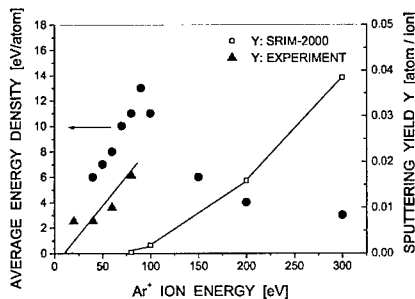
FIG.1: Deposited energy density and sputtering rate for Ar^+ ions measured experimentally and calculated using SRIM-2000
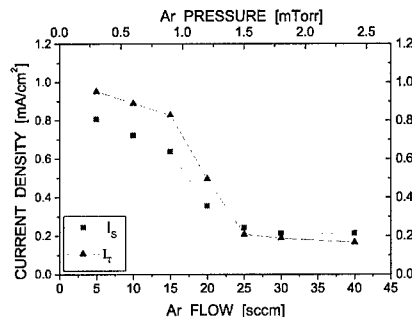
FIG.2: Substrate current density (I_S) and graphite target current density (I_T) plotted as a function of the argon pressure

TABLE I

	H^+	C^+	O^+	Ar^+	Experiment
Y [atoms C / ion]	0.010	0.044	0.014	<0.001	0.02
R_p [Å]	19	7	6	7	

the combined sputtering effects due to the various ion species present in the plasma are expected to alter the morphology of the films [7]. Although no detailed diagnosis of the plasma has been performed at this stage the presence of hydrogen has been observed and is attributed to the desorption occurring at the reactor walls. The results of NRA and ERDA analysis (not shown) consistently indicate that while about 30 at.% hydrogen is observed in the film deposited using floating potential, the content is reduced by ion bombardment to 3-4 at.% in the films deposited using the substrate bias of -80 V. Given the significant deposition time (~30 min) the thermally activated, hydrogen ion induced surface erosion known to occur at process temperatures of T≥400K may contribute to the total sputtering yield of Y=0.02 determined experimentally. The sputtering effects due to C^+ and Ar^+ ions are expected to be of a similar order of magnitude because the population of carbon ions within the plasma is estimated to be about 1% of the Ar^+ ion population.

FIG.2 shows the substrate and graphite target current densities (I_S and I_T, respectively) plotted as a function of the argon plasma pressure. Secondary electron emission is not taken into account in the assessment of the current density. It is assumed to be negligible for the ion energies used [8]. The current density values I_S and I_T are close to one another and decrease with increasing argon pressure, reflecting the relative density of the charged and neutral species within the plasma. Consequently the substrate current density may be varied by changing the plasma pressure. In the experiments reported in this work the DLC films were grown during 30 min using variable current density I_S. The deposition parameters are shown in Table II. We note that the results of RBS analysis (spectra not shown) indicate that when

TABLE II

	Pressure [mTorr]	Dose rate [10^{15} ions/cm²s]	Total dose [10^{19} ions/cm²]
FIG. 3 a	0.1	13	2.3
FIG. 3 b	0.2	9.4	1.5
FIG. 3 c	0.9	6.2	1.1
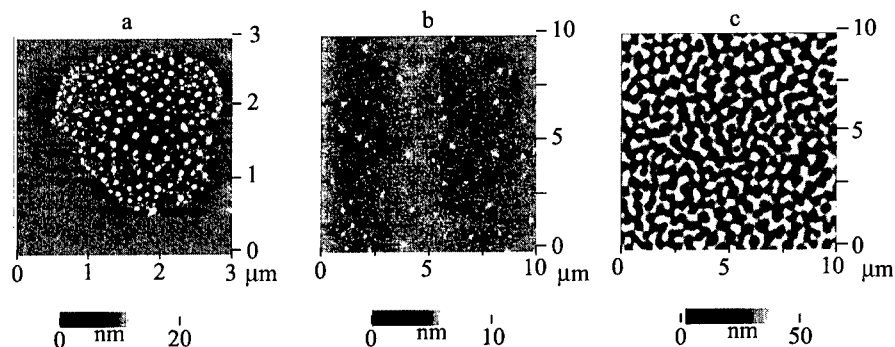
FIG.3 : AFM images of the films deposited using constant energy of 80 eV and variable dose-rate of 1.3×10^{16} (a), 9.4×10^{15} (b) and 6.2×10^{15} (c) [Ar^+ ions/cm^2s]

the substrate bias is increased from 0 V to -80 V, the residual argon content increases from zero to about 6 at.%. More than 99% of the argon atoms reaching the growing film is re-sputtered and/or disrobed during the growth.

The relationship between the dose, dose rate and the surface topography and microstructure of the film was investigated using AFM and XPS techniques. The AFM images corresponding to three different I_S values are shown in FIG.3.

The AFM image corresponding to the highest dose rate (FIG.3a) reveals that most of the DLC surface is flat. It also reveals the presence of a variety of self-organised, basket-like clusters of densely packed circular hillocks. The clusters are distributed randomly and separated from one another by a distance of several tenths of microns. The hillocks within the cluster are of various sizes reaching 20 nm in height. The auto-correlated, basket-like networking is believed to result from a strain-mediated nucleation and growth processes. Khachaturyan [9] discussed the corresponding mechanism. Unlike the conventional thermodynamic theory of phase transformations, Khachaturyan's approach includes stress energy contributions to the free energy of the system. The growing nucleus is seen as generating a stress field where the surface energy and the nucleation probability are enhanced. The latter effect leads to a directional ordering and mutual arrangement of the nuclei and eventually results in the formation of a partially ordered, "basket-like" pattern of hillocks where the stress energy of the whole structure is reduced.

The initial stress field required for the stress mediated nucleation to occur is tentatively attributed to high dose-rate effects enabling neighbouring binary collision cascades to overlap, creating high deposited energy density (~30 eV/atom) regions and leading to a significant redistribution of atomic bonds. The effects of cascade overlap have been investigated in the keV energy range and shown to lead to a non-linear enhancement in both damage creation and sputtering [9]. Taking into account the average space frequency of the basket-like patterns of $\sim 1 \times 10^{-4}$ /μm^2 observed for the dose rate of 1.3×10^{16} ions/cm^2s, an ion flux of 10^{16} ions/cm^2s represents a threshold value beyond which the 80 eV Ar ions cascade overlap effects become observable. At lower dose rates the effects are expected to vanish.

When the dose rate is reduced to 9.4×10^{15} [ions/cm^2s] the AFM image becomes dominated by a random network of individual hillocks (FIG.3b). The film appears to grows in the Stranski-Krastanow mode. Although the basket-like clusters are still observed, their spatial frequency

is significantly lower. The average density of hillocks in FIG. 3b is an order of magnitude lower than within a cluster (FIG.3a).

When the ion dose rate is further reduced to 6×10^{15} [ions/cm^{2}s] the surface erosion is also significantly reduced and the topography of the surface changes significantly (FIG.3c). The hillocks are now present all over the surface. They reach 50 nm in height and a significant degree of overlap is observed (FIG.3c). The average density of hillocks in FIG. 3b and 3c is similar, but they are different in size. Figures 3b and 3c are interpreted as corresponding to a similar nucleation dynamics and different stages of growth. Although the integrated ion dose is smaller for FIG. 3c, the corresponding average layer thickness is higher.

The samples shown in FIG. 3b and 3c were analysed using the XPS technique. The Ar/C signal ratio has been investigated as a function of the emergence angle. The results are summarised in FIG.4. The straight lines have been added to underline the trends. With decreasing angle of emergence the argon peak falls off faster than the overall carbon peak. Argon is not seen at the glancing angle indicating that the argon rich layer is buried underneath the surface. The difference in glancing angle at which the Ar signal disappears is attributed to the difference in depth Δx at which the argon reach layer is buried. Since a constant energy of 80 eV is used in this experiment, the values of Δx are believed to depend on the film density. A simple calculation shows that $\Delta x(\text{FIG.3c})/\Delta x(\text{FIG.3b}) \approx 0.5$. The relationship between the projected range for 80 eV Ar$^+$ and DLC density extracted from SRIM (FIG.5) indicates that the corresponding change in density is of about 1.2 g/cm^3. According to [5,6] an increase in density of 0.5 g/cm^3 corresponds to an increase in the sp^3-hybridised fraction of 25%. Consequently the sample shown in FIG.3c is expected to contain a significantly higher sp^3 fraction than the sample shown in FIG. 3b. The XPS analysis confirms the expectations. Implanted or subimplanted argon atoms have been shown to probe the residual stress in ultrathin films since intrinsic stress induces a change in the binding energy of Ar$2p$ electrons. The change, measurable by the XPS technique, is linearly proportional to the stress [11]. XPS analysis shows a 0.3 eV difference in the binding energy of Ar$2p$ electrons between the two samples shown in FIG. 3b and 3c with the latter showing the higher stress. The carbon hybridisation ratio corresponding to the film shown in FIG.3c has been analysed by peak fitting of the C1s feature in the XPS spectra (not shown). Following a detailed consideration of the prior work the C1s feature was fitted using four components that include sp^2 and sp^3 hybridisation and two chemical states associated with oxygen.
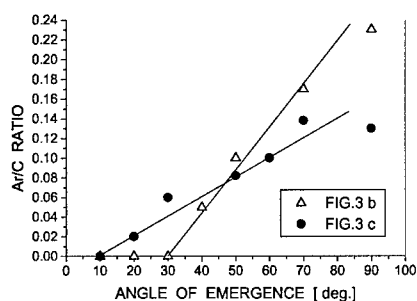
FIG.4: XPS Ar/C signal ratio for the samples shown in FIG. 3b and 3c.
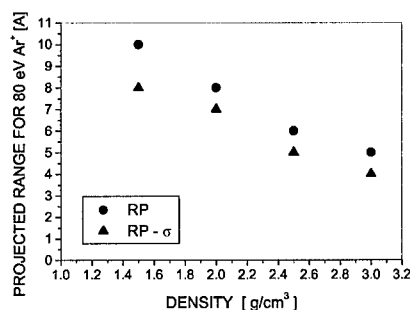
FIG.5: 80 eV Ar$^+$ ion range plotted as a function of carbon density [SRIM 2000]

The hybridisation analysis shows that the sp^3 ratio increases as the angle of emergence decreases thereby indicating that sp^3 carbon is outermost within the film structure. This result strongly suggests that sp^3 rich hillocks reside in a sp^2 rich "ocean". The fact that the XPS argon signal disappears at 10° emergence angle may also indicate that integration of argon occurs mainly within the sp^2 bonded regions. Assuming that the hillocks seen in FIG.3a are also sp^3 rich we tentatively conclude that the resistance to the surface etching by ion bombardment depends on hybridisation. Further study is required to confirm these preliminary conclusions.

CONCLUSIONS

We have provided experimental evidence that the surface topography and microstructure of the plasma deposited ta-C:H thins films strongly depend on the substrate current density. We have demonstrated that for ta-C:H films grown on a single crystal Si substrate the high dose rate effects may lead to a stress-mediated nucleation. Finally, we have shown that integration of argon within ta-C:H is enhanced by Ar^+ ion energy and occurs mainly within the sp^2 hybridised carbon fraction.

ACNOWLEDGMENTS

REFERENCES
1. W.Lu, K.Komvopoulos and S.W.Yeh, J.Appl.Phys. 89, 4 (2001)
2. L.Valentini, J.M.Kenny, G.Carlotti, G.Socino, L.Lozzi and S.Santucci, J.Appl.Phys. 89, 2 (2001)
3. A.Ilie, A.Hart, A.J.Flewitt, J.Robertson and W.I.Milne, J.Appl.Phys. 88, 10, 6002 (2000)
4. R.G.Lacerdaz, P.Hammer, F.L.FreireJr, F.Alvarez and F.C. Marques, Diamond and Related Materials 9, 796 (2000)
5. D.H.Lee, X.M.He, K.C.Walter, M.Nastasi, J.R.Tesmer and M.Tuszewski, Appl.Phys.Letters 73, 17, 2423 (1998)
6. J.Schwan, S.Ulrich, H.Roth, H.Ehrhardt, S.R.P.Silva, J.Robertson, R.Samlenski and R.Brenn, J.Appl.Phys. 79, 3, 1416 (1996)
7. W.Jacob, Thin Solid Films 326, 1 (1998)
8. E.S.Parilis et al., Atomic Collisions on Solid Surfaces, North-Holland, Amsterdam (1993)
9. A.G.Khachaturian, Theory of Structural Transformations in Solids, John Willey&Sons 1983 (ISBN 0-471-07873-5)
10. D.A.Thompson, Radiation Effects 56, 105-150 (1981)
11. A.LiBiassi, A.C.Ferrari, V.Stoloian, B.K.Tanner, J.Robertson and L.M.Brown, Diamond and Related Materials 9, 771 (2000)
12. W.Lu and K.Komvopulos, Appl.Phys.Letters 76, 22, 3206 (2000)

Comparison of CPM, PDS and Optical Transmittance of Amorphous Carbon Nitride Films Made by a Nitrogen Radical Sputter Method

Takashi Katsuno, Shoji Nitta and Hitoe Habuchi*

Department of Electrical Engineering, Gifu University, 1-1 Yanaido,

Gifu, 501-1193 Japan

*Department of Electrical and Computer Engineering, Gifu National College of Technology,

Shinsei-Chou, Motosu, Gifu, 501-0495 Japan

ABSTRACT

Amorphous carbon nitride films a-CN_X, deposited in our laboratory by a radical sputter method, show high photosensitivity P_S, where P_S is the ratio of photoconductivity σ_p and dark-electrical conductivity σ_d. A-CN_X made a layer-by-layer method, LLa-CN_X, has the highest photosensitivity in our various preparation conditions. The photoconductivity in a-CN_X and LLa-CN_X shows dependence on photon energy in the range 2 eV to 6.2 eV. The constant photocurrent method (CPM), photothermal deflection spectroscopy (PDS) and optical transmittance spectra are used to obtain the information in the optical energy band gap and defect states. A-CN_X and LLa-CN_X are good photoconductors especially at energy higher than 3 eV. Therefore it is not difficult to obtain CPM spectra in the high photon energy region. CPM spectra are obtained by dc- and ac- measurements. The value of the absorption coefficient α spectra obtained by dc-CPM is larger than that of ac-CPM, which increases with increasing frequency of the measurement. In this paper, CPM data is used to discuss a model of density of states (DOS) of a-CN_X by comparison with PDS and optical transmittance spectra.

INTRODUCTION

CPM is an effective method to study the near band gap energy region for photoconductive materials such as hydrogenated amorphous silicon a-Si:H and fullerene C_{60} [1-3]. Amorphous carbon nitride films a-CN_X shows good photoconductive properties and

very high dark resistivity [4-5]. A-CN$_x$ is interesting for applications to low dielectric constant materials and light emitting devices [5-7]. CPM is one of the method to study electronic properties near the optical band energy gap E$_0$. To the best of our knowledge, CPM has never investigated in carbon related materials except fullerene. CPM results are discussed in this paper with a model of density of states of a-CN$_x$, PDS and UV-VIS optical transmission data.

EXPERIMENTAL

We have prepared a-CN$_x$ using a graphite target of purity 99.999% by a nitrogen radical sputtering method. The layer-by-layer method, which is a cyclic process of a-CN$_x$ deposition by a nitrogen radical sputtering and surface treatment of thin a-CN$_x$ by atomic hydrogens, is used to get higher photoconductive LLa-CN$_x$ films [4-5]. In this process, sputter gas N$_2$ of purity 99.999% is used to create nitrogen radicals and molecular hydrogen H$_2$ of 99.99999% is used to produce atomic hydrogen for etching the surface. We have controlled the layer-by-layer system by a microcomputer to keep the process of sputtering and etching time at constant. Conditions for sputtering are rf 13.56 MHz with power of 85 W, N$_2$ sputtering gas of 0.12 Torr and the substrate temperature at 300 Celsius. For the etching of a-CN$_x$, atomic hydrogen is derived by the glow discharge of H$_2$ of 0.50 Torr at the same rf conditions to prepare nitrogen radicals. Table.1 shows gas-injection and -evacuation times and several physical properties of LLa-CN$_x$. The difference of preparation conditions
between LLa-CN$_x$ #103 and #116 are the number of the layer-by-layer process. Samples with same properties and a different thickness are prepared to fit for each experimental conditions. LLa-CN$_x$ #103 is prepared for CPM and optical transmittance, and LLa-CN$_x$ #116 is for PDS. The reason to use the thin film LLa-CN$_x$ #116 is to get the wide range of absorption coefficient α by PDS, from infrared to visible range.

Electrodes of 60 μm gap with 6 mm in width are prepared for CPM measurement by the vacuum evaporation of Al on LLa-CN$_x$. A pyroelectric detector, Hamamatsu Photonics P2613, is used to obtain light intensity F. Monochromatic light from a Xe lamp and a Nikon G250 monochromator with grating of 600 mm^{-1} are used as a light source. Keithley 6512 picoammeter is used to monitor the photocurrent until it becomes constant. The value of the photo intensity F is measured using a pyroelectric detector. For ac-CPM, constant

Table.1 Conditions to prepare LLa-CN$_X$ and their several physical properties.

Preparation conditions & properties	LLa-CN$_X$#103 [CPM, Optical T.]	LLa-CN$_X$#116 [PDS]
rf power	85 W	
substrate temperature T_s	300 Celsius	
(a) N$_2$ gas pressure & sputter time	0.12 Torr, 300 s	
(b) 1st evacuating time	30 s	
(c) H$_2$ gas pressure & etching time	0.50 Torr, 40 s	
(d) 2nd evacuating time	30 s	
Number for the layer-by-layer process	81	8
refractive index	1.83	—
film thickness [nm]	1100	~ 100
Tauc gap [eV]	1.67	~ 1.61
N/C ratio	0.64	0.64
defect density [cm^{-3}]	3.44×10^{18}	—

photocurrent I_p is transformed to voltage signal using Hamamatsu photonics C2719 amplifier, and we read the value on a lock-in-amplifier.

RESULTS AND DISCUSSION

The measurements of PDS and UV-VIS optical transmittance are the same as before [4, 6]. The absorption coefficient α is obtained as the inverse of the incident photon number, 1/F, under a constant photocurrent, I_p, by using conventional CPM assumptions [1-3, 9]. Fig.1 shows dc-CPM spectra of LLa-CN$_X$ films measured at constant photocurrent 50 fA, 80 fA, 1 pA and 15 pA, with the applied voltage of 32 V DC. Characteristics of LLa-CN$_X$ films are high resistivity and high photoconductivity. In the case of 1pA constant, it is possible to measure dc-CPM only from 4.2 eV to 4.7 eV. To sustain a constant photocurrenrt for wide range photon energy is not easy. It is also difficult to use a small photon number for CPM, which is limited by the sensitivity of a pyroelectric detector. Therefore it is needed to correct these spectra using correction factor 'a' as shown fig.2. In the correction, the data at 1 pA is took as a standard of photocurrent, and we multiply for each photocurrent; for example a=15 for I_p=15 pA. The obtained spectrum seems to be good under the assumption that the incident photon number is proportion to constant photocurrent I_p.
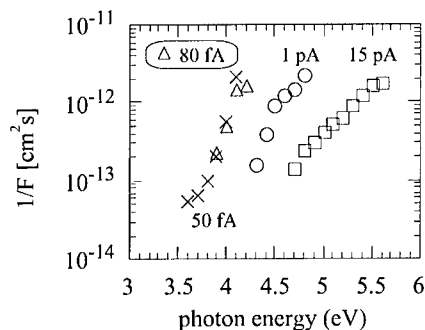
Figure.1 dc-CPM spectra
[LLa-CN$_x$#103]
(F [cm^{2}s]: photon number)
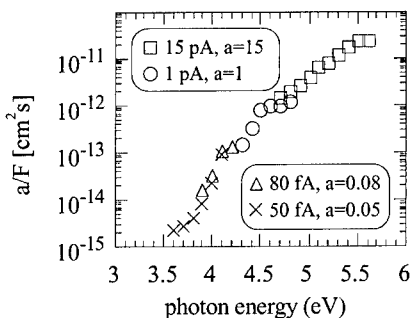
Figure.2 The correction of
dc-CPM spectra [LLa-CN$_x$#103]
(F [cm^{2}s]: photon number)

Ac-CPM measurements at different chopping frequency are also obtained by the same method. Fig.3 compares these measurements with dc-CPM of fig.2. The value of absorption coefficient α obtained from dc-CPM spectra is larger than that of ac-CPM, which increase with chopping frequency of the CPM measurement. In a-Si:H and C$_{60}$ solids, ac-CPM, measured at lower chopping frequency, are close to dc-CPM. But in LLa-CN$_x$ case, ac-CPM, at higher chopping frequency are close to dc-CPM. These difference may be dependent on the properties of localized electronic states. The origin of this difference has to be further investigated.
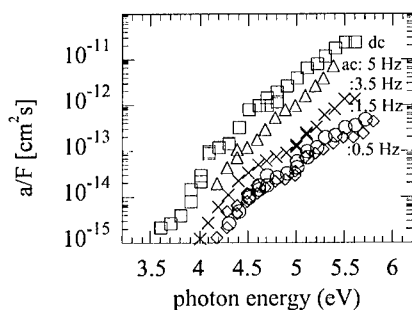
Figure.3
Comparison with ac- and
dc-CPM spectra.
(F [cm^{2}s]: photon number)
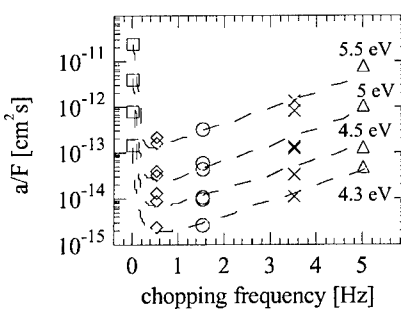
Figure.4
The dependence of CPM data, a/F, in LLa-CN$_x$
#103 at a fixed photon energy on chopping
frequency.(F [cm^{2}s]: photon number)
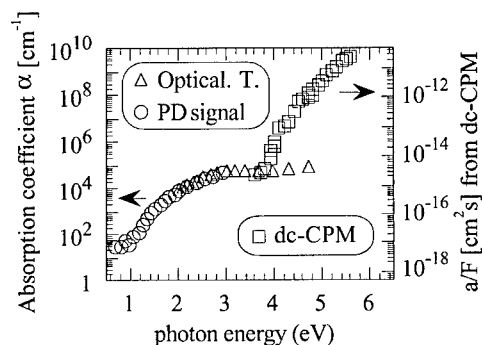
Figure.5

The value of absorption coefficient α from dc-CPM spectra are compared with that for PDS and optical transmittance spectra.
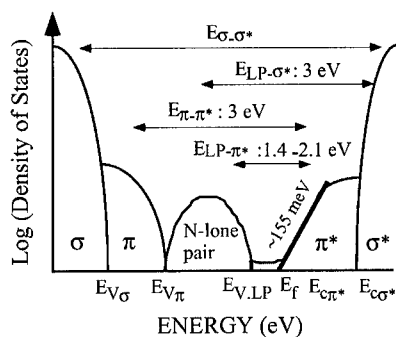
Figure.6

A model of the electronic state density of a-CN_x [4].

Fig.4 shows the dependence of CPM data, a/F, for LLa-CN_x #103 at a fixed photon energy on chopping frequency. The largest a/F value is that of dc-CPM. The minima of a/F for every photon energy are close to 0.5 Hz.

The value of absorption coefficient α from dc-CPM are compared with PDS and optical transmittance spectra in fig.5. In this figure, the increase of absorption coefficient α at 3.7 eV is similar to photoconductivity spectra of LLa-CN_x films [4].

The increase of excitation of electrons at about 3.7 eV in fig.5 can be attributed as shown fig.6 to a transition between a nitrogen lone pair band to a σ^* anti-bonding conduction band ($E_{LP-\sigma^*}$) or that from a π bonding valance band to a π^* anti-bonding conduction band ($E_{\pi-\pi^*}$) [4,10,11]. CPM data describes well the good photoconductive properties at photon energy hv>3.7 eV.

CONCLUSION

Dc- and ac-CPM are obtained for LLa-CN_x for first time. The frequency dependence of ac-CPM measurements needs to be further investigated. CPM spectra are showing the good photoconductive properties of LLa-CN_x. CPM data were discussed with a model of density states together with PDS and UV-VIS optical transmittance spectra.

REFERENCES

1. H. Habuchi, S. Nitta, T. Itoh, S. Hasegawa and S. Nonomura, in '*Advances in Superconductivity VI*', Vol. **2** , edited T. Fujita and Y. Shinohara, (Springer-Verlag, Tokyo, 1994) pp. 973-976.

2. H. Habuchi, S. Nitta, H. Maehara, and S. Nonomura, in '*Fullerenes and Photonics IV*', edited by Z. H. Kazafi (Proc. SPIE **3142**, 1997) p. 184.

3. S. Hasegawa, T. Nishiwaki, H. Habuchi, S. Nitta and S. Nonomura, Fullerene Sci. Technol. **3**, 163 (1995).

4. T. Katsuno, S. Nitta, H. Habuchi, T. Iwasaki, T. Itoh and S. Nonomura, in '*Amorphous and Nanostructured Carbon*', edited by J. P. Sullivan, J. Robertson, O. Zhou, T. B. Allen, B. F. Coll (Mater. Res. Soc. Proc. **593**, Boston, MA, 1999) pp. 499-504.

5. N. Takada, K. Arai, S. Nitta and S. Nonomura, Appl. Surf. Sci. **113**, 274 (1997).

6. T. Iwasaki, M. Aono, S. Nitta, H. Habuchi, T, Itoh and S. Nonomura, Diamond Related Mater. **8**, 440 (1999).

7. M. Aono, T. Katsuno, S. Nitta, T. Itoh and S. Nonomura, in '*Amorphous and Nanostructured Carbon*', edited by J. P. Sullivan, J. Robertson, O. Zhou, T. B. Allen, B. F. Coll (Mater. Res. Soc. Proc. **593**, Boston, MA, 1999) pp. 493-498.

8. M. Aono, S.Nitta, T. Katsuno, T. Itoh and S.Nonomura, Appl. Surf. Sci. **159-160**, 341 (2000).

9. S. Hasegawa, S. Nitta and S. Nonomura, J. Non-Cryst. Solids **198-200**, 544 (1996).

10. S. Souto, M. Pickholz, M. C. dos Santos and F. Alvarez, Phys. Rev. B **57**, 2536 (1998).

11. M. C. dos Santos and F. Alvarez, Phys. Rev. B **58**, 13918 (1998).

Incorporation of hydrogen and oxygen into (t)a-C:H thin films deposited using DECR plasma (*)

Fabrice Piazza[1], Dieter Grambole[2], Folker Herrmann[2], Gary Relihan[3], Marie France Barthe[4], Pierre Desgardin[4] and André Golanski[1]

[1] Centre National de la Recherche Scientifique (CNRS), Laboratoire PHASE, BP20, F-67037 Strasbourg, France

[2] Forschungszentrum Rossendorf e.V., Institut für Ionenstrahlphysik und Materialforschung Postfach 51 01 19, 01314 Dresden, Germany

[3] National Microelectronics Research Centre (NMRC), University College, Lee Maltings, Prospect Row, Cork, Ireland

[4] Centre National de la Recherche Scientifique (CNRS), Laboratoire CERI, 3 A rue de la Férollerie, F-45071 Orléans, France

ABSTRACT

A distributed electron cyclotron resonance (DECR) plasma reactor powered by a microwave generator operating at 2.45 GHz (800 W) was used to deposit (t)a-C:H thin films at RT on <100> Si substrates RF biased within the range $25 \leq |V_0| \leq 600$ V. C_2H_2 was used as precursor. The plasma pressure was varied within the range $0.1 \leq P \leq 1.5$ mtorr. The films were analysed using spectroscopic ellipsometry (SE) and Fourier transform infrared (FTIR) spectroscopy. The hydrogen content N_H and the density of the films were determined from nuclear reaction analysis (NRA) using the resonance at 6.385 MeV of the reaction: $^{15}N + ^{1}H \rightarrow ^{12}C + ^{4}He + \gamma$. Positron annihilation spectroscopy was used to detect the porosity. The evolutions of N_H as a function of the substrate ion current density n_+ and as a function of V_0 show that the hydrogen incorporation results from the competition between chemisorption and deposited energy density related effects. The increase of the hydrogen incorporation leads to a decrease in the film density and a lower deposition rate. The porosity of the films deposited at low pressure (~ 0.1 mTorr) with $V_0 = -80$ V has been detected. The comparison between results of SRIM-2000 simulations and the evolution of N_H as a function of V_0 shows that the porosity and the hydrogen content are not correlated. The absorption of oxygen and nitrogen for the low density films has been detected from the observation of the 3250-4000 cm^{-1} infrared (IR) band.

INTRODUCTION

Hydrogen is known to be a fundamental constituent of the plasma deposited amorphous hydrogenated carbon (t)a-C:H films. The hydrogen content N_H is usually close to 35 % and can reach ~ 62 % [1]. Studies have shown that N_H decreases when V_0 increases [2]. Although the hydrogen incorporation mechanisms have been extensively studied, there are not fully understood. The goal of the present work is to shed more light on those mechanisms. The film structure and some of the physical properties such as the film hardness and the density are known to depend closely on the hydrogen content [3] and on the nature of the C-H bonds [4]. Little is known about the film porosity. In this study, the correlation between the film density, the deposition rate, the hydrogen content and the porosity is studied.

EXPERIMENTAL DETAILS

The (t)a-C:H films were grown at RT on <100> Si substrates using a DECR plasma reactor. The microwave power operating at a frequency of 2.45 GHz was applied to 12 antennas located in the vicinity of the cylindrical reactor walls equipped with magnetic racetracks providing the 87.5 mT isomagnetic surface necessary for the resonance. The racetracks were designed to confine fast electrons. The experiments were performed using a microwave power of 800 W. The desired plasma pressure was obtained using a variable gas flow and measured using a MKS Baratron. C_2H_2 was used as the precursor gas and the plasma pressure was varied from 0.1 to 1.5 mTorr. The substrate holder was water cooled enabling deposition in the vicinity of RT. The negative bias V_0 applied to the substrate holder was regulated within the range between 25 and 600 V using a power supply operating at 13.56 MHz. The accelerating voltage was kept constant during deposition by an automatic modulation of the RF power. The hydrogen content was determined from nuclear reaction analysis (NRA) using the resonance at 6.385 MeV of the reaction: $^{15}N + {}^1H \rightarrow {}^{12}C + {}^4He + \gamma$. The effect of the hydrogen outdiffusion occurring during the bombardment with nitrogen ions has been taken into account. The films thickness was determined from spectroscopic ellipsometry (SE) combined with NRA data. The SE data were recorded using a phase modulated variable angle spectroscopic ellipsometer manufactured by Instruments S.A./Jobin-Yvon-Spex. They were recorded in the 1.5-4.5 eV spectral range in steps of 0.05 eV at an incidence angle of 70°. Reference optical properties for Si and SiO_2 were used. The (t)a-C:H layer was modelled using the Tauc-Lorentz dispersion model [5]. FTIR spectroscopy was performed using a Bio-Rad FTS-40 APC spectrometer in the transmission mode using a resolution of 4 cm^{-1}. The evolution of the 3250-4000 cm^{-1} band intensity and the evolution of the shape of the CH stretching band (2800-3100 cm^{-1}) as a function of V_0 for films deposited at 0.1 and 0.3 mTorr were investigated to obtain qualitative informations concerning the films structure. In order to access the films porosity positron annihilation experiments were performed with a slow positron beam.

RESULTS and DISCUSSION
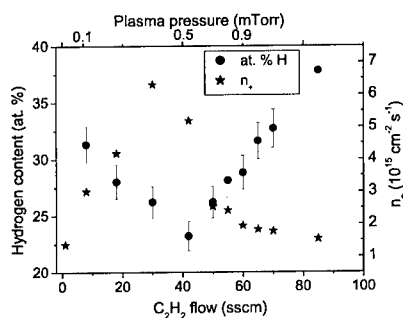
Figure 1. Hydrogen content and substrate current density n_+ as a function of the gas flow and pressure ($V_0 = -150$ V).
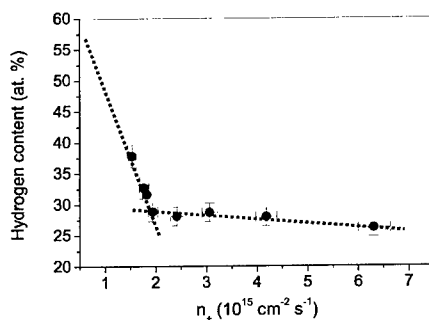
Figure 2. Hydrogen content as a function of the substrate current density ($V_0 = -150$ V).
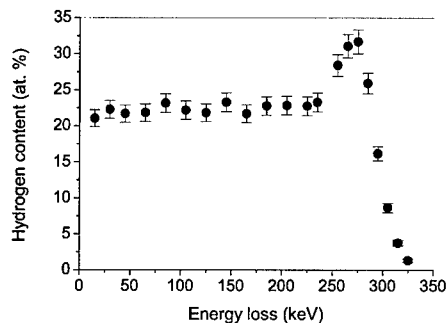
Figure 3. Hydrogen depth profile for a film grown at 0.5 mTorr with $V_0= -250$ V.
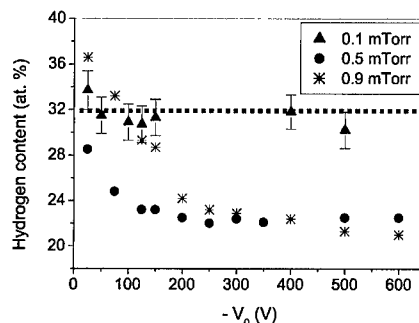
Figure 4. Hydrogen content as a function of the substrate bias for several pressures. The dot line has been added to underline the trend.

Figure 1 shows the evolution of N_H and of the substrate current density n_+ as a function of the pressure, for a substrate bias of $V_0= -150$ V. N_H is extracted from the NRA depth profiles. The n_+ value is deduced from the RF generator power delivered for a specific bias. The secondary electron emission is assumed to be negligible within the energy range investigated [6]. The n_+ value is representative of the amount of the predominant ions in the C_2H_2 plasma which are known to be $(C_2H_x)^+$ ions [2]. However a variable production of H^+ and $(C_4H_x)^+$ ions as a function of the pressure is also expected to contribute to n_+. Figure 1 shows that N_H is inversely proportional to n_+.

The correlation between N_H and n_+ is further demonstrated in figure 2 where N_H is plotted as a function of n_+. Two hydrogen incorporation regimes can be distinguished depending on the n_+ value. At the current densities higher than the threshold value $T\sim 1.9\times10^{15}$ cm^{-2} s^{-1} the hydrogen desorption rate is almost in dynamic equilibrium with the adsorption and subplantation rates. When the ion flux n_+ is reduced below the threshold value the hydrogen adsorption is significantly enhanced and the hydrogen content increases. Interestingly, when linearly extrapolated to $n_+=0$ the hydrogen content reaches ~ 70 %, a value close to the maximum content of 62 % reported in the literature [1]. The hydrogen incorporation mechanisms are considered to be related to the subplantation, the passivation of dangling bonds and to the exothermic hydrogenation of double bonds [7]. Experimental evidence of the role of dangling bonds is demonstrated in FIG. 3 showing the NRA depth profile of a film grown on Si substrate at 0.5 mTorr using $V_0= -250$ V. The hydrogen content almost doubles at the interface (t)a-C:H/Si where both carbon and silicon dangling bonds contribute to hydrogen adsorption during the initial phase of the growth. The hydrogen chemisoption was also observed for films deposited in the same reactor using Ar plasma and a graphite sputtering target. Films deposited at the floating potential have been shown to incorporate between 12 and 39 at.% of hydrogen depending on the amount of hydrogen desorbed from the reactor walls [8].

The hydrogen desorption process is significantly enhanced by the energy deposited in atomic collisions. The ion flux threshold value of 1.9×10^{15} cm^{-2} s^{-1} above which the desorption is reduced (FIG.2) is interpreted as corresponding to a complete coverage of the substrate surface by the individual ion impact zones. We note that according to SRIM-2000 simulations [9] the average energy density in an individual binary collision cascade induced by a 80 eV C^+ ion is close to 7 eV/atom. This value is much higher than the hydrogen displacement energy
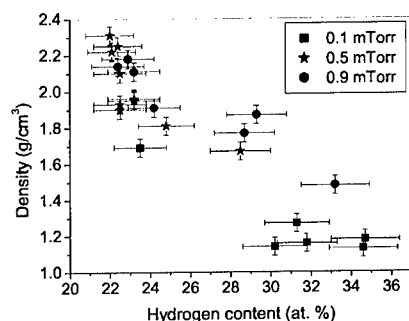
Figure 5. Films density as a function of the hydrogen content.
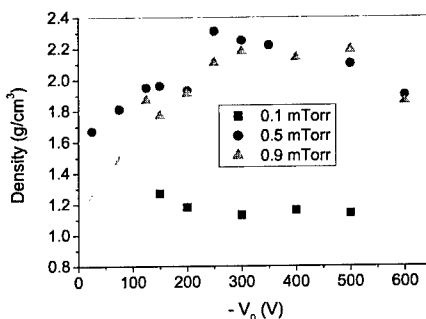
Figure 6. Density as a function of the substrate bias for several pressures.

(~2.5 eV) and higher than the hydrogen surface binding energy (<4.5 eV). It is also underestimated since the cascades created by the two carbon atoms from a $(C_2H_x)^+$ ion overlap. The amount of hydrogen remaining within the material depends on the outcome of the competition between the chemisorption, subplantation and desorption. Consequently it is expected to be strongly dependant on the ion energy. Figure 4 shows the evolution of N_H as a function of V_0 for several P values. At low pressure (0.1 mTorr) N_H ~32 % and remains constant within the investigated bias range. At higher pressures N_H first decreases with increasing bias, indicating that ion bombardment related effects (sputtering, outdiffusion) dominate over hydrogen incorporation. Then it remains constant, indicating that a dynamic equilibrium is reached between hydrogen incorporation and loss.

When the D values corresponding to films deposited at various pressure and substrate bias are plotted as a function of N_H a general trend emerges (figure not shown): the deposition rate decreases when the hydrogen content increases. The low deposition rate D (D~100 Å/min) observed at low pressure (0.1 mTorr) is attributed to the predominance of the passivation of dangling bonds by hydrogen radicals. At higher pressure ($\geq$ 0.5 mTorr) the growth rate is significantly higher (300$\leq$D$\leq$500 Å/min) because of a higher hydrogen desorption rate. At 0.9 mTorr the substrate current density is about the same as at 0.1 mTorr (figure 1). Yet, the deposition rate observed at 0.9 mTorr is higher than at 0.1 mTorr. The effect is attributed to a lower hydrogen incorporation rate at 0.9 mTorr. This is consistent with the observation of a relatively high concentration of hydrogen radicals within the plasma at low pressure [10] where the electron temperature is higher [2]. It is not possible to reach the deposition rate $\geq$ 50 nm/min when incorporating more that ~23 % of hydrogen. The lowest N_H value obtained using C_2H_2 as precursor is close to 20%. This limit is believed to be correlated to the amount of hydrogen within the reactor.

The film microstructure and physical properties depend closely on the hydrogen content. Figure 5 shows the film density ρ as a function of N_H. The denser films are those which exhibit the lowest N_H values. Figure 6 shows the evolution of ρ as a function of V_0 for several plasma pressures. For the films deposited at P>0.1 mTorr ρ first increases with $|V_0|$, reaches a maximum and then decreases. The increase in the density is known to correspond to an increase in the hybridisation ratio [2-3]. The maximum density is reached when the carbon atoms carried by $(C_2H_x)^+$ ions undergo a subplantation process with an energy of ~ 150 eV. This energy corresponds to highest sp^3 hybridisation [13].
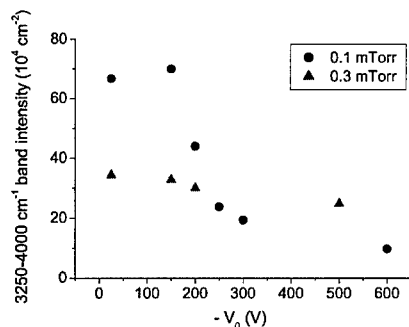
Figure 7. 3250-4000 cm^{-1} IR band intensity as a function of the substrate bias for two plasma pressures.
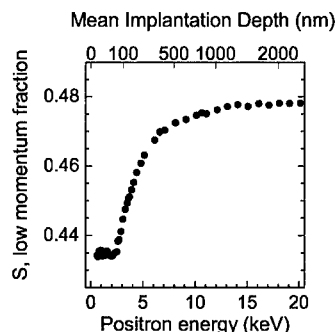
Figure 8. S parameter as a function of the positron beam energy for a film deposited at P=0.1 mTorr and with V_0= −80 V.

To shed more light on the hydrogen incorporation the films were analysed using FTIR spectroscopy. Figure 7 shows the evolution of the 3250-4000 cm^{-1} IR band intensity I_{OH} as a function of V_0 for films deposited at 0.1 and 0.3 mTorr. This band is known to contain OH, NH and NH$_2$ sub-bands [11]. The peak related to the H$_2$ vibration mode near 4135 cm^{-1} was not detectable in the present experimental conditions. The observed decrease in the intensity of the stretching band can not be unambiguously correlated to a decrease in the amount of hydrogen bound to the carbon network. Such plots should be taken with caution since the signal detected depends on the optical film properties which vary as a function of the process parameters. For $|V_0|$<200 V I_{OH} is greater at 0.1 mTorr than at 0.3 mTorr. According to [4, 12] this result indicates that the oxygen and nitrogen absorption is greater for the lower density films than for denser films. The difference in density between films deposited at 0.1 and 0.3 mTorr (FIG.6) is qualitatively visible in the different shape of the CH stretching bands (not shown). Whatever the pressure used, the C(sp^3)H$_2$ and C(sp^3)H modes seem to increase linearly with bias while the relative intensity of the Csp^{3}H$_3$ mode decreases.

One of the consequences of the ion energy transfer via elastic collisions is the production of vacancies. Positron Doppler broadening spectroscopy has been used to access the film porosity. The low momentum parameter S corresponding to the energy window 511 [−0.71;+0.71] keV centred at the positron annihilation peak is very sensitive to the presence of voids acting as positron trapping sites. The parameter S increases when open volumes are present in the material. To investigate the depth dependence of S, the S(E) curve was recorded as a function of the positron beam energy E within the range from 0.5 to 20 keV. The S(E) curve corresponding to a film deposited at low pressure (~0.1 mTorr) with V_0= −80 V is shown in FIG. 8. The constant S value corresponding to the a-C:H layer (S =0.4344) suggests that the film is homogeneous with respect to the porosity. The high S value indicates that the positron effective diffusion length is relatively short. The corresponding positron trapping rate is attributed to the presence of open volumes in the structure. We note that the size of the pores is small enough to make them undetectable by TEM. SRIM-2000 simulations show that the number of vacancies per C$^+$ ion increases almost linearly from ~0.3 to ~7.7 when the ion energy increases from 25 to 300 eV. However as shown in figure 4, N$_H$ remains constant when the substrate bias is increased above $|V_0|$>150 V. Consequently the porosity and the hydrogen content are not correlated.

CONCLUSIONS

- We have provided experimental evidence that the hydrogen incorporation within DECR plasma deposited (t)a-C:H films results from the competition between chemisorption, subplantation and ion bombardment enhanced desorption.
- We have demonstrated that the increase in the hydrogen incorporation leads to a decrease in the film density and deposition rate.
- We have shown that plasma deposited (t)a-C:H films are porous. The porosity and the hydrogen content are not correlated.
- We have confirmed earlier observations that absorption of oxygen and nitrogen increases when the density of the films decreases.

REFERENCES

[1] W. Jacob and W. Möller, *Appl. Phys. Lett.* **63**, 1771 (1993).
[2] M. Weiler, S. Sattel, T. Giessen, K. Jung, H. Ehrhardt, V.S. Veerasamy and J. Robertson, *Phys. Rev.* **B53**, 1594 (1996).
[3] J. Robertson, *Surf. Coat. Technol.*, **50**, 185 (1992).
[4] J. Ristein, R. T. Stief and L. Ley, *J. Appl. Phys.* **84**, 3836 (1998).
[5] G.E. Jellison, Jr. And F.A. Modine, *Appl. Phys. Lett.* **69**, 371 (1996); **69**, 2137 (1996).
[6] A. Benninghoven, F.G. Rüdenauer and H.W. Werner, *Secondary Ion Mass Spectroscopy*, edited by A. Wiley-Interscience Publication, John Wiley & sons.
[7] J. Küppers, *Surf. Sci. Rep.* **22**, 249 (1995).
[8] A. Golanski, D. Grambole, J. Hommet, F. Herrmann, P. Kern, L. McDonnell, F. Piazza and J.P. Stoquert, *MRS Spring Meeting 2001*.
[9] J.P. Biersack and W. Eckstein, *Appl. Phys.* **A34**, 814 (1984).
[10] B.K. Kim and T.A. Grotjohn, *Diam. Relat. Mater.* **9**, 654 (2000).
[11] N.B. Colthup, L.H. Daly and S.E. Wilberley, *Introduction to infrared and Raman Spectroscopy*, edited by Academic Press.
[12] D.P. Manage, J.M. Perz, F. Gaspari, E. Sagnes and S. Zukotynski, *J. Non-Crys. Solids* **270**, 247 (2000).
[13] Y. Lifshitz, *Diam. Relat. Mater.* **8**, 1659 (1999).

Preparation and properties of amorphous carbon oxynitrides a-CN$_x$O$_y$ films made by a nitrogen radical sputter method and by the layer-by-layer method

Yohko Naruse, Shoji Nitta and Hitoe Habuchi*
Department of Electrical Engineering, Gifu University,
1-1 Yanaido, Gifu, 501-1193, Japan
*Department of Electrical and Computer Engineering, Gifu National College of Technology,
Sinsei-cho, Motosu-gun, Gifu, 501-0495, Japan

ABSTRACT

We have tried to prepare amorphous carbon oxynitrides (a-CN$_x$O$_y$) films by the oxygen radical treatment (ORT) of amorphous carbon nitrides (a-CN$_x$) and also by the layer-by-layer method. Properties of a-CN$_x$O$_y$ films were studied with X-ray photoelectron spectroscopy (XPS), photothermal deflection spectroscopy (PDS), ultraviolet-visible (UV-VIS) optical transmittance spectra, Raman spectra and electron spin resonance (ESR). Oxygen radical affects to a-CN$_x$ by etching, termination of defects and oxidation. A-CN$_x$O$_y$ films are interesting for the application to luminescent materials and also to low dielectric constant materials.

INTRODUCTION

The amorphous phase of carbon nitride (a-CN$_x$) made by a nitrogen radical sputter method shows high photosensitivity and high resistively [1-3]. A-CN$_x$ has attractive properties as a low dielectric constant material for ultra large-scale integration ULSI [4-6]. The hydrogen plasma treatment on a-CN$_x$ is a very effective method to refine electronic properties. The hydrogen-plasma, i.e. atomic hydrogen, etches a-CN$_x$, decreasing dangling bonds density but hydrogen is not included into a-CN$_x$ not like the hydrogen termination in a-Si:H [2]. A cycle process of the deposition of thin a-CN$_x$ film and the hydrogen-plasma treatment, which is called the layer-by-layer (LL) process, has been used to make LLa-CN$_x$ films to refine a-CN$_x$. It has been reported that LLa-CN$_x$ has higher photosensitivity and smaller dielectric constant than a-CN$_x$ and shows photoluminescence, including ultraviolet light to 3.5 eV [6~7].

In this paper, we are interested to study the effect of oxygen radicals to a-CN$_x$, especially to prepare amorphous carbon oxynitrides (a-CN$_x$O$_y$) films. Properties of a-CN$_x$O$_y$ films are studied using X-ray photoelectron spectroscopy (XPS), photothermal deflection spectroscopy (PDS), ultraviolet-visible (UV-VIS) transmittance spectra and Raman spectra. Preliminary study on preparation of the layer-by-layer a-CN$_x$O$_y$, i.e. LLa-CN$_x$O$_y$ is also presented.

EXPERIMENTALS

The radio frequency (rf) magnetron sputtering apparatus is used for a nitrogen radical sputtering of a graphite target with a sputter gas of nitrogen molecules to prepare a-CN$_x$ films.

At first, we have tried to prepare a-CN$_x$O$_y$ films by using nitrogen and oxygen gases together as a sputter gas, but no film growth has been observed, because the etching properties of plasma

made by a mixed O_2-N_2 gas is stronger than the growth rate.

Therefore, we have tried to prepare a-CN_xO_y by the oxygen radical treatment (ORT) using oxygen plasma on surface of a-CN_x, which is deposited by a nitrogen radical sputter of carbon target. A-CN_x films made by a nitrogen radical sputter of carbon target contain a larger amount of nitrogen N/C ~ 0.5 - 0.86 compared with the other methods such as ECR and filtered cathodic arc method [8-10]. The nitrogen molecule gas of purity 99.999 % or oxygen gas of 99.999 % was used with gas pressure of 0.12 Torr. Rf of 13.56 MHz was used with power of 85 W. Substrates of Corning 7059 were used with substrate temperature, T_s, of room temperature (RT), 80, 200, 300 and 400 °C. Graphite target of 3 inches in diameter was used with a of samarium-cobalt (Sm-Co) magnets to hold magnetic field for magnetron condition. Time to prepare a-CN_x by a nitrogen radical sputter were 8 hr for T_s=RT, 6.5 hr for T_s=80 °C, 6 hr for T_s=200 and 300 °C, and 9.5 hr for Ts=400 °C. ORT were done for 30 min except a sample at T_s=80 °C for 15 min.

Properties of films are studied by XPS with SHIMADZU ESCA-850, UV-VIS transmittance spectra with HITACHI U-4000S, Raman spectroscopy with RENISHAHW RAMANSCOPE-2000, electron spin resonance (ESR) with JEOL JES-FE1X, and PDS.

EXPERIMENTAL RESULTS

Composition of carbon, nitrogen and oxygen in a-CN_xO_y films were studied with XPS of C_{1s}, N_{1s} and O_{1s}. In XPS of C_{1s}, the increase nearly at 290 eV was observed after ORT, corresponding with the increase of carbon-oxygen bonds. This result is also confirmed for XPS of O_{1s}. Figure 1 shows composition ratios of C, N and O before and after ORT at the surface of samples, which were obtained with the integrated intensities of each XPS.
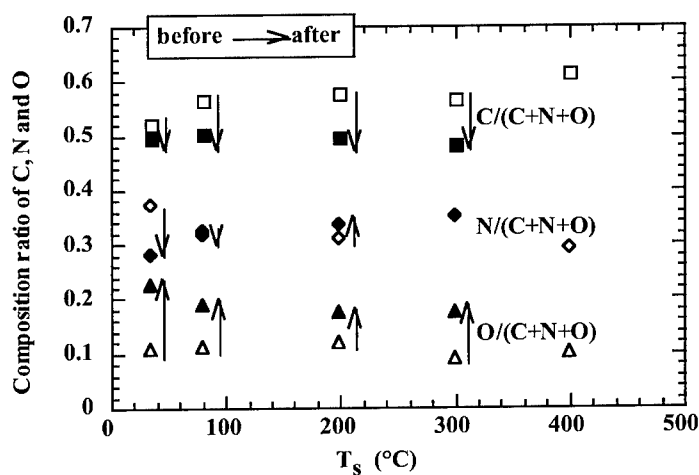
Figure 1. Dependence of composition ratio for C, N and O/[C+N+O] on substrate temperature T_s. Before ORT (white plots) is the ratio of a-CN_x, after ORT (black plots) is the ratio of a-CN_xO_y.

Oxygen for a-CN$_x$ before ORT is understood as incorporated by water and/or oxygen in air when samples were exposed to air before ORT, because oxygen for a-CN$_x$ before ORT is not observed inside the sample. Generally, carbon contents decrease for samples made at every T$_s$ with ORT. Nitrogen contents, roughly speaking, don't depend on ORT. Oxygen contents increase with ORT. A-CN$_x$ prepared at 400 °C was etched away after ORT.

Figure 2 shows the UV-VIS optical transmittance spectra before and after ORT. Generally transmittance increases after ORT and absorption edge shifts to smaller wavelength.

Figure 3 shows the change of film thickness, d, before and after the ORT, which were obtained from the interference pattern of optical transmittance spectra with a method shown in reference [6]. The film thickness increased or decreased depending especially on the substrate and treatment temperature. As pointed at figure 1, a-CN$_x$ made at 400 °C is etched out after ORT.

Figure 4 shows the dependence of refractive indices, n, for samples on T$_s$, which are also obtained from the interference pattern of UV-VIS optical transmittance spectra [6]. In every sample, the refractive indices decreased with ORT.

Figure 5 shows Tauc optical energy gap, E$_o$, obtained by Tauc plot of absorption coefficients obtained from UV-VIS transmittance spectra [11]. In every condition, E$_o$ increased after ORT.

Urbach tails were clearly observed in samples before and after ORT in PDS spectra, for samples prepared at 300 °C. Urbach energies E$_u$ before and after ORT were 142 and 137 meV respectively. The change of Urbach energy E$_u$ is showing the sharpen conduction band edge by ORT.

If the rules of peak position shift in Argon laser Raman spectra observed for DLC could apply to a-CN$_x$ [12,13], sp^3 bonds could say increase or decrease after the ORT depending on the preparation conditions.
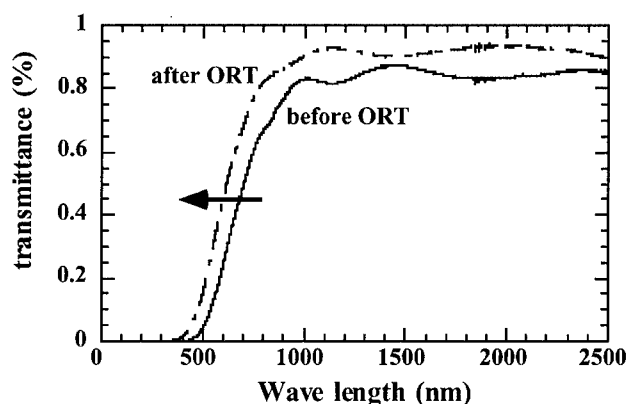
Figure 2. UV-VIS transmittance spectra of a-CN$_x$ and a-CN$_x$O$_y$ prepared and treated at 300 °C. By those spectra, film thickness, refractive indices and optical energy gap were obtained. Before ORT is a-CN$_x$ spectrum, after ORT is a-CN$_x$O$_y$ spectrum.
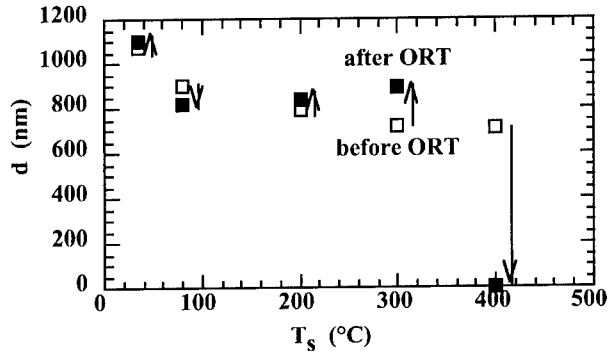
Figure 3. Film thickness d of a-CN$_x$ and a-CN$_x$O$_y$ depend on substrate temperature T$_s$. White squares are for a-CN$_x$ (before ORT) and black squares are for a-CN$_x$O$_y$ (after ORT).

Defect densities, N$_s$, obtained by ESR, also increased or decreased depending on the preparation conditions; for examples, N$_s$ = 4.9×10^{18} cm^{-3} decreased to 4.73×10^{18} cm^{-3} after ORT for a-CN$_x$ prepared at 35 °C and N$_s$ = 1.46×10^{18} cm^{-3} to 3.12×10^{18} cm^{-3} after ORT for a-CN$_x$ prepared at 300 °C. The change of N$_s$ by ORT was not so large, because only the surface region of a sample was affected by the ORT, where the oxygen content in the sample was controlled by diffusion of oxygen in samples [14]. To observe the effect of ORT more clearly, LLa-CN$_x$O$_y$ were prepared and used for ESR experiment. N$_s$ of LLa-CN$_x$O$_y$ prepared at 35 and 300 °C are 4.02×10^{18} and 8.38×10^{17} cm^{-3}, respectively. These values of N$_s$ are smaller than a-CN$_x$.
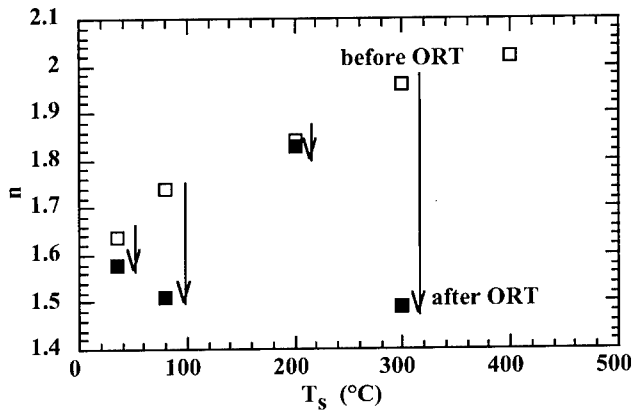
Figure 4. Refractive index n of a-CN$_x$ and a-CN$_x$O$_y$ depend on substrate temperature. White squares are for a-CN$_x$ (before ORT) and Black squares are for a-CN$_x$O$_y$ (after ORT).
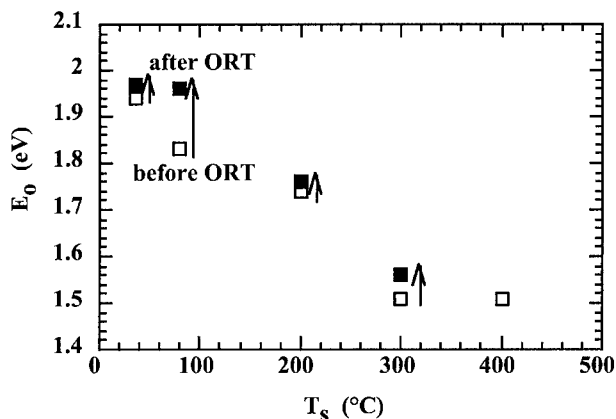
Figure 5. Tauc optical energy gap E_o of a-CN_x and a-CN_xO_y depend on substrate temperature T_s. White squares are for a-CN_x (before ORT) and black squares are for a-CN_xO_y (after ORT).

DISCUSSION

From above experimental results on the increase of oxygen and carbon-oxygen chemical bonds and on the increase or decrease of film thickness and defect densities, both of oxidation, i.e. inclusion of oxygen into a-CN_x, and etching of a-CN_x occurred in the ORT. At a condition of the decrease the film thickness, etching effect was stronger than oxidation, and so defect density increase by cutting bonds. When film thickness increased with ORT, the defect termination by oxygen atoms was stronger that to create defect by etching. Raman spectra were affected by ORT by changing chemical bonds. The reason to increase the band gap energy is mainly explained the shift of the band gap edge states to high or deep energy with the bonding and termination by oxygen.

Total content of nitrogen and oxygen x+y in a-CN_xO_y is about 1, which is larger than maximum value of x=0.86 for a-CN_x made by a nitrogen radical sputter method at present [3]. This result is a very attractive point of ORT, especially to get lower dielectric constant materials [4-6]. An oxygen atom has two chemical bonds, therefore forming less dense materials especially near the surface region, because carbon has 3 or 4 bonds and nitrogen has 3 bonds usually.

Another interesting point of a-CN_xO_y is the increase of ultraviolet range between 3 to 3.5 eV in photoluminescence (PL) spectra excited by helium-cadmium laser [14]. The reason of the increase of PL at ultraviolet range can be explained by the increase of band gap, the decrease of defect states and the increase of radiative centers by OPT.

CONCLUSIONS

Amorphous carbon oxynitride a-CN_xO_y films were prepared by oxygen radical treatment on

amorphous carbon nitride a-CN$_x$ films made by a nitrogen radical sputter method. Oxygen has mainly three effects on a-CN$_x$; oxidation, i.e. inclusion of oxygen into a-CN$_x$, etching of a-CN$_x$ and termination of defect states in a-CN$_x$. A-CN$_x$O$_y$ films are attractive for applications as luminescent materials especially from blue to ultraviolet range up to 3.5 eV and also as low dielectric materials.

ACKNOWLEDGEMENTS

REFERENCES

1. N. Takada, K. Arai, S. Nitta and S. Nonomura, *Applied Surface Science* **133**, 274 (1997).
2. S. Nitta, N.Takada, K. Sugiyama, T. Ito and S. Nonomura, *J. Non-Cryst. Solids*, **227**, 655 (1998).
3. T. Iwasaki, M.Aono, S. Nitta, H. Habuchi, T. Itoh and S. Nonomura, *Diamond Related Materials* **8**, 440 (1999).
4. M. Aono, S. Nitta, T. Iwasaki, H. Yokoi, T. Itoh and S. Nonomura, in *Low-Dielectric Constant Materials*, edited by J. P. Hummel, K. Endo, W. W. Lee, M. E. Mills and S-Q. Wang (Mater. Res. Soc. Symp. Proc. Vol. 565, 1999) pp. 291-296.
5. M. Aono, T. Katsuno, S. Nitta, T. Itoh and S. Nonomura, in *Amorphous and Nanostructured Carbon*, edited by J.P. Sullivan, J. Robertson, O. Zhou, T.B. Allen and B.F. Coll, (Mater. Res. Soc. Symp. Proc. Vol. 593, 2000) pp. 493-498.
6. M. Aono, Y. Naruse, S. Nitta and T. Katsuno, *Diamond and Related Materials*, in press.
7. T. Katsuno, S. Nitta, H. Habuchi, T. iwasaki, T. Itoh and S. Nonomura, in *Amorphous and Nanostructured Carbon*, edited by J.P. Sullivan, J. Robertson, O. Zhou, T.B. Allen and B.F. Coll, (Mater. Res. Soc. Symp. Proc. Vol. 593, 2000) pp. 499-504.
8. S. Bhattacharyya, C. Vallee, C. Cardinaud and G. Turban, *Diamond and Related Materials* **8** 586 (1999).
9. S.E. Rodil, W.I. Milne, J. Robertson and L.M. Brown, *Applied Phys. Lett.* **77**, 1458 (2000).
10. S.E. Rodil, W.I. Milne, J. Robertson and L.M. Brown, *11th European Conf. on Diamond, Diamond-Like Materials, Carbon Nanotubes, Nitrides and Silicon Carbide*, Abstract Book, 8.4b (2000, Porto).
11. R.A. Street, Hydrogenated amorphous silicon, (*Cambridge U.P.*, 1991).
12. A. C. Ferrari and J. Robertson, *Phys. Rev. B*, **61**, 14095 (2000).
13. A. C. Ferrari and J. Robertson, in *Amorphous and Carbon*, edited by J.P. Sullivan, J. Robertson, O. Zhou, T.B. Allen and B.F. Coll, (Mater. Res. Soc. Symp. Proc. Vol. 593, 2000) 299.
14. Y. Naruse et al., to be submitted.

Field Emission

Nanodevice fabrication on hydrogenated diamond surface using atomic force microscope

Minoru Tachiki, Tohru Fukuda, Hokuto Seo, Kenta Sugata, Tokishige Banno, Hitoshi Umezawa and Hiroshi Kawarada
School of Science & Engineering, Waseda University, Tokyo, Japan.
CREST, Japan Science and Technology Corporation (JST), Japan
E-mail: tachiki@mn.waseda.ac.jp

ABSTRACT

Nanofabrication on a hydrogen-terminated diamond surface is performed using an atomic force microscope (AFM) anodization. Locally insulated areas less than 30 nm are successfully obtained. Side-gated field effect transistors (FETs) are fabricated using the local anodization, and they operate successfully. Single hole transistors composed of one side-gated FET and two tunneling junctions are also fabricated and operate at liquid nitrogen temperature (77 K).

INTRODUCTION

Recently, nanofabrication technology using a scanning probe microscope (SPM) has attracted special interest [1-4]. The fabrication of several nanoscale devices has been reported based on this technique, including nanoscale FETs and single electron transistors (SETs), which have been fabricated by the local anodization of Si, Ti and compound semiconductors [5-8].

Hydrogen termination (H-termination) of diamond surfaces is important because it can stabilize the surface structure. Furthermore, H-terminated diamond is also attractive for electrical applications because it induces p-type surface conduction even in undoped diamond [9-11]. Recently, our group has demonstrated the fabrication and the operation of field-effect transistors (FETs) using a surface conductive layer, and has obtained high transconductance [12,13]. The thickness of this surface conductive layer was estimated to be less than 10 nm, and the surface hole density to be $\sim 10^{13}$ cm^{-2} [11]. On the other hand, an oxygen-terminated (O-terminated) diamond surface is insulating. This means that diamond has an advantage over other semiconductor materials in the fabrication of a surface nanostructure using a SPM-based processing technology.

Since undoped diamond is basically an insulating material, we can conclude that H-terminated diamond has a semiconductor-on-insulator structure. In the case of Si, special techniques such as separation by implanted oxygen (SIMOX) etc. are needed to fabricate the electrically isolated thin conducting layer. In diamond, an electrically isolated surface conductive layer is easily obtained by eliminating the surface H-termination. Recently, local anodization on H-terminated diamond surface was performed using a metal (Au, Rh, etc.) coated conductive atomic force microscope (AFM) cantilever by applying voltage bias to the sample surface [14-17]. Up to the present, local insulation (30-60 nm in line width) has been successfully achieved using AFM. The nm scale separation of H-terminated surface and O-terminated surface will produce new types of nanoscale surface quantum devices such as single charge tunneling devices etc.. In the present study, the fabrication and operation of side-gated diamond metal-insulator-semiconductor FETs (MISFETs) are demonstrated using anodized surface as a gate insulator. Using the locally anodized double tunneling barrier and aforementioned side-gated FET structure, fabrication and operation of single hole transistor is also demonstrated.
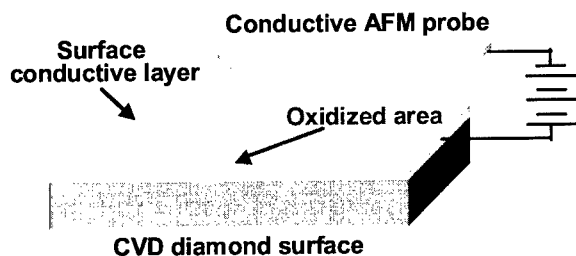
Figure 1. Schematic of AFM nanofabrication on the hydrogen-terminated diamond film surface.

EXPERIMENTAL

For sample preparation, microwave-plasma-assisted chemical vapor deposition (CVD) with a CH_4/H_2 gaseous source is used. Undoped homoepitaxial diamond thin films are fabricated on high-pressure, high-temperature (HPHT) synthetic (001) diamond single-crystal substrates. After the deposition, undoped diamond films are exposed to hydrogen plasma to perform hydrogen termination. A scanning probe microscope system (Seiko Instruments: SPI3800N) and Au or W_2C-coated conductive AFM probes made of Si are used to perform surface anodization (figure 1). In the device fabrication process, electron beam lithography is used for the ohmic gold electrode fabrication, and channel isolation was carried out by Ar ion irradiation before the AFM anodization.

RESULTS AND DISCUSSION

Figure 2(a) shows an AFM topographic image of the modified diamond surface after line scanning under 5 V sample bias applied in air. In this case, surface protrusion is observed in the
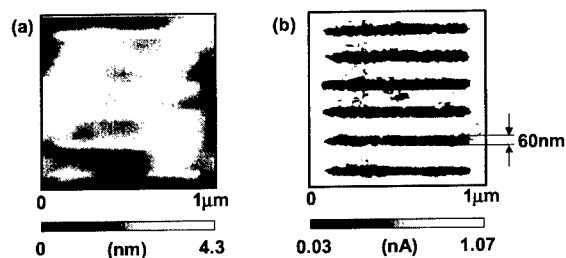
Figure 2. (a) Topographic images of diamond film surface after AFM modification (bias: 5 V, scan speed: 100 nm/s), (b) Current image under the application of 2 V sample bias

H-terminated
surface

Ohmic
electrode

(a) Before anodization

Anodized line

(b) After anodization
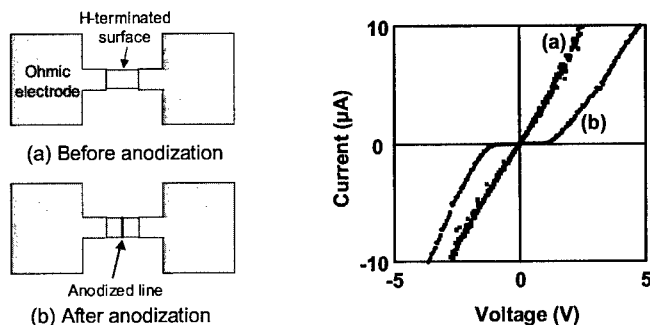
Voltage (V)

Figure 3. Current-voltage characteristics of H-terminated diamond suraface across the anodized region.

AFM-anodized area of 60 nm line width. In figure 2(b), the current image simultaneously obtained with topographic measurement is shown. During the current measurement, 2 V bias which is below the anodizing voltage is applied to the sample surface. In this figure, one can see that local insulation is successfully achieved. The insulated line width is about 60 nm. Current-voltage characteristics are measured across the anodized line at room temperature. Before the anodization, the current-voltage relation is almost ohmic (figure 3(a)). After making the anodized line (line width 60 nm), the current is suppressed at low -1 V $<V<1$ V (figure 3(b)). At a higher bias range ($|V|>1$ V), the current starts flowing through the insulated line by Fowler-Nordheim (F-N) tunneling and/or thermionic emission. Consequently, one can say that anodized region can be used as the potential barrier to the hole existing in surface conductive layer.

Figure 4 shows the schematic and the I_{DS}-V_{DS} characteristics of side-gated diamond FET fabricated by AFM local anodization. Source-drain channel is separated from the gate surface conductive area by anodized region. Current saturation is observed in the statistic characteristics,

Insulated area
by local
anodization

Ar$^+$ Irradiated
area (isolation)

Gate

Hydrogenated
surface
(p-type conductive)

Source

Drain

Gate

1 μm

Gate voltage V_{GS} (V)

Drain voltage V_{DS} (V)
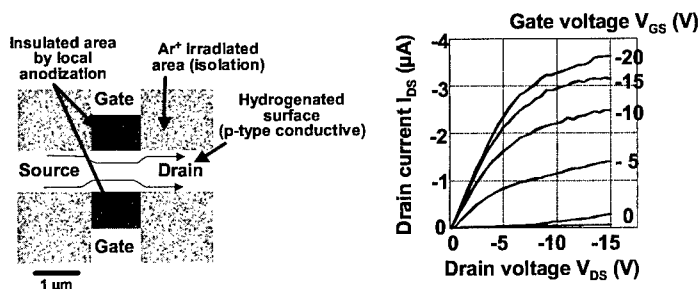
Figure 4. Schematic and statistic characteristics of side-gated FET (gate length: 1 μm) using local anodization by AFM.
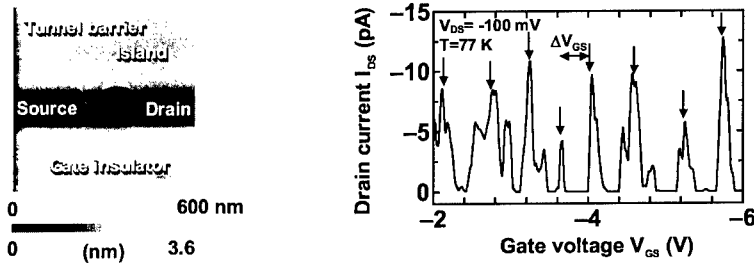
Figure 5. AFM image and V_{GS}-I_{DS} characteristic of diamond single hole transistor fabricated by AFM nano anodization.

and channel current is well modified by the field effect. Threshold gate voltage is 0 V, though slight short channel effect occurs at higher drain bias. Channel is depleted even at 0 V gate bias. This is attributed to the surface carrier trap existing at the anodized region.

Based on these results, single hole transistor is fabricated using AFM-anodized area as a gate insulator and tunneling barriers. Figure 5 shows the AFM image and measured characteristic of the fabricated single hole transistor. A conductive island (100×120 nm^2) is separated from source and drain by the anodized tunneling barriers (40 nm in width). In the V_{GS}-I_{DS} characteristic under -100 mV drain bias condition measured at liquid nitrogen temperature (77 K), clear current oscillation is observed. This oscillation can be attributed to the coulomb blockade oscillation. However, the area of the island deduced from the period of this oscillation ($\Delta V_{GS} \sim 0.4$ V) is in the order of nm. This value is smaller than aforementioned island area. If we consider the carrier depletion in the island, many smaller conductive regions appears in the isolated island. Subpeaks besides the main oscillation peaks in the current oscillation also suggests this multiple island model.

CONCLUSIONS

Local insulation on H-terminated diamond surface conductive layer was performed using AFM-based nano anodization. Based on this technology, the operation of 1 μm side-gated diamond MISFETs is performed using anodized surface as a gate insulator. This FET operates in enhanced mode and field-effect modulation of channel current is successfully achieved by the side-gated MIS structure. Using the locally anodized double tunneling barrier and side-gated FET structure, fabrication and operation of single hole transistors are also demonstrated for the first time. In the V_{GS}-I_{DS} characteristic, coulomb blockade oscillation is observed even at liquid nitrogen temperature (77 K).

REFERENCES

1. J. A. Dagata, J. Schneir, H. H. Harary, C. J. Evans, M. T. Postek and J. Bennett, Appl. Phys. Lett. **56**, 2001 (1990).
2. J. A. Dagata, W. Tseng. J. Bennett, J. Schneir and H. H. Harary, Appl. Phys. Lett. **70**, 3661 (1991).
3. M. Yasutake, Y. Ejiri and T. Hattori, Jpn. J. Appl. Phys. **32**, L1021 (1993).

4. E. S. Snow and P. M. Campbell, Appl. Phys. Lett. **64**, 1932 (1994).
5. P. M. Campbell, E. S. Snow and P. J. McMarr, Appl. Phys. Lett. **66**, 1388 (1995).
6. K. Matsumoto, M. Ishii and K. Segawa, J. Vac. Sci. & Technol. **B14**, 1331 (1996).
7. K. Matsumoto, Y. Gotoh, T. Maeda, J. A. Dagata and J. S. Harris, Jpn. J. Appl. Phys. **38**, 477 (1999).
8. S. Sasa, T. Ikeda, K. Anjiki and M. Inoue, Jpn. J. Appl. Phys. **38**, 480 (1999).
9. T. Maki, S. Shikama, M. Komori, Y. Sakaguchi, K. Sakuta and T. Kobayashi, Jpn. J. Appl. Phys. **31**, L1446 (1992).
10. H. Kawarada, Surf. Sci. Rep. **26**, 205 (1996).
11. K. Hayashi, S. Yamanaka, H. Watanabe, T. Sekiguchi, H. Okushi and K. Kajimura, J. App. Phys. **81**, 744 (1997).
12. H. Umezawa, K. Tsugawa, S. Yamanaka, D. Takeuchi, H. Okushi and H. Kawarada, Jpn. J. Appl. Phys. **38**, L1222 (1999).
13. H. Umezawa, H. Taniuchi, T. Arima, M. Tachiki, K. Tsugawa, S. Yamanaka, D. Takeuchi, H. Okushi and H. Kawarada, Jpn. J. Appl. Phys. **39**, L908 (2000).
14. M. Tachiki, T. Fukuda, K. Sugata, H. Seo H. Umezawa and H. Kawarada, Proceedings of the Third International Symposium on the Control of Semiconductor Interfaces, Karuizawa October, 578 (1999).
15. M. Tachiki, T. Fukuda, K. Sugata, H. Seo, H. Umezawa and H. Kawarada, Appl. Surf. Sci. **159-160**, 578 (2000).
16. M. Tachiki, T. Fukuda, K. Sugata, H. Seo, H. Umezawa and H. Kawarada, Jpn. J. Appl. Phys. **39**, 4631 (2000).
17. M. Yanagisawa, H. Tai, I. Yagi, D.A. Tryk, A. Fujishima and L. Jiang: Proceedings of the Sixth International Symposium on Diamond Materials, Honolulu, Hawaii, October, 423 (1999).

RAMAN AND EELS STUDIES ON NANOCRYSTALLINE DIAMOND PREPARED IN A LOW PRESSURE INDUCTIVELY COUPLED PLASMA

KATSUYUKI OKADA, KOJI KIMOTO, SHOJIRO KOMATSU,
and SEIICHIRO MATSUMOTO
Advanced Materials Laboratory, National Institute for Materials Science
1-1 Namiki, Tsukuba, Ibaraki 305-0044, Japan
okada.katsuyuki@nims.go.jp

ABSTRACT

Nanocrystalline diamonds with several hundred nm in diameter have been prepared in a 13.56 MHz low pressure inductively coupled CH_4/H_2 or $CH_4/CO/H_2$ plasma. The bonding structures were investigated by Raman spectroscopy and electron energy loss spectroscopy (EELS). Visible (514 nm) and UV (325, 244 nm) excited Raman spectra with CO additive exhibit peaks at ⁓1150 cm^{-1} assigned to sp3 bonding and at 1332 cm^{-1} due to zone center optical phonon mode of diamond, respectively. It indicates that the UV excitations are possibly sufficient to excite the σ state of both sp2- and sp3-bonded carbon. The high resolution EELS (HREELS) spectra with CO additive show peaks at ⁓1100 cm^{-1} assigned to C-C stretching vibration of sp3 bonding and at ⁓700 cm^{-1} corresponding to the bending vibration of sp3 bonding. It is qualitatively agreement with the Raman spectra. Furthermore the EELS spectrum without CO additive exhibits two peaks at 284 eV and at 292 eV corresponding to π * states and σ * states, respectively, and is similar to that of graphite rather than that of sp^2-rich amorphous carbon. The EELS spectrum with CO additive, on the other hand, shows a peak at 292 eV due to σ * states and is similar to that of diamond. A slight peak appears at ⁓285 eV corresponding to π * states. It consequently implies that the particles almost consist of sp^3 bondings and that the small amount of sp^2 bondings are considered to exist in grain boundaries. The EESL spectra are consistent with the results of Raman scattering and HREELS.

INTRODUCTION

Amorphous and nanostructured carbon materials have attracted considerable attention in the last twenty years since the chemical vapor deposition of diamond was developed, followed by fullerenes and carbon nanotubes. From applied perspectives, they are being extensively studied for electron-emitting elements, cold-cathode sources, and ultrahard tribological coatings, etc. From fundamental perspectives, on the other hand, the structure of these materials contains both three-fold coordinated (sp^2-bonded) and four-fold coordinated (sp^3-bonded) carbon atoms. The phonon density of state (PDOS) and the fraction of sp^3 bondings were quantitatively measured by Raman spectroscopy[1,2] and electron energy loss spectroscopy (EELS).[3]

Nanocrystalline diamond films also have drawn remarkable attention[4] because they have a low coefficient of friction and low electron emission threshold voltage. The small grain size (approximately 5-100 nm) gives films with valuable tribology and field-emission properties,[5] being compared with those of conventional polycrystalline diamond films. We have tried to prepare diamond films in a 13.56 MHz low pressure inductively coupled plasma (ICP).[6] The resultant deposits were found to be nanocrystalline diamond and diamond-like carbon (DLC)

films as characterized by scanning electron microscopy (SEM), transmission electron microscopy (TEM). The CO additive to a CH_4/H_2 plasma brought about the morphological change from a platelet deposit to a particle one. The diameter of particles were 200-500 nm. The vibrational studies of the nanocrystalline diamond were performed with Raman spectroscopy[7] and high resolution EELS (HREELS).[8] The qualitative analysis of the bonding structures has been carried out.

EELS in TEM has been demonstrated as powerful techniques for performing microanalysis and studying the electronic structure of materials. The energy loss near edge structure (ELNES) is sensitive to the crystal structure. The C-K edge of diamond and graphite are typical example. For trigonal sp^2-bonded carbon, the spectrum within the first 30 eV of the edge can be separated into two broad features, corresponding to the π * states between 282 and 288 eV and the σ * states between 290 and 320 eV, whilst for tetrahedral sp^3-bonded carbon only the σ * peak is observed between 289 and 320 eV.[9] Bruley's two-window technique by integrating intensities of the π * and σ * peaks has demonstrated the quantitative analysis of the sp^2 content in the samples.[3] In this paper, we first review the previous Raman and HREELS results, then report the high resolution TEM (HRTEM) observations and the EELS measurements of the nanocrystalline diamond.

EXPERIMENT

The detailed description of the low pressure ICP system and the deposition procedure was previously reported elsewhere.[6] The nanocrystalline diamond and DLC were grown in an ICP at 1 kW, 900 °C of the substrate (silicon wafer) temperature, 2 hours of the deposition duration, in a CH_4/H_2 or $CH_4/CO/H_2$ plasma at 45 to 50 mTorr.

The procedures of the Raman measurements with three different excitation wavelength (514, 325, 244 nm) and the HREELS measurements were described previously.[7,8] The EELS measurements were carried out by using a Hitachi HF-3000 dedicated HRTEM fitted with a GATAN-GIF parallel acquisition electron energy loss spectrometer (PEELS) operating at 300 keV. The microscope vacuum was less than 1.2×10^{-6} Pa. The typical energy resolution of the instrument was approximately 0.7 eV. To acquire EELS, the typical CCD readout times were 5 sec.

RESULTS AND DISCUSSION

As we have reported previously,[6] the CO additive to a CH_4/H_2 plasma brought about the morphological change from a platelet deposit to a particle one. The diameter of particles were 200-500 nm. Besides, the number of encountered particles was increased with increasing CO concentration. Figure 1 shows the 514 nm excited Raman spectra with different [CO]. The Raman spectrum without CO additive [Fig. 1(a)] exhibits two peaks at $\sim$1355 cm^{-1} (D peak) and at $\sim$ 1580 cm^{-1} (G peak) assigned to sp^2 bonding. New peaks appear at $\sim$1150 cm^{-1} and at $\sim$1480 cm^{-1} with CO additive [Fig. 1(b)]. The former peak is derived from sp^3 bonding[10] although it was recently proposed[11] that the peak is attributed to sp^2 bonding of *trans*-polyacetylene oligomer. Both D and G peaks become relatively small compared with those of Fig. 1(a). With increasing [CO] as shown in Fig. 1(c), the intensity of the peak at $\sim$1150 cm^{-1}
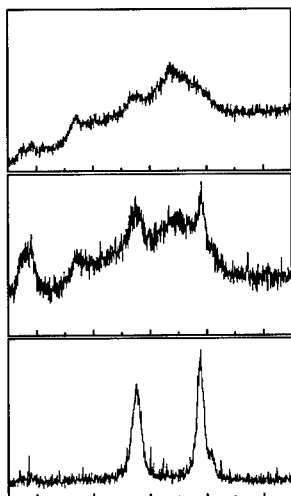
Figure 1. 514 nm excited Raman spectra with different gas mixture: (a) [CH₄]/[CO] =4.5/0 sccm, (b) [CH₄]/[CO]=4.5/1.0 sccm, and (c) [CH₄]/[CO]=4.5/10 sccm, respectively.
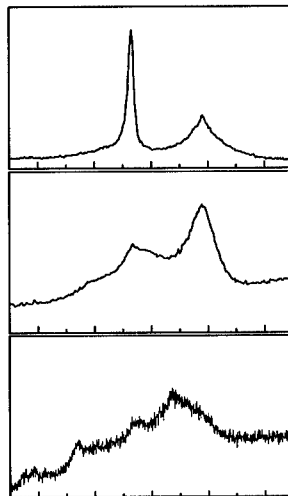
Figure 2. Raman spectra of Sample C ([CH₄] /[CO]=4.5/10 sccm) with different excitation wavelength: (a) 514 nm, (b) 325 nm, and (c) 244 nm, respectively.

becomes strong, while the G peak turns into a shoulder and the D peak becomes small. Figure 2 shows a sequence of Raman spectra of [CO]=10 sccm with different excitation wavelength. Compared with the spectrum of 514 nm excitation, the 325 nm excited Raman spectrum exhibits a clear peak at 1332 cm^{-1} and the remarkable enhancement of the peak at ∽1580 cm^{-1}, while the peak at ∽1150 cm^{-1} turns into a shoulder. In 244 nm excited Raman spectrum, the peak at 1332 cm^{-1} is only enhanced whereas the peak at ∽1580 cm^{-1} is weakened. Neither peak nor shoulder can be recognized at ∽1150 cm^{-1}. The 514 nm excited Raman spectra do not exhibit a clear diamond peak at 1332 cm^{-1}, though the peak due to sp^3-bonded carbon network appears at ∽1150 cm^{-1}. This is explained by the resonance enhancement in the Raman cross section in the sp^2-bonded carbon network.[12] The enhancement of the peaks at both 1332 cm^{-1} and ∽1580 cm^{-1} in the 325 nm excitation suggests that the resonance enhancement of Raman cross section due to sp^2-bonded carbon still remains and that the σ - σ * transition in both sp^2- and sp^3-bonded carbon is possibly induced. The remarkable enhancement of the peak at 1332 cm^{-1} and the diminution of the peak at ∽1580 cm^{-1} in the 244 nm excitation reveals that the resonance Raman effect due to sp^2-bonded carbon is suppressed and that the σ - σ * transition in both sp^2- and sp^3-bonded carbon is probably dominant.[1,2]
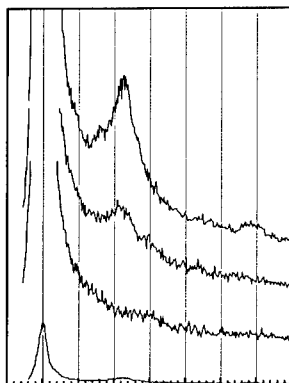
Figure 3. HREELS spectra with various [CH₄]/[CO]: (a) [CH₄]/[CO]=3.0/0, (b) [CH₄]/[CO]=4.5/8.0, and (c) [CH₄]/[CO]=4.5/10, in sccm, respectively. The elastic peak for (c), reduced by a factor of 25, is shown in comparison.

Figure 3 presents the HREELS spectra with different [CO]. In Fig. 3(a) without CO additive, the spectrum has a faint peak at $\sim$1500 cm^{-1} derived from C=C stretching mode of three-fold bonded carbon atoms.[13] The whole spectrum is similar to that of a single crystal graphite (0001) surface.[14] With CO additive as shown in Fig. 3(b), one can see a peak at $\sim$1100 cm^{-1}, which is assignable to C-C stretching mode of four-fold bonded carbon atoms.[13] The peak at $\sim$1500 cm^{-1} disappeared. With increasing [CO] as shown in Fig. 3(c), the intensity of the peak at $\sim$1100 cm^{-1} became strong. In addition, a shoulder centered at $\sim$700 cm^{-1} appeared. These features of the vibrational DOS are consistent with the theoretical results for random network models of t-aC.

Figure 4 shows the HRTEM image of platelet deposit without CO additive. Fig.4(b) corresponds to the high magnification image of the bottom left-hand side of Fig. 4(a). The lattice image is clearly shown in Fig. 4(b). The interplanar spacing is 0.203 nm, which is agreement with the d value of graphite (110). The EELS spectrum corresponding to Fig. 4(a) is shown in Figure 5. It exhibits two peaks at 284 eV and at 292 eV corresponding to π * states and σ * states, respectively, and is similar to that of graphite rather than that of sp^2-rich amorphous carbon.[3] In case of anisotropic materials like this platelet deposit, it is difficult to estimate accurately the fraction of sp^2/sp^3 by using Bruley's two-window technique. In graphite the π * transition requires a transfer of momentum parallel to the c-axis, while the momentum transfer of the σ * transition is perpendicular to the c-axis.[15]

Figure 6 shows the HRTEM image of a part of particle deposit with [CO]=10 sccm. Fig.6(b) corresponds to the high magnification image of the bottom left-hand side of Fig. 6(a). The careful observation reveals that the particle consists of small particles of approximately

several tens of nanometers in diameter. The lattice image is clearly shown in Fig. 6(b). The
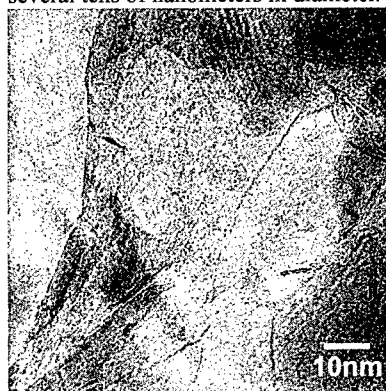
Figure 4(a). HRTEM image of the deposit
with [CH$_4$]/[CO]=4.5/0 in sccm.
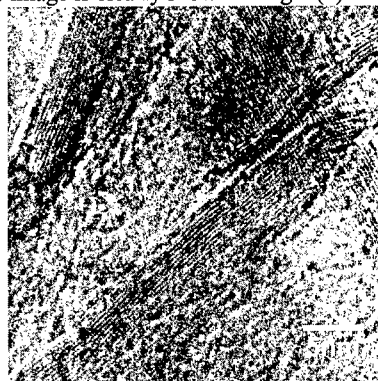
Figure 4(b). The high magnification image
of the bottom left-hand side of Fig. 4(a).
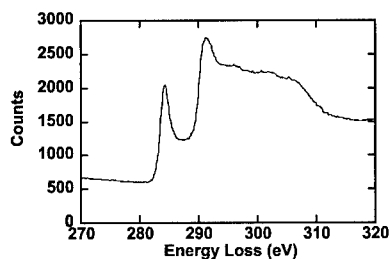
Figure 5. EELS spectrum corresponding
to Fig. 4(a)

interplanar spacing is 0.206 nm, which is agreement with the d value of diamond (111). The
EELS spectrum corresponding to Fig. 6(a) is shown in Figure 6. It shows a peak at 292 eV due to
σ * states and is similar to that of diamond rather than sp^3-rich tetrahedral amorphous carbon.[3] A
slight peak appears at ᷍285 eV corresponding to π * states. The small amount of sp^2 bondings
are considered to exist in grain boundaries between small grains of several ten nm in diameter.

CONCLUSIONS
            The bonding structures of nanocrystalline diamonds prepared in a 13.56 MHz low
pressure inductively coupled CH$_4$/H$_2$ or CH$_4$/CO/H$_2$ plasma were investigated by Raman
spectroscopy, HREELS, and EELS. The EELS spectrum without CO additive exhibits two peaks
at 284 eV and at 292 eV corresponding to π * states and σ * states, respectively, and is similar to
that of graphite rather than that of sp^2-rich amorphous carbon. The EELS spectrum with CO
additive, on the other hand, shows a peak at 292 eV due to σ * states and is similar to that of
diamond. It consequently implies that the particles almost consist of sp^3 bondings and that the
small amount of sp^2 bondings are considered to exist in grain boundaries. The EESL spectra are
consistent with the results of Raman scattering and HREELS.
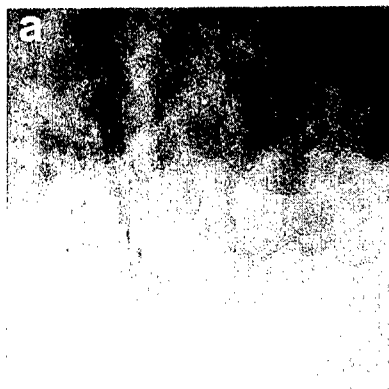
Figure 6(a). HRTEM image of the deposit with [CH₄]/[CO]=4.5/10 in sccm.

Figure 6(b). The high magnification image of the bottom left-hand side of Fig. 6(a).
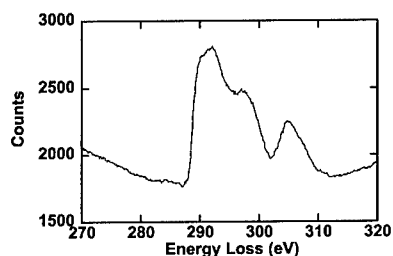
Figure 7. EELS spectrum corresponding to Fig. 6(a)

REFERENCES
1. K.W.R.Gilkes, D.N.Batchelder, J.Robertson, and W.I.Milne, Appl. Phys. Lett. **70**, 1980(1997).
2. V.I.Merkulov, J.S.Lannin, U.S.Veerasamy, and W.I.Milne,Phys. Rev. Lett. **78**, 4869(1997).
3. J.Bruley, D.B.Williams, J.J.Cuomo, and D.P.Pappas, J. Microscopy **180**, 22(1995).
4. D.M.Gruen, Annu. Rev. Mater. Sci. **29**, 211(1999).
5. A.A.Talin, L.S.Pan, H.J.Doerr, and R.F.Bunshah, Appl. Phys. Lett. **69**, 3842(1996).
6. K.Okada, S.Komatsu, and S.Matsumoto, J. Mater. Res. **14**, 578(1999).
7. K.Okada, H.Kanda, S.Komatsu, and S.Matsumoto, J. Appl. Phys. **88**, 1674(2000).
8. K.Okada, T.Aizawa, R.Souda, S.Komatsu, and S.Matsumoto, Diamond Relat. Mater.(in press).
9. R.F.Egerton and M.J.Whelan, J. Elect. Spect. Relat. Phenom. **3**, 232(1974).
10. R.J.Nemanich, J.T.Glass, and R.E.Shroder, J. Vac. Sci. Technol. **A6**, 1783(1988).
11. A.C.Ferrari and J.Robertson, Phys. Rev. B (in press).
12. J.Wagner, M.Ramsteiner, Ch.Wild, and P.Koidl, Phys. Rev. **B40**, 1817(1989).
13. H.Ibach and D.L.Mills, Electron Energy Loss Spectroscopy , Academic Press, London, 1982.
14. C.Oshima, T.Aizawa, R.Souda, and Y.Ishizawa, Solid State Commun. **65**, 1601(1988).
15. N.D.Browning, J.Yuan, and L.M.Brown, Ultramicroscopy **38**, 291(1991).

DENSITY FUNCTIONAL BASED TIGHT BINDING STUDY OF C_2 and CN DEPOSITION ON (100) DIAMOND SURFACE

Michael Sternberg[§], Peter Zapol[‡], Thomas Frauenheim[§], John Carlisle[‡], Dieter M. Gruen[‡], and Larry A. Curtiss[‡]

[‡]Materials Science and Chemistry Divisions, Argonne National Laboratory, Argonne, IL 60439
[§]Universität Paderborn, Fachbereich Physik, Theoretische Physik, D-33098 Paderborn, Germany

ABSTRACT

A density-functional based tight binding method was used to study elementary steps in the growth of ultrananocrystalline (UNCD) diamond. It was shown previously that C_2 dimers are the dominant growth species in hydrogen-poor argon plasmas. Recent experimental evidence shows that nitrogen addition to the plasma profoundly changes the morphology of the UNCD film. CN species are believed to play a major role. Reactions of C_2 and CN molecules with reconstructed diamond (100) surfaces were studied. A single CN prefers an end-on attachment to a surface atom on the unhydrided (100) surface with its C end down. It is shown how further C_2 addition to the surface leads to CN-mediated diamond growth and how the CN species remain on top of the growing diamond layer.

INTRODUCTION

Diamond film growth from argon/methane plasmas produces ultrananocrystalline diamond (UNCD) with an average size of 3-10 nm.[1] Nitrogen addition to the plasma in the amount of 1% to 20% strongly influences growth and renucleation rates as well as the composition of the resulting films. These films have a range of unique mechanical and electronic properties, which are associated with small crystallite size and large number of grain boundaries.[2]

The renucleation rate in UNCD growth is several orders of magnitude higher than that in the conventional diamond synthesis from hydrogen/methane plasmas. Examination of plasma emission spectra detected a Swan band produced by carbon dimers.[3] This led to studies of diamond growth mechanisms on (100) and (110) surfaces using carbon dimers as precursors.[4,5,6,7] In contrast, hydrogen abstraction and surface reactions with hydrocarbons such as methyl radicals play a central role in the established mechanisms of conventional microcrystalline diamond growth.[8] On the basis of quantum chemical modeling of C_2 reactions with the unhydrided and hydrogen-covered diamond surfaces, it was proposed that reconstructed hydrogen-free surface sites can act as chemically active nucleation sites after dicarbon insertion.[5,6] Strongly exothermic reactions leading to diamond growth on unhydrided and monohydrided diamond surface were calculated as well. Subsequently, a growth mechanism on the (110) surface based on C_{2n} chain formation and coalescence was investigated using a density-functional-based tight-binding method (DFTB).[7]

In view of the strong modification of the growth process by nitrogen addition to the plasma, it is interesting to investigate the nitrogen role in the growth process. One of the common plasma species in this case is the CN molecule.[3] In the present paper we examine the interaction of the CN radical with the unhydrided diamond (100) surface using the DFTB method. Further, we study the concurrent adsorption of a CN molecule and several C_2 molecules to shed light on the modification of the growth mechanism.

THEORETICAL METHODS

The molecular dynamics calculations were performed using a density functional based tight binding (DFTB) method with self-consistent charges using the approach of Frauenheim, Seifert, et al.[9,10] The basis functions and the tight-binding matrix elements in this scheme are obtained from reference density functional calculations. A self-consistent charge scheme is based on the second order expansion of the density functional over electron density fluctuations. This term is expressed through Mulliken charges and calculated self-consistently at each simulation step. The self-consistent charge scheme is necessary to correctly take into account effects of surface polarization. The method has been applied successfully to diamond systems including studies of surfaces and diffusion problems.

The surface is modeled using a two-dimensional slab geometry with a thickness of 8 carbon monolayers. The bottom layer is saturated by a fixed monolayer of pseudohydrogen atoms, which do not interact with each other. The lateral extent of the periodic supercell is 4x4 unit cells. For all atomic structure calculations, we used the Γ-point approximation to sample the Brillouin zone.

For the adsorption studies, the molecules were placed sequentially on the surface and then their geometries were optimized using a conjugate gradient method. Calculations of the transition states between different geometries have yet to be performed. Previous studies indicated very low adsorption barriers of the order of 0.1 eV for C_2 depositions[7] in a similar environment.

RESULTS

The clean (100) diamond surface has two broken bonds per atom before reconstruction. The reconstruction leads to the formation of double bonds between nearest neighbors and results in a (2x1) pattern of dimer rows. The bond lengths of the C(100)–(2x1) reconstruction agree to 1% with first-principles calculations[11]. We obtain an optimized bond length of 1.40 Å for the surface dimer, at an equilibrium diamond lattice constant of 3.562 Å.

We have chosen the optimized geometries of an adsorbed carbon dimer on the reconstructed (100) diamond surface in its two most stable configurations as initial positions for the conjugate gradient search of CN stable configurations. The two positions for a C_2 molecule are shown in Fig. 1. The first position (Fig. 1a) is the most stable geometry for a carbon dimer. Both carbon atoms are inserted into C–C double bonds on neighboring surface dimers. This geometry is topologically identical to the surface dimer, and would thus constitute a growth site. The other position (Fig. 1b) represents a carbon dimer vertically inserted into just one surface C–C bond and strongly tilted by 73° relative to the surface normal. This configuration is believed to lead to the nucleation of a new diamond crystallite since the adsorbed molecule is highly chemically active.
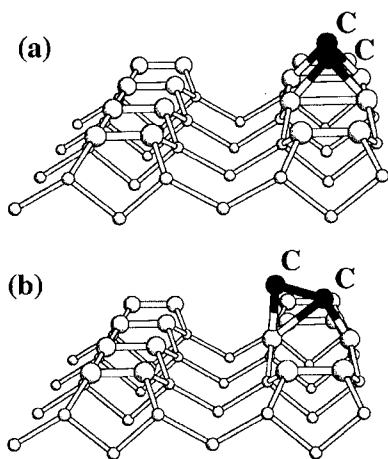
Figure 1. Stable geometries for C_2 adsorption on diamond (100) surface. Large circles denote surface atoms and black circles denote adsorbed atoms.

As a first step in studies of the growth processes involving nitrogen, we have investigated the adsorption of a CN molecule on the reconstructed diamond (100) surface using the stable C_2 sites as initial geometries. Since CN is a heteropolar molecule, insertions with either the carbon or nitrogen end down in the second configuration were considered. The most stable configuration for a CN molecule, shown in Fig. 2, has carbon forming a bond with the surface carbon atom.
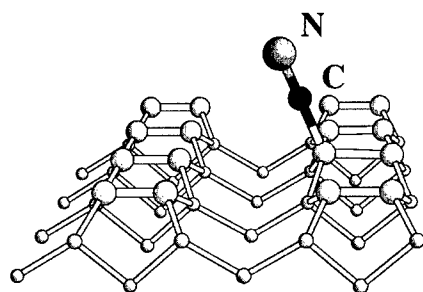
Figure 2. The most stable geometry of CN radical adsorbed on (100) diamond surface. Nitrogen is shown as a larger gray circle.

This orientation is more stable than the one with the nitrogen end down. The configuration parallel to the surface with both carbon and nitrogen atoms inserted into adjacent surface dimer bonds (analogous to Fig. 1a) is unstable and relaxes to the geometry shown in Fig. 2. The tilt angle of the adsorbed CN dimer is 23°. The binding energy is 4.86 eV, which is smaller than 6.43 eV and 5.44 eV for carbon dimer in the configurations shown in Fig.1a and 1b, respectively.

We have also considered the addition of C_2 dimers, as they would condense from the gas phase onto the surface in the presence of an adsorbed CN molecule with the intention to elucidate possible growth mechanisms. As a next step, we have simulated the adsorption of an additional C_2 dimer in the vicinity of a CN molecule on the surface. If the carbon dimer is attached beyond the immediate vicinity of the adsorbed CN molecule, i.e., on different sites, there are no chemical interactions between them.
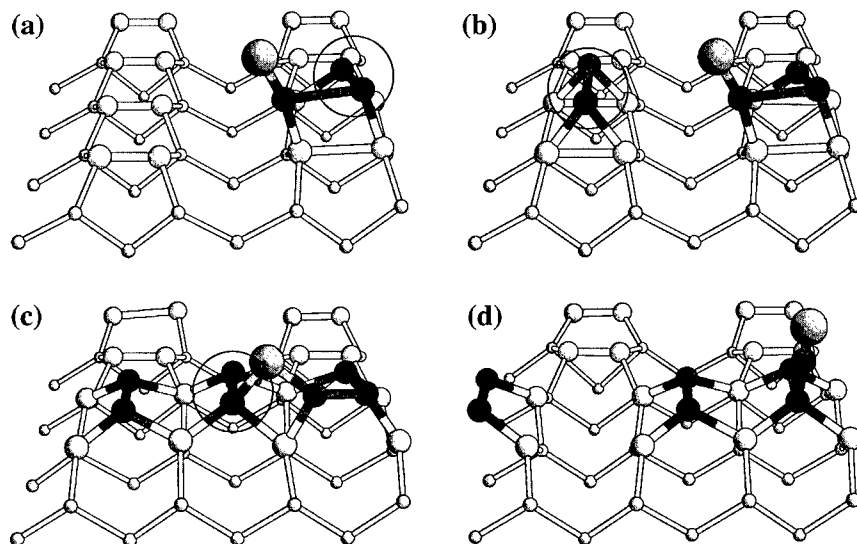
Figure 3. Steps in the CN-mediated diamond growth mechanism. The new adsorbed molecule at each step a)-c) is circled. The surface layer of the periodic supercell is shown larger. Atom notations are the same as in Figs. 1 and 2.

However, when the adsorbed C_2 shares a surface dimer with the CN molecule, as shown in Fig. 3a, the resulting complex is stable with a binding energy of 5.2 eV for the C_2 (10.1 eV for both adsorbates). One end of the carbon dimer forms bonds with the carbon atom of the CN molecule and the surface atom next to the CN adsorption site, whereas the other end is inserted into the adjacent surface dimer in the same fashion as in the configuration shown in Fig. 1a.

It is highly probable that there will be another C_2 adsorbed in the vicinity of the formed CN–C_2 complex, as shown in Fig. 3b. We will consider it as a next growth step although the order of these two events does not influence the reaction energetics and has no importance for the growth rate. This step is relevant in setting the stage for favorable adsorption of one more C_2 dimer that results in the structure shown in Fig. 3c. This geometry was optimized by the conjugate gradient method and turned out to be a local minimum. The binding energy for this C_2 attachment is 9.6 eV. This energy is larger than in the initial adsorption stages because the added C_2 leads to a more favorable tetrahedral coordination with its partners. Note that the nitrogen atom is attached to two carbon atoms in this structure. In order to probe the configuration space for other low-energy structures, a molecular dynamics simulation at 1000 K was performed starting from the structure in Fig. 3c. This led to the final structure shown in Fig. 3d. This structure is more stable than the starting configuration by 3.3 eV. Furthermore, one of the dimers performs a site hop. Examination of the structure shows that all adsorbed C_2's form part of the next layer of the growing diamond (100) surface. At the same time, the final configuration for the CN molecule is equivalent to the starting configuration shown in Fig. 2. As a net result, the CN dimer has moved onto the top of the next layer of the growing surface.

Thus, the CN-mediated growth mechanism, which is described above, consists of five steps: (i) adsorption of a CN molecule with its carbon end down; (ii) attachment of a C_2 dimer to the CN and the surface; (iii) independent attachment of another C_2 in the vicinity of the surface complex; (iv) bridging these adsorbates with another C_2 and formation of the second CN bond; and (v) low-barrier transformation of the structure to a more stable minimum with CN on top of the growing layer. All steps of this mechanism are exothermic.

The proposed mechanism provides initial insight into the growth process of UNCD. It can be inferred that nitrogen prefers to be located near the surface of the material rather than to be incorporated into the bulk. Indeed, the measured concentration of nitrogen in the material is very small (0.2% for 20% N_2 in the plasma) and it is thought to be located in the grain boundaries. Another result of this simulation is the conclusion that adsorbed CN species are much less reactive than the adsorbed C_2 species in Fig. 1b. This is due to the fact that N, which has a triple bond to C, would not interact with another molecule as easily as carbon that has two electrons available for chemical bonding in the latter configuration. The most reactive site after CN adsorption is the surface carbon atom next to the adsorbed CN molecule. Therefore, it is plausible that CN would block some surface sites that otherwise could be available for the nucleation of new crystallites and decrease the overall nucleation rate, while growth of the existing diamond lattice is promoted. Indeed, the experimental observation is that at higher nitrogen concentrations in the plasma the ratio of growth rate to nucleation rate increases, which leads to an increase in the crystallite size. Detailed investigations of other mechanisms of diamond growth from CN and C_2 precursors that would include a set of additional factors such as interactions of CN species, participation of hydrogen and reactions at other diamond surfaces are needed in order to fully characterize reactions involved in UNCD synthesis and provide opportunities to fully control the growth process.

CONCLUSIONS

Density-functional-based tight-binding calculations of CN radical adsorption on a diamond (100) surface gives a binding energy of 4.86 eV for the most stable geometry of the adsorbed molecule, which is a tilted vertical adsorption with the carbon end down. Further studies of C_2 adsorption in the vicinity of CN at the surface resulted in a growth mechanism with the CN molecule staying on top of the growing layer. These studies help to understand ultrananocrystalline diamond growth processes from hydrogen-poor plasmas.

ACKNOWLEDGMENT

REFERENCES

1. D. M. Gruen, S. Liu, A. R. Krauss, J. Luo and X. Pan, *Appl. Phys. Lett.,* **64**, 1502 (1994).
2. D.M. Gruen. *Annu. Rev. Mater. Sci.,* **29**, 211-59, (1999).
3. A.N. Goyette, J.E. Lawler, L.W. Anderson, D.M. Gruen, T.G. McCauley, D. Zhou, and A.R. Krauss, *J. Phys. D: App. Phys.,* **31**, 1975 (1998).
4. D. A. Horner, L. A. Curtiss, and D. M. Gruen, *Chem. Phys. Lett.,* **233**, 243 (1995).
5. P. Redfern, D. A. Horner, L. A. Curtiss, and D. M. Gruen, *J. Phys. Chem.,* **100**, 11654 (1996).
6. D. M. Gruen, P. C. Redfern, D. A. Horner, P. Zapol, and L. A. Curtiss, *J. Phys. Chem. B,* **103**, 5459 (1999).
7. M. Sternberg, M. Kaukonen, R. N. Nieminen, Th. Frauenheim, *Phys. Rev. B,* **63**, 165414 (2001).
8. S. J. Harris and D. G. Goodwin , *J. Phys. Chem.,* **97**, 23 (1993)
9. D. Porezag, Th. Frauenheim, Th. Kohler, G. Seifert, and R. Kaschner, *Phys. Rev. B,* **51**, 12947 (1995).
10. M. Elstner, D. Porezag, G. Jungnickel, J. Elsner, M. Haugk, Th. Frauenheim, S. Suhai, G. Seifert, *Phys. Rev. B,* **58**, 7260 (1998).
11. J. Furthmüller, J. Hafner and G. Kresse *Phys. Rev. B,* **53**, 7334 (1996).

AUTHOR INDEX

SUBJECT INDEX